The impact of planetary boundary layer dynamics on mountaintop trace gas variability

Temple Rosenberger Lee
Winchester, Virginia

Bachelor of Science, University of Virginia, 2007
Master of Science, University of Virginia, 2011

A Dissertation presented to the Graduate Faculty
of the University of Virginia in Candidacy for the Degree of
Doctor of Philosophy

Department of Environmental Sciences

University of Virginia
May, 2015

ABSTRACT

The variability of trace gases at surface monitoring stations is affected by multi-scale meteorological processes that are particularly complicated over mountainous terrain. A detailed understanding of the impact of meteorological processes on mountaintop trace gas variability is vital to help distinguish trace gas measurements affected by local pollutant sources from measurements representative of background mixing ratios. Although this knowledge is present for tall mountaintops, the trace gas variability at low mountaintops is more complicated because of their location at the transition between the planetary boundary layer (PBL) and free atmosphere (FA). The goal of this dissertation is to improve scientific understanding of the physical processes affecting trace gas mixing ratios sampled at low mountaintops. To fulfill this goal, this dissertation presents the first use of trace gas measurements from Pinnacles (38.61 N, 78.35 W, 1017 m above sea level [msl]), a mountaintop monitoring site in the Appalachian Mountains. This dissertation also uses in situ meteorological measurements from the site, trace gas and meteorological observations from nearby stations, and numerical simulations. Observations from Pinnacles indicate that wind shifts are an important driver of the diurnal trace gas variability. Cold fronts induce increases in CO and CO_2 mixing ratios of >100 ppb and >20 ppm, respectively, on timescales <3 h. Wind shifts from the northwest to the south on fair weather days yield daytime CO increases. On days without these wind shifts, CO mixing ratios decrease. On this subset of days, the height of the afternoon valley PBL height, z_i, relative to the ridgetop was expected to be a significant driver of the trace gas variability. To investigate this hypothesis, z_i estimates were needed for the Page Valley upwind of Pinnacles. To this end, a technique was developed to estimate z_i over the Page Valley using observations from Dulles Airport, IAD (38.98 N, 77.49 W, 87 m msl), which is the sounding station nearest Pinnacles, as well as output from reanalysis products and numerical simulations with the Weather Research and Forecasting model. Page Valley z_i were found to be 200-400 m higher than those from IAD, and thus an offset was applied to better estimate z_i over the Page Valley from the IAD soundings. The corrected z_i were then used to investigate the influence of PBL dilution on the trace

gas measurements from Pinnacles. Days with z_i below the ridgetop height have a daytime CO increase caused by the transport of valley PBL air to the mountaintop. Days with z_i exceeding the ridgetop exhibit a daytime CO decrease caused by dilution and entrainment of FA air. Case studies and numerical simulations with a Lagrangian Particle Dispersion Model (LPDM) were used to understand these physical processes in more detail and investigate how mountaintop measurements can best be used in applications requiring regionally-representative values. On days when z_i exceeds the ridgetop, afternoon trace gas measurements from low mountaintops are most similar to measurements from the tops of tall towers in flat terrain, based on comparisons between LPDM simulations with topography included and LPDM simulations from which the topography was removed. In summary, in this dissertation it is found that mesoscale to synoptic scale wind shifts are important drivers of the trace gas variability at low mountaintops and result in trace gas characteristics typical of other, much taller mountaintops. The wind shifts result in different upwind emission sources being sampled and can help estimate emissions and reduce flux estimate uncertainties over upwind areas. On days with constant winds and PBLs exceeding the ridgetop height, trace gas measurements have characteristics of monitoring sites in flat terrain and can be used in applications requiring regionally-representative values.

TABLE OF CONTENTS

LIST OF TABLES

LIST OF FIGURES

LIST OF ACRONYMS

ACARS	Aircraft Communications, Addressing, and Reporting System
AGL	Above Ground Level
ARL	Air Resources Laboratory
CALIOP	Cloud-Aerosol Lidar with Orthogonal Polarization
CALIPSO	Cloud-Aerosol Lidar and Infrared Pathfinder Satellite Observations
CASTNET	Clean Air Status and Trends Network
CFSR	Climate Forecast System Reanalysis
CI	Clearness Index
DEQ	Department of Environmental Quality
ECMWF	European Center for Medium-range Weather Forecast
EDUCT	Education in Complex Terrain Meteorology
ESRL	Earth System Research Laboratory
FA	Free Atmosphere
HRRR	High-resolution Rapid Refresh
HYSPLIT	Hybrid Single Particle Lagrangian Integrated Trajectory
IAD	Washington-Dulles International Airport
ICIMOD	International Centre for Integrated Mountain Development
LC	Luray Caverns
LIDAR	Light Detection and Ranging
LPDM	Lagrangian Particle Dispersion Model
LSM	Land Surface Model
LST	Local Standard Time
MBE	Mean Bias Error
MODIS	Moderate Resolution Imaging Spectroradiometer
MOU	Memorandum of Understanding
MSL	Mean Sea Level
MYJ	Mellor-Yamada-Janjić
MYNN2	Mellor-Yamada-Nakanishi-Niino Level 2.5

NAM	North American Model
NARR	North American Regional Reanalysis
NCAR	National Center for Atmospheric Research
NCEP	National Center for Environmental Prediction
NOAA	National Oceanic and Space Administration
NWP	Numerical Weather Prediction
PAN	Peroxyacetyl Nitrate
PBL	Planetary Boundary Layer
PNC	Particle Number Concentration
PPB	Parts per Billion
PPM	Parts per Million
RACCOON	Regional Atmospheric Continuous CO_2 Network
RAMMPP	Regional Atmospheric Measurement Modeling and Prediction Program
RUC	Rapid Update Cycle
SNP	Shenandoah National Park
SNP HQ	Shenandoah National Park Headquarters
TEMF	Total Energy Mass Flux
TM5	Transport Model 5
USGS	United States Geological Survey
UTC	Coordinated Universal Time
UVA	University of Virginia
WRF	Weather Research and Forecasting
YSU	Yonsei University

LIST OF SYMBOLS AND VARIABLES

θ	potential temperature
θ_v	virtual potential temperature
CO	carbon monoxide
CO_2	carbon dioxide
g	gravitational acceleration
LHF	latent heat flux
O_3	ozone
q	specific humidity
R_b	bulk Richardson number
R_c	critical Richardson number
SHF	sensible heat flux
SWR	shortwave radiation
T	temperature
TKE	turbulent kinetic energy
u	zonal wind component
u_*	friction velocity
v	meridional wind component
WD	wind direction
WS	wind speed
z	height
z_i	planetary boundary layer height

ACKNOWLEDGEMENTS

This dissertation would not have been possible without the contributions of many people. I first thank my adviser, Stephan De Wekker, for his guidance, encouragement, intellectual support, and for providing me the opportunity to work on many exciting projects. Many thanks to the other committee members, Robert Davis, Sergei Egorov, and Todd Scanlon, for their insights, support, and feedback.

Instrumenting a 17 m tower at a mountaintop and then maintaining the extensive suite of trace gas and meteorological measurements for nearly 7 years, in addition to a myriad of other supporting measurements across the region, was a significant endeavor that would not have been possible without the support of many individuals. Many thanks to Jonathan Kofler and Jonathan Williams (NOAA ESRL) for installing the CO and CO_2 monitoring equipment at our research site in 2008 and for the many conversations on the phone to help troubleshoot sporadic problems with the monitoring equipment; Arlyn Andrews (NOAA ESRL) for data quality control; Alan Williams and Elizabeth Garcia (NPS) for visits to the site when weather conditions made it impossible for me to access the site; Jim Schaberl and Jeb Wofford (formerly at NPS) for assistance with site permits; William Brown (NCAR) for the deployment of the wind profiler and sounding system during the 2009 EDUCT field experiment; Stephen Chan and Daniel Muth (formerly at UVA) for providing insights about instrument and tower maintenance during my early years as a graduate student; Matthew Lingvai and Željko Večenaj (formerly at UVA) for help with the installation of the on-site meteorological instruments and the construction of the on-site shed in 2008; Calvin Peters (formerly at Virginia Tech) for helping in the design and fabrication of a replacement roof for the shed in 2013; and to the many UVA undergraduate students with whom I have worked and who assisted with field work, including Lewis Armistead, Nathan Brown, Sidney Bush, Brittany Craven, Sydney Delmar, Kelsey Everard, Effie George, Douglas Lawrence, Angang Li, Christopher Muir, Amelia Nystrom, Elizabeth Stoner, Patricia Tertell, and Ralph Turlington.

I especially want to thank and acknowledge two individuals, Željko Večenaj and Sandip Pal. When I encountered several obstacles while completing this dissertation research, Željko and Sandip helped to keep me focused on my goal of completing my PhD and provided a critical role in my development as a scientist.

I acknowledge former members of the De Wekker lab group, both past and present, including Nevio Babić, Mohamadou Diallo, Kevin Godwin, Yufei He, Stephanie Phelps, Mark Sghiatti, Guan Song, and Michael van den Bossche; the many colleagues with whom I have collaborated, including Arlyn Andrews (NOAA ESRL); Russell Dickerson (University of Maryland); Xinrong Ren (NOAA ARL); David Hondula (Arizona State University); Adrianne Brand, Evan Grant, and Ruscena Wiederholt, (USGS); Jeb Wofford (formerly at NPS); Bjørn-Gustaf Brooks and Ankur Desai (University of Wisconsin); and others who contributed intellectually to this work, particularly Jennie Moody (UVA) and Arnico Panday (ICIMOD).

I thank the UVA Department of Environmental Sciences administrative staff, especially Cindy Allen, Debra Shifflett, David Smith, Jerry Stenger, William Tomanek, and Gerald Williamson, who supported this research by helping order and ship meteorological instruments, facilitating reimbursement for my many trips to our field sites, helping to ship calibration cylinders to NOAA, providing computing assistance, and assisting with the myriad of other tasks vital to keeping things running smoothly.

I acknowledge and thank my funding sources, including the National Oceanic and Atmospheric Administration, the National Science Foundation, the National Park Service, Virginia Uranium Incorporated, and the UVA Environmental Sciences Department.

I am grateful for the friendships of many individuals, but especially Nevio Babić, Abi Bhattachan, Kevin Godwin, Stephanie Phelps, David Seekell, and Mark Sghiatti. Whether it was through light-hearted banter in the office or discussions about H-indices over too many cups of coffee, the presence of these people helped to make graduate school a positive experience. Many thanks are owed to my girlfriend, Sarah Hemenway, for her encouragement and for patiently tolerating my ramblings on installing towers in cow fields and the intricacies of numerical weather prediction models.

Finally, I thank my family for their unending love and support throughout my entire educational career, including my sister Gretchen and my uncle Michael, but especially my parents.

DEDICATION

For listening to my nightly weather reports as a child, for providing the love and support that helped me to overcome many hurdles in graduate school, and for always encouraging me to pursue my lifelong dream of becoming an atmospheric scientist, I dedicate this dissertation to my mom.

EPIGRAPH

Forsan et haec olim meminisse iuvabit.

—Virgil

Line 203, Book I, *Aeneid*

CHAPTER 1

INTRODUCTION

1.1. Background and motivation

The change in the concentration of a passive trace gas with time in the planetary boundary layer (PBL) over a flat surface depends upon turbulent mixing processes including convection, entrainment, horizontal advection, and the change in sources and sinks of this gas. For a trace gas that is emitted continuously and in the absence of horizontal advection, there is an inverse relationship between PBL height and the near-surface trace gas concentration (e.g. Gibert et al., 2007). At sunrise, surface heating results in the growth of the PBL. As the depth of the PBL increases due to mechanically and convectively generated turbulence, trace gases become mixed over this growing volume of air, and the concentrations decrease. The rate of decrease in the trace gas concentration slows as the PBL reaches a quasi-equilibrium height during the afternoon. Around sunset, the cooling of the Earth's surface results in the formation of a near-surface nocturnal PBL, above which is located the residual layer which has the properties of the daytime well-mixed PBL. The formation of a near-surface stable layer favors trace gas accumulation near the surface which continues during the nighttime, resulting in increasing near-surface concentrations. This diurnal pattern of trace gas variability, summarized in Figure 1.1a, has been found to occur for a variety of trace gases in many previous studies at sites in flat terrain (e.g. Pochanart et al., 2003; Volz-Thomas et al., 2003; Elanksy et al., 2007; Popa et al., 2010; Winderlich et al., 2010; Sahu et al., 2011; Pal et al., 2015).

Although there is considerable knowledge about the trace gas variability over flat terrain, trace gas variability over mountainous regions is less well-understood due to the local-to mesoscale transport processes occurring in these areas (e.g. De Wekker et al., 1998; Whiteman, 2000; Gangoiti et al., 2001; De Wekker et al., 2005; Rotach and Zardi, 2007; van der Molen and Dolman, 2007; De Wekker et al., 2009; Chow et al., 2013). Over valleys, the growth of the daytime PBL and resulting decrease in pollutant (i.e. trace gases and aerosols) concentration (e.g. Gupta et al., 2006; Pal et al., 2014) is complicated by the presence of up-valley and down-valley flows (e.g. McKendry et al., 1998; Pérez-Landa et al., 2007). Thermally-driven up-valley flows transport pollutants up the valley during the daytime, and down-valley flows transport pollutants down the valley during the nighttime (e.g. Banta et al., 1997; McKendry et al., 1998; Gohm et al., 2009). These flows can be affected by synoptic-scale flows (e.g. Schmidli et al., 2009), flow through tributaries connected to the main valley (e.g. Fast et al., 2006), cold air pooling, and dynamically-forced flows (e.g. Whiteman, 2000; De Wekker and Mayor, 2009; Gohm et al., 2009; Chow et al., 2013). At mountaintops, the variability of pollutants is oftentimes affected by pollutant concentrations over the upwind valley or adjacent plain. Whereas convective mixing within the valley PBL has been cited as one of the dominant causes for pollutants being transported from the valley PBL to the mountaintop during the daytime (e.g. Baltensperger et al., 1997; Seibert et al., 1998), other processes, including slope flows (e.g. Kleissl et al., 2007; De Wekker et al., 2009), mountain venting (e.g. De Wekker et al., 2004; Henne et al., 2005), and wind shifts on the mesoscale (e.g. Schmidt et al., 1996) to synoptic-scale (e.g. Zellwegger et al., 2003) also affect pollutant variability at mountaintops on diurnal timescales.

Gaining knowledge about the trace gas variability over mountaintops is vital because mountaintops oftentimes remain above the PBL in the overlying free atmosphere (FA) and thus can provide important information about background trace gas mixing ratios, unlike valley or slope locations. Understanding which mountaintop measurements represent valley PBL air and which measurements represent FA air is important to, e.g. studying long term trends in FA trace gas mixing ratios (e.g. Gilge et al., 2010; Dils et al., 2011; Qi et al., 2012; Zhang and Zhou, 2013) and for using the measurements in inverse carbon transport models (Peters et al., 2007; Brooks et al., 2012) and in air chemistry models (e.g. Novelli et al., 1998). Many of these models have a coarse spatial resolution, on the scale of 1 x 1° grid spacing (e.g. Peters et al., 2007), which prevents them from capturing the aforementioned local- to mesoscale processes which significantly impact mountaintop trace gas and aerosol variability (e.g. Thoning et al., 1989; Baltsensperger et al., 1997; Lugauer et al., 1998; De Wekker et al., 2009). Thus, there exists no diurnal signature in trace gas variability in cases when these local- to mesoscale transport processes are absent and when the PBL is well below the mountaintop, as shown in previous studies (e.g. Baltsensperger et al., 1997; Lugauer et al., 1998) and summarized in Figure 1.1b. However, when there is a large influence of PBL air from adjacent valley(s) at the mountaintop, trace gas mixing ratios at the mountaintop increase during the daytime. This increase, illustrated in Figure 1.1c, has been reported for many trace gas species (e.g. Weiss-Penzias et al., 1996; Necki et al., 2003; Obrist et al., 2008) and aerosols (e.g. Baltensperger et al., 1997; Lugauer et al., 1998; Coen et al., 2011; Gallagher et al., 2011).

From these previous studies, one may infer that the PBL height relative to a mountaintop is an important driver of the diurnal trace gas variability at mountaintop locations and affects the degree to which mountaintop trace gas measurements are representative of FA air. In the scenario shown in Figure 1.1b, the absence of valley PBL influence results in mountaintop trace gas mixing ratios being representative mostly of FA values (e.g. Baltensperger et al., 1997; Lugauer et al., 1998). This pattern is typical of many tall mountaintops (e.g. Fang et al. 2013) that are isolated from the effects of pollutants emitted within the PBL over the upwind adjacent valleys. However, mountaintop trace gas variability becomes more complicated when valley PBL air affects the mountaintop measurements. Trace gas measurements made during situations when the valley PBL influences the mountaintop, as shown in Figure 1.1c, are expected to be representative of valley trace gas measurements during the daytime (e.g. Thoning et al., 1989) and representative of either residual layer or FA measurements during the nighttime. These scenarios occur either when the valley PBL is deep, e.g. during the warm season (e.g. Baltensperger et al., 1997; Lugauer et al., 1998), or when the mountaintop has low prominence (i.e. the mountaintop's height above the surrounding valley or plain).

Much of the scientific understanding on mountaintop trace gas variability comes from long-term mountaintop observation platforms, which are typically installed at tall mountaintops away from PBL influences. Mauna Loa, Hawaii, is among the best-known mountaintop trace gas monitoring sites because it has the longest trace gas record of any monitoring site globally and has long been viewed as a bellwether for long-term trends in atmospheric CO2 mixing ratio (e.g. Keeling, 1978). However, trace gases, in addition to

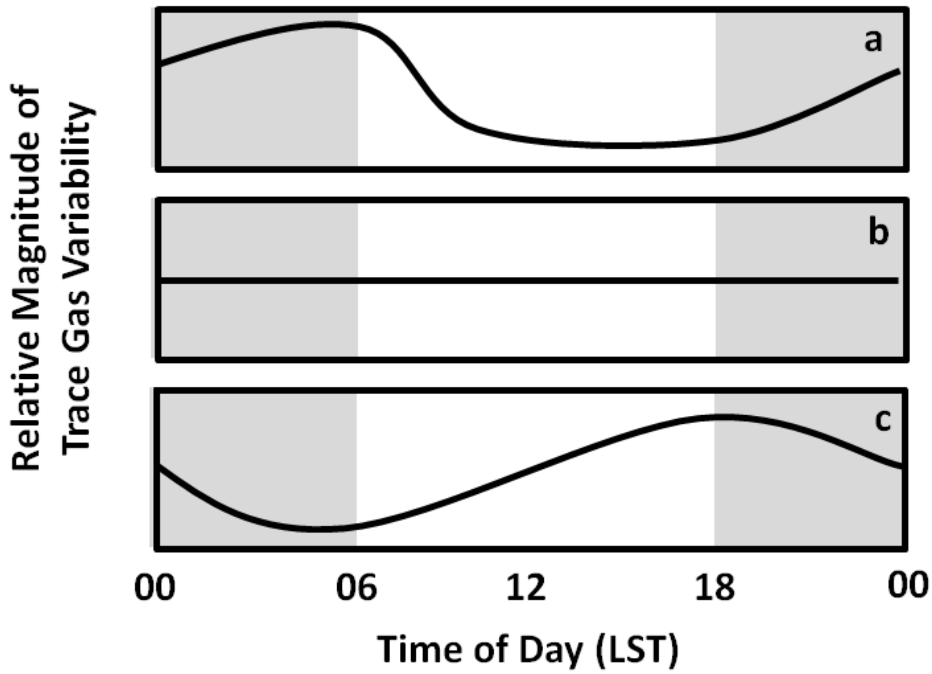

Figure 1.1: Conceptual model of the diurnal trace gas variabilty starting with a set concentration of trace gas and assuming no advection or sources or sinks for a site in flat terrain (a), a mountaintop without valley PBL influence (b), and a mountaintop with valley PBL influence (c). Shaded and non-shaded areas represent nighttime and daytime, respectively.

aerosols, are monitored at many other sites globally (Table 1.1). These measurements come not only from isolated oceanic mountaintops, e.g. Mauna Loa (Keeling et al. 1976; Keeling et al., 1978) or the Réunion Island observatory (e.g. Bhugwant et al., 2001), but also from continental mid-latitude monitoring sites. For example, CO_2 mixing ratios have been measured at Schauinsland, a mountaintop in the German Black Forest since 1972 (e.g. Schmidt et al., 2003), and trace gas and aerosol monitoring stations have existed for >20 years at mountaintops in the European Alps (e.g. Kasper and Pauxbaum, 1998; Lugauer et al., 1998; Nyeki et al., 1998; Apadula et al., 2003). Whereas most of the mountaintop trace gas and/or aerosol monitoring sites are located in the Northern Hemisphere (Figure 1.2) where the majority of Earth's landmass and thus major mountain ranges are located, three mountaintop monitoring sites are located in the Southern Hemisphere, i.e. Chacaltaya Mountain in the Bolivian Andes (e.g. Adams et al., 1977), Africa's Mount Kenya (e.g. Henne et al., 2008a), and the Réunion Island observatory (e.g. Bhugwant et al., 2001).

Since 2000, there has been an increasing number of new mountaintop trace gas and aerosol monitoring stations installed globally. Trace gas monitoring sites were installed in China in the early 2000s at Mount Tai, Mount Huang, and Mount Hua (Wang et al., 2011). A network of CO_2 monitoring sites was installed in the Rocky Mountains of the western US in 2005 as part of the Regional Atmospheric Continuous CO_2 Network in the Rocky Mountains (Rocky RACCOON) (e.g. De Wekker et al., 2009; Brooks et al., 2012), and trace gas and air chemistry measurements began at Mount Bachelor, a mountaintop in the Oregon Cascades, in 2004 (e.g. Jaffe et al., 2005). There has also been a trend toward installing monitoring stations at low mountaintops since 2000. Measurements began in 2006 at Ochsenkopf (1024 m msl), a monitoring station in the Fichtelgebirge Mountains of northern Bavaria in Germany (e.g. Thompson et al., 2009), and in 2008 at Pinnacles (1017 m msl), a trace gas monitoring site in the Appalachian Mountains of the eastern US (Lee et al., 2012).

Table 1.1: Summary of worldwide mountaintop monitoring stations, elevation, beginning of trace gas or aerosol monitoring, variable(s) sampled, and the reference. In this table, only mountaintops which have yielded at least one peer-reviewed publication are included. Note that for many mountaintops (e.g. Mauna Loa), there exist multiple publications that refer to or use the measurements. In these instances, the first citation that refers to multi-year aerosol and/or trace gas measurements is listed.

Station Name	Coordinates	Location	Elevation (m msl)	Start of trace gas/aerosol measurements	Measurements	Reference
Chacaltaya Mountain	16.4 S, 68.1 W	Andes, Bolivia	5421	1975	Aerosols	Adams et al., 1977
Pyramid Observatory	28.0 N, 86.8 E	Himalayas, Nepal	5050	2006	Aerosols, Trace gas	Bonasoni et al., 2008
Colle Gnifetti	45.9 N, 7.9 E	Alps, Switzerland	4452	1988	Aerosols	Lugauer et al., 1998
Qilian Shan	39.5 N, 96.5 E	Kunlun Mountains, China	4180	2005	Aerosols	Xu et al., 2013
Mount Waliguan	36.3 N, 100.9 E	Tibetan Plateau, China	3816	1994	Trace gas	Zhou et al., 2003
Mount Fuji	35.4 N, 138.7 E	Honshu Island, Japan	3776	2002	Trace gas	Igarashi et al., 2006
Mount Kenya	0.062 N, 37.3 E	Kenya	3678	2002	Trace gas,	Henne et al.,

					Meteorology	2008a
Niwot Ridge	40.1 N, 105.6 W	Rocky Mountains, USA	3523	2005	CO_2	Brooks et al., 2012
Plateau Rosa	46.0 N, 7.7 E	Pennine Alps, Switzerland	3480	1989	CO_2	Apadula et al., 2003
Jungfraujoch	46.5 N, 8.0 E	Bernese Alps, Switzerland	3471	1995	Trace gas, Aerosols	Nyeki et al., 1998
Mauna Loa	19.5 N, 155.6 W	Hawaiian Island	3397	1957	CO_2	Keeling et al., 1976
Hidden Peak	40.6 N, 111.7 W	Rocky Mountains, USA	3351	2005	CO_2	Brooks et al., 2012
Storm Peaks Lab	40.5 N, 106.7 W	Rocky Mountains, USA	3210	1995	CO_2	Obrist et al., 2008
Sonnblick	47.1 N, 13.0 E	Hohe Tauern Mountains, Austria	3105	1993	Trace gas, Aerosols	Kapser and Puxbaum, 1998
Zugspitze	47.4 N, 11.0 E	Wetterstein Mountains, Germany	2962	1978	Trace gas, Aerosols	Gilge et al., 2010
Basic Environmental Observatory (BEO) Moussala	42.2 N, 23.6 E	Rila Mountains, Bulgaria	2925	2006	Trace gas, Meteorology	Angelov et al., 2011
Pic du Midi	42.9 N, 0.14 E	Pyrenees, France	2877	1982	Trace gas	Marenco et al., 1994
Lulin	23.5 N, 120.9 E	Taiwan	2862	2006	Trace gas	Ou Yang et al., 2011
Mount Lemmon	32.4 N, 110.8 W	Santa Catalina Mountains, USA	2790	2002	Aerosols	Shaw, 2007
Mount Bachelor	44.0 N, 121.7 W	Cascade Mountains	2764	2004	Aerosols	Fischer et al., 2010
Réunion	21.2 S, 55.7 E	Réunion Island	2632	1997	Trace gas, Aerosols	Bhugwant et al., 2001
Izana Observatory	28.3 N, 16.5 W	Canary Islands	2390	1990	Trace gas, Aerosols	Kentarchos et al., 2000
PICO-NARE	38.4 N, 28.4 W	Azores	2225	2001	Trace gas	Kliessl et al., 2007
Whistler	50.1 N, 123.0 E	Coast Mountains, British Colombia	2182	2002	Aerosols	Gallagher et al., 2011
Mount Cimone	44.2 N, 10.7 E	Apennine Mountains, Italy	2165	1978	CO_2	Ciattaglia et al., 1987
Mount Hua	34.5 N, 110.1 E	Shaanxi Province, China	2064	2004	O_3	Li et al., 2007
Kasprowy	49.2 N , 20.0 E	Western Tatras, Poland	1987	1994	Trace gas, Meteorology	Necki et al., 2003
Naintal	29.4 N, 79.5 E	Himalayas	1958	2009	Trace gas, Meteorology	Sarangi et al., 2014
Mount Washington	44.3 N, 71.3 W	Appalachian Mountains, Eastern US	1917	1987	O_3	Fischer et al., 2004
Mount Huang	30.1 N, 118.2 E	Anhui Province, China	1836	2004	O_3	Li et al., 2007
Mount Abu	24.7 N, 72.8 E	Rajasthan, India	1680	2009	Trace gas	Francis, 2012
Mount Tai	36.3 N, 117.1 E	Shandong Province, China	1534	2003	Trace gas	Gao et al., 2005

Whiteface	44.4 N, 73.9 W	Appalachian Mountains, Eastern US	1483	1961	Trace gas, Precipitation chemistry, Meteorology	Gong and Demerjian, 1997
Puy-de-Dôme	45.8 N, 2.9 E	French Alps	1464	2002	Trace gas, Aerosols	Venzac et al., 2011
Schauinsland	47.9 N, 7.9 E	Black Forest, Germany	1284	1972	CO_2	Schmidt et al., 2003
Hornisgrinde	48.6 N, 8.2 E	Black Forest, Germany	1164	1992	Trace gas	Vögtlin et al., 1996
Ochsenkopf	50.0 N, 11.8 E	Black Forest, Germany	1024	2006	Trace gas Meteorology	Thompson et al., 2009
Pinnacles	38.6 N, 78.4 W	Appalachian Mountains, Eastern US	1017	2008	Trace gas, Meteorology	Lee et al., 2012
Hohenpeissenberg	48.1 N, 11.1 E	Bavaria, Germany	985	1971	Trace gas	Gilge et al., 2010

As summarized in Figure 1.2, many of the mountaintops where trace gases and aerosols are measured are >1500 m above mean sea level (msl) (e.g. Thoning et al., 1989; Baltensperger et al., 1997; Balzani Lööv et al., 2008; Henne et al., 2008b; Obrist et al., 2008; De Wekker et al., 2009) and have high topographic prominence. Thus, much of our conceptual understanding of mountaintop trace gas variability is based on observations made at these locations which typically remain above the valley PBL away from local trace gas sources and sinks (e.g. Baltensperger et al., 1997; Luguaer et al., 1998). In contrast with these mountaintops, mountaintops with low prominence oftentimes lie at the transition between the regional PBL and overlying FA. Thus, the trace gas variability at these locations is complex (e.g. Schmidt et al., 1996) and is arguably more complicated than the trace gas variability over flat terrain or at other, much taller mountaintops. Acquiring knowledge about the controls on the trace gas variability at low mountaintops is vital if the trace gas measurements from these locations are to be reliably used in models requiring background trace gas mixing ratios. In addition, many of the physical processes occurring over mountainous terrain that impact the trace gas variability are poorly resolved by numerical models (e.g. Chow et al., 2013). Knowledge of the drivers of trace gas variability at mountaintop monitoring sites provides vital information on how to best use mountaintop trace gas observations in modeling applications (e.g. Pillai et al., 2011).

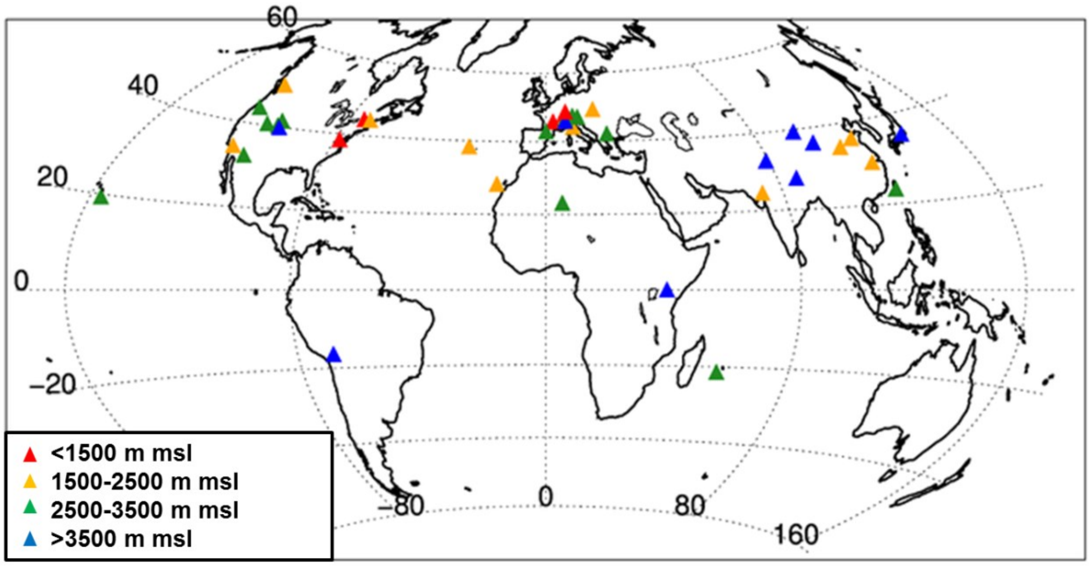

Figure 1.2: Global distribution of mountaintop trace gas and aerosols monitoring locations identified in Table 1.1 color coded by elevation. Mountains <1500 m above mean sea level (msl), 1500-2500 m msl, 2500-3500 m msl, and >3500 m msl are denoted by red, orange, green, and blue triangles, respectively.

1.2. Dissertation goals and research questions

Based on the previous section, one may conclude that the drivers of the trace gas variability, particularly at low mountaintops, are not well-understood. Therefore, the goal of this dissertation is improve scientific understanding of the trace gas variability at low mountaintops by studying the dominant drivers affecting this variability. To this end, this dissertation is divided into three sections which have a specific goal and questions that are answered to achieve each goal. In each of the three sections, there are 1-2 chapters. Each chapter is self-contained and has its own abstract, introduction, methods, results, conclusions, and acknowledgements. Nearly all of the work presented in this dissertation was completed while the author of this dissertation was a PhD student at the University of Virginia between 2011 and 2015. The exception was Chapter 2; approximately half of the work presented in Chapter 2 was completed while the author was an MS student and thus appears in the author's MS thesis (i.e. Lee, 2011).

The goal of the first section of the present dissertation (Chapter 2 and 3) is to understand the characteristics of the CO and CO_2 mixing ratio at a low mountaintop. In this section of the dissertation, the following questions are addressed:

- How do CO and CO_2 mixing ratios measurements from a low mountaintop vary diurnally and seasonally?
- What meteorological factors affect the CO and CO_2 variability at a low mountaintop?

The goal of the second section is to investigate the relationship between PBL height and the diurnal mountaintop trace gas variability. This section (Chapter 4 and 5) addresses the following questions:

- What are the characteristics of PBL height in the region surrounding a low mountaintop?
- How does the PBL height relative to the mountaintop affect the diurnal variability of trace mixing ratios measured at a mountaintop?

The goal of the third section of this dissertation is to determine how trace gas mixing ratio measurements from low mountaintops can best be used in applications requiring regionally-representative values. In this section (Chapter 6), the following question is addressed:

- How does the PBL height relative to the ridgetop affect the degree to which mountaintop trace gas measurements are representative of the regional PBL?

This dissertation concludes with a summary of the salient findings from each chapter, a discussion of the implications of this dissertation’s findings to the broader scientific community, and avenues for future research directions in Chapter 7.

1.3. Research approach

To fulfill the goals and answer the questions enumerated in Section 1.2, this dissertation uses a selection of trace gas and meteorological data sets, numerical modeling simulations with the Weather Research and Forecasting (WRF) model (Skamarock et al., 2008), a state-of-the-art atmospheric mesoscale model, and the Lagrangian particle dispersion model (LPDM) FLEXPART (Stohl et al., 1998; Stohl et al., 2005). The dissertation presents the first use of data from Pinnacles (38.61 N, 78.35

W, 1017 m msl), an observation site at a mountaintop in the southern Appalachians at which CO and CO_2 mixing ratios have been monitored continuously since 2008. As the measurements from Pinnacles are essential to the research presented in this dissertation, the Appendix summarizes the maintenance and quality assurance and quality control procedures that were followed at Pinnacles by the author of this dissertation during the site's operation from July 2008 through March 2015. The procedures described in the Appendix were vital to ensure the high-quality data set used in this dissertation and need to continue to be followed to ensure that high-quality measurements from the site continue in the future.

CHAPTER 2

CARBON DIOXIDE VARIABILITY DURING COLD FRONT PASSAGES AND FAIR WEATHER DAYS AT A FORESTED MOUNTAINTOP SITE[1]

[1] Modified from Lee, T. R., De Wekker, S. F. J., Andrews, A. E., Kofler, J., and Williams, J. 2012. Carbon dioxide variability during cold front passages and fair weather days at a forested mountaintop site. *Atmos. Environ.* **46**, 405-416.

Abstract

This study describes temporal carbon dioxide (CO_2) changes at a new meteorological site on a mountaintop in the Virginia Blue Ridge Mountains during the first year of measurements. Continental mountaintop locations are increasingly being used for CO_2 monitoring, and investigations are needed to better understand measurements made at these locations. We focus on CO_2 mixing ratio changes on days with cold front passages and on fair weather days. Changes in CO_2 mixing ratios are largest during cold front passages outside the growing season and on clear, fair weather days in the growing season. 67% (60%) of the frontal passages during the non-growing (growing) season have larger postfrontal than prefrontal CO_2 mixing ratios. The increase in CO_2 mixing ratio around the frontal passage is short-lived and coincides with changes in CO and O_3. The CO_2 increase can therefore be used as an additional criterion to determine the timing of frontal passages at the mountaintop station. The CO_2 increase can be explained by an accumulation of trace gases along frontal boundaries. The magnitude and duration of the CO_2 increase is affected by the wind speed and direction that determine the source region of the postfrontal air. Southward-moving fronts result in the largest prolonged period of elevated CO_2, consistent with the postfrontal advection of air from the Northeastern United States where anthropogenic contributions are relatively large compared to other areas in the footprint of the mountaintop station. These anthropogenic contributions to the CO_2 changes are confirmed through concurrent CO measurements and output from NOAA's CarbonTracker model.

2.1. Introduction

Changes in carbon dioxide (CO_2) at a given location are determined by a combination of meteorological, biological, and anthropogenic processes on a wide range of temporal and spatial scales. On a diurnal time scale, respiration and shallow nocturnal boundary layers result in an increase in CO_2 mixing ratio during the night, whereas daytime boundary layer growth and uptake of CO_2 contribute to a decrease in CO_2 mixing ratio during the day. These diurnal changes are most pronounced during fair weather conditions in the growing season. During the winter when photosynthetic activity is small or absent, anthropogenic emissions can cause large diurnal changes. Synoptic events, particularly cold front passages, also contribute to CO_2 changes and are sometimes found to be larger than the typical diurnal changes. Hurwitz et al. (2004) and Wang et al. (2007) noted large increases in CO_2 mixing ratio at Park Falls—a site in a mixed forested ecosystem in northern Wisconsin—during synoptic events. Parazoo et al. (2008) studied CO_2 changes during cold front passages in the summer and winter at 16 monitoring sites and found that CO_2 mixing ratios decreased at some sites and increased at other sites. Geels et al. (2004) concluded that both the magnitude of the synoptic CO_2 changes and the mechanisms affecting these CO_2 changes vary among sites. These studies have attributed the CO_2 changes to vertical downmixing and horizontal advection of CO_2, to changes in local and upwind CO_2 fluxes due to changes in local weather, and to CO_2 accumulation along frontal boundaries caused by deformational flow.

The amplitude of the diurnal CO_2 cycle typically decreases with height above the surface. For example, at the aforementioned site in northern Wisconsin, typical summer changes in CO_2 at 30 m above ground level (agl) are as high as 40 ppm, decreasing to only 7 ppm 396 m agl during the same time period (Hurwitz et al., 2004). At locations high enough within the afternoon boundary layer where vertical gradients in CO_2 mixing ratios are small, CO_2 measurements are assumed to be representative of spatial scales up to 10^6 km^2 (Gloor et al., 2001). These principles have been the basis of the establishment of a network of tall towers (100-400 m in height) beginning in the 1990s to monitor CO_2 mixing ratios in the continental US (Bakwin and Tans, 1995; Bakwin et al., 1998; Davis et al., 2003; Andrews et al., 2009). Data from this tall tower network are crucial for the estimation of regional and continental carbon fluxes in inverse carbon transport models (e.g. Peters et al., 2007; Schuh et al., 2010).

Recently, continuous monitoring stations have been established at mountaintop stations in the continental US (Stephens et al., 2005; Andrews et al., 2009). It is well-known that CO_2 changes on diurnal or smaller time scales can be very different at individual mountaintop locations, warranting the need for careful evaluation of measurements at these locations (e.g. Keeling et al., 1976; Thoning et al., 1989). Studies on CO_2 changes in mountainous terrain have primarily focused on the effects of thermally-driven flows under anti-cyclonic synoptic conditions. Upslope flows can cause an increase or decrease in CO_2 mixing ratios at a mountaintop location depending, for example, on whether the advected air is rich in respired or otherwise emitted CO_2 or if CO_2 is depleted by photosynthetic uptake (Keeling et al., 1976; Sun et al., 2007; De Wekker et al., 2009; Saito et al., 2009). CO_2 changes during frontal passages at mountaintop stations have not been studied except for a case study by Brooks et al. (2010). They found a step-like increase in CO_2 mixing ratio 1-2 days prior to a summer cold front passage at a mountaintop location in the central Rocky Mountains which they attributed to decreased CO_2 uptake upwind of the mountaintop location.

A systematic investigation of CO_2 changes during fair weather days and during cold front passages at a mountaintop location is useful for several reasons. For example, based on previous studies mentioned above, such an investigation can help estimate regional CO_2 fluxes in the footprint of that location and elucidate the relative importance of anthropogenic and biogenic CO_2 sources to the changes in the presence of other trace gas measurements such as CO. Also, for an accurate estimation of regional fluxes, it is important that CO_2 changes are captured in carbon transport models. Based on observational studies in flat terrain, we expect that these CO_2 changes are large during fair weather days and frontal passages.

In this study, we investigate these CO_2 changes at a new mountaintop site in the central Appalachian Mountains during its first year of operation with the objectives to 1) determine the characteristics of the CO_2 changes during cold front passages and fair weather days and 2) elucidate the causes for the observed CO_2 changes using output from a backward trajectory model and a carbon transport model.

2.2. Data and methods

2.2.1. Observations

Measurements were obtained from an instrumented 17 m tower at Pinnacles (38.61 N, 78.35 W), located along the crest of the Virginia Blue Ridge Mountains 1017 m above mean sea level (msl) in a mixed deciduous forest with a mean canopy height of about 14 m. East of the Blue Ridge is the Virginia Piedmont; to the west is the approximately 40 km wide Shenandoah Valley that is bifurcated by the shorter Massanutten Mountain range approximately 20 km west of Pinnacles (Figure 2.1). The climate is temperate with approximately 130 cm of rainfall annually along the ridges (National Cartography and Geospatial Center, 1999) evenly distributed throughout the year. Much of the precipitation is caused by convective events during the summer and by frontal systems in the remainder of the year. Skyline Drive, a tourist road that runs southwest-northeast along the crest of the Blue Ridge, is 120 m southeast of Pinnacles. Analyses of traffic counter data, obtained from the National Park Service, showed that weekends have 2-3 times the number of cars as weekdays. Nonetheless, an unpaired two-sample t-test confirms there are no statistically significant differences in CO_2 mixing ratios on weekdays and weekends, which is consistent with previous studies in the region that have found no relation between local traffic emissions and CO (e.g. Poulida et al., 1991) or O_3 (e.g. Cooper, 1997).

Meteorological measurements at Pinnacles began in July, 2008, and the continuous CO_2 monitoring system was added in late August, 2008. Meteorological measurements include temperature and humidity at 4 heights (2 m, 5 m, 10 m, and 17 m agl), wind speeds at 2 heights (10 m and 17 m agl), barometric pressure, rainfall, and incoming and outgoing short- and long-wave radiation. These instruments sample at 1 Hz, and half-hour averages are stored on a data logger. Data from a CSAT sonic anemometer at 17 m agl and an open-path LI-COR 7500 water vapor and CO_2 gas analyzer are stored at 10 Hz and used to estimate latent heat and CO_2 fluxes.

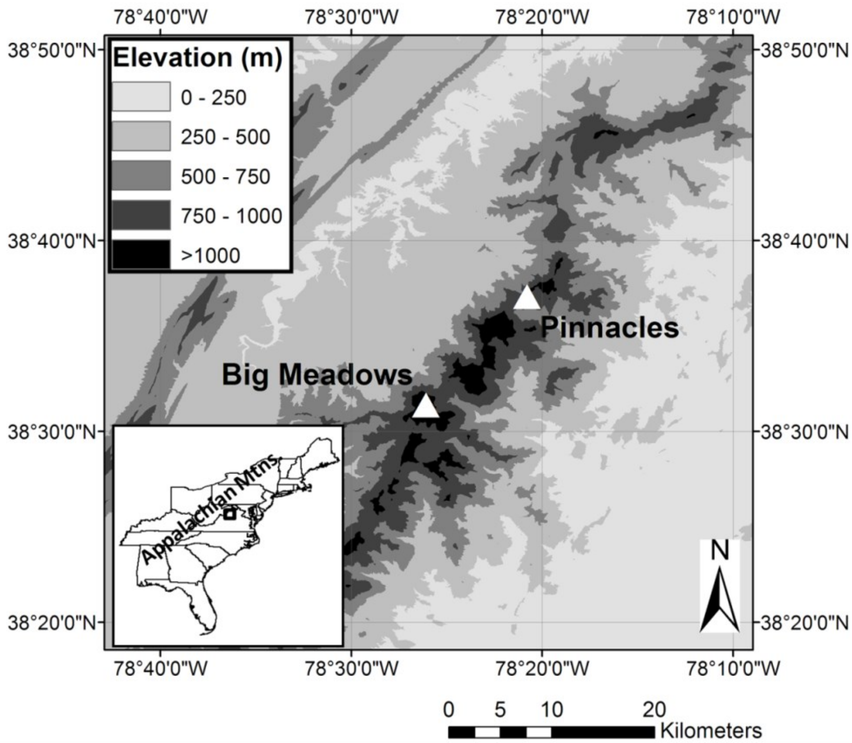

Figure 2.1: Topographic map showing the relative location of Pinnacles and Big Meadows (white triangles). Shading shows elevation msl. Inset map shows location of the study area, denoted by a black box, in the eastern US.

In this paper, the first year of CO_2 and meteorological records from Pinnacles was used, with data obtained from 1 September 2008 through 31 August 2009 used in all analyses. The CO_2 data record is mostly complete, aside from two gaps: a one-week gap in early September, 2008 and a three-week gap in late February through middle March 2009, both of which were due to power failures at the site. In the 1-year data set, measurements of CO_2 mixing ratio were made approximately every 10 minutes at each height.

There were three gaps in the meteorological data: a 20-day gap at the beginning of September, a 2-week gap in December, and another 2-week gap in early March. During these gaps, data from the nearby station Big Meadows were used. Big Meadows (38.53 N, 78.35 W) is located 14 km south of Pinnacles along the same mountain ridge at 1079 m msl, 62 m higher in elevation than Pinnacles. Winds are measured 10 m agl; temperature and relative humidity are measured 2 m and 10 m agl. Whereas some differences are found in the meteorological conditions between the two sites, these differences do not change the conclusions of this study.

2.2.2. Cold front identification

Surface temperature contrasts have long been considered paramount to determining the location of synoptic-scale fronts (Bjerknes, 1919). However, temperature contrasts alone should not be used as the sole criterion for frontal determination. This is particularly the case in complex terrain where surface temperature contrasts may be attributed to local phenomena, including land-sea breeze circulations or thermally-driven mountain flows (e.g. Whiteman, 2000). Instead, it is useful to combine temperature contrasts with changes in other meteorological variables such as pressure and moisture (e.g. Sanders and Doswell, 1995). Shafer and Steenburgh (2007) conducted a 25-year climatology on cold front passages in the Intermountain West by studying changes in surface temperature, pressure, and cross-frontal temperature gradients, and Parazoo et al. (2008) used gridded temperature, wind, and moisture fields to identify cold fronts. However, even with using changes in multiple meteorological variables, determining weak fronts is difficult because no objective definition exists to differentiate between a weak cold front and, e.g., a local terrain-induced effect (Steenburgh and Blazek, 2001).

Combining surface charts with in situ meteorological observations is another method to identify cold fronts. Kunz and Speth (1997) studied the impacts of cold fronts on surface ozone mixing ratios in the mountains of the Black Forest, Germany. Once fronts were identified, in situ meteorological measurements were used to pinpoint the timing of the frontal passages and to reduce the inherent subjectivity in frontal analysis from weather charts (e.g. Uccellini et al., 1992; Sanders, 1999). We followed an approach similar to Kunz and Speth and first identified cold fronts using surface analyses produced 8 times daily (00, 03, 06, 09, 12, 15, 18, and 21 UTC) by the National Oceanic and Atmospheric Administration (NOAA) Hydrometeorological Prediction Center (Roth, 2006). Temperature, pressure, and humidity data from Pinnacles and Big Meadows were used to corroborate each front's passage and pinpoint the time of passage, defined by the passage of the front's pressure trough and a temperature decrease (e.g. Sanders, 1999). Some cold fronts that were identified from synoptic charts did not fit this definition, which is not uncommon at locations along and east of mountainous areas such as the Appalachian Mountains (e.g. O'Handley and Bosart, 1996). The identification and timing of the frontal passage is very subjective in these cases. Therefore, cold fronts that did not possess a pressure trough or a postfrontal temperature decrease were eliminated, resulting in the removal of 15 of the 55 fronts that had been identified using synoptic charts. Seven of the remaining 40 cold front passages were eliminated because of missing CO_2 mixing ratio measurements, reducing the total number of cold fronts considered in this study to 33.

2.2.3. Determination of fair weather days

Fair weather days were determined using a clearness index (CI), which is the ratio of the sum of daily total incoming solar radiation to the theoretical maximum amount of incoming solar radiation. The theoretical maximum solar radiation is computed using an algorithm described by Whiteman and Allwine (1986), with days with a CI≥0.70 classified as clear days (e.g. Whiteman et al., 1997). One-fourth of all days within our data set had a CI≥0.70, and about one-fifth had a CI≥0.75. Adjusting the threshold for clear days between 0.70 and 0.75 did not affect the conclusions made about CO_2 changes on fair weather days.

2.2.4. CarbonTracker

We used output from the carbon transport model CarbonTracker, available online (ftp://ftp.cmdl.noaa.gov/ccg/co2/carbontracker/), to elucidate the causes of the CO_2 changes during frontal passages at Pinnacles. CarbonTracker was developed by the NOAA Earth System Research Laboratory to improve our understanding of and quantify the North American carbon budget. The model assimilates CO_2 mixing ratios obtained from a network of 63 sites worldwide and simulates atmospheric CO_2 transport using transport model 5 (TM5) [for a full description, see Peters et al. (2007)]. Mid-afternoon measurements (i.e. 1200-1600 LST) are assimilated for flat terrain sites because these CO_2 measurements are representative of a broad spatial area (e.g. Gloor et al., 2001; Bakwin et al., 2004). However, nighttime measurements (i.e. 0000-0400 LST) are typically assimilated for mountaintop stations because daytime measurements can be affected by local processes such as upslope flows (e.g. De Wekker et al., 2009). CO_2 mixing ratios from Pinnacles are assimiliated into CarbonTracker since the beginning of the measurements in September 2008.

2.2.5. HYSPLIT

We used the Hybrid Single Particle Lagrangian Integrated Trajectory (HYSPLIT) model to determine source regions of frontal CO_2. HYSPLIT is a kinematic backward trajectory model initialized using 3-dimensional wind fields from the North American Model (NAM) with a grid spacing of 12 km [for a full description, see Draxler and Hess (2004)]. We found that trajectories initialized 100 m agl best captured the clockwise wind shift observed at Pinnacles during cold front passages. Thus, we initialized trajectories 100 m agl 12 h postfrontal and ran the trajectories backward 48 h.

2.3. Results and discussion

2.3.1. Daily and seasonal CO_2 changes

Daily mean CO_2 mixing ratios measured at Pinnacles between 1 September 2008 and 31 August 2009 at Pinnacles ranged from 361.4 ppm to 408.1 ppm with larger values in winter than in summer (Figure 2.2a). Daily mean CO_2 mixing ratios decreased with height above the ground, with the largest decrease occurring between 5 and 10 m agl in the canopy layer (Figure 2.2b). Daily mean summertime CO_2 mixing ratios 5 m agl were 4-6 ppm higher than CO_2 mixing ratios measured 10 m and 17 m agl, suggesting more CO_2 uptake by the forest canopy (leaves) than by plants on the forest floor. Differences in CO_2 mixing ratio between the 10 and 17 m levels were mostly <1 ppm. During the fall, winter, and spring, differences among the 3 different measuring heights were <1 ppm.

These seasonal changes in CO_2 mixing ratio are strongly correlated to seasonal changes in vegetation activity, a finding consistent with other temperate mid-latitude sites (e.g. Greco and Baldocchi, 1996). In late April, the vegetation becomes photosynthetically active, as indicated by an increase in daytime latent heat and CO_2 fluxes (Figure 2.2c). The net CO_2 uptake results in the observed decreases in CO_2 mixing ratio during the growing season which we define as the period from 1 May 2009 through 31 August 2009.

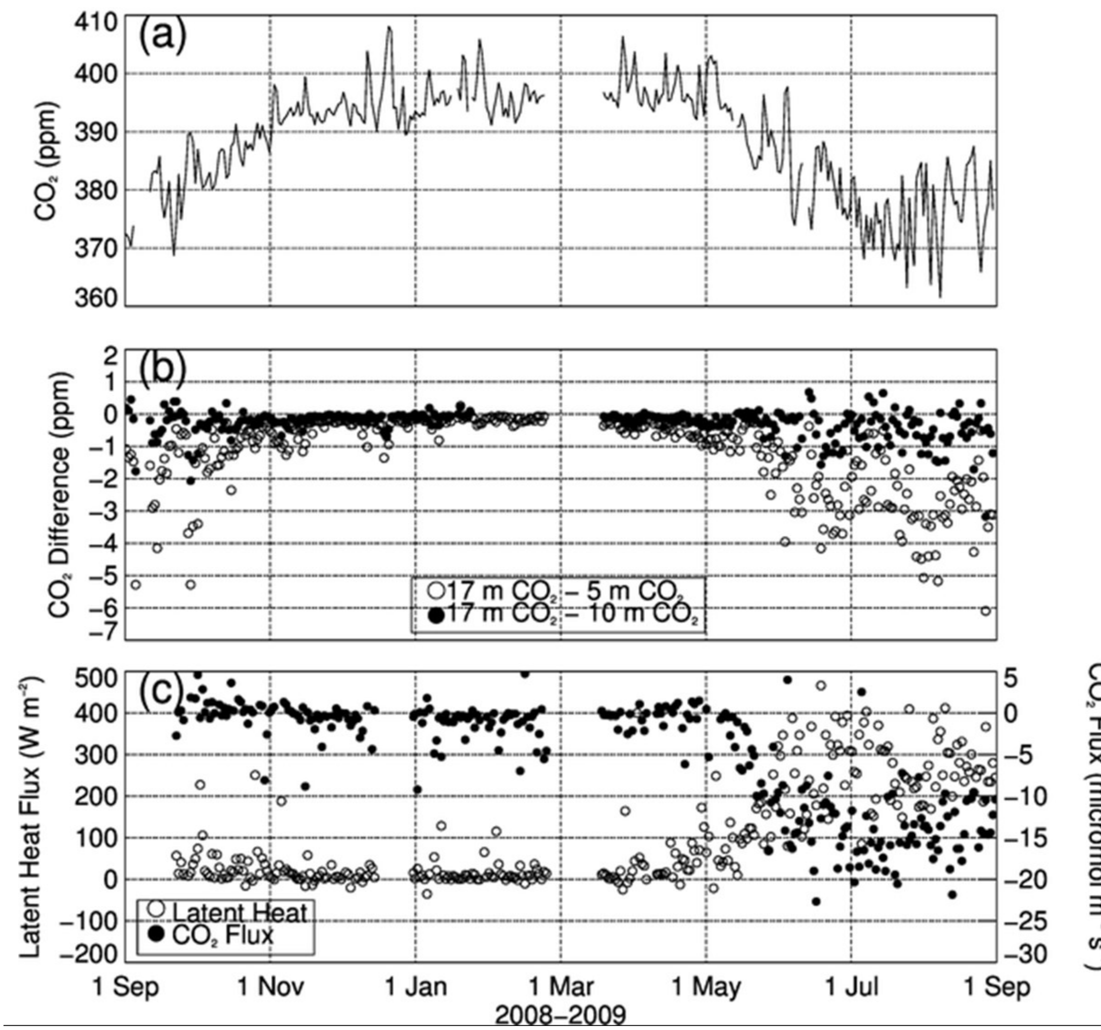

Figure 2.2: Daily mean CO_2 mixing ratio (a), daily CO_2 mixing ratio difference between 17 m and 5 m agl (open circle) and between 17 m and 10 m agl (closed circle) (b), and daytime latent heat flux (open circle) and CO_2 flux (closed circle) between 1 September 2008 and 31 August 2009 (c).

Superimposed on the seasonal changes are diurnal CO_2 changes. We defined the daily CO_2 difference as the difference between the daily maximum and minimum CO_2 mixing ratio. Daily CO_2 differences 17 m agl ranged from 1 to 40 ppm (Figure 2.3). These differences are largest on fair weather days during the growing season and cold front passages in the non-growing season (black vertical lines at the top of Figure 2.3). In the next section, we will focus in more detail on CO_2 changes during frontal passages and their comparison to fair weather days.

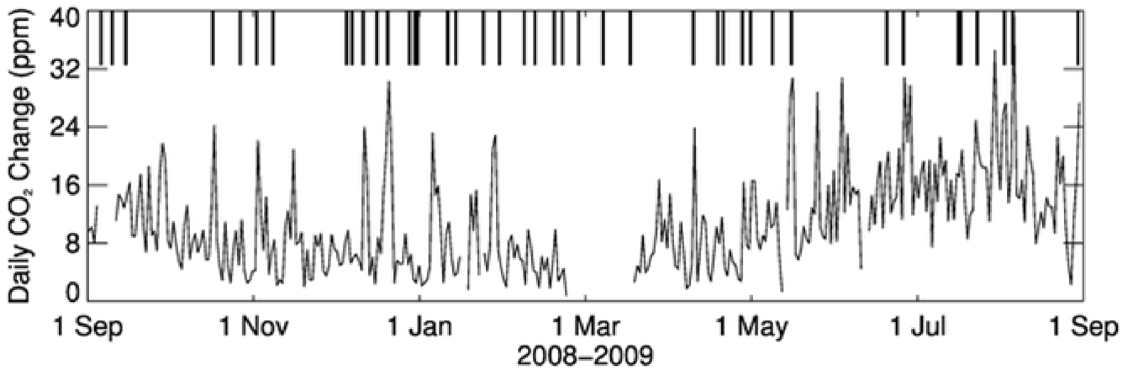

Figure 2.3: Daily CO_2 mixing ratio difference at 17 m agl between 1 September 2008 and 31 August 2009. Vertical black lines indicate days with cold front passages.

2.3.2. Contrasting CO_2 changes on cold front passages with clear days.

We selected a 24 h period around each frontal passage to facilitate a direct comparison with the diurnal CO_2 change on fair weather days. Daily means were subtracted from the hourly values to remove the seasonal change in CO_2 mixing ratio. Furthermore, the mean diurnal cycle in a particular season was removed from all days during that season to discern CO_2 changes not caused by local CO_2 uptake and release. Overall, changes in CO_2 mixing ratio during cold front passages were greater than those observed on fair weather days (Figure 2.4). CO_2 mixing ratios often increased during frontal passages. To determine the magnitude of the CO_2 change in different seasons, we subtracted the mean CO_2 mixing ratio 3 h prefrontal from the mean CO_2 mixing ratio 3 h postfrontal and repeated this procedure for ±6 and ±12 h from the frontal passage. We found that 67% of the cold front passages in the non-growing season and 60% of cold fronts in the growing season had larger CO_2 mixing ratios postfrontal than prefrontal. The difference between postfrontal and prefrontal CO_2 mixing ratios was largest in the fall, followed by spring and winter (Table 1), though large variability existed around the mean. An unpaired two-sample t-test confirmed that the differences ±6 and ±12 h from the frontal passage were statistically significant at the 0.05 confidence level in the fall, winter, and spring. Following the increase in CO_2 at the frontal passage, CO_2 mixing ratios often returned to their prefrontal values within 12 h of the cold front passage. There were exceptions, however, when CO_2 mixing ratios did not return to their prefrontal values until 1-2 days postfrontal, a behavior we examine in more detail later in Section 2.3.3.

Table 2.1: Mean differences and standard deviations between postfrontal and prefrontal CO_2 mixing ratios for ±3, ±6, and ±12 h from the time of the cold front passage. Bold values are statistically significant at the 0.05 confidence level based on an unpaired two-sample t-test.

Season	Time	Mean of Postfrontal-Prefrontal CO_2 (ppm)	Standard Deviation of Postfrontal-Prefrontal CO_2 (ppm)
Fall	3 h	**6.3**	**7.5**
	6 h	**6.2**	**7.6**
	12 h	**3.9**	**6.0**
Winter	3 h	1.0	2.4
	6 h	**1.9**	**4.3**
	12 h	**1.9**	**3.9**
Spring	3 h	4.3	7.5
	6 h	**4.6**	**4.8**
	12 h	**2.1**	**2.4**
Summer	3 h	-0.5	5.4
	6 h	2.1	8.3
	12 h	0.9	7.4

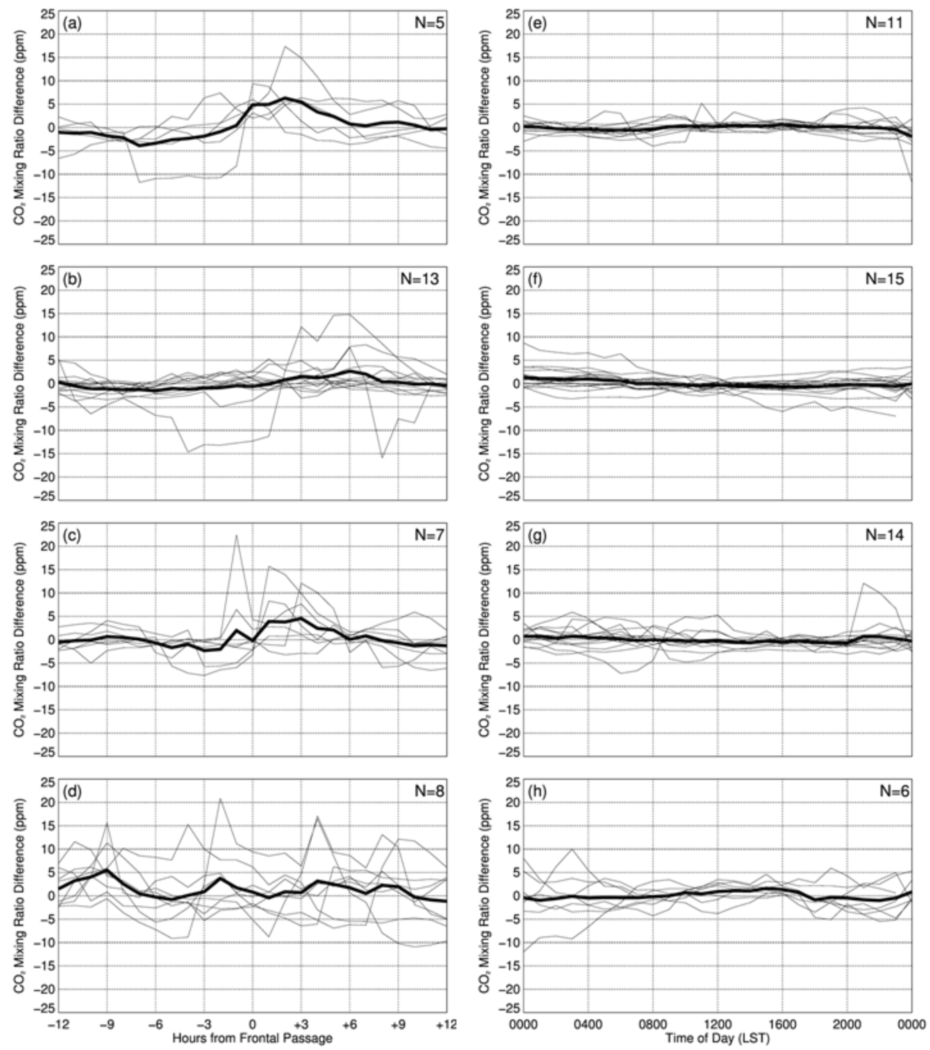

Figure 2.4: Hourly CO_2 mixing ratio ±12 h from cold front passages and on clear days in the fall (panel a, panel e), winter (panel b, panel f), spring (panel c, panel g), and summer (panel d, panel h) with the 24 h mean CO_2 mixing ratio and mean diurnal cycle subtracted. Thick black line shows the mean of all cases. The number of cases in each category is shown in upper right corner of each subfigure.

Generally, CO_2 changes during cold front passages were smaller in winter than in the spring and fall. A notable exception occurred during the 20 December cold front passage, in which absolute CO_2 mixing ratios increased from 399.4 ppm at 0500 LST to 426.2 ppm at 1000 LST—the highest hourly CO_2 mixing ratio observed during the 1 yr period of record. Examination of other times with large changes in CO_2 mixing ratio showed that 6 of the 10 events with the largest 1 h changes occurred within ±3 h of cold front passages (Table 2.2). The remaining four events occurred in the presence of other synoptic features such as warm fronts and prefrontal troughs. Eight of the 10 events with the largest magnitude of hourly CO_2 change were characterized by positive changes. The two events with negative changes occurred during the growing season and coincided with stronger observed surface CO_2 uptake at Pinnacles. These events demonstrate the importance of biogenic surface fluxes to the CO_2 variability during synoptic events in the growing season. Large changes in CO_2 mixing ratio outside the growing season cannot be attributed to biogenic surface fluxes.

Table 2.2: Largest 1 h changes in CO_2 mixing ratios at Pinnacles and their causes.

Date	1 h change in CO_2 (ppm)	Synoptic conditions at Pinnacles
7Z, 17 May 2009	22.4	Cold front
6Z, 6 August 2009	19.4	Cold front
11Z, 11 April 2009	19.2	Cold front
8Z, 17 May 2009	-18.1	Cold front
15Z, 16 May 2009	17.9	Warm front to north
12Z, 28 September 2008	17.7	Surface trough
12Z, 2 November 2008	17.4	Cold front
13Z, 2 August 2009	-16.6	Surface trough
12Z, 19 December 2008	15.0	Warm front to south
11Z, 20 December 2008	14.0	Cold front

Removal of the mean diurnal CO_2 cycle results in a small CO_2 variability on fair weather days in all seasons. There were a few exceptions, however. CO_2 mixing ratios on 21 January 2009 changed 15.7 ppm. The previous day had been characterized by high

CO_2 mixing ratios near 410 ppm and weak winds. Increased mixing on 21 January helped to weaken this CO_2 anomaly, thereby causing the precipitous CO_2 decrease. We also found a 13.4 ppm increase in CO_2 mixing ratios between 2000 and 2100 LST on 28 April 2009 which coincided with the passage of a prefrontal trough.

Observed changes in CO_2 mixing ratio at Pinnacles were comparable to the magnitude of published CO_2 changes at the Park Falls, Wisconsin tall tower during cold fronts and fair weather days (e.g. Hurwitz et al., 2004; Wang et al., 2007). The largest hourly increase in CO_2 mixing ratio during a cold front at Pinnacles was 18 ppm 17 m agl during the 11 April 2009 cold front passage. The largest described increase at Park Falls was 22 ppm at 30 m agl and 17 ppm at 396 m agl, with most of this change occurring in a 90 second period around the time of the frontal passage due to downmixing of air with comparatively high CO_2 mixing ratios. Most frontal CO_2 changes at Park Falls were due to postfrontal transport of air from northern regions with comparatively less CO_2 uptake (Hurwitz et al., 2004). In contrast to previous studies (e.g. Wang et al., 2007; Parazoo et al. 2008), we generally found no large, abrupt CO_2 changes during summer cold front passages at Pinnacles. Instead, we found that larger increases in CO_2 mixing ratio occurred during cold fronts in the spring and fall than in the summer. We also found no evidence of a step-like increase in CO_2 mixing ratios prior to frontal passages, as was found at mountaintop CO_2 monitoring sites in the Rocky Mountains (Brooks et al., 2010). Instead, increases in CO_2 mixing ratio at Pinnacles occurred within a narrow window, often within ±3 h of the passage of the frontal trough, similar to observations of CO_2 changes from some sites that Parazoo et al. (2008) considered. One reason for these consistent increases is that shear and deformational flow around cold fronts (e.g. Hess, 1959) can orient positive CO_2 anomalies along fronts and transport CO_2 and other passive tracers (e.g. Banic et al., 1986) thousands of kilometers from their source regions (Parazoo et al., 2008), inducing increases in surface CO_2 mixing ratios during frontal passages.

We found no significant relationship between the magnitude and longevity of CO_2 change during a frontal passage and the frontal intensity determined by in situ differences in temperature, dew point temperature, pressure, and cross-frontal temperature gradient. However, we found different characteristics of the CO_2 change associated with differences in wind direction shift and wind speed among the cold front passages. Most frontal passages were associated with an eastward-moving front and a wind shift from the southwest to northwest. Only three frontal passages were associated with a southward-moving front and a wind shift from the northwest to southeast. These contrasting cases provide an opportunity to understand some of the causes of the observed CO_2 changes during cold front passages at Pinnacles, as discussed next.

2.3.3. Relationship between CO_2 changes and wind during cold front passages

Eastward-moving fronts induce a wind shift from southwesterly prefrontal to northwesterly postfrontal (Figure 2.5a) and were associated with a wind speed maximum at the time of the frontal passage (Figure 2.5b). Following the wind shift and frontal passage, CO_2 mixing ratios returned to their prefrontal levels within 12 h postfrontal (Figure 2.5c). CO mixing ratios also increased around the time of the frontal passage (Figure 2.5d), and O_3 mixing ratios often decreased (Figure 2.5e) as shown in previous studies (e.g. Cooper and Moody, 2000). However, these changes were not as clear as changes in CO_2 mixing ratio.

Three southward-moving fronts induced a wind shift from the northwest to the southeast (Figure 2.5f) and a wind speed increase (Figure 2.5g). Two of these fronts had CO_2 (Figure 2.5h) and CO (Figure 2.5i) mixing ratios that remained high and did not return to their prefrontal values until 24-48 h postfrontal; O_3 mixing ratios similarly did not reach their prefrontal mixing ratios until 24-36 h postfrontal (Figure 2.5j).

The different cases described above demonstrate the importance of wind speed and direction changes to changes in CO_2 mixing ratio at Pinnacles. The 20 April front that had the smallest postfrontal CO_2 increase had the largest postfrontal wind speeds, suggesting mechanical mixing dissipates positive postfrontal CO_2 anomalies. This effect was also seen for eastward moving fronts with mean postfrontal wind speeds <6 m s^{-1}. For larger wind speeds, increases in postfrontal CO_2 mixing ratios were small in magnitude and duration. It thus appears that at least part of the observed differences in CO_2 mixing ratio changes among different cold fronts can be explained by differences in wind speed and direction, a finding consistent with previous studies (e.g. Tohjima et al., 2010).

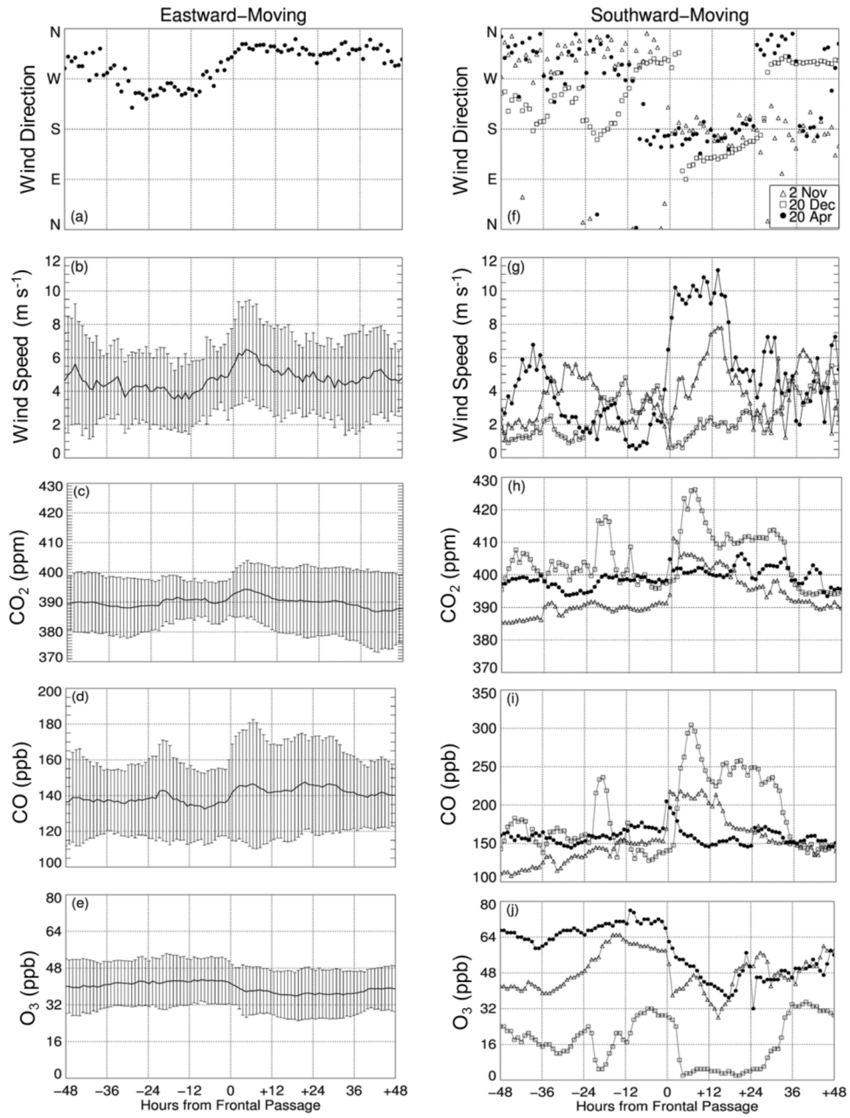

Figure 2.5: Mean wind direction (a), mean wind speed (b), mean CO_2 mixing ratio (c), mean CO mixing ratio (d), and mean O_3 mixing ratio (e) during 30 eastward-moving cold fronts. Error bars represent ±1 standard deviation from the mean. Panels (f) through (j) show corresponding changes during 3 southward-moving fronts that induced a postfrontal southeasterly wind shift: 2 November 2008 (hollow triangle), 20 December 2008 (hollow square), and 20 April 2009 (filled circle).

Wind speed and direction differences imply changes in air mass source region which we investigated using HYSPLIT. Backward trajectories simulated by HYSPLIT showed postfrontal air originating northwest of Pinnacles associated with eastward-moving cold fronts (Figure 2.6a). Southward-moving cold fronts induced a wind shift from the northwest prefrontal to the southeast postfrontal and transported air from north and east of Pinnacles. An exception was the cold front passage on 20 December 2008. This front approached the region from the west before moving south over Pinnacles, during which its forward motion decreased. In contrast to the observations, near-surface southeasterly flow was not evident in the HYSPLIT backward trajectories until 12-18 h postfrontal. Local effects that were important in this case where the front slowed and weakened as it encountered the Appalachian Mountains were thus not captured by the near-surface NAM wind fields that are used by HYSPLIT.

The southeasterly winds that occurred following southward-moving fronts were due to anti-cyclonic flow associated with high pressure north of Pinnacles. Such a flow pattern is consistent with previous descriptions of southward-moving fronts in the eastern US, also known as “backdoor” cold fronts (e.g. Bluestein, 1993). The backward trajectories for the southward-moving fronts had about half the length of trajectories associated with eastward-moving fronts. Backward trajectories associated with southward-moving fronts (Figure 2.6b) remained closer to the surface than eastward-moving fronts (Figure 2.6c), implying they were influenced more by surface anthropogenic emissions. In fact, these trajectories moved over source regions that included the highly-industrialized Northeast US with large anthropogenic emissions, as confirmed by output from VULCAN, a high-resolution fossil fuel emissions data set (Gurney et al., 2009) (Figure 2.6d). In general, a smaller mean height of the backward trajectory closer to the surface emissions resulted in a larger postfrontal increase in CO_2 mixing ratio.

The relatively high anthropogenic contribution to the CO_2 mixing ratio for the southward-moving fronts is also confirmed by Figure 2.7 which shows the CO_2 and CO mixing ratios as a function of the wind direction for the non-growing season. CO_2 and CO mixing ratios are highest when winds are from the south and southeast, which we attribute to the transport of polluted air southward from the Northeast US and then west-

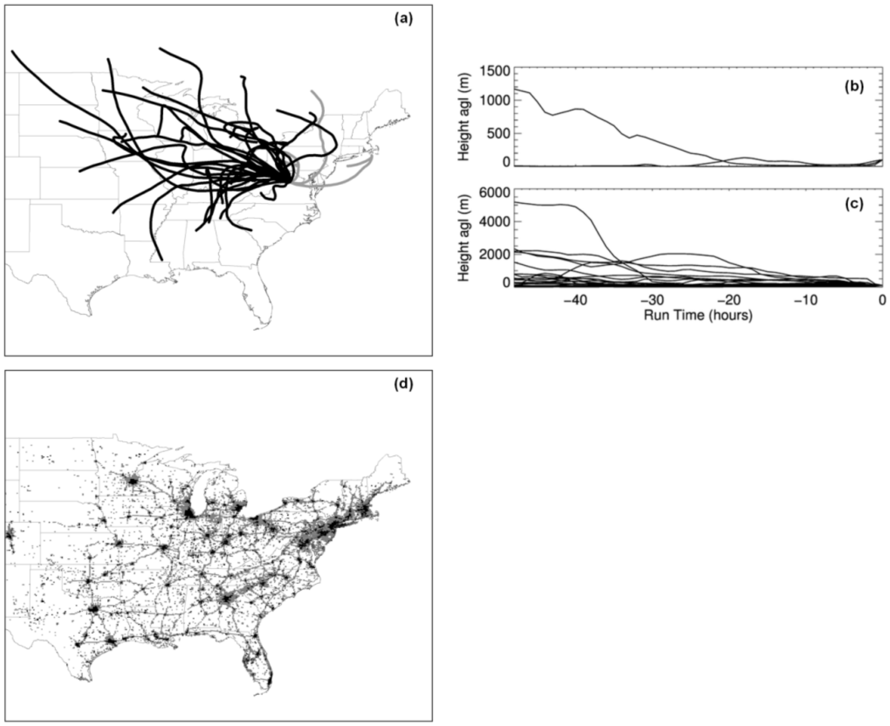

Figure 2.6: HYSPLIT backward trajectories, initialized 12 h postfrontal and run backward for 48 h for 30 eastward-moving cold fronts (black lines) and 3 southward-moving cold fronts (gray lines) (a). Panels (b) and (c) show height of backward trajectories agl for southward-moving and eastward-moving cold fronts, respectively. Note the different vertical scale in b and c. Panel (d) shows VULCAN-derived total annual fossil fuel emissions >10,000 and >100,000 tonnes carbon per 10 km^2 grid box per year in gray and black, respectively.

ward and northward to Pinnacles. Negligible differences are found between median CO_2 mixing ratios for southwesterly winds and northwesterly winds and thus postfrontal mixing ratios return to their prefrontal values rapidly following the passage of eastward-moving fronts. Based on these results, we constructed a conceptual model summarizing CO_2 changes during frontal passages (Figure 2.8):

- Short-lived CO_2 increases accompany eastward-moving cold fronts (Figure 2.8a) that induce a wind shift to the northwest (Figure 2.8b).
- CO_2 mixing ratios quickly decline postfrontal as the front moves offshore (Figure 2.8c, 2.8d).

- Southward-moving fronts create larger, more persistent positive CO_2 anomalies postfrontal than eastward-moving fronts as winds shift from the northwest to southeast (Figure 2.8e, 2.8f).
- The prolonged elevated CO_2 is due to transport of polluted air that is advected southward from the Northeast US and then westward to Pinnacles (Figure 2.8g, 2.8h).

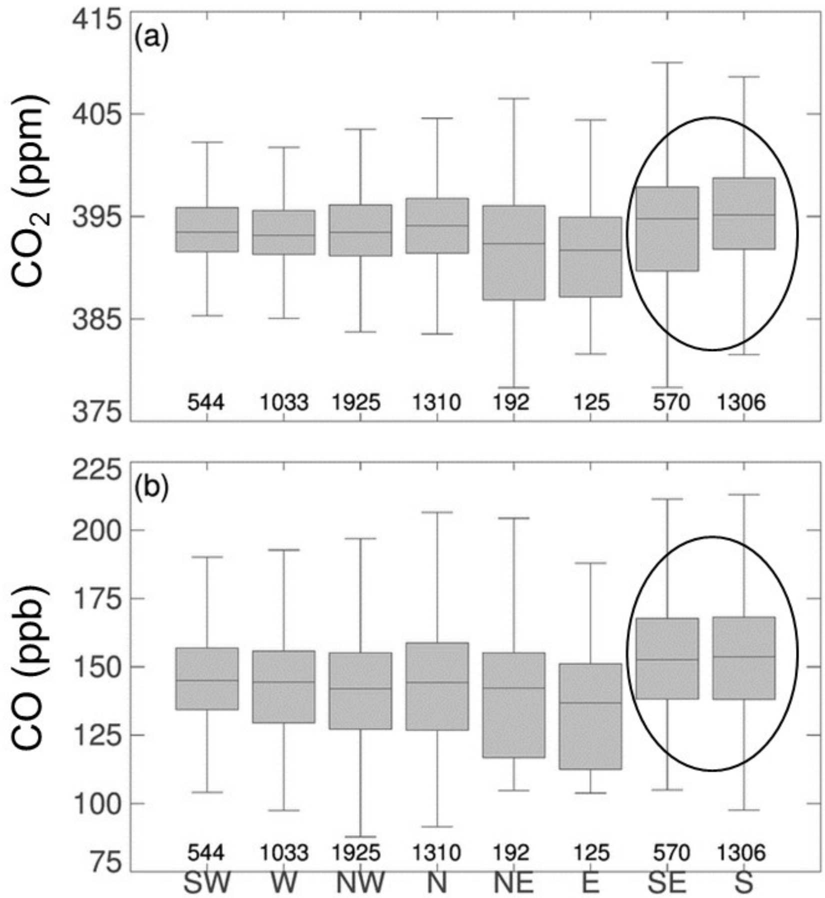

Figure 2.7: Box-and-whisker plot of CO_2 (a) and CO (b) mixing ratio as a function of wind direction at Pinnacles from 1 September 2008 through 30 April 2009. The box encloses the inter-quartile range (25^{th}-75^{th} percentiles), and the whiskers extend out to the 12.5^{th} and 87.5^{th} percentiles. Outliers not shown for ease of readability. Numbers shown are the number of cases per category. The total number of cases is 7025. Circles highlight the higher CO_2 and CO deviations associated with southerly and southeasterly flows.

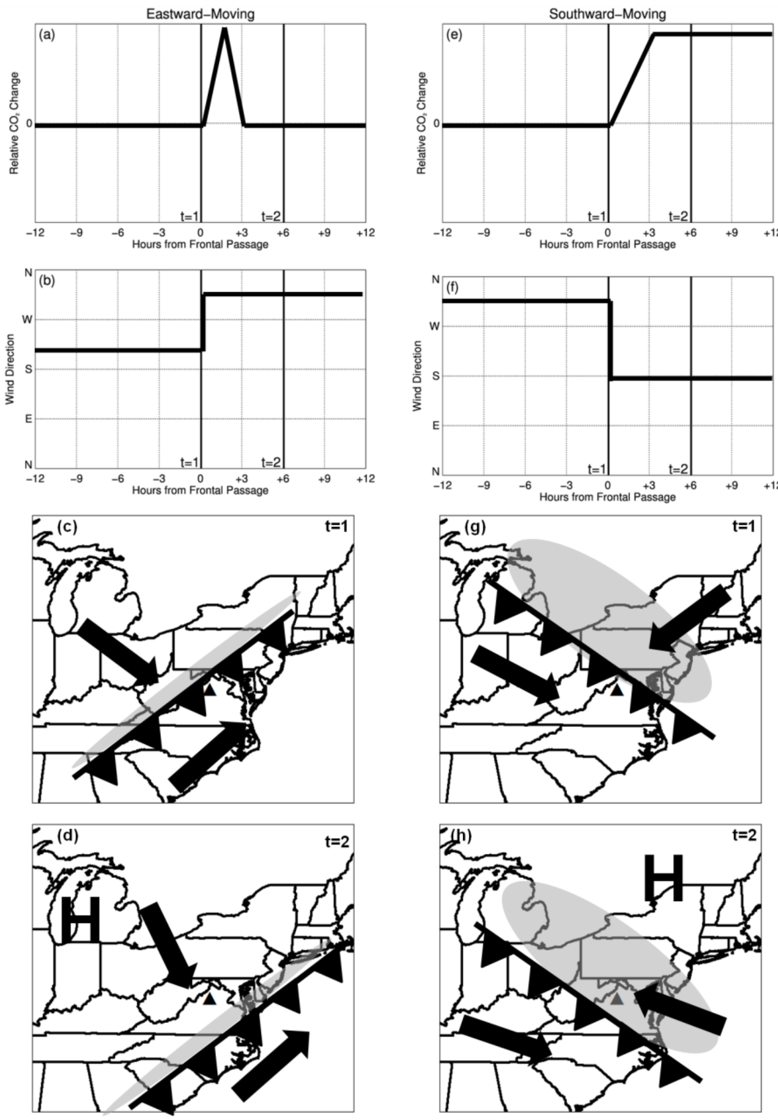

Figure 2.8: Conceptual model for eastward-moving (left panel) and southward-moving (right panel) cold fronts. First and second panel show relative changes in CO_2 (panel a, panel e) and wind direction (panel b, panel f), respectively. Bottom panels show a schematic of frontal location and dominant transport pathways at time step t=1—the time of the frontal passage (panel c, panel g), and time step t=2—6 h postfrontal (panel d, panel h). Pinnacles is denoted by a black triangle on the map; gray shading shows areas of relatively high CO_2 mixing ratio. Approximate location of the anticyclone is denoted by **H**.

2.3.4. Comparison with CarbonTracker

We can further elucidate the causes of the observed CO_2 variability using CarbonTracker because it differentiates among CO_2 contributions from different natural and anthropogenic sources. To gain confidence in the ability of CarbonTracker to simulate CO_2 mixing ratios at Pinnacles, we first compared CarbonTracker output with the observations at Pinnacles. Note from Section 2.2.4 that only nighttime data from Pinnacles are assimilated in CarbonTracker. Differences exist between the elevation of the model grid box containing Pinnacles and the real elevation of Pinnacles. We found that the fourth model level (842 m msl) best captures the 17 m CO_2 changes, explaining 86% of the total variance during the first year of measurements.

We found that CarbonTracker was able to describe the increases in CO_2 mixing ratio during frontal passages and on fair weather days at Pinnacles (Figure 2.9a, 2.9b). Because of the coarse spatial and temporal model resolution, modeled CO_2 changes were smeared out over a longer time period and more damped than the observed CO_2 changes. CarbonTracker captured the magnitude of the mean increases in CO_2 mixing ratio during

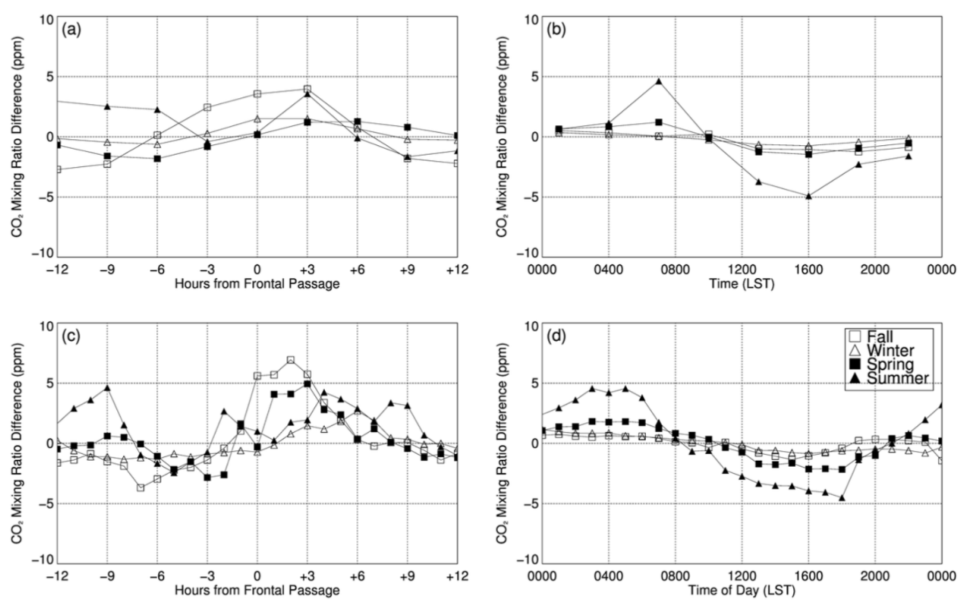

Figure 2.9: CarbonTracker-modeled mean CO_2 mixing ratio ±12 hours from time of cold front passage (a) and during clear days (b) in the fall (open square), winter (open triangle), spring (filled square) and summer (filled triangle). Same for (c) and (d), but for observed CO_2 mixing ratios.

fronts in each season, yet underestimated some of the large increases during individual fronts. The model also agreed well with observations on fair weather days, with little diurnal CO_2 change on fair weather days in the fall, winter, and spring, and large diurnal changes during the summer (Figure 2.9c, 2.9d).

CarbonTracker captured the longer-lived positive CO_2 anomalies that occurred following southward-moving cold fronts compared to eastward-moving cold fronts. Postfrontal CO_2 changes cannot be attributed to an advection of latitudinal "background" CO_2 gradients because the frontal CO_2 changes at Pinnacles are largest when latitudinal CO_2 gradients are weakest, i.e. during the spring and fall. We conclude that most of the frontal CO_2 increase is due to transport from source regions at a regional scale. To investigate this further and to gain some insight into the causes of the observed CO_2 variability, we used CarbonTracker output. Among the constituent contributors to total CO_2 (background, biogenic, fires, ocean, fossil fuel), we find that the largest postfrontal CO_2 changes in the grid box containing Pinnacles are due to fossil fuel. We also find that the contribution of fossil fuel CO_2 is larger and persisted longer following southward-moving fronts than eastward-moving fronts (Figure 2.10). Consistent with HYSPLIT backward trajectories, CarbonTracker suggests that the CO_2 responsible for these observed changes is transported from the Upper Midwest and Northeast US during east- and south-moving cold fronts, respectively, over a time scale of 1-2 days. The results of our investigation of CO_2 changes during frontal passages suggest that the Upper Midwest and Northeast US are dominant source regions affecting postfrontal CO_2 variability at Pinnacles. The assimilation of Pinnacles data into CarbonTracker should further constrain flux uncertainties in these areas (e.g. Schuh et al., 2010).

Regardless of the presence of cold front passages, much of the day to day changes in CO_2 at Pinnacles are explained by transport from different source regions with the highest CO_2 mixing ratios characterized by the presence of slow-moving, near-surface backward trajectories originating from the Northeast US. Conversely, days with the lowest CO_2 mixing ratios had fast-moving backward trajectories descending towards Pinnacles indicating that these trajectories remained above the boundary layer and thus were not directly affected by surface emissions.

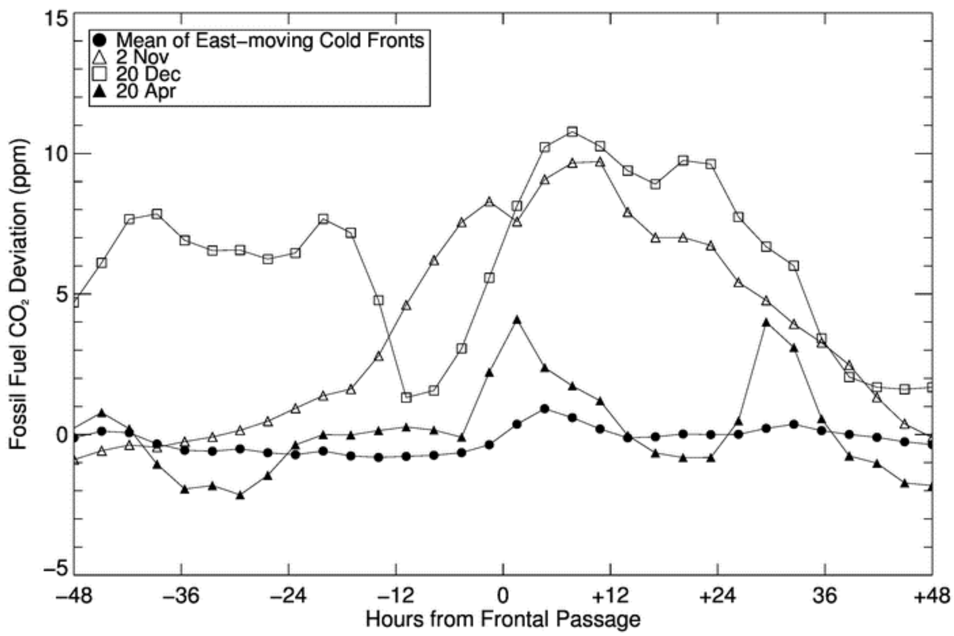

Figure 2.10: Fossil fuel CO_2 deviation (annual means removed) as a function of time during 30 eastward-moving fronts and the 3 southward-moving fronts.

2.4. Conclusions and implications

We presented the first meteorological and CO_2 mixing ratio observations from Pinnacles, a new mountaintop CO_2 monitoring site established in the Appalachian Mountains in the eastern US. We focused on the important role of cold fronts at modulating sub-diurnal CO_2 changes and contrasted these changes with diurnal changes on fair weather days. We found that changes in CO_2 during cold fronts were often larger than changes observed on fair weather days. Oftentimes, an increase was observed in the CO_2 mixing ratio around the time of the frontal passage. This finding is consistent with previous studies of CO_2 transport and provides further evidence of strong horizontal CO_2 gradients that exist within the atmosphere (e.g. Hurwitz et al., 2004; Parazoo et al., 2008; Parazoo et al., 2011).

We also found that the CO_2 increase was short-lived (about 3 h) during eastward-moving fronts, whereas CO_2 mixing ratios did not return to their prefrontal levels until up to 2 days following the passage of southward-moving cold fronts. The increase in CO_2 mixing ratio is consistent with the notion of the organization of positive CO_2 anomalies along cold fronts caused by shear and deformational flow. However, the CO_2 mixing ratio change did not appear to depend on the frontal intensity as determined by temperature, dew point temperature, pressure, and cross-frontal temperature gradient. The differences in postfrontal CO_2 mixing ratios between the different types of fronts can be explained by the differences in wind speed, wind shift, and source regions. In the case of southward-moving fronts, air masses from urban and industrial areas in the Northeast US advected towards Pinnacles. Transport pathways were longer for eastward-moving cold fronts and originated in the Upper Midwest. Regardless of frontal passages, synoptic situations in which air is transported from the Northeast US result in the largest CO_2 mixing ratios at Pinnacles.

This research has implications for the inverse carbon modeling and atmospheric dynamics communities. Data from well-calibrated CO_2 measurement sites in complex terrain, such as Pinnacles, can be affected by local meteorology that is difficult to simulate in models currently used in studies of the North American carbon budget (e.g. Peters et al., 2007; Butler et al., 2010; Schuh et al. 2010). The coarse spatial resolution of these models cannot be expected to completely represent atmospheric processes in mountainous regions. Yet, studies have indicated that a significant amount of carbon storage may be occurring in mountainous forests (Sun et al., 2009). Knowledge of drivers of CO_2 variability at mountaintop monitoring sites provides information that can inform decisions about how to assimilate CO_2 data from these sites into models. The present study shows that cold fronts are important drivers of CO_2 variability at Pinnacles. Therefore, if carbon transport models capture the transport processes associated with cold fronts, assimilation of Pinnacles measurements can help constrain flux estimate uncertainties in the source regions of postfrontal CO_2, i.e. the Upper Midwest and Northeast US. In future work, we will evaluate if the assimilation of Pinnacles CO_2 data has an impact on simulated CO_2 fluxes and CO_2 mixing ratios in CarbonTracker. Higher resolution transport modeling may be needed so that atmospheric processes in complex terrain are properly simulated and mountaintop CO_2 observations are reliably assimilated into inverse carbon models.

Finally, the present study demonstrates that pronounced changes in CO_2 mixing ratios during frontal passages can help pinpoint the time of cold front passages. This is especially helpful in mountainous terrain where frontal identification is difficult (e.g.

O'Handley and Bosart, 1996) but important for diagnosing deep convection (e.g. Sanders and Doswell, 1995) and for investigating frontal interactions with orography. The use of CO_2 as a tracer has been successfully explored in studies to better understand boundary layer dynamics in mountainous areas (e.g. Sun and De Wekker, 2011) and is expected to have similar potential for the investigation of frontal dynamics.

2.5. Acknowledgements

We thank assistants from the Shenandoah National Park and students in the University of Virginia Department of Environmental Sciences for helping to maintain data collection at Pinnacles. Bjørn-Gustaf Brooks and Andy Jacobson provided useful insight regarding CarbonTracker, and Robert Davis, Ankur Desai, Todd Scanlon, and Jason Shafer provided helpful feedback during the preparation of this manuscript. We also thank two anonymous reviewers whose comments helped improve the manuscript. CarbonTracker results were provided by NOAA ESRL, Boulder, Colorado, USA from the website at http://carbontracker.noaa.gov.

CHAPTER 3

METEOROLOGICAL CONTROLS ON THE DIURNAL VARIABILITY OF CARBON MONOXIDE MIXING RATIO AT A MOUNTAINTOP MONITORING SITE IN THE APPALACHIAN MOUNTAINS[1]

[1] Modified from Lee, T. R., De Wekker, S. F. J., Pal, S., Andrews, A. E., and Kofler, J., 2015. Meteorological controls on the diurnal variability of carbon monoxide mixing ratio at a mountaintop monitoring site in the Appalachian Mountains. *Accepted to Tellus B*.

Abstract

The variability of trace gases such as carbon monoxide (CO) at surface monitoring stations is affected by meteorological forcings that are particularly complicated over mountainous terrain. A detailed understanding of the impact of meteorological forcings on trace gas variability is challenging, but is vital to distinguish trace gas measurements affected by local pollutant sources from measurements representative of background mixing ratios. In the present study, we investigate the meteorological and CO characteristics at Pinnacles (38.61 N, 78.35 W, 1017 m above mean sea level), a mountaintop monitoring site in northwestern Virginia, USA, in the Appalachian Mountains, from 2009 to 2012, and focus on understanding the dominant meteorological forcings affecting the CO variability on diurnal timescales. The annual mean diurnal CO cycle shows a minimum in the morning between 0700 and 0900 LST and a maximum in the late afternoon between 1600 and 2000 LST, with a mean (median) daily CO amplitude of 39.2±23.7 ppb (33.2 ppb). CO amplitudes show large day-to-day variability. The largest CO amplitudes, in which CO mixing ratios can change >100 ppb in <3 h, occur in the presence of synoptic disturbances. Under fair weather conditions, local- to regional-scale transport processes are found to be more important drivers of the diurnal CO variability. On fair weather days with northwesterly winds, boundary layer dilution

causes a daytime CO decrease, resembling the variability observed atop tall towers in flat terrain. Fair weather days with a wind shift from the northwest to the south are characterized by an afternoon CO increase and resemble the variability observed at mountaintops influenced by the vertical transport of polluted air from adjacent valleys.

3.1. Introduction

Observations of atmospheric trace gas mixing ratios are required for many applications, including air quality models and inverse carbon transport models. An understanding of the trace gas variability and the factors affecting this variability is important for these applications (e.g. Seinfeld and Pandis, 2006; De Wekker et al., 2009; Steyn et al., 2012). A few hundred meters above the surface in flat terrain, trace gas mixing ratios decrease in the well-mixed convective boundary layer during the daytime. At these heights, measurements are representative of spatial scales on the order of 10^6 km^2 in the afternoon (Gloor et al., 2001), which has led to the establishment of a network of tall towers with heights up to 500 m above ground level (agl). Whereas much of the focus of the network is on monitoring carbon dioxide (CO_2) to help reduce uncertainties in regional- to continental-scale carbon budgets (e.g. Bakwin and Tans, 1995), carbon monoxide (CO) and a suite of other trace gases are sometimes measured as well. CO is important because of its use as a tracer of anthropogenic emissions and because it is the main sink for hydroxyl radicals (OH) on the global scale (e.g. Thompson, 1992; Henne et al., 2008b).

Trace gas measurements are also increasingly being made at mountaintops around the world (e.g. Levin et al., 1995; Henne et al., 2008a; Thompson et al., 2009; Ramonet et al., 2010; Andrews et al., 2014). Between 2004 and 2008, trace gases measurements began at mountaintops in the continental US in the Cascade Mountains (Jaffe et al., 2005), Rocky Mountains (De Wekker et al., 2009), and Appalachian Mountains (Lee et al., 2012). Mountaintops are oftentimes used for the measurement of background, or free atmospheric (FA) trace gas mixing ratios because, at times, mountaintops are located above the regional planetary boundary layer (PBL). Within the PBL, CO mixing ratios are oftentimes higher than within the FA because of near-surface anthropogenic emissions, biomass burning (e.g. Crutzen and Andrea, 1990), and CO production, which occurs via methane oxidation and the oxidation of organic compounds emitted from vegetation (e.g. Zimmerman et al., 1978; Seinfeld and Pandis, 2006). CO emissions within the PBL can be transported to nearby mountaintops via multiple dynamical forcings on a variety of spatiotemporal scales. Daytime convective mixing, upslope flows (De Wekker et al., 2009), mountain venting (e.g. De Wekker et al., 2004; Henne et al., 2004; Henne et al., 2005), and wind shifts on the mesoscale (e.g. Schmidt et al., 1996) to synoptic-scale (e.g. Zellwegger et al., 2003) influence trace gas mixing ratios on timescales of up to a few hours and reduce the degree to which mountaintop trace gas measurements are representative of background values (e.g. Brooks et al., 2012). Many studies have found that these transport processes result in a daytime increase in CO mixing ratios at mountaintops (e.g. Forrer et al., 2000; Gao et al., 2005; Balzani Lööv et al., 2008; Henne et al., 2008b; Obrist et al., 2008). Daytime increases are also reported for other trace gases (e.g. Weiss-Penzias et al., 2006; Necki et al., 2003) and aerosols (e.g. Baltensperger et al., 1997; Lugauer et al., 1998).

Although previous work has focused on the trace gas and aerosol variability observed at tall mountaintops and those with high topographic prominence (e.g. Thoning et al., 1989; Baltensperger et al., 1997; De Wekker et al., 2009), there has also been considerable work describing the trace gas variability at low mountaintops (e.g. Schmidt et al., 1996; Schmidt et al., 2003; Thompson et al, 2009; Ramonet et al., 2010; Pillai et al., 2011). Whereas tall mountaintops typically remain above the regional PBL away from local trace gas sources and sinks (e.g. Baltensperger et al., 1997), low mountaintops oftentimes lie at the transition between the regional PBL and overlying FA. Thus, the trace gas variability at these locations is very complex (e.g. Schmidt et al., 1996). For many applications, it is important to differentiate periods when these mountaintops sample clean, pristine air masses from periods when local emission sources and transported contributions are sampled. This knowledge can, for example, provide an estimate of the contribution of fossil fuel emissions to the in situ CO_2 variability (e.g. Bakwin and Tans, 1995) and improve the estimate of regional- to continental-scale carbon sources and sinks from inverse carbon transport models (e.g. Peters et al., 2007; Gerbig et al., 2009; Schuh et al., 2010; Lac et al., 2013).

In the current study, we present CO and meteorological observations from a recently established mountaintop monitoring site in the Appalachian Mountains that we refer to as Pinnacles. The objectives of this paper are to 1) investigate the dominant meteorological drivers affecting the diurnal CO variability at Pinnacles, and 2) contrast the characteristics of the CO variability at Pinnacles with those at other mountaintop sites, as well as tall tower sites located in flat terrain. Following a previous study focusing on CO_2 observations from Pinnacles (Lee et al., 2012) and studies at other mountaintop locations (e.g. Schmidt et al., 1996; Pillai et al., 2011; Brooks et al., 2012), we hypothesize that the largest CO changes occur 1) during air mass changes that accompany cold front passages and 2) during the daytime under fair weather conditions when convective mixing and upslope flows transport CO-rich PBL air to the mountaintop. To investigate these hypotheses, we use four years of CO mixing ratio and meteorological measurements from Pinnacles. Following a discussion of the on-site measurements in Section 3.2, we provide an overview of the monthly and diurnal cycles of the meteorological variables and CO mixing ratios in Sections 3.3.1 and 3.3.2. In Section 3.3.3, we compare the amplitudes of the mean diurnal CO cycles at Pinnacles with the amplitudes observed at other mountaintop CO monitoring sites around the world. In Sections 3.3.4 and 3.3.5, we differentiate between days with the largest diurnal CO changes and days with the smallest CO changes and investigate the dominant meteorological forcings on these days. We conclude the paper with a discussion of our results and possible implications in Section 3.4.

3.2. Data and methods

3.2.1. Site description

Pinnacles (38.61 N, 78.35 W) is located 1017 m above mean sea level (msl) in the Shenandoah National Park (SNP) along the crest of the Virginia Blue Ridge Mountains in the eastern US (Figure 3.1a). The nearest potential CO emissions source is Skyline Drive, a scenic tourist road oriented southwest-northeast along the crest of the Blue Ridge Mountains 120 m southeast of Pinnacles. Other nearby CO emission sources include the town of Luray, with a population of about 5000, located 15 km west of Pinnacles in the Page Valley. Washington DC, the nearest metropolitan area, is located 120 km northeast

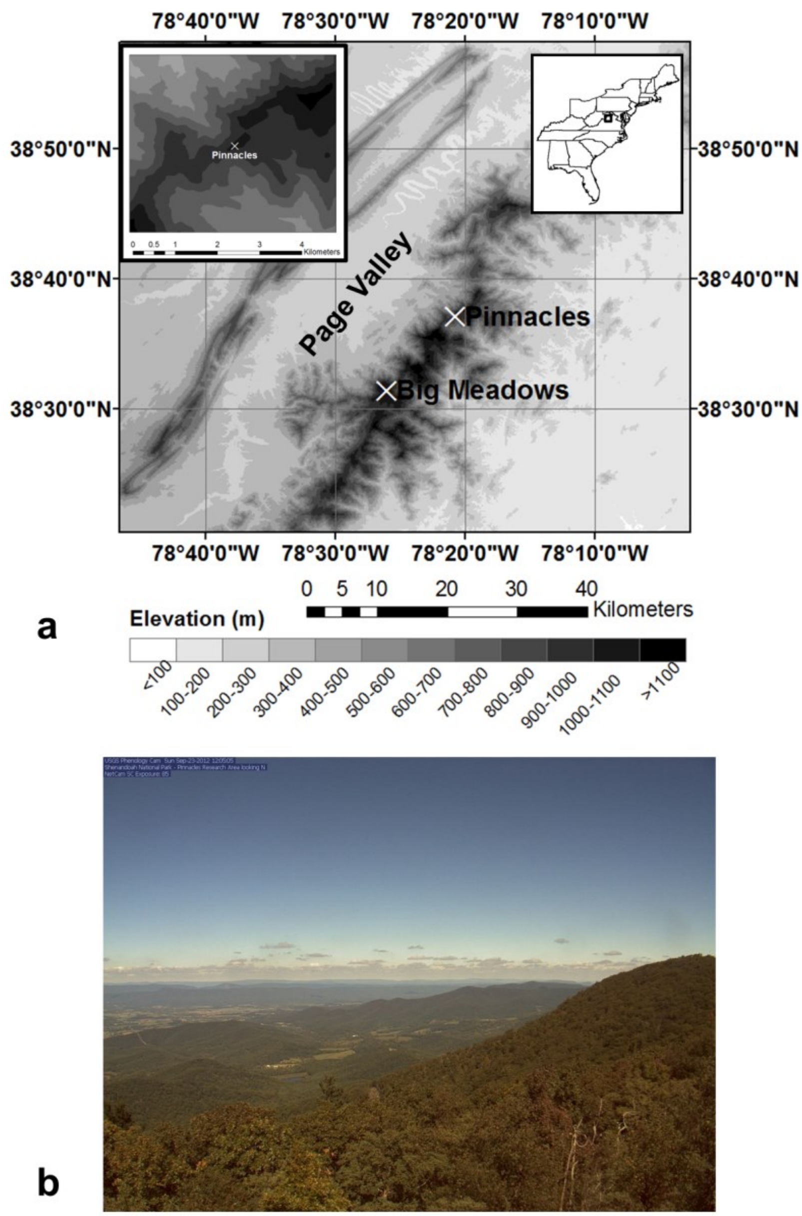

Figure 3.1: Topographic map (a) indicating the location of Pinnacles (white X) relative to Big Meadows and the Page Valley. Shading shows elevation msl. The inset map at the top left shows the topography in a 5 km x 5 km box surrounding Pinnacles. The inset map at the top right indicates the study location, denoted by a black box, in the eastern US. Topography data are from the US Geological Survey and have a 10 m resolution. Panel (b) shows a web camera image taken at 1205 LST 23 Sep 2012 from the site showing the Page Valley northwest of Pinnacles.

of Pinnacles. In addition to anthropogenic emissions, other regional CO sources include CO emissions from biomass burning in upwind regions (e.g. Crutzen and Andrea, 1990).

3.2.2. Trace gas measurements

Pinnacles is part of the NOAA Global Greenhouse Gas Reference Network (http://www.esrl.noaa.gov/gmd/ccgg/). Measurements are made through collaboration with the NOAA Earth System Research Laboratory (ESRL). CO and CO_2 mixing ratios have been measured at 5, 10, and 17 m agl since August 2008 along a 17 m tower at the site. Both CO and CO_2 are sampled approximately every 10 min at each height, and half-hour means of these data are used in all analyses. In the present paper, we use data collected during the first four full years of measurements from 1 January 2009 to 31 December 2012. The CO and CO_2 data record over this period is 84% complete, but there are occasional gaps due to on-site power outages and miscellaneous system malfunctions.

CO and CO_2 are measured using a Thermo Electron Corporation 48C CO analyzer and Li-COR 7000 closed path gas analyzer, respectively. Instrumentation, calibration, and measurement uncertainty are described in detail in Andrews et al. (2014). The measurements are fully automated, and NOAA-supplied field calibration standards are directly traceable to the World Meteorological Organization's mole fraction scales for CO and CO_2 maintained at the NOAA ESRL. The CO and CO_2 analyzers both suffer from baseline drift, so the analyzer baseline is measured every 30-40 min for CO and every 2 h for CO_2. The instrument calibration frequency has varied over the duration of the measurement period. Currently, the CO analyzer is calibrated every 23 h using calibration standards of 100 ppb and 350 ppb. The CO_2 analyzer is calibrated every 11 h using four standards: 350 ppm, 380 ppm, 410 ppm, and 460 ppm. Additional target cylinders track measurement reproducibility at approximately 220 ppb (400 ppm) for CO (CO_2). Detailed uncertainty estimates and algorithms are provided in the data files available from NOAA ESRL (Andrews et al., 2014). Random and non-random (i.e. systematic) measurement uncertainties are reported separately during archival and post-processing. These uncertainties come from three sources: atmospheric trace gas variability, measurement uncertainty, and scale uncertainty. The total uncertainty is the sum of these three uncertainties (Andrews et al., 2014). The atmospheric variability represents the standard deviation of the trace gas mixing ratio over the 30-second period during which the trace gas of interest is sampled. Measurement uncertainty is a function of multiple systematic uncertainties, e.g. differences in moisture content of the samples which can affect the measured trace gas mixing ratio and extrapolation uncertainties that arise when trace gas samples are made that are outside the calibrated range of the monitoring system. The scale uncertainty arises from the uncertainties in the calibration standards themselves (Zhao and Tans, 2006). Total uncertainties are typically <6 ppb for CO and <0.1 ppm for CO_2 (Andrews et al., 2014).

We exclude data from periods when the analyzers were performing poorly, which is rare but may occur during, e.g. periods when the room temperature fluctuates significantly or when the trace gas observations are highly variable. Therefore, we compute a total uncertainty that is the quadrature sum of the non-random measurement uncertainty and the standard deviation over the measurement period, which includes random analyzer noise and real atmospheric variability. At Pinnacles, 82.7% (98.2%) of the CO measurements sampled at 17 m agl have a total uncertainty <5 ppb (<10 ppb), and 95.6% (99.9%) of the CO_2 measurements have an uncertainty <0.1 ppm (<0.2 ppm). In our analyses, we remove CO measurements whose total uncertainty exceeds 10 ppb.

3.2.3. Meteorological measurements

Meteorological measurements at Pinnacles began in July, 2008 and include temperature, humidity, wind, radiation, pressure, and rainfall (Table 3.1). Data from a CSAT sonic anemometer and Li-COR 7500 water vapor and CO_2 gas analyzer are used to compute 30 min mean sensible heat, latent heat, and CO_2 fluxes. To complement these measurements, a web camera was installed 17 m agl in October, 2009 facing northwest into the Page Valley (c.f. Figure 3.1). Images are recorded every 15 min.

The meteorological data set is mostly complete (>90%), but there are occasional gaps in the data due to data logger malfunctions and on-site power outages. Data quality assurance and quality control procedures include filtering the cup anemometer wind data by removing all wind measurements made when the wind speed is 0 m s^{-1} for >30 min. Extended periods (sometimes >12 h) of 0 m s^{-1} wind speeds are caused by rime ice on the instruments that occasionally occurs between October and April. Wind speeds of 0 m s^{-1}

for >12 h also occurred when the cup anemometer's potentiometer malfunctioned for several periods in summer 2009 and summer 2011. Because temperature and humidity are measured at multiple levels along the tower, we remove measurements that are unrealistically different from the others, and we remove flux measurements made during periods of precipitation.

Measurements of temperature, humidity, wind, insolation, and precipitation from Big Meadows (38.52 N, 78.44 W, 1079 m msl), another mountaintop meteorological monitoring site located 14 km south of Pinnacles (c.f. Figure 3.1a), are used to fill in occasional gaps in the Pinnacles data record. Because frozen precipitation is not measured at Pinnacles but is a routine occurrence between October and April, we use precipitation data from Big Meadows (which has a heated rain gauge) to determine precipitation patterns.

3.2.4. Trajectory model

We run the Hybrid Single Particle Lagrangian Integrated Trajectory (HYSPLIT) model for a selection of cases discussed in Section 3.3.2 to understand source regions for periods of high CO mixing ratios. HYSPLIT is a kinematic backward trajectory model (Draxler and Hess, 2004) that we initialize using wind fields from the North American Model (NAM) (e.g. Janjić et al., 2010; Janjić et al., 2011). The NAM has a horizontal grid spacing of 12 km and 60 vertical levels, 34 of which are below 5 km. Sensitivity tests using other meteorological models to provide the wind fields for HYSPLIT indicate that the source regions identified are unaffected by our choice of meteorological model. We initialize trajectories every hour for the time periods of interest and run trajectories backward for 72 h starting at 100 m agl. We choose 100 m agl because previous work at the site has shown that trajectory simulations with this starting height agreed best with observations from the site (Lee et al. 2012).

Table 3.1: Meteorological variable, sampling instrument, sampling height(s), and sampling technique for each meteorological variable measured at Pinnacles. Data from the CMP3 pyranometer are used to compute CI.

Variable	Instrument	Sampling Height(s) (m agl)	Sampling Technique
Air temperature and humidity	Vaisala HMP45C	2, 5, 10, 17	30 min means of 1 Hz samples
Barometric pressure	Vaisala CS105 pressure sensor	14	30 min means of 1 Hz samples
CO_2 flux, latent heat flux	CSAT sonic anemometer, LI-COR 7500 water vapor and CO_2 gas analyzer	17	30 min means of 10 Hz samples
Incoming and outgoing shortwave and longwave radiation	Hukseflux 4-component net radiometer	17	30 min means of 1 Hz samples
Incoming shortwave radiation	Kip and Zonen CMP3 pyranometer	17	30 min means of 1 Hz samples
Rainfall	TR-525I tipping bucket rain gauge	3	30 min total
Sensible heat flux	CSAT sonic anemometer	17	30 min means of 10 Hz samples
Wind direction	MetOne 034B windset	10, 17	30 min sample
Wind speed	MetOne 034B windset	10, 17	30 min means of 1 Hz samples

3.2.5. Reanalysis products

We use the North American Regional Reanalysis (NARR) to assist with the interpretation of our observations. NARR uses boundary conditions from the National Center for Environmental Prediction (NCEP) global reanalysis, NCEP Eta model, and surface and rawinsonde observations to generate meteorological fields over North America at a 32 km spatial resolution and 3 h temporal resolution. There are 29 vertical levels, 17 of which are below 5 km (Mesinger et al., 2006). NARR data are obtained from ftp.cdc.noaa.gov/NARR. Whereas higher resolution models such as the NAM are also available, NAM compares well with NARR over the region of interest (c.f. Chapter 4), and thus we are confident in our choice to use NARR.

3.3. Results and discussion

3.3.1. Meteorological characteristics of the site

The region around Pinnacles is classified as humid subtropical in the Piedmont east of the Blue Ridge Mountains and is humid continental along and west of the Blue Ridge Mountains (e.g. Lee et al., 2012; Lee et al, 2014). At Pinnacles, mean afternoon temperatures 17 m agl range from -2°C in January to 22°C in July (Figure 3.2a). Water vapor mixing ratios 17 m agl are smallest (largest) in winter (summer), with mean values around 3 g kg^{-1} (11.0 g kg^{-1}), and the mean daily amplitude is about seven times larger in summer than in winter. Rainfall is evenly distributed throughout the year, and total annual rainfall in 2009, 2010, 2011, and 2012 is 1396 mm, 1467 mm, 1493 mm, and 1079 mm, respectively.

Mean afternoon sensible heat fluxes range from <100 W m^{-2} in December to 250 W m^{-2} in April (Figure 3.2b). Latent heat fluxes begin increasing in April and are larger than the sensible heat fluxes from June to September, with the highest values near 300 W m^{-2} in June. The latent heat fluxes agree with those reported by Lee et al. (2012) during the site's first year of measurements and with measurements reported at other mid-latitude continental locations located in similar climate regimes as Pinnacles (e.g. Greco and Baldocchi, 1996; Yi et al, 2001).

Mean wind speeds, averaged over 0000-2400 LST (UTC-5), are strongest in the winter (5.2 m s^{-1}) and weakest in the summer (2.8 m s^{-1}), and nighttime winds are about 1 m s^{-1} larger than daytime winds (Figure 3.2c). Winds typically shift from the northwest at night to the south during the late afternoon, contributing to the bimodality in wind direction present in all seasons (Figure 3.3).

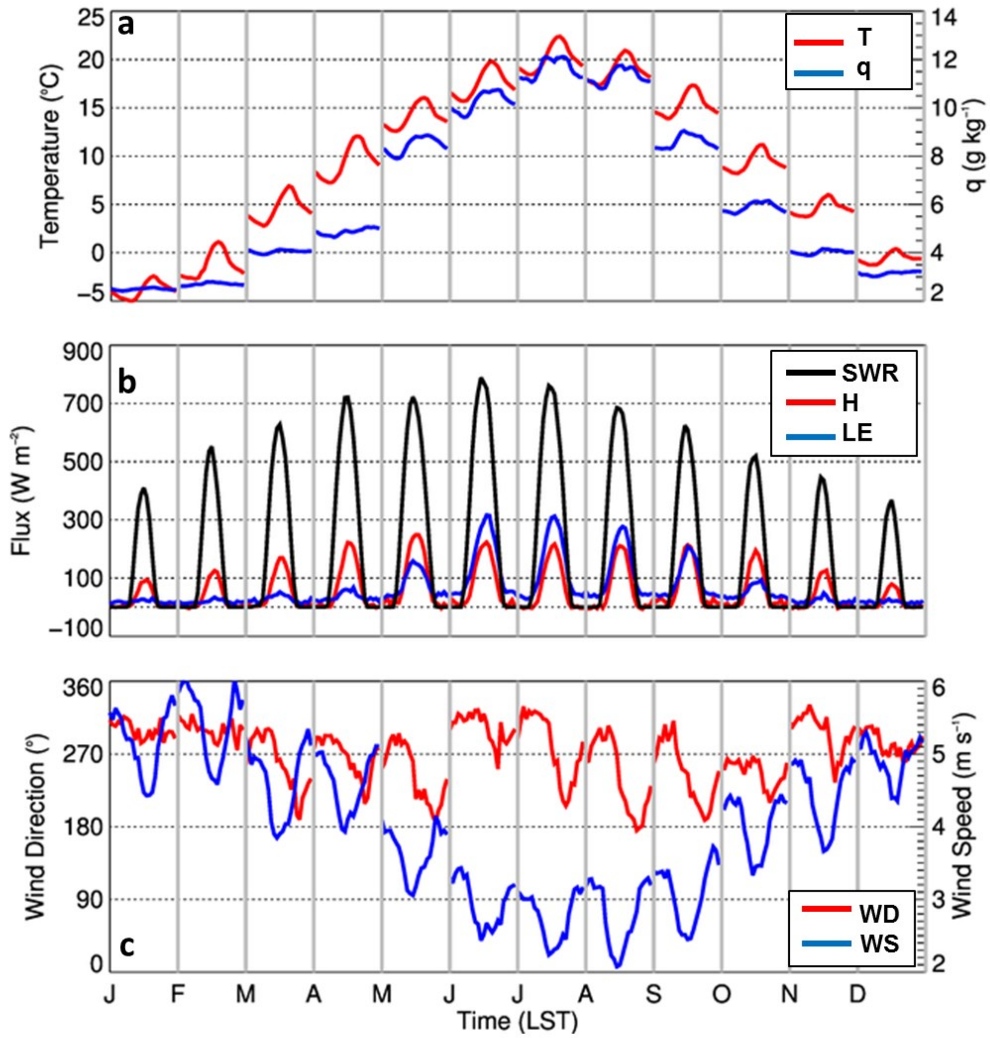

Figure 3.2: Mean diurnal time series by month of temperature (*T*) (red line) and water vapor (*q*) (blue line) (a); shortwave radiation (*SWR*) (black line), sensible heat (*H*) (red line) and latent heat (*LE*) (blue line) (b); wind direction (*WD*) (red line) and wind speed (*WS*) (blue line) (c). Vertical gray lines distinguish different months. Means represent measurements from 1 January 2009 – 31 December 2012. All measurements are made at 17 m agl at Pinnacles. Sensible and latent heat fluxes <-20 W m^{-2} are not included in the mean cycle. Because these are mean diurnal time series by month, the time series is discontinuous.

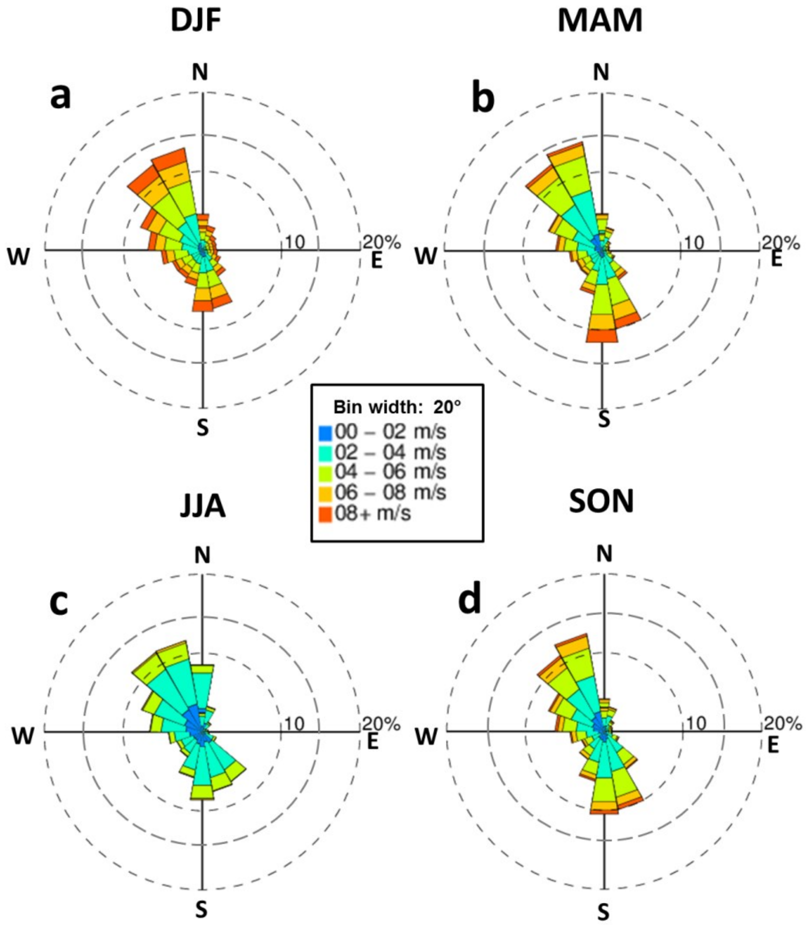

Figure 3.3: Wind distribution at 17 m agl at Pinnacles in winter (DJF) (a), spring (MAM) (b), summer (JJA) (c), and fall (SON) (d) from 1 January 2009 – 31 December 2012. Data completion percentage is 83.2%, 86.8%, 58.5%, and 79.2%, respectively.

3.3.2. Seasonal CO cycle

Between 2009 and 2012, the mean CO mixing ratio at 17 m agl at Pinnacles was 144.3±23.8 ppb. Annual mean (median) CO mixing ratios at 17 m agl in 2009, 2010, 2011, and 2012 were 139.2 ppb (137.7 ppb), 148.8 ppb (146.6 ppb), 145.1 ppb (144.0 ppb), and 144.7 ppb (144.8 ppb), respectively. Monthly mean CO at 17 m agl ranges from 160.3 ppb in March to 126.8 ppb in October (Table 3.2). CO mixing ratios are slightly higher near the surface. Mean CO mixing ratios measured at 5 m and 10 m agl are 146.6±24.4 ppb and 145.4±24.1 ppb, respectively, and exhibit the same diurnal and

Table 3.2: Monthly mean and median CO; monthly mean and median afternoon (1200-1600 LST) CO; monthly mean and median nighttime (0000-0400 LST) CO; and monthly maximum and minimum CO. All values are measured at 17 m agl at Pinnacles for the period 1 January 2009 – 31 December 2012.

Month	Mean (Median) CO (ppb)	Mean (Median) Afternoon CO (ppb)	Mean (Median) Nighttime CO (ppb)	Maximum CO (ppb)	Minimum CO (ppb)
Jan	156.7 (151.1)	156.6 (150.7)	155.6 (151.0)	335.7	101.5
Feb	158.4 (156.5)	158.5 (156.5)	159.5 (157.2)	250.4	98.3
Mar	160.3 (159.2)	160.3 (159.0)	161.0 (159.6)	241.5	108.3
Apr	159.3 (156.4)	157.5 (154.8)	161.1 (157.7)	448.9	94.9
May	146.3 (144.9)	148.0 (145.1)	146.3 (145.2)	240.9	94.6
Jun	140.8 (136.9)	140.9 (136.8)	140.7 (137.6)	224.8	82.8
Jul	135.9 (131.5)	138.1 (133.6)	134.6 (131.6)	229.3	80.8
Aug	140.8 (137.9)	141.2 (137.1)	140.1 (138.6)	289.5	76.6
Sep	131.8 (130.4)	132.4 (129.6)	132.0 (131.2)	274.8	68.1
Oct	126.8 (124.7)	127.0 (125.5)	125.9 (124.4)	254.5	80.4
Nov	138.4 (134.9)	139.7 (136.9)	137.9 (134.4)	251.7	65.7
Dec	141.4 (139.4)	142.7 (139.8)	140.6 (138.5)	289.0	96.4

seasonal trends as the measurements at 17 m agl. In this paper, we focus on CO measurements made at 17 m agl.

The seasonal CO cycle is caused by the seasonality of OH, which peaks in the summer, and larger anthropogenic emissions during the winter (e.g. Novelli et al., 1998), and is consistent with other continental mid-latitude sites (e.g. Popa et al., 2010). The CO cycle is consistent from year to year (Figure 3.4), but there are multiple times when the half-hour mean CO mixing ratio remains above one standard deviation from the mean for >1 diurnal cycle. For example, over the period 7-11 August 2010, CO mixing ratios remained above 180 ppb, resulting in mean monthly CO mixing ratios that were higher in August 2010 than in other Augusts.

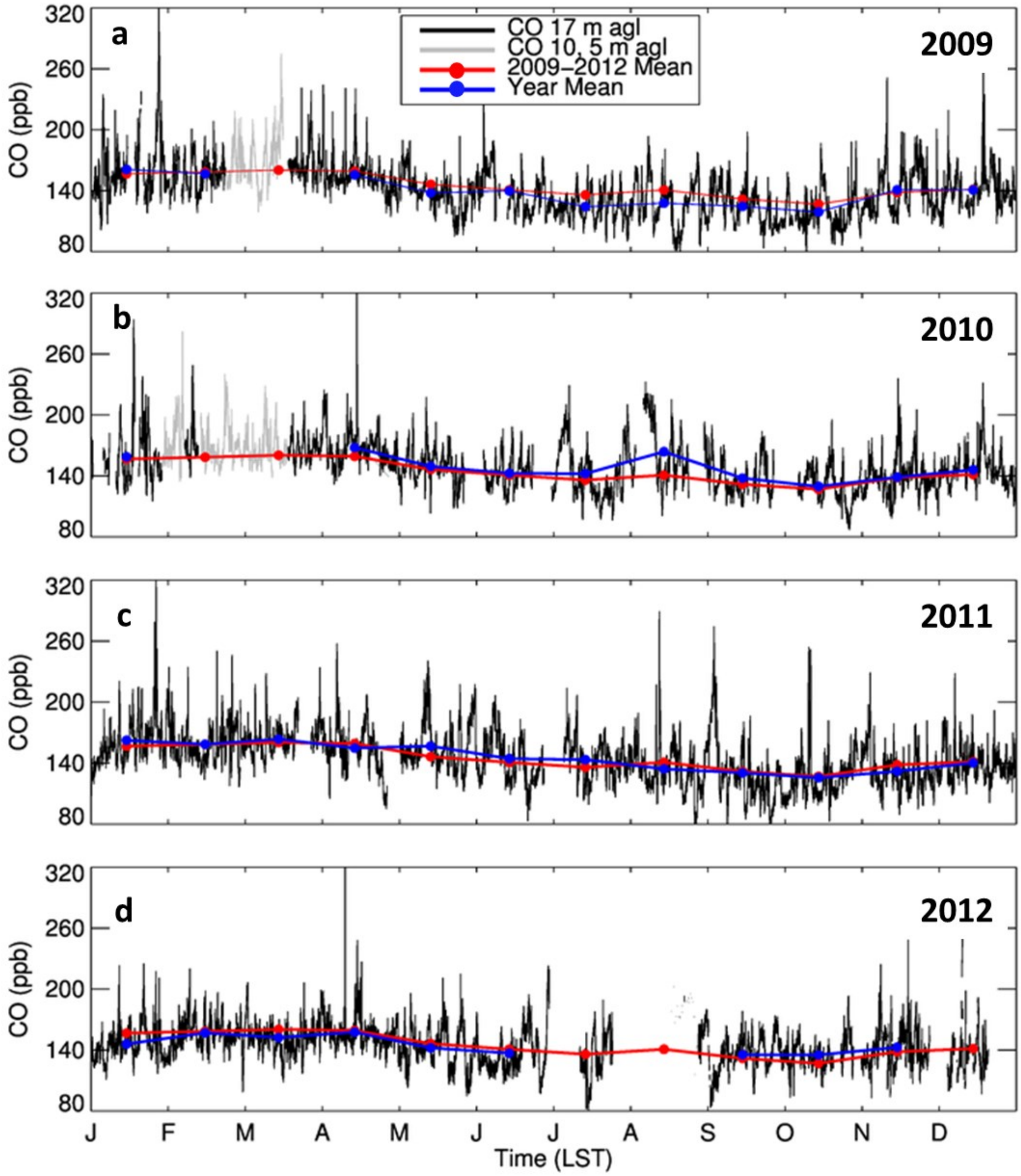

Figure 3.4: Half-hour mean CO at 17 m agl at Pinnacles in 2009 (a), 2010 (b), 2011 (c), and 2012 (d) (black line). Data gaps have been filled in using data from 5 m and 10 m agl (gray line) when available. Superimposed red and blue lines represent monthly means for all years and the individual years, respectively, for months with >50% data completion. Data completion at 17 m agl for 2009, 2010, 2011, and 2012 is 89.2%, 74.7%, 93.1%, and 78.3%, respectively. Measurements with an uncertainty >10 ppb are not shown.

During these and other periods such as in late June 2012 (when CO mixing ratios remained >170 ppb for about 24 h), the elevated CO mixing ratios were mainly due to a combination of emissions from forest fires in the region and by the buildup of polluted air caused by weak synoptic forcing. We use output from the satellite-borne Moderate Resolution Imaging Spectroradiometer (MODIS), which provides information on the timing and locations of fires (e.g. Justice et al., 2002; Giglio et al., 2003). Output from MODIS indicates that forest fires were present a few tens to a few hundred kilometers upwind of Pinnacles during the periods of elevated CO mixing ratio. Furthermore, web camera images from Pinnacles showed hazy skies and reduced visibility over these periods, and synoptic analyses, as well as HYSPLIT backward trajectories, further corroborated weak near-surface anti-cyclonic flow.

In addition to cases when CO mixing ratios remain high for >1 diurnal cycle, there are multiple times when CO mixing ratios increase to values 2-3 times larger than the mean. These events happen on timescales <3 h; examples of these events are discussed in more detail in Section 3.3.4.

3.3.3. Diurnal CO cycle

On diurnal timescales, CO increases during the daytime, beginning around 0900 LST in the winter and 1-2 h earlier in the other seasons (Figure 3.5). In all seasons, there is a maximum in the late afternoon-early evening that is followed by a nighttime decrease. The mean diurnal CO cycle has the largest amplitude in the winter (7.1 ppb) and smallest amplitude in the summer (4.0 ppb). Mean daytime CO increases of this magnitude have been reported at other mountaintops (e.g. Forrer et al., 2000; Henne et al., 2008b; Obrist et al., 2008) and are attributed to the vertical mixing and transport of valley PBL air to the mountaintop during the daytime. Nocturnal CO decreases at other mountaintops (e.g. Balzani Lööv et al., 2008) are caused by sinking motions that transport cleaner air from the FA to the mountaintop (e.g. Schmidt et al., 1996).

In contrast with what we find at Pinnacles, previous studies reported larger mean daily CO amplitude in the summer than in winter because convective mixing is strongest during the summer (e.g. Atlas and Ridley, 1996; Forrer et al., 2000; Gao et al., 2005;

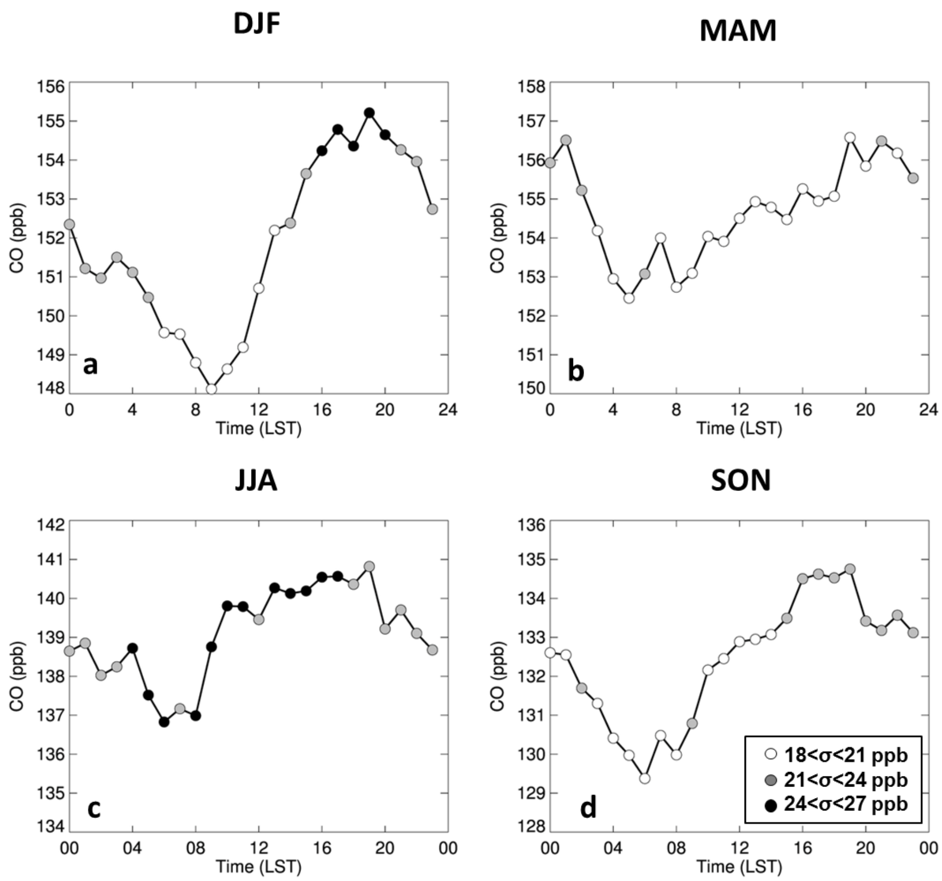

Figure 3.5: Mean diurnal CO cycle at 17 m agl at Pinnacles from 1 January 2009 – 31 December 2012 in winter (DJF) (a), spring (MAM) (b), summer (JJA) (c), and fall (SON) (d). White, gray, and black circles indicate standard deviations 18-21 ppb, 21-24 ppb, and 24-27 ppb, respectively. Data completion for winter, spring, summer, and fall is 80.7%, 84.7%, 78.4%, and 91.9%, respectively. Note different values but the same range for each y-axis.

Balzani Lööv et al., 2008; Henne et al., 2008b). For example, at Mount Kenya (3678 m msl) in Africa, the amplitude of the mean diurnal CO cycle in the late summer (i.e. the dry season) is nearly double the amplitude of the mean diurnal cycle in the late winter (i.e. the wet season) (Henne et al., 2008). Larger diurnal CO amplitudes in the warm season have also been reported at tall mountaintops such as Mauna Loa (3397 m msl) in Hawaii (Atlas and Ridley, 1996), Jungfraujoch (3580 m msl) in the European Alps (Balzani Lööv et al., 2008).

To put our findings from Pinnacles into the context of findings from other mountaintops, we compute the relationship between the amplitude of mean diurnal CO cycle and the mountaintop's elevation above mean sea level using studies from seven other global mountaintop monitoring sites which report the mean diurnal CO amplitude as a function of season. We find a positive relationship between elevation and the mean diurnal CO amplitude (Table 3.3), indicating that taller mountaintops have higher CO amplitudes. The taller mountaintops are more strongly and/or more frequently influenced by FA air, which is cleaner than air in the adjacent valley PBL, particularly at night. Thus, on days when valley PBL air affects the mountaintop, which typically occurs during the daytime in the summer (e.g. Baltensperger et al., 1997; Lugauer et al., 1998), there is a larger change in the CO mixing ratio than there is when the mountaintop is unaffected by valley PBL air, which typically occurs in winter.

Table 3.3: CO amplitude in different seasons from other mountaintops in the literature at which CO has been studied. CO amplitudes are not available (NA) in all seasons at all sites.

Mountaintop	Elevation (m)	Winter CO Amp. (ppb)	Spring CO Amp. (ppb)	Summer CO Amp. (ppb)	Fall CO Amp. (ppb)	Reference
Mount Kenya	3678	9	15	25	20	Henne et al., 2008b
Jungfraujoch	3580	3	10	11	5	Forrer et al., 2000
Mount Lulin	2862	22	16	20	23	Ou-Yang et al., 2014
Mount Bachelor	2763	NA	8	NA	NA	Weiss-Penzais et al., 2006
Mei-Feng, Taiwan	2269	50	20	10	75	Lin et al., 2011
Whistler	2182	3	3	5	3	MacDonald et al., 2011
Mount Tai	1534	NA	NA	110	100	Gao et al., 2005
Pinnacles	1017	7	5	4	6	This study

However, there are many other factors besides elevation that affect the observed trace gas variability, including mountaintop shape (e.g. Igarashi et al., 2006), meteorological variability (e.g. Cooper and Moody, 2000; Lee et al., 2012; Pandey Deolal et al., 2014), boundary layer heights (c.f. Chapter 4), and proximity to local emissions sources (e.g. Gao et al., 2005). For example, a mountaintop such as Mount Tai

(1534 m msl) in China's Shandong province, despite its relatively low elevation, has a large mean diurnal CO cycle in the summer with a CO amplitude >100 ppb due to the site's proximity downwind of anthropogenic CO emissions (Gao et al., 2005). The effect of boundary layer heights is investigated in detail in Chapter 4 in which it is found that CO amplitudes at Pinnacles increase with decreasing boundary layer heights. The importance of meteorological variability to the diurnal CO behavior is further investigated in the next section.

3.3.4. Daily CO amplitude variability

During the 4-year period of interest, the CO amplitude, which we define as the difference between the daily maximum and daily minimum half-hour CO mixing ratio, ranged from 10.4 ppb to 293.7 ppb, and the mean (median) amplitude was 39.2±23.7 ppb (33.2 ppb) (Figure 3.6). Daily CO amplitudes are typically largest in winter (44.4±26.2 ppb) and smallest in summer (36.7±18.4 ppb) but show much variability around the mean. Daily amplitudes above the 90th percentile (i.e. >67 ppb), and therefore also the largest mean daily CO amplitudes, occur most often during the winter. Note that the daily CO amplitudes are much larger than the amplitude of the mean daily CO cycles because averaging removes some of the day-to-day CO variability.

We compare the days with the largest (>90th percentile) and the smallest CO amplitudes (<10th percentile) to determine the dominant meteorological forcings affecting CO variability during these types of days. Because of seasonal differences in CO mixing ratio and daily CO amplitude, we differentiate among seasons. Within any season, days with the smallest (largest) CO amplitudes occur on days with the largest (smallest) amounts of incoming shortwave radiation and the largest (smallest) diurnal temperature ranges, which is in contrast to previous studies on the diurnal CO variability at other mountaintops (e.g. Gao et al., 2005).

Independent of season, the largest diurnal CO changes oftentimes occur on timescales <3 h and are independent of time of day. For example, CO increased from 145 ppb to 241 ppb between 0600 and 0800 LST on 11 April 2009. Synoptic analyses reveal that a cold front passed through the region during this time, inducing a wind shift from the southwest to northwest that resulted in a short-lived CO increase, during which CO

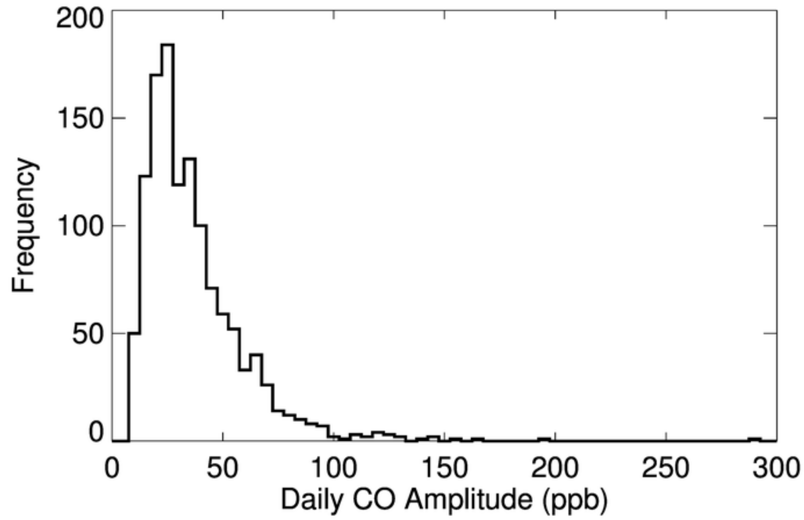

Figure 3.6: Frequency distribution of daily CO amplitude, defined as the difference between the daily maximum and minimum half-hour CO mixing ratio, from 1 January 2009 – 31 December 2012 at 17 m agl at Pinnacles. Each bin size is 5 ppb.

mixing ratios remained >200 ppb for 2 h. Analysis of other variables measured on-site indicates that this CO increase was accompanied by a CO_2 increase and water vapor decrease. HYSPLIT backward trajectories (not shown) indicate that the prefrontal air originated over the southeastern US and had less contact with surface emissions than the postfrontal trajectories that passed over polluted regions in the northeastern US prior to arriving at Pinnacles.

Another example of a large CO change was on 26 January 2011 when CO mixing ratios increased from 176 ppb to 322 ppb between 1400 and 1600 LST during the passage of a coastal winter storm east of Pinnacles. Consistent with the 11 April 2009 frontal passage, the CO increase during the 26 January event coincided with a CO_2 increase and water vapor decrease. HYSPLIT trajectory analyses show that the CO, CO_2, and water vapor changes were caused by an air mass change that occurred as the coastal storm moved away from Pinnacles, resulting in polluted air from the northeastern US being transported to Pinnacles.

From these examples, as well as from other cases not discussed, we conclude that the largest diurnal CO changes occur in the presence of synoptic disturbances, which induce wind shifts that transport air from polluted upwind source regions to Pinnacles.

This finding is consistent with our hypothesis stated in Section 3.3.1, as well as with previous studies in flat terrain (e.g. Hurwitz et al., 2004) and at mountaintops (e.g. Zellwegger et al., 2003; Brooks et al., 2012) including Pinnacles (Lee et al., 2012). However, our finding that days with the smallest CO amplitude typically occur on days with strong insolation appears counterintuitive and is contrary to our hypothesis. Strong insolation is expected to facilitate the vertical transport of air from upwind valleys to nearby mountaintops by convective mixing and upslope flows, processes which induce large changes in pollutant concentrations on diurnal timescales (e.g. Baltensperger et al., 1997; Lugauer et al., 1998). To better understand this apparent contradiction, we isolate fair weather days and investigate the CO variability on these days in the next section.

3.3.5. CO variability on fair weather days

We identify fair weather days by calculating a clearness index (CI) for each day in the four-year data set using solar radiation measurements. Following Whiteman and Allwine (1986), we calculate the maximum total incoming solar radiation that could be received at Pinnacles (i.e. the theoretical maximum). We then sum the total amount of incoming solar radiation measured at Pinnacles and divide this value by the theoretical maximum to determine the CI (Whiteman et al., 1999a). We find that CO amplitude decreases as a function of CI. This pattern is most apparent when binning the CO amplitude into different categories based on CI. Days with the smallest CI have both the largest mean CO amplitudes and largest interquartile ranges. Furthermore, the 90^{th} percentile of these cases have CO amplitudes >80 ppb, whereas the clearest days have CO amplitudes approximately half this value (Figure 3.7). Days with low CI are typically cloudy, rather than hazy, based on web camera images from the site, and have stronger winds than days with high CI. Mean 17 m wind speeds on days with the lowest (highest) CI are around 5.3 m s^{-1} (3.8 m s^{-1}) because cloudy days are more prone to the impacts of synoptic disturbances, which induce higher wind speeds, and result in larger daily changes in CO mixing ratios (c.f. Section 3.3.4). In contrast, days with higher CI are not impacted by synoptic disturbances, and thus the CO amplitudes on these days are usually smaller. We classify days with a high CI as fair weather days, using a CI threshold of 0.6

(i.e. above the 50th percentile). We note, though, that our results are not significantly impacted by our choice of the CI threshold.

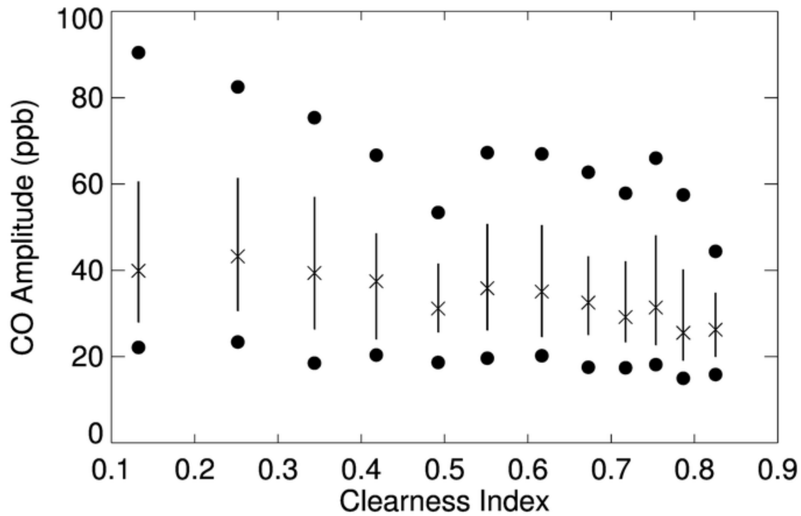

Figure 3.7: Daily CO amplitude as a function of clearness index, divided into 12 bins (N=78 for each bin), from 1 January 2009 – 31 December 2012. Black X's represent 50th percentile; lines extend out to 25th and 75th percentiles; black circles represent the 10th and 90th percentiles.

Our analyses reveal that there are fair weather days with large diurnal CO amplitudes and fair weather days with small diurnal CO amplitudes, and thus we further investigate the factors causing this variability. Since advective processes are a major factor in determining the local rate of change of a trace gas mixing ratio, we focus next on a discussion of the role of horizontal wind speed and direction on the CO variability. Previous work has found that diurnal wind direction changes are an important component of the climatology at other mountaintop monitoring sites (e.g. Atlas and Ridley, 1996; Kleissl et al., 2007). These wind direction changes are attributed to thermal circulations and are associated with the transport of pollutant-rich PBL air to nearby mountaintops (e.g. Baltensperger et al., 1997; Lugauer et al., 1998). Thus, to help understand the impact of wind direction changes on the CO variability at Pinnacles, we determine the mean CO mixing ratio as a function of wind direction. Winds from the east, southeast, and south (southwest, west, and northwest) happen 32% (45%) of the time and correspond with a mean CO mixing ratio of 147.5 ppb (141.8 ppb) (Figure 3.8). Southerly winds have already been shown to correlate with higher CO and CO_2 mixing ratios during the cool season in previous studies at the site (Lee et al. 2012), and we find this to be true in the other seasons as well. Because wind shifts to the south are an important part of the climatology at Pinnacles (c.f. Figure 3.2c) and are associated with higher CO mixing ratios, we hypothesize that the CO variability on fair weather days can be explained by the presence or absence of a wind shift to the south during the daytime. Therefore, we use Pinnacles' wind measurements and classify fair weather days based on the presence or absence of a southerly wind shift. We first determine the mean wind direction for four six-hour periods: 00-06 LST, 06-12 LST, 12-18 LST, and 18-00 LST. 90% of the 628 days fair weather days had a CO record >50% complete during the day and are investigated further. 49% of these days have a steady wind direction throughout the day, i.e. the wind direction varied by <90° (Table 3.4). Consistent with the climatology discussed in Section 3.3.1, northwesterly winds are most common and occur predominantly during the winter months. Of the fair weather days with a constant wind direction, 67% have northwesterly winds throughout the day, whereas 4% have mean winds from the northeast. Since northwesterly winds are most common and because CO varies as a function of wind direction (c.f. Figure 3.8), we classify days as Type I if the mean wind direction in each six-hour period is from the northwest.

The remaining 51% of the fair weather days have a wind shift. A wind shift from the northwest during the first half of the day (00-12 LST) to a different wind direction during the second half of the day (12-24 LST) is most common and happens on 48% of this subset of days. On 56%, 35%, and 9% of this subset of days, there is an afternoon counterclockwise wind shift to the southwest, southeast, and northeast, respectively. We classify days with an afternoon wind shift to the southwest or southeast as Type II days. The remaining fair weather days have a wind shift other than what is differentiated here; they are classified as neither Type I nor Type II and are revisited in Section 3.3.5.3. In summary, 33% and 22% of all fair weather days are classified as Type I and Type II days, respectively.

Table 3.4: Number and percentage of fair weather days with steady winds and fair weather days without steady winds.

Classification of Fair Weather Days	Number	Percentage of Fair Weather Days
Steady winds	277	49
Steady northwesterly winds (Type I)	187	33
Days with a wind shift	288	51
Days with a wind shift from northwesterly to southerly (Type II)	126	22
Days that are not Type I or Type II	252	45

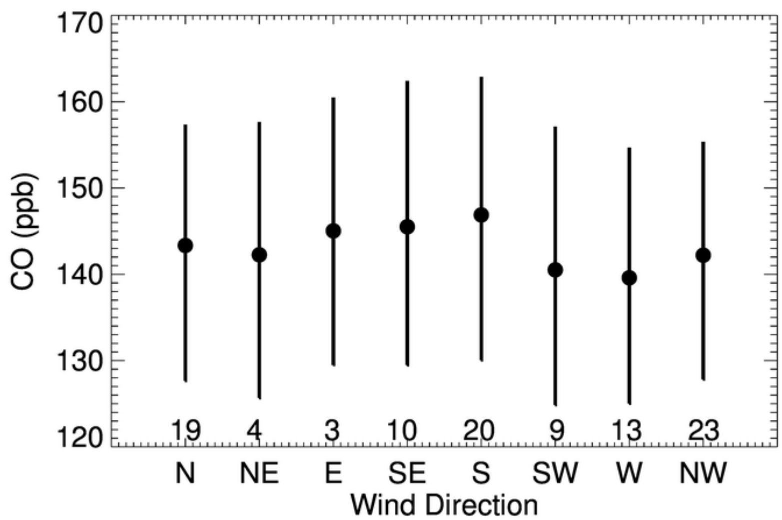

Figure 3.8: Mean CO mixing ratio ±1 standard deviation as a function of wind direction from 1 January 2009 – 31 December 2012 at 17 m agl at Pinnacles. Numbers shown are the percentage of the total. Numbers do not add to 100% because of rounding.

Type I and Type II days have the similar mean CI (0.75). Mean afternoon (1200-1600 LST) shortwave radiation for Type I and Type II days is 624 W m^{-2} and 633 W m^{-2}, respectively, whereas mean afternoon sensible heat fluxes on Type I and Type II days are 171 W m^{-2} and 206 W m^{-2}, respectively. There are no seasonal differences in the occurrences of Type I or Type II days, although days with strong (weak) mean winds are most common in winter (summer) (Table 3.5) which is consistent with the climatology (c.f. Figure 3.2). Synoptic analyses indicate that Type I days are most common following cold front passages, and mean winds are 0.7 m s^{-1} higher than on Type II days. The diurnal behavior of wind direction on Type I and Type II days at Pinnacles also happens at Big Meadows and nearby monitoring sites in flat terrain.

Table 3.5: Occurrence of Type I and Type II days as a function of season.

	Winter	Spring	Summer	Fall
Type I, all	4.2	15.8	10.9	10.7
Type I, Light winds (<3.9 m s^{-1})	4.2	7.6	9.0	4.9
Type I, Strong winds (>3.9 m s^{-1})	9.7	8.2	1.9	5.8
Type II, all	9.2	11.4	8.4	9.1
Type II, Light winds (<3.3 m s^{-1})	1.7	3.3	6.5	5.5
Type II, Strong winds (>3.3 m s^{-1})	7.5	7.1	3.0	2.7

We use NARR to characterize the synoptic conditions on Type I and Type II days and to investigate the underlying causes of the wind shift on Type II days. Both Type I days and Type II days have a near-surface anticyclone southwest of Pinnacles. Consistent with Type I days, composites of the 900 mb (i.e. the approximate elevation of Pinnacles) wind fields at 0900 UTC (0400 LST) on Type II days indicate the presence of northwesterly flows across Virginia (Figure 3.9a). Consistent with the observations, NARR composites of the 900 mb wind fields indicate a counterclockwise wind shift on Type II days, with southwesterly winds in the afternoon. This wind shift is most pronounced in the lee of the Appalachian Mountains, but is largely absent west of the Appalachian Mountains and along the immediate coast (Figure 3.9b). This diurnal wind shift is also present in the surface (10 m agl) NARR composites. The mean v-component of the wind along and immediately east of the Blue Ridge Mountains is -1 m s^{-1} (northerly) in the 0900 UTC NARR composites, but is +2 m s^{-1} (southerly) on the 2100 UTC NARR composites (not shown). These wind shifts have been documented in previous studies in other mountainous regions, e.g. the European Alps (e.g. Lugauer and Winkler, 2005) and Rocky Mountains (e.g. Whiteman et al., 1999b), and have been attributed to the diurnal cycle of diabatic heating (e.g. Whiteman, 2000). The wind shift that we observe is also present several hundred kilometers away from the Appalachian Mountains, and it is not clear if these wind shifts are caused by the diabatic heating of the mountain slopes in this region or by other processes such atmospheric tides (e.g. Mass et al., 1991).

3.3.5.1. Type I days

On Type I days, both the mean and median diurnal CO cycles exhibit a decrease between 0000 LST and 0800 LST when winds are from the northwest, consistent with the diurnal CO cycles shown in Figure 3.5. Following a short-lived mid-morning CO maximum, CO decreases to a minimum between 1400 and 1800 LST and closely follows the diurnal cycle in water vapor (Figure 3.10). Following the afternoon CO minimum, CO begins increasing due to pollutants accumulating within a stabilizing PBL. Differentiating by mean wind speed, we find that there is a short-lived CO and water vapor maximum around 1000 LST that likely coincides with the arrival of valley PBL air at the mountaintop on days with weak winds (and thus less synoptic forcing). Following the short-lived CO increase, mixing and dilution within the growing daytime PBL result in a late afternoon CO minimum at Pinnacles.

The observed CO variability on Type I days contrasts with findings on the diurnal trace gas and aerosol variability at other mountaintops at which vertical transport of valley PBL air causes a daytime trace gas and aerosol increase (e.g. Baltensperger et al.,

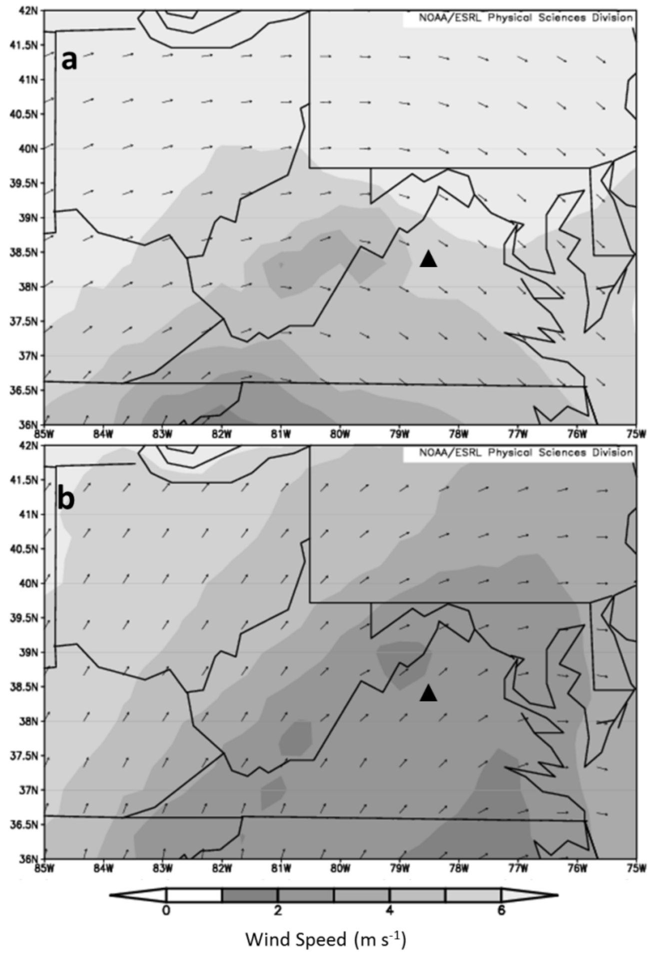

Figure 3.9: NARR composites on Type II days of 900 mb wind speed and direction at 0900 UTC (a) and 2100 UTC (b). The location of Pinnacles is indicated by a black triangle. Data are available from <ftp://ftp.cdc.noaa.gov/NARR/>

1997; Weiss-Penzias et al., 2006) and also contrasts with the mean seasonal diurnal cycles of CO at Pinnacles. The presence of constant wind directions throughout the entire diurnal cycle at Pinnacles is an important characteristic of the diurnal CO variability on Type I days with a daytime CO minimum. This diurnal cycle has been reported for other trace gas species. For example, peroxyacetic nitric anhydride (PAN), which depending on ambient temperature has a relatively long atmospheric lifetime (e.g. Seinfeld and Pandis, 1996) that enables it to be transported over long distances (e.g. Fahey et al., 1986), was sampled at a mountaintop monitoring site approximately 360 km southwest of Pinnacles in the late 1980s (e.g. Roberts et al., 1995). Consistent with our findings in the diurnal

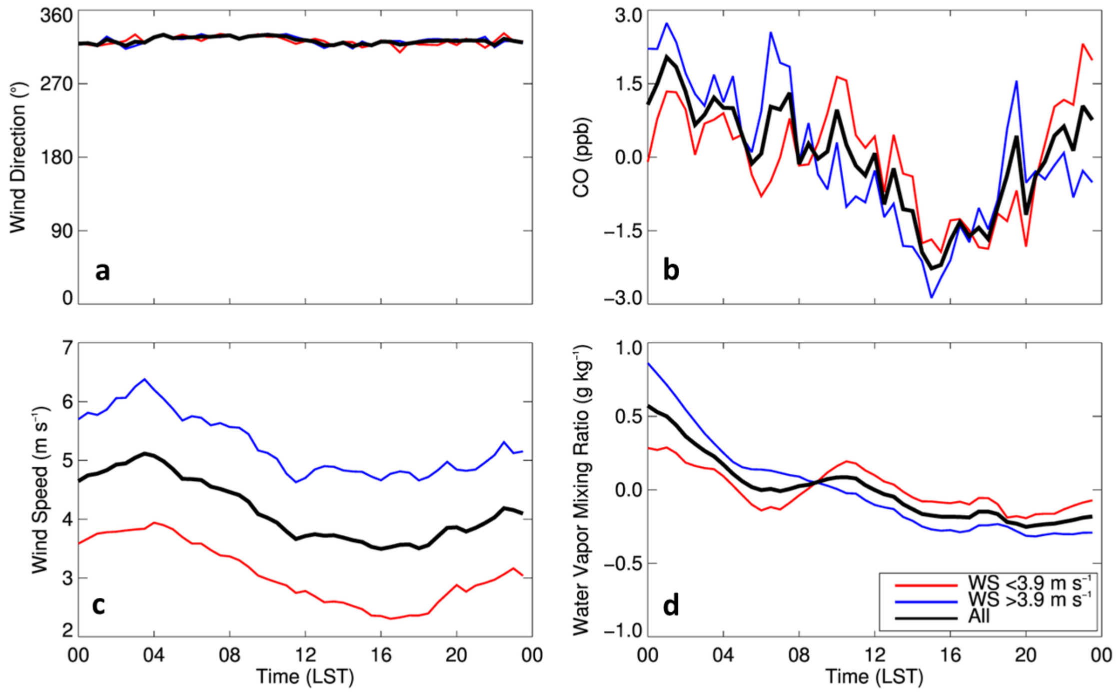

Figure 3.10: Mean wind direction (a), CO (b), wind speed (c), and water vapor (d) on Type I fair weather days. Red, blue, and black lines represent Type I days with light winds (<3.9 m s^{-1}, N=94), Type I days with strong winds (>3.9 m s^{-1}, N=93), and all Type I days (N=187), respectively. Daily means are removed from panels (b) and (d) for clarity. All measurements are made at 17 m agl at Pinnacles.

CO cycle on Type I days, the mean diurnal cycle in PAN during the summertime shows a daytime decrease (Roberts et al., 1995). This daytime decrease is consistent with the diurnal cycle of trace gas variability over flat terrain (e.g. Popa et al., 2010). A few hundred meters above the surface in flat terrain, there is oftentimes a short-lived mid-morning trace gas increase due to the arrival of polluted air contained within the nocturnal PBL (e.g. Schmidt et al., 2014). As the PBL increases in depth, turbulent mixing within the PBL causes trace gas mixing ratios to decrease (e.g. Popa et al., 2010; Schmidt et al., 2014). The PBL depth represents the height to which turbulent mixing dominates and is an important driver of trace gas and aerosol variability over flat terrain (e.g. Seibert et al., 2000; Gibert et al. 2007) and valleys (e.g. Pal et al., 2014).

Based on the findings in the present study, the PBL height is similarly expected to be another important driver of the CO variability at mountaintops like Pinnacles, in particular on Type I days. Continuous PBL height observation platforms for Pinnacles and its immediate surroundings are not available. The sounding station nearest Pinnacles where twice-daily rawinsonde observations are available is Dulles Airport (IAD), which is located 90 km northeast of Pinnacles. If we assume that PBL heights from the IAD rawinsonde observations are the same as at Pinnacles, we find that days with deep PBLs (i.e. those exceeding the mountaintop height) have a daytime CO decrease, consistent with what we find for Type I days. In a forthcoming paper, we investigate in more detail how PBL heights near Pinnacles affect the mountaintop trace gas variability.

3.3.5.2. Type II days

On Type II days, an afternoon shift in wind direction has a significant effect on CO variability, and the amplitude of both the median and mean CO cycle is about twice the amplitude of Type I days (Figure 3.11), illustrating the dominance of horizontal advection over vertical mixing. During the nighttime, CO decreases. As winds begin to shift towards the south during the late morning, CO and water vapor begin increasing and peak around 1900 LST. Strong mechanical mixing causes smaller CO peaks on days with strong winds compared to days with weak winds. Following the daytime increase, CO decreases as winds shift towards the west.

Unlike Type I days, the observed pattern of CO variability on Type II days is more consistent with the mean diurnal CO cycles shown in Figure 3.5 and with the mean diurnal CO cycles reported at other mountaintops (e.g. Weiss-Penzias et al., 2006; Henne et al., 2008b; Obrist et al., 2008). Lee et al. (2012) found that high CO and CO_2 on days with south and southeast winds is caused by the near-surface transport of air masses southward from the Northeast and Mid-Atlantic and then northwestward to Pinnacles. Thus, the transport of emissions from these areas may be explain the high CO mixing ratios observed at Pinnacles during the afternoon on Type II days. However, Skyline Drive, a tourist road through Shenandoah National Park, is also directly upwind of Pinnacles during the afternoon on Type II days. To investigate the possible effect of Skyline Drive on the CO measurements, we select Type II days with weak winds, i.e. when Skyline Drive is expected to have the largest impact on the CO measurements, and differentiate among the seasons due to seasonal differences in traffic volume. Although

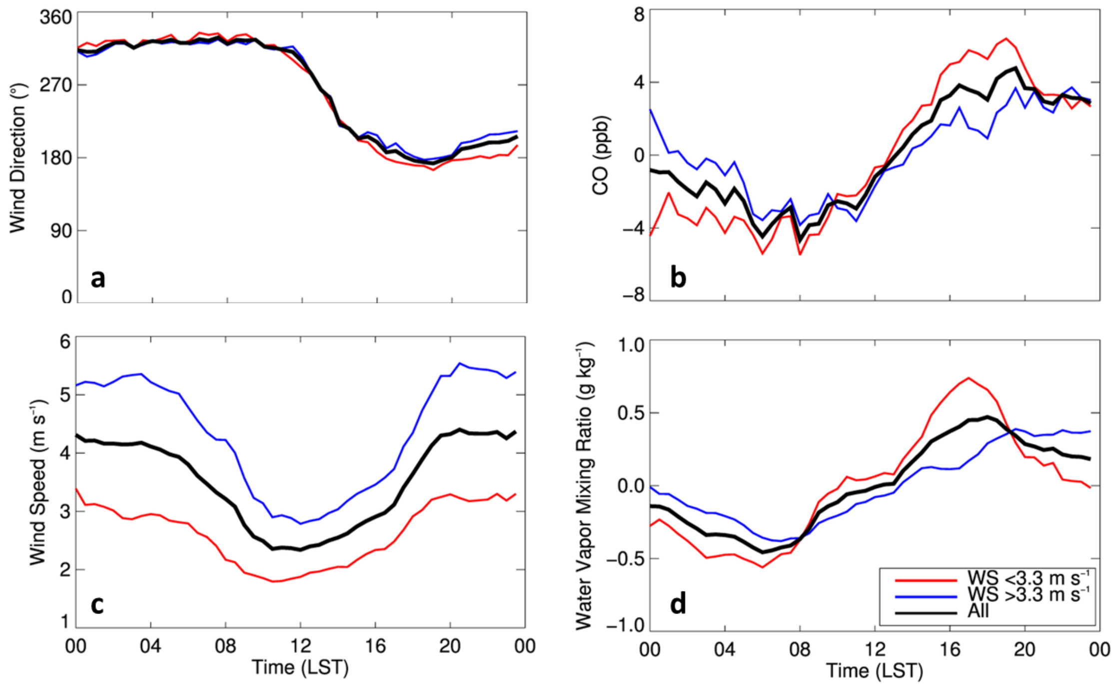

Figure 3.11: Same as Figure 3.10 but for Type II days. Red, blue, and black lines represent Type II days with light winds (<3.3 m s^{-1}, N=62), Type II days with strong winds (>3.3 m s^{-1}, N=64), and all Type II days (N=126), respectively. Note the y-axes in panels (b) and (c) are different from Figure 3.10.

emissions are typically higher during the summer and fall because of larger traffic volumes, we find no evidence of a larger afternoon peak in these seasons compared with other seasons. Furthermore, the CO maximum occurs several hours after the peak in traffic along Skyline Drive. Thus, we infer that there is no significant influence of Skyline Drive on CO mixing ratios measured at Pinnacles, which is consistent with previous studies in the region which also found no significant relation between traffic volume and CO_2 at Pinnacles (Lee et al., 2012), or CO (e.g. Poulida et al., 1991) and O_3 (e.g. Cooper and Moody, 2000) at Big Meadows.

3.3.5.3. CO variability on other fair weather days

Analysis of fair weather days not classified as Type I or Type II underscores the importance of wind shifts to the Pinnacles CO variability. On the days not classified as Type I or Type II (45% of the remaining fair weather days), the wind direction change differed from the Type II classification. Fair weather days with wind shifts to the northwest had CO decreases because, as previously discussed, northwest winds are associated with lower CO mixing ratios than southerly winds. Conversely, fair weather days with southerly wind shifts had daytime increases in CO. These characteristics of the CO variability on days not classified as Type I or Type II highlight the finding that, when wind direction changes occur at Pinnacles, they have a greater impact on the diurnal CO variability than PBL dilution.

3.4. Conclusions and implications

In this study, we presented an overview of 4 years (1 January 2009 – 31 December 2012) of meteorological and CO measurements from Pinnacles, a new mountaintop monitoring site in the Appalachian Mountains, and investigated the hypothesis that the largest CO variability occurs during cold front passages and on fair weather days due to the transport of polluted PBL air to the mountaintop. We found that CO typically increases from a minimum between 0500 and 0900 LST to a maximum between 1600 and 2000 LST. Consistent with our hypothesis, the largest CO changes, with half-hourly means up to around 320 ppb, occur in the presence of synoptic disturbances, as previously found for CO_2 changes at the site (Lee et al., 2012). Contrary to our hypothesis, though, the smallest CO changes happen on fair weather days (i.e. days with a CI>0.6 and about 50% of all days), which we further investigated by classifying fair weather days into two regimes based on the presence or absence of a wind shift. On days with steady northwesterly winds at the site (Type I days or 33% of the fair weather days), mixing and dilution within the daytime PBL is the dominant driver of CO variability. Thus, daytime PBL heights are an important driver of the trace gas variability at the site and are investigated in detail in a forthcoming study.

On days with a wind shift from the northwest to the south (Type II days or 22% of the fair weather days), the CO increase is about twice the magnitude of the CO change on days without wind shifts, and the site samples different upwind source regions. From these analyses, we conclude that the diurnal CO cycle at Pinnacles is largely driven by a daytime wind shift to the south which causes a daytime CO increase. This wind shift happens not only on Type II days, but is an important part of the climatology (c.f. Figure

3.2c) and is partly driven by synoptic–scale forcings (i.e. frontal passages) and by local- to mesoscale forcings (i.e. diurnal mountain circulations).

The results in this study provide new insights into the use of trace gas measurements from low mountaintops like Pinnacles in applications that require background trace gas measurements. The nighttime CO decrease and daily minimum between 0500 and 0900 LST present in the mean diurnal CO cycle indicates the transport of FA air to the site. Therefore, pre-dawn trace gas measurements, particularly those in winter, are likely to be most representative of background CO values.

When we differentiated between fair weather days with a wind shift and days without a wind shift, we found that the diurnal CO variability is analogous to findings from other, taller mountaintops (e.g. Forrer et al. 2000; Balzani Lööv et al., 2008; Henne et al., 2008b; Obrist et al., 2008) on fair weather days with a wind shift. The wind shift results in different upwind emission sources being sampled and may allow trace gas measurements from Pinnacles to help estimate emissions and reduce flux estimate uncertainties in upwind areas (e.g. Schuh et al., 2010), provided that the models accurately represent atmospheric transport over complex terrain.

Finally, our findings are the first to indicate that, in other conditions (i.e. fair weather days with steady winds), CO mixing ratios at low mountaintops like Pinnacles decrease during the daytime, which is nearly identical to what happens at tall towers in flat terrain. As noted earlier, there is a short-lived late morning CO increase that occurs both atop tall towers and at Pinnacles. Whereas the increase atop tall towers is caused by the arrival of polluted nocturnal PBL air (e.g. Yi et al., 2001; Pal et al., 2015), the increase at mountaintops is caused by the arrival of polluted PBL air contained within the nocturnal valley PBL. As the PBL depth increases, CO decreases at the tops of tall towers and at low mountaintops like Pinnacles. Thus, local impacts on afternoon trace gas measurements made during these situations (i.e. about 60% of the days without clouds) are expected to be minimized, and mountaintop trace gas measurements can be considered along with tall tower measurements in applications requiring regionally-representative values.

3.5. Acknowledgments

This research and maintenance of the Pinnacles research station was partly funded by an MOU between the NOAA ESRL Global Monitoring Division and the University of Virginia and by NSF-CAREER Grant ATM-1151445. The authors thank staff from SNP, especially Elizabeth Garcia and Alan Williams, and students from the Environmental Sciences Department at the University of Virginia for helping to maintain data collection at Pinnacles, especially Nevio Babić, Stephanie Phelps, and Mark Sghiatti. Many thanks to Željko Večenaj at the University of Zagreb for on-site support in 2008, 2009, and 2012, and to Jonathan Williams at NOAA ESRL. We also thank the anonymous reviewer whose suggestions helped us improve the manuscript.

CHAPTER 4

ESTIMATING PLANETARY BOUNDARY LAYER HEIGHTS OVER A VALLEY FROM RAWINSONDE OBSERVATIONS AT A NEARBY AIRPORT: A CASE STUDY FOR THE PAGE VALLEY IN VIRGINIA, USA[1]

[1] Lee, T. R. and De Wekker, S. F. J., draft. Estimating planetary boundary layer heights over a valley from rawinsonde observations at a nearby airport: A case study for the Page Valley in Virginia, USA. *J. Appl. Meteorol. Clim.*

Abstract

The daytime planetary boundary layer (PBL) height, z_i, is an essential parameter required for many applications, including weather forecasting and air quality dispersion modeling. Estimates of z_i are not easily available and oftentimes come from twice-daily rawinsonde observations at airports, typically at 00 and 12 UTC. In many applications, questions often arise regarding the applicability of z_i retrieved from these twice-daily observations to surrounding locations. Obtaining this information requires knowledge of the z_i spatial variability which is limited, particularly in regions with mountainous terrain. The goal of the present study is to review methodologies reported in the literature to address this issue and develop methodologies further for the case study of estimating daytime z_i in the Virginia Blue Ridge Mountains. Our approach includes using rawinsonde observations from the nearest sounding station, Dulles Airport (IAD), which is located 90 km northeast of the Page Valley, as well as North American Regional Reanalysis (NARR) output and simulations with the Weather Research and Forecasting (WRF) model. When we select days on which z_i from NARR compare well with z_i determined from the IAD soundings, we find that z_i is larger (on the order of 200-400 m) over the Page Valley than at IAD and that these differences are typically larger in the summer than winter. WRF simulations indicate that z_i is larger over the Page Valley because of larger sensible heat

fluxes and indicate that z_i has terrain-following characteristics both on days with deep PBLs and on days with shallow PBLs.

4.1. Introduction

Turbulent mixing processes within the planetary boundary layer (PBL) govern the exchange of heat, moisture, momentum, and aerosols between Earth's surface and the overlying free atmosphere (e.g. Stull, 1988). The height of the PBL, z_i, represents the maximum height to which these turbulent mixing processes occur. On diurnal timescales, z_i is oftentimes deepest in the afternoon. Thus, the afternoon z_i is vital to describing the vertical mixing of trace gases and pollutants in air quality dispersion studies (e.g. Dabberdt et al., 2004). Whereas the role of z_i on the trace gas variability over flat terrain is well-understood (e.g. Pochanart et al., 2003; Volz-Thomas et al., 2003; Elanksy et al., 2007; Popa et al., 2011; Sahu et al., 2011), this knowledge is limited for mountainous regions. Previous studies have suggested that air masses representative of background concentrations are sampled at mountaintops when the valley z_i remains well below the mountaintop, whereas local to regional pollutant sources affect the mountaintop trace gas variability when the valley z_i reaches or exceeds the mountaintop height (e.g. Raatikainen et al., 2014). Acquiring this information is vital if mountaintop trace gas measurements are to be reliably used in applications that require background trace gas measurements, e.g. air chemistry models and inverse carbon transport models.

Estimates of z_i can come from many different platforms, including wind profilers, lidars, sodars, tethered balloons, masts, rawinsonde observations, aircraft observations (e.g. Clifford et al., 1994; Nyeki et al., 2000) and, since 2006, from space-borne lidars such as the Cloud-Aerosol Lidar with Orthogonal Polarization (CALIOP) on the Cloud-Aerosol Lidar and Infrared Pathfinder Satellite Observations (CALIPSO) satellite (Winker et al., 2007; Jordan et al., 2010). Each of these platforms has its own distinct advantages and disadvantages [see Seibert et al., 2000 for more details].

Among the other platforms enumerated above, rawinsondes observations, typically made at airports, are well-suited for long-term daily and sub-daily z_i estimates because they are made at least twice per day at hundreds of sites worldwide. Thus, rawinsondes observations have been used to develop z_i climatologies on continental- to global-scales (e.g. Holzworth, 1964; Seidel et al., 2010; Liu and Lang, 2010; Seidel et al., 2012; Wang and Wang, 2014). However, rawinsonde observation platforms are unevenly distributed globally and are hundreds of kilometers apart in many areas. If rawinsonde observations or other z_i observations are unavailable for a particular location of interest, one approach is to use z_i obtained from the nearest sounding station as a proxy (e.g. Hondula et al., 2013). Another approach is to use geostatisical interpolation procedures (e.g. Cressie, 1993), e.g. kriging with external drift (Kretschmer et al., 2013; Kretschmer et al., 2014), to spatially interpolate rawinsonde z_i to data sparse regions.

A downside of assuming that the z_i obtained from the nearest sounding station is a good proxy for surrounding locations or with using the above geostatisical interpolation procedures is that these approaches neglect the physical processes affecting spatial variability in z_i that occurs between individual point observations of z_i. Differences in z_i over the scale of hundreds of kilometers (i.e. the typical distance between rawinsonde observation stations) can be several hundred meters (e.g. Bianco et al., 2011; Bohnenstengel et al., 2011; Xie et al., 2013). Since sensible heat flux (*SHF*) governs z_i, spatial differences in *SHF* due to e.g. soil moisture (e.g. Avissar and Schmidt, 1998; Segall et al., 1988; Desai et al., 2006; Ma et al., 2011) and land use (e.g. Bianco et al., 2011) are often cited as main drivers of spatial z_i differences. In complex terrain, thermally and dynamically driven flows also affect spatial z_i differences (e.g. Kossmann et al., 1998; De Wekker, 2002; Bianco et al., 2011). Accounting for these processes is important for understanding the z_i spatial variability between point observations. Thus, another approach for obtaining z_i estimates is to use reanalysis or forecasting products, which assimilate rawinsonde observations and cover at least partially the physical processes driving the z_i spatial variability. For example, the High-Resolution Rapid Refresh (HRRR) model provides z_i estimates at 3 km spatial scales (e.g. Olson and Grell, 2014), and the Weather Research and Forecasting (WRF) model can generate z_i estimates at 1 km spatial scales (e.g. Xie et al., 2012). Even so, in regions with complex or mountainous terrain, z_i estimates at this high resolution may not always be valid because of the subgrid z_i spatiotemporal variability (e.g. Kossmann et al., 1998; Kalthoff et al., 2000). Furthermore, the models used to generate these z_i estimates can have difficulty resolving atmospheric processes at these spatial scales, particularly over mountainous terrain (e.g. Zong and Chow, 2013).

In the current paper, we develop an approach to estimate z_i that uses a combination of z_i obtained from a sounding station and z_i obtained from reanalysis products. We demonstrate our approach for the estimation of afternoon z_i over the Page Valley, located in the Blue Ridge Mountains in Virginia, USA, although our approach could be used to estimate z_i at other nearby locations as well. Acquiring reliable z_i estimates over the Page Valley in particular, though, is vital because the valley is located about 15 km upwind of a long-term mountaintop trace gas monitoring site where select atmospheric trace gases have been continuously monitored since 2008 (e.g. Lee et al., 2012). Reliable afternoon z_i estimates over the Page Valley are necessary to determine the degree to which the nearby mountaintop trace gas measurements are affected by local to regional pollutant sources. The sounding station nearest the Page Valley where twice-daily rawinsonde observations are available is located at Dulles Airport (IAD) (38.98 N, 77.49 W, 87 m msl), 90 km northeast of the Page Valley (Figure 4.1a) in a suburban setting about 35 km northwest of Washington DC. Due to the regional topography, discussed in more detail in the next section, the Page Valley receives less rainfall annually than IAD. Thus, we hypothesize that, despite the relatively close proximity of the Page Valley to IAD, z_i will be larger over the Page Valley than at IAD because less moisture causes more net radiation to be partitioned into *SHF* over the Page Valley than near IAD, resulting in larger z_i over the Page Valley. To test this hypothesis, we first present our approach to obtain z_i estimates for the Page Valley from the IAD rawinsonde observations. We then investigate the underlying physical processes responsible for the z_i variability in this region using WRF simulations. We conclude the paper with a discussion of the errors arising when using z_i from sounding stations to estimate z_i at surrounding locations.

4.2. Methods

4.2.1. Site description

The Page Valley is oriented south-southwest to north-northeast, is approximately 80 km long, averages 10-15 km wide, and ranges from around 200 m above mean sea

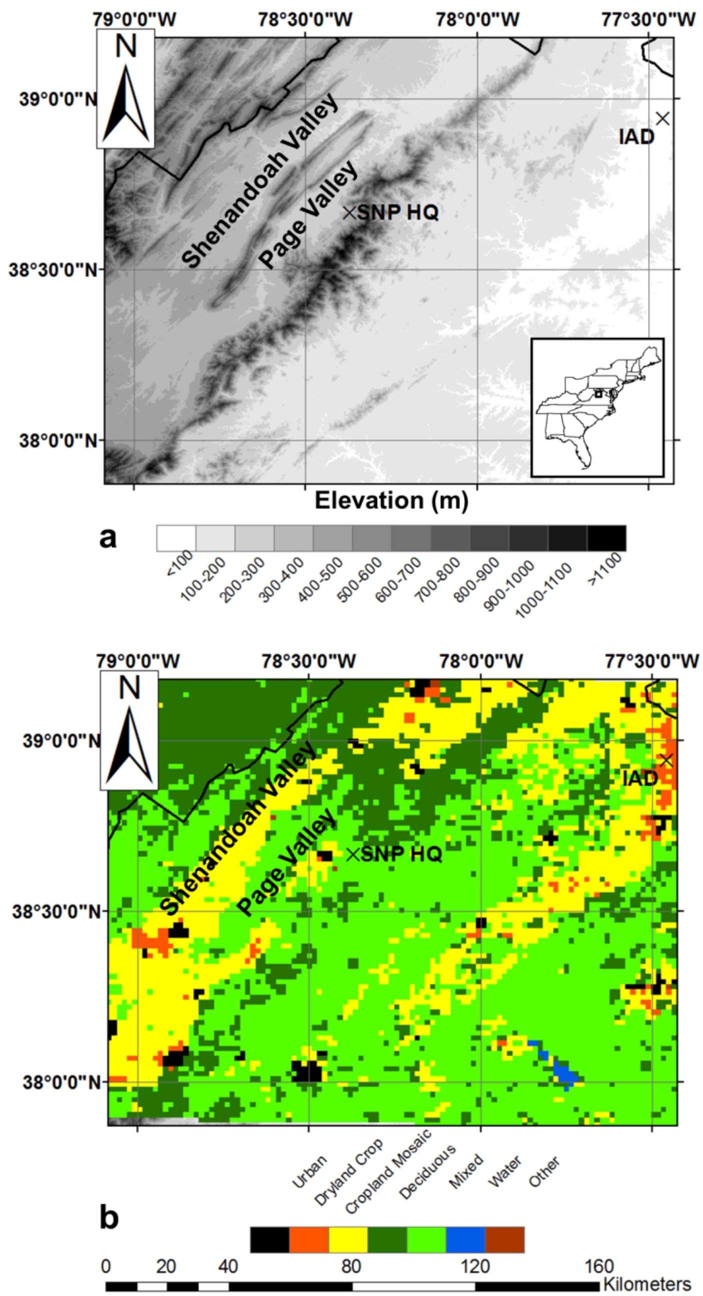

Figure 4.1: Panel (a) shows the regional topography (shaded) over the innermost WRF domain with the locations of SNP HQ (Shenandoah National Park Headquarters) and Dulles Airport (IAD) identified using black X's relative to the Page and Shenandoah Valleys; inset map at the bottom right shows the location of the study region, denoted by a black box, in the eastern US. Panel (b) shows the dominant land use types (shaded). Elevation and land use data are from the US Geological Survey.

level (msl) on its northern end to about 400 m msl on its southern end. The Page Valley is part of the larger Shenandoah Valley and is separated from the rest of the Shenandoah Valley by the Massanutten Mountains which have a maximum elevation of about 800 m msl. East of the Page Valley are the Blue Ridge Mountains with a ridgeline 1000-1200 m msl. The valleys are mostly rural and have a total population of about one million (e.g. Davis et al., 2010).

The regional climate is humid subtropical at the lower elevations but is humid continental along and west of the Blue Ridge. Rainfall in the region is evenly distributed throughout the year (e.g. Lee et al., 2012; Lee et al., 2014), but varies across the Blue Ridge. The Page Valley receives 85 cm annually and is among the driest locations in Virginia. The ridgetops surrounding the Page Valley receive 135 cm of rainfall annually; locations east of the Blue Ridge, including the sounding station at IAD, receive around 105 cm (e.g. National Cartography and Geospatial Center, 1999).

4.2.2. Data sets

4.2.2.1. Valley rawinsonde observations

Rawinsonde observations have been made in the Page Valley during the Education in Complex Terrain Meteorology (EDUCT) field experiment as a component of an undergraduate mountain meteorology course taught at the University of Virginia, as well as outreach activities with nearby high schools. Rawinsondes were launched on five days in April and three days in October. Of the eight days with soundings, four days had afternoon soundings from Shenandoah National Park Headquarters (SNP HQ) (38.67 N, 78.37 W, 351 m msl). SNP HQ is located in a small basin approximately 1 km wide in the eastern part of the Page Valley and is separated from the rest of the Page Valley by a 100 m hill.

4.2.2.2. Rawinsonde observations at IAD

Rawinsonde observations are made at IAD at 00 UTC (19 LST) and 12 UTC (07 LST) and are obtained from the University of Wyoming sounding archive (weather.uwyo.edu/upperair/sounding.html) and are used to calculate z_i. Many different techniques exist to determine z_i from rawinsonde observations, e.g. the parcel method (e.g. Seibert et al., 2000), elevated inversion depth (e.g. Holzworth, 1964; Seidel et al., 2012), humidity gradients (e.g. von Engeln and Teixeira, 2013), refractivity gradients (e.g. Seidel et al., 2010; Wang and Wang, 2014), maximum potential temperature gradient (e.g. Stull, 1988; Seidel et al., 2010), and bulk Richardson (R_b) method (Vogelezang and Holtslag, 1996) [see Seidel et al., 2010 for a review]. Although these methods produce the same seasonal cycle in z_i, the median difference in daytime z_i among the methods for all sites within a global radiosonde network is 440 m, and the interquartile range is from 210 m to 750 m (Seidel et al., 2010). Of these methods, the R_b method has been shown most suitable identifying z_i because it determines z_i as a function of both buoyancy-driven and mechanically-driven turbulence (e.g. Seidel et al., 2012). For this reason, we use the R_b method and compute the R_b profile using the following equation:

$$R_i = \frac{\frac{g}{\theta_{vs}}(\theta_{vz} - \theta_{vs})(z - z_s)}{(u_z - u_s)^2 + (v_z - v_s)^2 + (bu_*^2)} \tag{4.1}$$

In Equation 4.1, g is the gravitational acceleration; θ_v is the virtual potential temperature; z is the height; u and v are the zonal and meridional wind components, respectively; b is a constant; and u_* is the surface friction velocity. The subscripts s and z denote values at the surface and values at height z, respectively. Following Seidel et al. (2012), we ignore surface frictional effects. We also set θ_{vs} to the value at the first measurement height, which is typically 2 m above ground level (agl). Because the first measurement height is so near the surface and surface winds are not reported in rawinsonde observations, we use 0 m s^{-1} for the surface winds, which is a practice consistent with many previous studies (e.g. Menut et al., 1999; Seidel et al, 2012; Korhoren et al., 2014; Zhang et al., 2014). In each R_b profile, we scan upward from the surface and determine the first height, z, where R_b exceeds a critical threshold, R_c, and linearly interpolate between z and $z - 1$ to determine z_i. Following previous studies (e.g. Vogelezang and Holtslag, 1996; Seidel et al., 2012), we set R_c equal to 0.25.

4.2.2.3. Aircraft Profiles

Vertical profiles of temperature and wind are also obtained from the Aircraft Communications, Addressing, and Reporting System (ACARS) data set (http://madis.noaa.gov/madis_acars.html) and are used for comparison with IAD z_i and for model evaluation on select days. ACARS provides meteorological observations from aircraft during takeoffs and landings and has been used to estimate z_i over regions where afternoon z_i estimates are unavailable (e.g. Drue et al., 2010; Yver et al., 2013). ACARS data are available at IAD from fall 2009 through the present.

4.2.2.4. Surface observations

We evaluate our WRF simulations using surface meteorological observations from IAD and the Page Valley, as well as Pinnacles and Big Meadows, which are two long-term mountaintop monitoring stations in the Blue Ridge Mountains (e.g. Lee et al., 2014). In the Page Valley, meteorological observations are obtained from a MesoWest fire weather station (e.g. Horel et al., 2002) at SNP HQ, which has hourly measurements of temperature and relative humidity 2 m agl, wind speed and direction 6.1 m agl, incoming shortwave radiation, and precipitation.

4.2.2.5. Gridded z_i products

Gridded z_i can come from reanalysis products, e.g. the North American Regional Reanalysis (NARR) (Mesinger et al., 2006), as well as from numerical weather prediction (NWP) models, e.g. the European Center for Medium-range Weather Forecast (ECMWF) model, North American Model (NAM), Rapid Update Cycle (RUC), etc. Although NWP models have a higher spatial resolution than reanalysis products, NWP models are based on forecasts, but reanalysis products are forecasts that are corrected a posteriori using surface and upper air observations. For this reason, output from coarser-resolution reanalysis products has better agreement with observations than output from higher-resolution NWP models (e.g. Yver et al. 2013). Therefore, we use the reanalysis product NARR to help quantify the regional spatiotemporal z_i variability. However, we also discuss comparisons with other reanalysis products, e.g. the National Center for Environmental Prediction (NCEP) Climate Forecast System Reanalysis (CFSR) (e.g. Saha et al., 2010), and comparisons with higher-resolution products, e.g. the NAM.

NARR assimilates boundary conditions from the NCEP Department of Energy global reanalysis, NCEP Eta model, and surface and rawinsonde observations to generate meteorological fields at a 32 km resolution over North America. NARR has 29 vertical levels, 13 of which are below 3000 m (Mesinger et al., 2006). NARR output is available at a 3 h temporal resolution daily at 00, 03, 06, 09, 12, 15, 18, and 21 UTC over North America and is available from ftp.cdc.noaa.gov/NARR. NARR outputs z_i at a 32 km resolution. These z_i are computed using a level 2.5 Mellor-Yamada closure scheme that determines z_i based on vertical profiles of turbulent kinetic energy (TKE) (Janjić, 1990). We compute z_i from the NARR meteorological fields ourselves using the R_b method discussed in Section 4.2.2.2 so that NARR z_i can be directly compared with the IAD rawinsonde z_i. We compute z_i from NARR ourselves because previous studies have shown that different z_i detection techniques can yield z_i differences of several hundred meters (e.g. Seidel et al., 2010). At IAD, the 00 UTC NARR-derived z_i computed using the TKE method correlate well with z_i computed in NARR using the R_b method ($r=0.82$, $p<0.01$), but results in z_i approximately 500 m larger for the selected time period.

4.2.3. WRF simulations

We use the WRF model to investigate underlying physical processes responsible for the spatiotemporal z_i variability in this region. WRF is a compressible non-hydrostatic model which uses a staggered Arakawa-C grid (Skamarock, 2008). We use three model domains with two-way nesting that have a horizontal grid spacing of 9 km, 3 km, and 1 km, respectively. The outermost domain encompasses most of the eastern US; the second domain includes the Mid-Atlantic region; and the innermost domain includes the entire Page Valley and IAD. The size of the innermost domain is 150 km x 150 km. Our simulations have 84 vertical levels between the surface and model top of 100 mb, and the thickness of the vertical levels increases gradually with height. The five lowest sigma levels of 0.997, 0.995, 0.992, 0.990, and 0.987 correspond with heights of approximately 19 m, 41 m, 56 m, 78, and 93 m agl, respectively. Terrain and vegetation information are obtained from a US Geological Survey data set with a 1 km spatial resolution. Over the innermost domain, the majority (53%) of the vegetation is mixed deciduous forest, and the remainder is mostly deciduous forest (23%) and cropland (21%) (Figure 4.1b) and reflects the actual land use in the area based on satellite imagery (not shown). NARR is used to supply the boundary conditions for the simulations. In all WRF domains, we apply the Dudhia shortwave radiation scheme (Dudhia, 1989), the rapid radiative transport model longwave scheme (Mlawer et al., 1997), the WRF 3-class simple ice microphysics scheme (Hong et al., 2004), and Pleim-Xiu land surface model (Xiu and Pleim, 2001). The Pleim-Xiu land surface model includes a surface model to describe soil moisture and evapotranspiration and is coupled with the nonlocal asymmetric convection model (Xiu and Pleim, 2001). In the two outermost domains, we apply the Kain-Fritsch cumulus scheme (Kain and Fritsch, 1990).

We investigate the model sensitivity to a selection of PBL parameterization schemes commonly used in WRF. Different PBL schemes make varying assumptions about the transport of heat, moisture, and momentum between the Earth's surface and overlying atmosphere. Local schemes compute turbulent fluxes at each point in the model domain using modeled meteorological variables and gradients from the neighboring grid boxes (e.g. Stensrud, 2007). Nonlocal schemes include a parameterized term to account for nonlocal transport (e.g. Stensrud, 2007). In the present study, we investigate the spatiotemporal z_i variability using two local PBL parameterization schemes: the Mellor-Yamada-Janjić (MYJ) scheme (Janjić, 1990), Mellor-Yamada-Nakanishi-Niino level 2.5 (MYNN2) scheme (Nakanishi and Niino, 2009), as well as two non-local PBL schemes: the Yonsei University (YSU) scheme (Hong et al., 2006) and the total energy mass flux (TEMF) scheme (Angevine et al., 2010). The MYNN2 scheme is newer than the MYJ scheme and improves some of the weaknesses of the MYJ scheme, e.g. slow daytime PBL growth (e.g. Sun and Ogura, 1980), by incorporating more realistic diagnostic equations for turbulent length scale (Nakanishi and Niino, 2009). The YSU PBL scheme is a first-order closure scheme that uses a nonlocal K approach and nonlocal gradient adjustment term (e.g. Hong et al., 2006; Xie et al., 2012), and TEMF is a 1.5-order closure scheme that describes vertical mixing by computing eddy diffusivity from the sum of turbulent kinetic and turbulent potential energy (Angevine et al., 2010). We perform WRF simulations for two days with multiple afternoon rawinsonde observations from the Page Valley: 9 April 2009, a day with a deep afternoon PBL, and 23 October 2010, a day with a shallow afternoon PBL. Although some PBL parameterization schemes explicitly calculate z_i, for a consistent comparison of z_i using different parameterization schemes, we compute z_i from the model output using the R_b method described in Section 4.2.2.2.

4.2.4. Approach to estimate z_i over the Page Valley

To estimate daytime z_i over the Page Valley, we use sounding observations from IAD and NARR output. In our approach, we first estimate the afternoon z_i from the 00 UTC IAD sounding and compare these z_i with afternoon NARR z_i. We then determine a correction, based on physical processes occurring in the region of interest, which we apply to the IAD sounding z_i to determine z_i over the Page Valley.

4.2.4.1. Determining afternoon z_i from IAD rawinsonde observations

In the eastern US, 00 UTC occurs at 1900 LST. For this reason, soundings at IAD are after local sunset between late August and late April. Near-surface cooling causes the formation of a near-surface stable layer around sunset which obfuscates afternoon z_i determination (e.g. Wang and Wang, 2014). To obtain reliable estimates of afternoon z_i from the IAD sounding observations, we remove this stable layer. To this end, we develop an approach to determine the afternoon z_i from the IAD rawinsonde observations. We compute the θ_v gradient, $\frac{d\theta_v}{dz}$, between each interpolated level below 500 m msl. If $\frac{d\theta_v}{dz} \leq 0$ K, we use the surface value of θ_v in Equation 4.1 to calculate R_b. If $\frac{d\theta_v}{dz} > 0\,K$, we scan upward in the profile, up to 500 m msl (based on a presumed minimum depth of the afternoon z_i for this region), and in Equation 4.1 we use the value of θ_v at the height where $\frac{d\theta_v}{dz}$ is at a minimum. If $\frac{d\theta_v}{dz} > 0\,K$ at each level between the surface and 500 m msl, we use the value of θ_v at 500 m msl in Equation 4.1. For consistency with Equation 4.1, we set $u_s = v_s = 0\,m\,s^{-1}$.

We demonstrate the above technique using rawinsonde data on two days in fall, 2010. Radiative near-surface cooling led to the formation of a near-surface stable layer in the 00 UTC sounding on 1 October and 11 November. Using surface values to determine z_i yields z_i 128 m and 113 m msl, respectively (Figure 4.2), which do not agree with the afternoon NARR z_i on these days, which are 1712 m and 694 m msl, respectively, and are unrealistic values for the afternoon z_i over this region of the US (e.g. Aneja et al., 2000). When we apply our technique to the rawinsonde observations, we find revised z_i from the rawinsonde observations of 1781 m and 801 m msl, respectively. These z_i

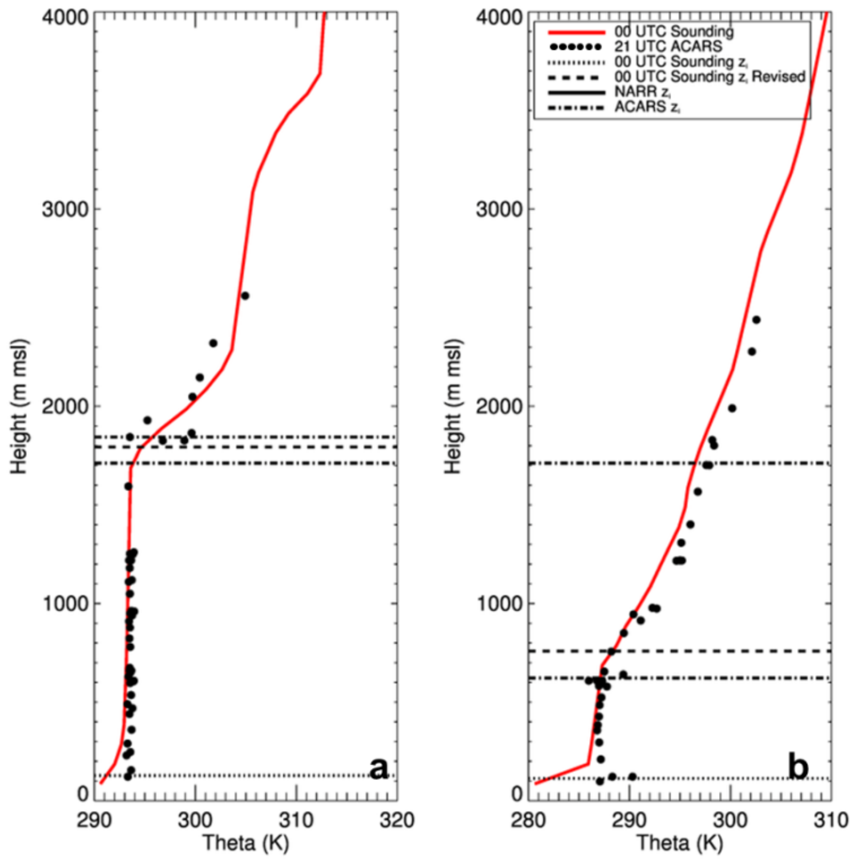

Figure 4.2: Application of our afternoon z_i detection technique to two IAD soundings from fall, 2010: 1900 LST 1 October 2010 (a) and 1900 LST 11 November 2010 (b). Red line is the IAD sounding; black dots are mid-afternoon (1500 LST) ACARS-derived potential temperature sounding within a 0.25° x 0.25° box (approximately 28 x 28 km) centered on IAD; horizontal dotted line is z_i determined from the IAD sounding without applying our technique to remove the near-surface stable layer; horizontal dashed line is z_i determined from the IAD sounding with the application of our technique; horizontal dash-dot line is z_i determined from NARR; and horizontal solid line is z_i determined from ACARS profile. In all cases, z_i is calculated using the R_b method. Because moisture measurements are unavailable in the ACARS profiles at IAD, we assume that $\theta_v \approx \theta$. Note different scales but the same range on the x-axis.

values are <150 m different from afternoon z_i determined from NARR and from the afternoon ACARS observations on these days.

The improved afternoon z_i from the IAD rawinsonde observations are further evident when we compare z_i over the entire 4-year period of interest. Without applying our technique, the correlation between the 00 UTC IAD rawinsonde observations and afternoon NARR z_i is r=0.40 (p<0.01), and the rawinsonde z_i is 255±639 m lower than the NARR z_i. Applying our technique reduces the mean difference and standard deviation to 72±479 m and improves the correlation to r=0.56 (p<0.01). Important to note, though, is that our approach does not account for subsidence, which can result in z_i decreases of 200 m between the mid-afternoon and early evening (e.g. Blay-Carreras, 2014). However, the errors caused by subsidence are less than the standard deviations in z_i, which are reduced from 639 m to 479 m with the application of our technique. These errors occur because, in some cases, there are weak R_b and θ_v vertical gradients. When these gradients are weak, z_i is not well-defined (e.g. von Engeln et al., 2003). Consequently, there exists a weak relationship between rawinsonde observations and reanalysis output that has been found by other researchers (Table 4.1). For example, Schmid and Niyogi (2011) analyzed z_i for a 10-year period in Oklahoma, USA and found correlations between rawinsonde and NARR z_i ranging from 0.39 in spring to 0.58 in winter. Korhonen et al. (2014) found a correlation of 0.58 between rawinsonde and reanalysis z_i obtained from the ECMWF model over South Africa. In both the Schmid and Niyogi (2011) and Korhonen et al. (2014) studies, rawinsonde z_i was larger than z_i from the reanalysis, which is consistent with z_i climatologies over North America and Europe (Seidel et al., 2012) and with our findings. Studies in regions with mountainous terrain have found lower correlations when evaluating model output, even when using higher resolution models. For example, Ketterer et al. (2014) found that correlations between z_i from the COSMO-2 model, run at a 2.2 km resolution over the European Alps, and z_i obtained from wind profilers and ceilometers ranged from 0.3-0.5.

Table 4.1: Pearson correlation coefficient (r) between IAD rawinsonde z_i and NARR z_i computed using the R_b method as a function of season for the period 1 January 2009 – 31 December 2012 compared with correlation coefficients obtained from a 2002-2010 from a study in Oklahoma, USA. All values shown are significant at the 0.01 confidence level.

	DJF	MAM	JJA	SON
00 UTC rawinsonde vs. NARR $\boldsymbol{z_i}$ at IAD with removal of near-surface stable layer	0.72	0.67	0.29	0.60
00 UTC rawinsonde vs. NARR $\boldsymbol{z_i}$ at IAD with removal of near-surface stable layer and well-defined $\boldsymbol{z_i}$	0.78	0.76	0.59	0.67
Rawinsonde and NARR $\boldsymbol{z_i}$ in Oklahoma, USA (Schmid and Niyogi, 2011)	0.58	0.39	0.43	0.56

4.2.4.2. Removal of days with poorly-defined $\boldsymbol{z_i}$

Since we need to have confidence in our reanalysis product to assist with determining differences in z_i between IAD and the Page Valley, we follow von Engeln et al. (2003) and remove days on which z_i are not well-defined. These days are characterized by the absence of a well-defined elevated θ_v inversion. To this end, we calculate NARR θ_v gradients every 100 m vertically for each sounding and filter cases with poorly-defined elevated θ_v gradients, which we define as those <1.0 K 100 m^{-1}. Sensitivity tests (not shown) with this threshold indicate that the conclusions in this study are not significantly impacted by our choice of this threshold. The removal of days lacking a well-defined elevated inversion reduces the number of days that we consider for further analysis by about 50%. The percentage of cases remaining varies seasonally; about 80% of the days remain in the winter and <20% of the days remain in the summer (Table 4.2). The removal of these cases improves the relationship between IAD rawinsonde z_i and NARR z_i (c.f. Table 4.1). Over the 4-year period of interest, r=0.74 (p<0.01), and the mean difference is 1±378 m. On seasonal timescales, r ranges from 0.59 (p<0.01) in summer to 0.78 (p<0.01) in winter (Figure 4.3), and the mean monthly NARR z_i compare better with the IAD rawinsonde observations. Sensitivity tests show that this correlation is not biased by an unequal number of cases in the different seasons.

Independent of season, NARR underestimates z_i, consistent with the previous discussion. The z_i underestimates occur most often on days with z_i larger than about 1500 m and are caused by a cool bias of a couple degrees Celsius throughout the depth of the PBL (not shown), which results in lower z_i. Because z_i is typically largest in the late spring and summer, NARR's cool bias may explain the lower correlations between NARR z_i and IAD sounding z_i in these seasons. There are occasional differences of 1-2 km between NARR z_i and the IAD sounding z_i. These large differences occur either on days when there are multiple elevated inversions or on days when either the NARR or IAD sounding R_b profile slightly exceeds R_c at a given height but the other profile does not.

Table 4.2: Percentage and number of days with a well-defined elevated θ_v inversion as a function of season at IAD for 1 Jan 2009 – 31 Dec 2012.

	Percentage (number) of days with well-defined inversion
DJF	79% (285)
MAM	36% (131)
JJA	13% (47)
SON	47% (170)

We attempt to further filter days with large biases by filtering cloudy days, on which z_i is oftentimes not well-defined (e.g. Grimsdell and Angevine, 1998), as well as windy days when significant rawinsonde drift may occur (e.g. McGrath et al., 2006; Seidel et al., 2011). To this end, we identify clear or "fair weather" days using a clearness index. The clearness index (Whiteman et al., 1999a) represents the ratio between the total amount of incoming solar radiation received at a given location summed for an entire day and the calculated maximum amount of incoming solar radiation that could be received at that location, the latter of we calculate following Whiteman and Allwine (1986). However, we find no significant improvement of the relationship between the rawinsonde and NARR z_i when we remove cloudy days (i.e. days with a low clearness index), nor when we remove days with rainfall. We also try removing rawinsonde observations made during windy conditions, which we classify as days with 700 mb wind speeds >15 m s^{-1}. However, we find no significant improvement to the relationship between the IAD rawinsonde z_i and NARR z_i. One explanation is that rawinsonde drift is on the spatial scale of a few kilometers in the lower troposphere (Seidel et al., 2011), and thus the rawinsondes typically remain within the IAD NARR grid box during their ascent through the PBL.

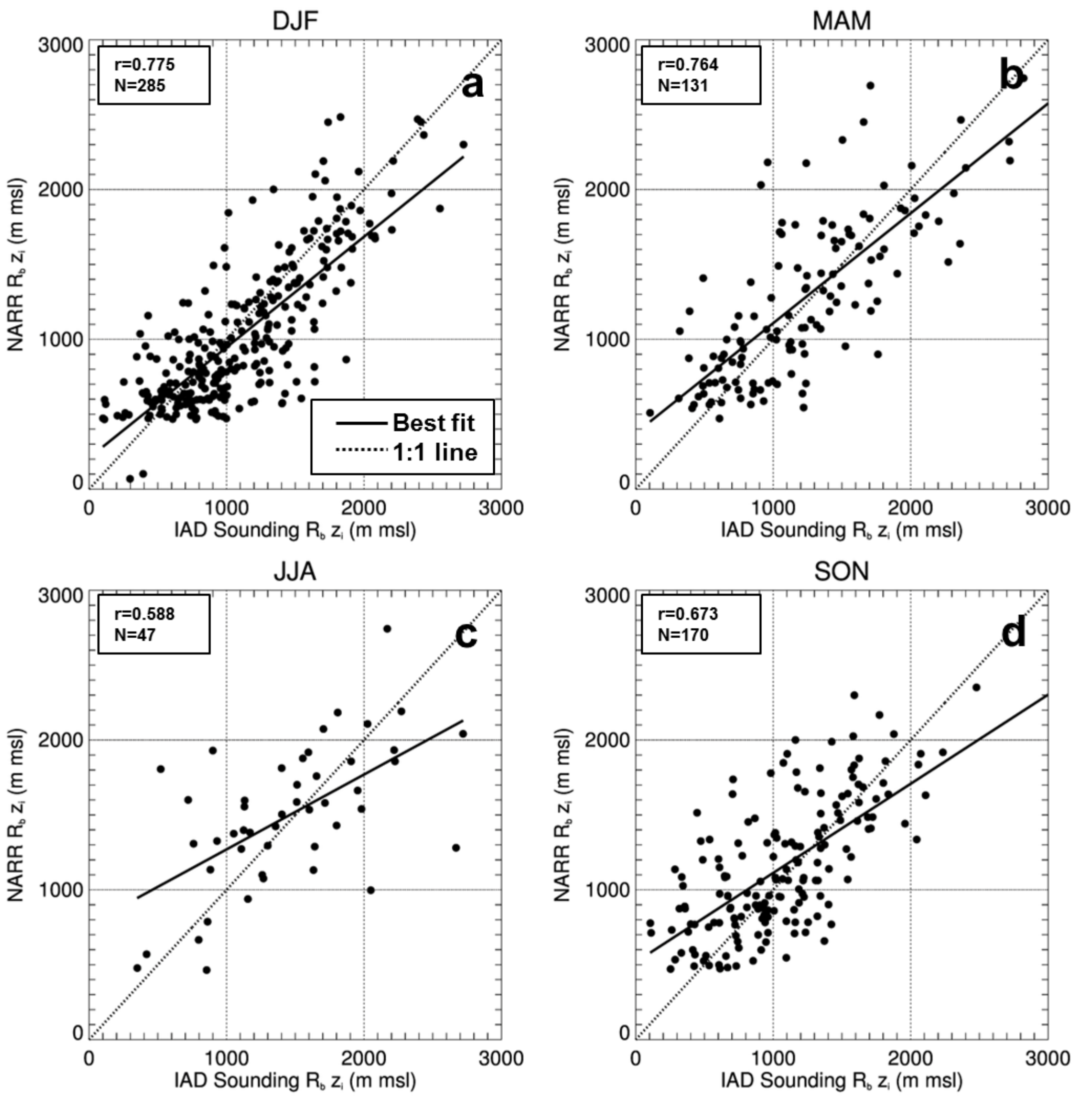

Figure 4.3: Comparison between NARR z_i and IAD rawinsonde z_i for winter (a), spring (b), summer (c), and fall (d) for 1 January 2009 – 31 December 2012 for days in which z_i is well-defined. Dotted and solid lines indicate 1:1 line and line of best fit, respectively. Pearson correlation coefficient (r) and the number of cases (N) are noted in the upper left of each Figure 4.3. All correlations are significant at the 0.01 confidence level.

From these analyses, we conclude that removing days on which z_i is not well-defined improves the relationship between the NARR z_i and IAD rawinsonde z_i. NARR captures the seasonal z_i cycle at IAD (Figure 4.4), with mean monthly differences between NARR z_i and IAD rawinsonde z_i of 117±153 m msl. However, daily differences between NARR z_i and IAD rawinsonde z_i are sometimes as large as 1-2 km (c.f. Figure 4.3). Because of the good agreement on monthly timescales, we use NARR to determine if there are z_i differences between IAD and the Page Valley present on monthly timescales. We then use the higher resolution WRF model to investigate the physical processes responsible for the z_i differences on daily timescales.

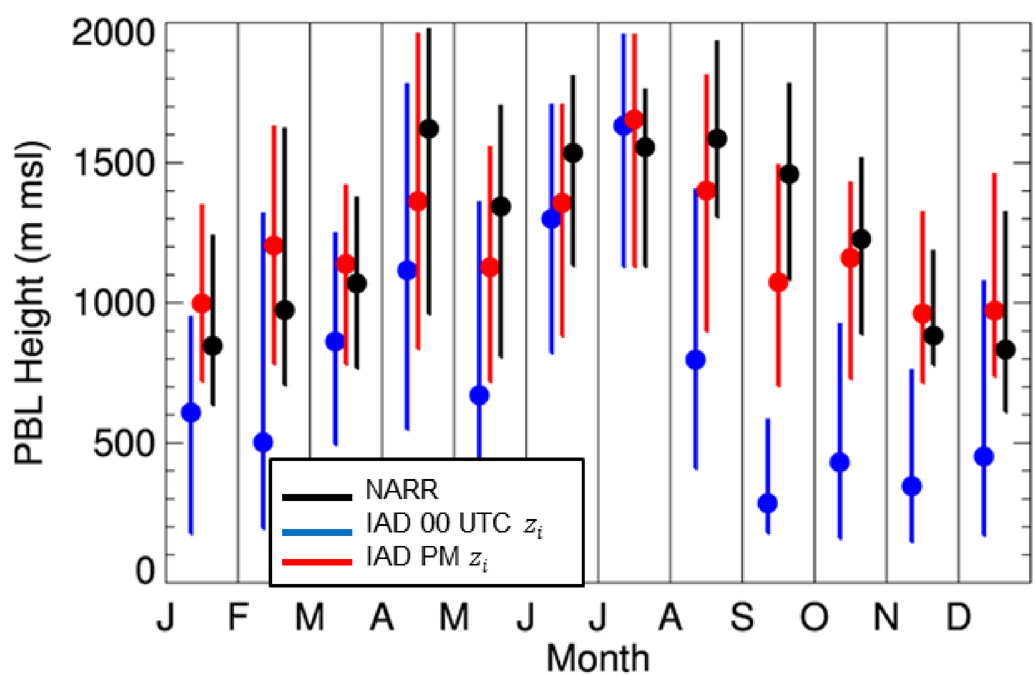

Figure 4.4: Comparison between mean z_i ±1 standard deviation at IAD determined from the 00 UTC IAD sounding (blue), 00 UTC IAD sounding with the application of our afternoon z_i detection technique (red), and 21 UTC NARR z_i at IAD (black) as a function of month over the period 1 January 2009 – 31 December 2012 for days in which z_i is well-defined. All z_i are computed using the R_b method. Offset within each month is to highlight the variability among the different methods.

4.3. Results and discussion

4.3.1. Spatial z_i variability on monthly timescales

To quantify z_i differences between IAD and the Page Valley, we calculate z_i from NARR for the grid box containing IAD and the grid box containing SNP HQ and the Page Valley on the subset of days with well-defined z_i at IAD. We differentiate between z_i, which is height of the PBL relative to sea level, and PBL depth, which is height of the PBL relative to the underlying topography. Making this distinction is required to quantify the degree to which the PBL is affected by the underlying topography, which affects how well z_i observations from IAD can be used as a proxy for z_i over the Page Valley. For the 4-year period of interest, there is good agreement between NARR z_i at IAD and NARR z_i over the Page Valley ($r=0.94$, $p<0.01$), and r exceeds 0.9 in all seasons. The z_i over the Page Valley is typically 200 m larger than at IAD during the winter and up to 400 m larger than IAD in late summer (Figure 4.5). Differences in PBL depths between the sites are negligible in the winter and in the summer are about 200 m larger over the Page Valley than at IAD. Differentiating by z_i with respect to the maximum ridgetop height (1200 m msl), we find that z_i over the Page Valley is 218±174 m larger than at IAD on days when z_i at IAD is below the ridgetop height. On days when z_i at IAD is above the ridgetop, the z_i over the Page Valley is 157±160 m larger than at IAD.

We observe a similar pattern when we use other products during select time periods. For example, the mean monthly z_i in April 2009 from higher-resolution NAM are 200 m higher over the Page Valley than at IAD, whereas the difference in NARR is 184 m between the two sites. Similar results are found using z_i obtained from the CFSR (not shown). The similarities among the different reanalysis and model products provide us with confidence that the z_i differences we are finding between the Page Valley and IAD are not an artefact of NARR's resolution.

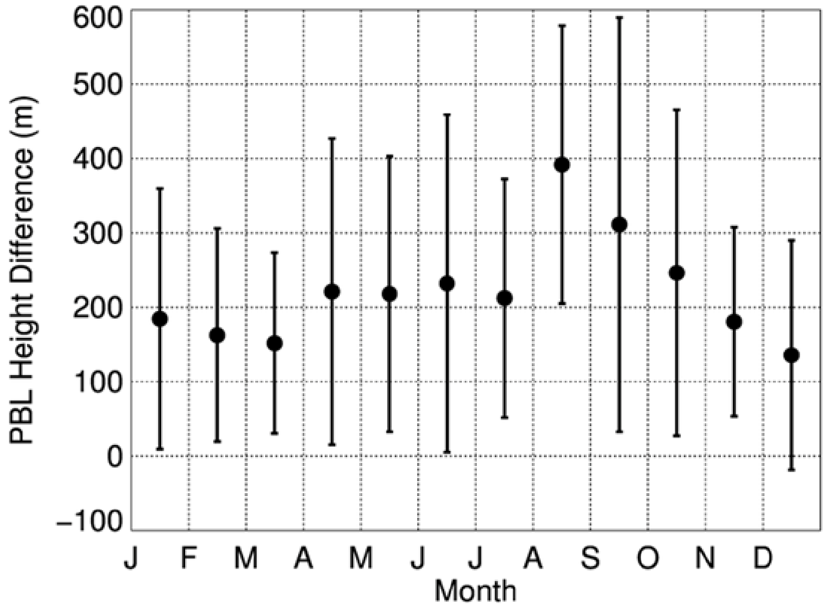

Figure 4.5: Mean difference in 21 UTC NARR z_i ±1 standard deviation between the Page Valley and IAD as a function of month for the period 1 January 2009 – 31 December 2012.

4.3.2. Drivers of z_i variability on monthly timescales

From the analyses in the previous section, we conclude that z_i and PBL depths are typically larger over the Page Valley than near IAD. Although the elevation difference of about 200 m explains some of the differences in z_i between the two sites, elevation differences cannot explain the summertime z_i differences. To test the hypothesis from Section 4.1 that deeper PBLs over the Page Valley are caused by drier conditions over the Page Valley, we use regional observations, NARR, and WRF simulations. Surface observations of afternoon *SHF* show a bimodal pattern during the year; one maximum occurs in April and a secondary maximum occurs in late August and September (Lee et al., 2015). On the subset of days with well-defined z_i NARR *SHF* follows the same pattern, and *SHF* differences between the Page Valley and IAD are positively correlated with z_i differences between the two locations ($r=0.74$, $p<0.01$) (Figure 4.6). Furthermore, the precipitation differences between the Page Valley and IAD are largest in late summer and correlate with larger z_i differences ($r=-0.59$, $p=0.04$). With less rainfall over the Page Valley, there is on average less soil moisture. Therefore, a larger percentage of incoming

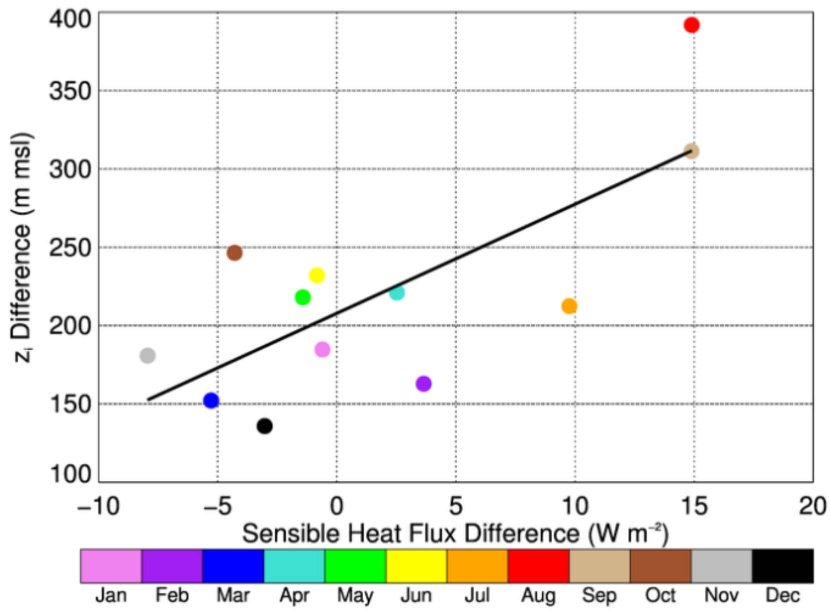

Figure 4.6: Mean monthly difference between 21 UTC z_i over the Page Valley and IAD as a function of the difference in mean monthly *SHF* between the Page Valley and IAD. Colored circles indicate different months; black line indicates the line of best fit.

radiation is typically partitioned into *SHF* than latent heat flux (*LHF*), yielding larger z_i over the Page Valley than near IAD. The differences in *SHF* between the Page Valley and IAD become largest in late summer when moisture differences are largest, resulting in the largest z_i differences during this time.

While *SHF* differences can explain the z_i differences between IAD and the Page Valley on monthly timescales, we cannot rule out the role of subsidence differences as an explanation for the z_i variability. Thus we compute mean monthly composites of vertical velocity (omega) in NARR for the same subset of days with well-defined z_i. Monthly NARR composites indicate smaller omega (i.e. less positive values of omega and thus less subsidence) at 850 mb and 700 mb during the late summer over IAD than over the Page Valley (not shown), which would cause larger z_i at IAD than in the Page Valley. Because we typically observe larger z_i and larger PBL depths over the Page Valley, we conclude that synoptic-scale subsidence cannot explain z_i differences between the Page Valley and IAD on monthly timescales.

Thus, the larger z_i over the Page Valley are caused by drier conditions that lead to larger *SHF* in the Page Valley than near IAD. Also important to z_i differences are wind flow patterns in mountainous terrain that are a function of the underlying topography (e.g. Kalthoff et al., 1998; Kossmann et al., 1998; De Wekker, 2002; Bianco et al., 2011). Because NARR's resolution cannot resolve the regional topography and the flow patterns within and because we find large differences between NARR z_i and IAD rawinsonde z_i on daily timescales, we perform WRF simulations on two select days with rawinsonde observations from the Page Valley to contrast days with large z_i variability and days with small z_i variability. In the following section, we use these simulations to investigate the underlying z_i differences between IAD the Page Valley.

4.3.3. Drivers of z_i variability on daily timescales

All WRF runs well simulate daytime near-surface temperatures in the region and the diurnal change in z_i at IAD and in the Page Valley [details of the model evaluation are found in the appendix to this chapter, i.e. Section 4.6], providing us with confidence that our simulations can be used to help further understand the z_i differences between IAD and the Page Valley. All simulations indicate that the z_i growth rate, $\frac{dz_i}{dt}$, after sunrise is largest along the mountain ridges than in the valleys because of higher static stability in the valleys that suppresses z_i growth (Figure 4.7a). Between 0800 and 1000 LST, z_i increases to 2000-2500 m msl over the region (Figure 4.7b). Over the eastern part of the domain, $\frac{dz_i}{dt}$ during this time is smaller than near the Page Valley due to a deeper near-surface stable layer at 0800 LST. By 1200 LST, z_i over the region ranges from around 2500 m msl near IAD to 2900 m msl over the Page and Shenandoah Valley (Figure 4.7c), and there is little additional z_i increase during the early afternoon (Figure 4.7d). On 23 October, $\frac{dz_i}{dt}$ is much smaller. At 0800 LST, the PBL depth is around 100 m agl across the ridges and <50 m in the valleys and Piedmont (Figure 4.8a). Between 0800 LST and 1200 LST, the PBL depth increases by around 500 m across the region (Figure 4.8b, 8c) and reaches a maximum height of 600-800 m over the region while generally following the underlying topography (Figure 4.8d).

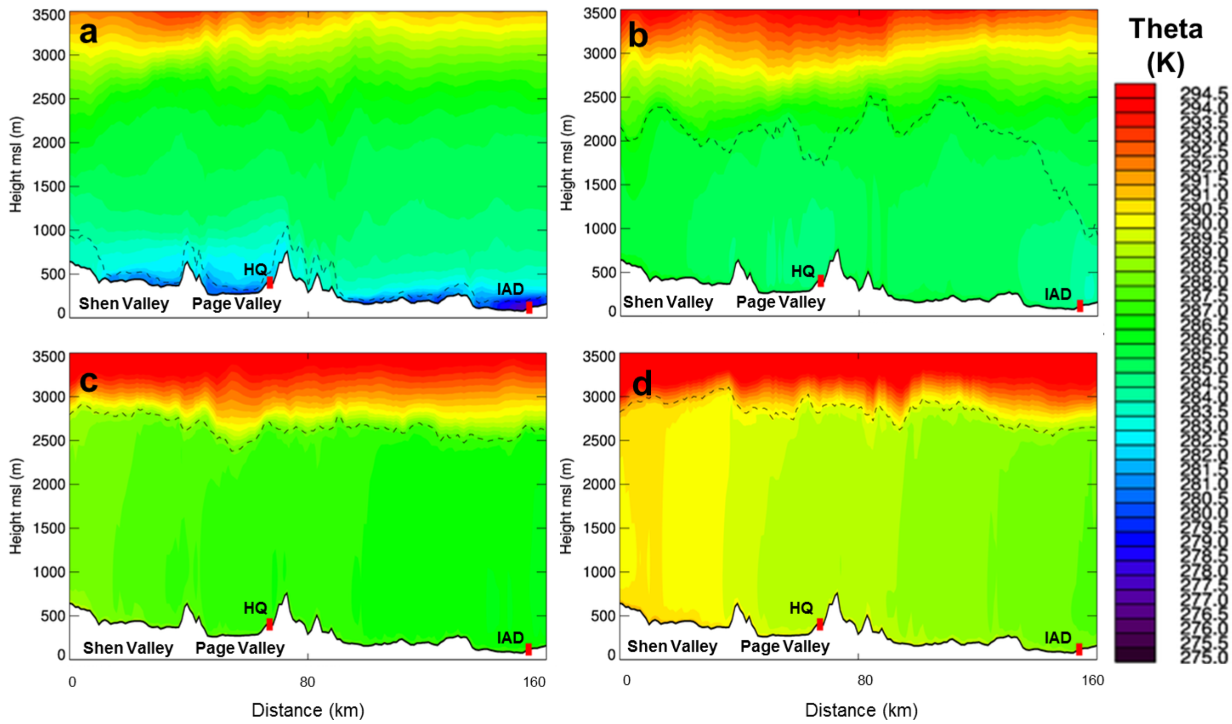

Figure 4.7: Potential temperature cross-section through SNP HQ (left red bar) and IAD (right red bar), shaded every 0.5 K, using WRF simulations with the YSU PBL scheme at 0800 LST (a), 1000 LST (b), 1200 LST (c), and 1400 LST (d) on 9 April 2009. Dashed line indicates z_i computed using the R_b method. The locations of the Shenandoah and Page Valleys are indicated on the figure.

Despite the differences in afternoon z_i on 9 April and 23 October, a common feature of both days is the presence of larger z_i over the Page Valley than near IAD, which is consistent among the four PBL parameterization schemes that we studied, as well as our findings from Section 4.3.1 and the rawinsonde observations made at both sites on these days. Because our WRF simulations have high spatial resolution, we can use them to investigate some of the other causes of larger z_i over the Page Valley. Unlike findings from other valleys (e.g. Bianco et al., 2011), the simulated near-surface wind fields and vertical velocities indicate no near-surface flow convergence that would cause larger z_i over the Page Valley. Instead, near-surface winds across the region are westerly on 9 April and southwesterly on 23 October. Analyses of soil moisture fields (not shown) indicate that the differences between the Page Valley and IAD are largest in the

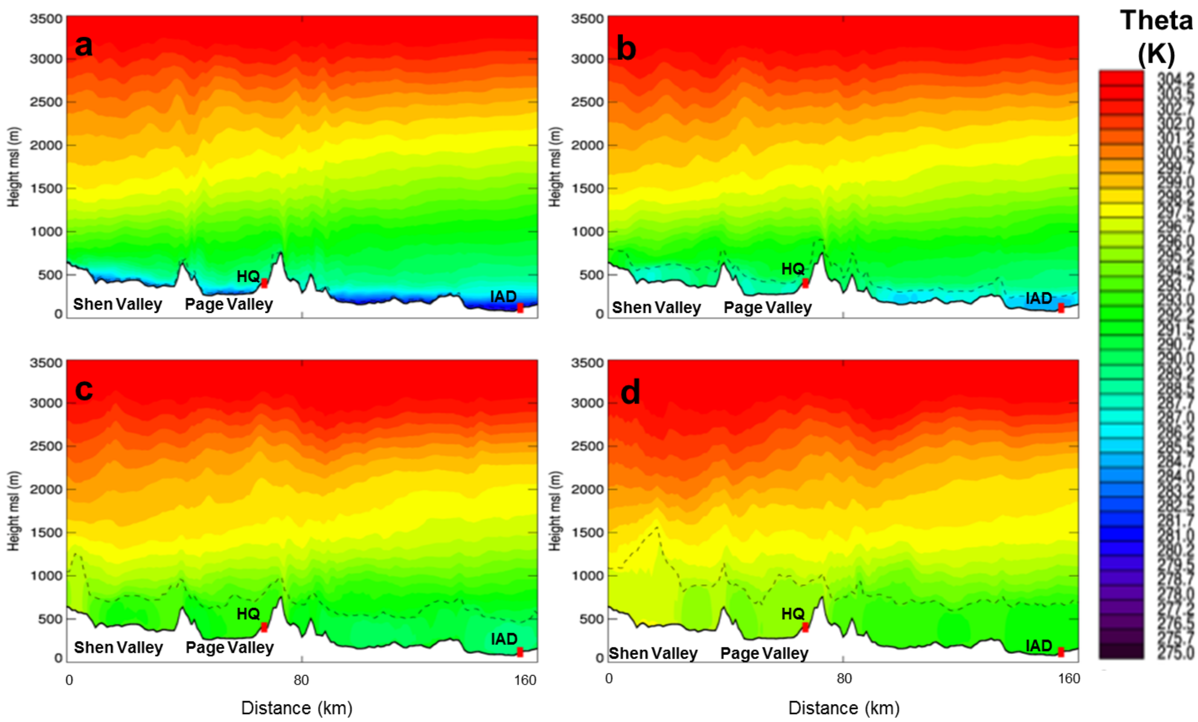

Figure 4.8: Same as Figure 4.7 but for 23 October 2010. Potential temperature is shaded every 0.25 K.

afternoon, which result in larger *SHF* over the Page Valley than near IAD. For example, mean afternoon (1200-1600 LST) *SHF* on 9 April range from 339-407 W m^{-2} at SNP HQ depending on the PBL parameterization scheme used. At IAD, mean afternoon *SHF* for the four PBL parameterization schemes are consistently lower and range from 218-299 W m^{-2}.

Thus, our WRF simulations provide further evidence that z_i and PBL depth differences between IAD and the Page Valley are caused by soil moisture and *SHF* differences between the two locations. Since the Page Valley is about 200 m higher in elevation than IAD, we use WRF to investigate the role of topography on the differences in z_i and PBL depth between the sites, as NARR cannot fully resolve the regional topography. To this end, we compute the correlation between z_i and elevation for each grid point over the innermost domain following De Wekker (2002). For a terrain-following PBL, the correlation, r, is 1; for a non-terrain-following PBL, $r = 0$. Over the innermost WRF domain, r exceeds 0.9 between 00 and 08 LST on both 9 April and 23 October (Figure 4.9), indicating a terrain-following PBL during this time on both days.

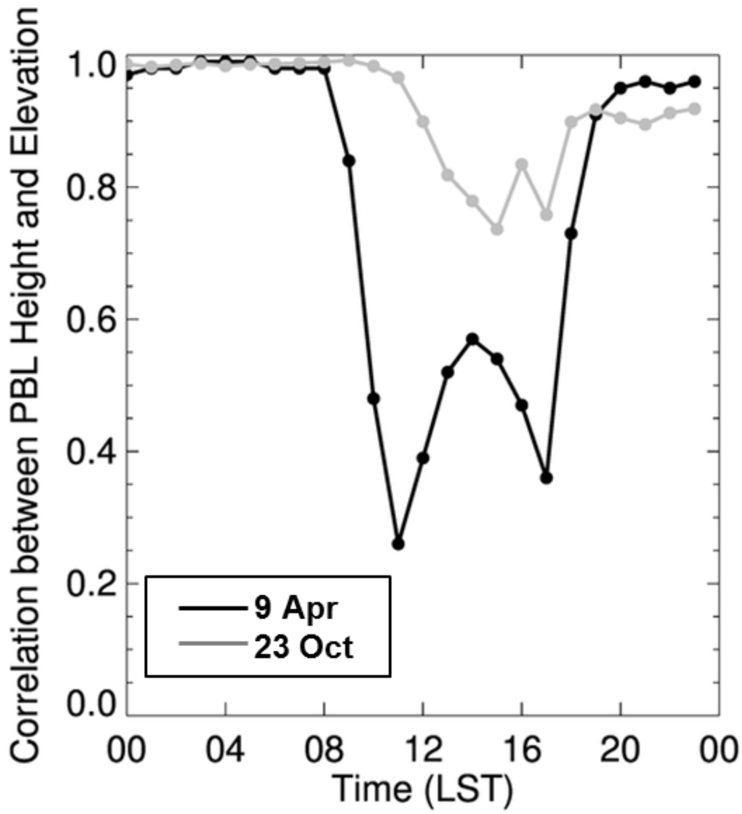

Figure 4.9: Pearson correlation coefficient, r, between PBL height computed using the R_b method and elevation over the innermost WRF domain for 9 April 2009 (black) and 23 October 2010 (gray).

At 0800 on 9 April, r decreases to a minimum of about 0.25 at 1100 LST but increases to 0.6 during the mid-afternoon because higher *SHF* causes deeper PBLs over the Page Valley. Whereas r decreases during the daytime on 23 October, the decrease is smaller than on 9 April, and r remains above 0.75, providing additional evidence that the PBL more closely follows the terrain on 23 October than on 9 April. This issue affects how well z_i from sounding stations can be used as a proxy for z_i at nearby locations and is addressed in the next section.

4.3.4. Implications for using airport soundings to estimate regional z_i

In summary, to use the 00 UTC rawinsonde observations in the eastern US, or at other locations where 00 UTC is in the early evening local time, to estimate z_i at surrounding locations, one must consider the following limitations of this approach which are summarized below.

1. The rawinsonde launch time may coincide with a time that a near-surface stable layer has recently formed (e.g. Wang and Wang, 2014).
2. There are differences between z_i from observations and output from reanalysis products (e.g. Schmid and Niyogi, 2011; Korhonen et al., 2014) and numerical simulations (e.g. Ketterer et al., 2014).
3. In some cases, z_i is not well-defined (e.g. von Engeln et al., 2003; Dabberdt et al., 2004).
4. There can exist z_i variability over spatial scales of around 100 km caused by physical processes, including spatial differences in *SHF* (e.g. Ball, 1960; Avissar and Schmidt, 1998), soil moisture (e.g. Desai et al., 2006; Ma et al., 2011), wind flow patterns (e.g. Kossmann et al., 1998; Bianco et al., 2011), and subsidence (e.g. Dayan et al., 1988).

To reduce the impact of the first three limitations on estimating z_i over the Page Valley from IAD rawinsonde observations, we computed z_i from the IAD rawinsonde observations and NARR meteorological fields using the R_b method, removed the near-surface stable layer from the 00 UTC IAD rawinsonde observations, and selected days with well-defined z_i. Even so, daily differences between NARR z_i and rawinsonde z_i were sometimes as large as 1-2 km which led us to conclude that NARR cannot be used to assess the regional spatial z_i variability on daily timescales.

Because the mean monthly NARR z_i, calculated using the R_b method, compare well with the mean monthly rawinsonde z_i (c.f. Figure 4.4), we use NARR to help quantify the errors associated with using IAD z_i to determine z_i over the surrounding region and corroborate these errors with our WRF simulations. To this end, we compute the mean difference between the NARR grid box containing IAD and the NARR grid boxes extending from IAD southwestward into the Page and Shenandoah Valleys. We find that mean z_i differences increase as a function of distance from IAD and are largest in the summer when z_i is largest and differences in near-surface moisture differences are largest, but typically smallest in winter (Figure 4.10). Thus, a location such as the Page

Valley 100 km southwest of IAD has a z_i difference ranging from 326 m in winter to 412 m in summer.

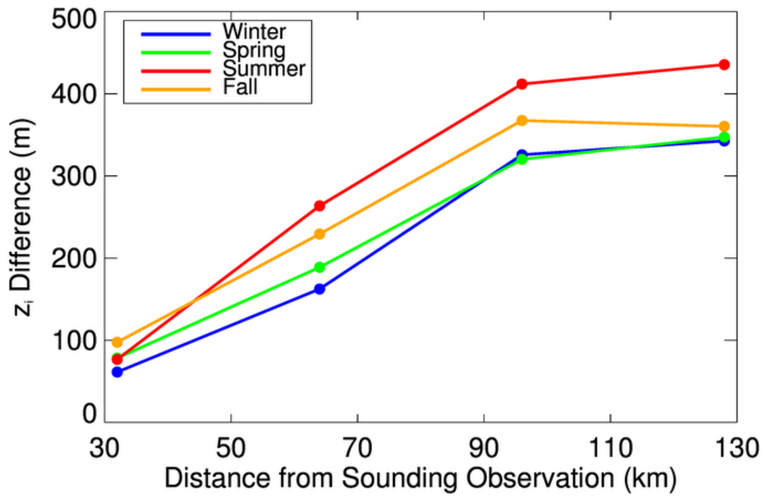

Figure 4.10: Mean difference in afternoon NARR z_i between the grid box containing IAD and z_i along a transect extending from IAD southwestward through the Page and Shenandoah Valleys for winter (blue), spring (red), summer (red), and fall (orange) for days with well-defined z_i at IAD.

Important to note, though, is that NARR cannot fully resolve the regional topography. The WRF simulations indicated considerable z_i variability at spatial scales <32 km both on days with a shallow PBL (c.f. Figure 4.8) and a day with a deep PBL (c.f. Figure 4.7). However, the seasonal standard deviations in z_i from NARR are comparable with standard deviations in z_i over the innermost WRF domain on 9 April and 23 October. The mid-afternoon standard deviations over the innermost WRF domain in afternoon z_i are about 250 m and 300 m on 9 April and 23 October, respectively, while the standard deviations in NARR z_i in spring and fall at a distance 100 km from IAD is 234 and 187 m. The larger standard deviations in WRF on 23 October occur because z_i more closely follows the terrain, which induces larger errors in the z_i estimates. Therefore, the z_i standard deviations will be larger over regions with more mountainous topography than over regions with flat, homogenous terrain.

4.4. Summary and conclusions

In the present study, our goal was to estimate z_i with z_i obtained from a sounding station and reanalysis products, using the Page Valley as a case study. Fulfilling this goal required evaluating reanalysis and model output for the region and investigating the underlying physical processes responsible for the regional spatiotemporal z_i variability. Comparisons between rawinsonde z_i and NARR z_i showed low correlations that have also been reported in previous studies (e.g. Schmid and Niyogi, 2011). The correlations between rawinsonde z_i and NARR z_i improved when we recalculated z_i after removing the near-surface stable layer from the 00 UTC θ_v profile and considered only cases when the z_i was well-defined. Applying the technique of filtering the near-surface stable layer to other regions where 00 UTC is in the early evening will facilitate improved estimations of maximum daytime z_i from rawinsonde observations, which are vital in weather forecasting and air quality applications.

We then quantified spatial differences in z_i between the Page Valley and IAD and found that the PBL is typically larger over the Page Valley than IAD. Differences in z_i between the sites show little dependence on the maximum z_i at IAD; mean z_i are 218 m larger over the Page Valley on days with shallow z_i, but 157 m larger over the Page Valley on days with deep z_i. To help understand the drivers responsible for the larger z_i over the Page Valley than at IAD, we performed WRF simulations. The different PBL schemes yielded the same conclusions about the drivers of the z_i differences between IAD and the Page Valley and indicated that larger *SHF* over the Page Valley leads to deeper PBLs. The simulations also indicated that z_i exhibits terrain-following characteristics both on days with deep PBLs and days with shallow PBLs.

From the WRF simulations and from the comparisons between the sounding observations and NARR, we conclude that z_i over the Page Valley are typically 200-400 m higher than over IAD. These differences need to be included when estimating z_i in the Page Valley from z_i at IAD. Once these differences are considered, the z_i for the Page Valley will be used to investigate the impact of the valley z_i relative to the mountaintop on the diurnal mountaintop trace gas variability in a forthcoming study.

4.5. Acknowledgments

We thank William Brown from the National Center for Atmospheric Research for conducting the rawinsonde launches at SNP Headquarters in April 2009. We also thank the support of the undergraduate and graduate students from the spring 2009, fall 2010, fall 2011, and fall 2012 mountain meteorology courses taught at the University of Virginia.

4.6. Appendix

4.6.1. WRF evaluation

To have confidence in our WRF simulations, we focus on how well the different PBL parameterization schemes simulate daytime temperature and z_i evolution over the region. On 9 April at SNP HQ and IAD, the mean bias error (MBE) in afternoon 2 m temperatures between the observations and model is <1°C with the MYNN2 and YSU PBL schemes, but -2°C and 4°C with the MYJ and TEMF schemes, respectively. Comparisons between the SNP HQ rawinsonde observations and simulations on 9 April show good agreement (Figure 4.A.1). Although differences in the potential temperature profiles among the simulations vary by <2°C, the YSU scheme best simulates the potential temperature profile and z_i (Table 4.A.1). On 23 October, the simulations have a cool bias of 1-2°C in the SNP HQ potential temperature profile (Figure 4.A.1). The simulations do not capture the near-surface stable layer present in the 1800 LST sounding but do capture the surface temperature decrease around this time. Despite these biases at SNP HQ, the simulations provide good estimates of afternoon z_i at SNP HQ and have a MBE <200 m for the different PBL schemes.

These findings on the sensitivity to different PBL schemes are consistent with previous work (e.g. Borge et al., 2008; Gilliam and Pleim, 2010; Hu et al., 2011; Xie et al., 2013). Nonlocal PBL schemes such as the YSU scheme better simulate nonlocal transport in the daytime PBL compared to local schemes (e.g. Hu et al., 2011; Xie et al., 2013). Although the TEMF scheme is a nonlocal scheme, the TEMF scheme is more suited for simulating stable and shallow, cloud-topped PBLs (Angevine et al., 2010; Angevine et al., 2012). Consequently, the TEMF scheme does a poorer job than the YSU scheme simulating deep daytime convective PBLs. Whereas underestimates are larger with local schemes, modifications to the MYJ scheme that have been incorporated into the MYNN2 scheme improve the representation of vertical mixing in the daytime PBL (Nakanishi and Niino, 2009) and yield better agreement with the SNP HQ and IAD observations than the MYJ scheme. From the sensitivity tests discussed here, we conclude that, while differences in maximum afternoon z_i among the four PBL parameterization schemes studied vary by 500 m, all simulations capture the daytime z_i evolution in the Page Valley and at IAD.

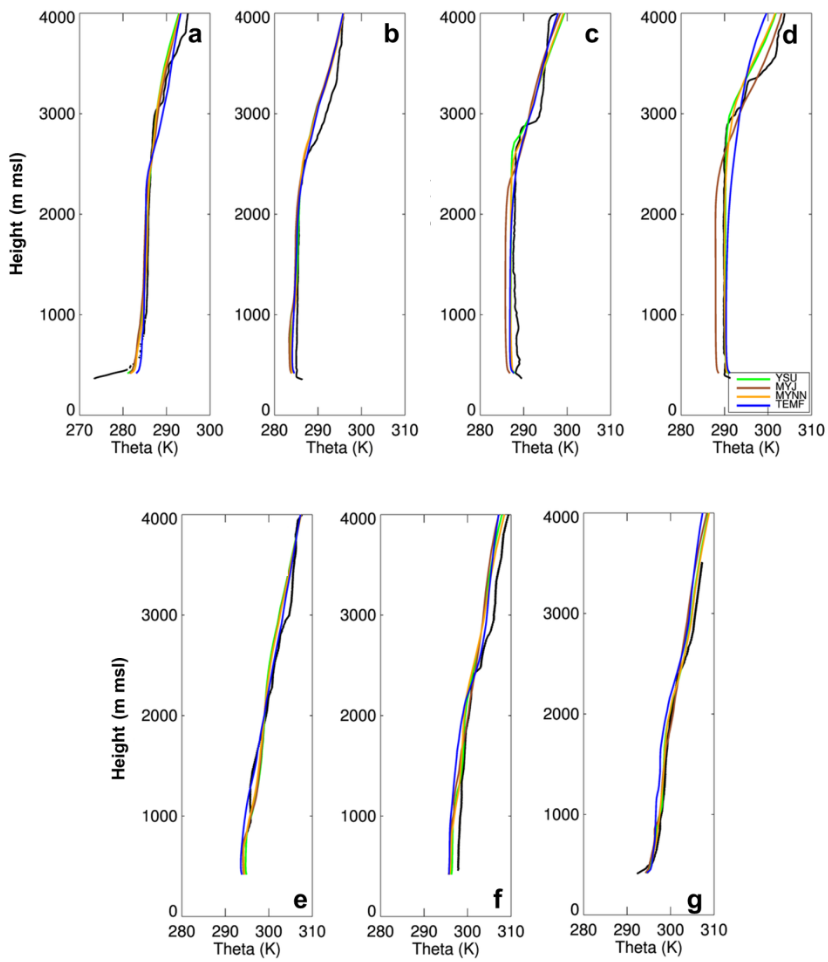

Figure 4.A.1: Potential temperature profiles on 9 April 2009 at 0600 LST (a), 0900 LST (b), 1200 LST (c), and 1500 LST (d); 23 October 2010 at 1300 LST (e), 1600 LST (f) and 1800 LST (g) at SNP HQ from observations (black line), YSU (green line), MYJ (brown line), MYNN2 (orange line), and TEMF (blue line) PBL schemes. The model output are the means over the 9 model grid boxes surrounding SNP HQ. Note different scales but the same range on the x-axis.

Table 4.A.1: z_i in m msl at SNP HQ from the 4 soundings on 9 April 2009 and 3 soundings on 23 October 2010 and model-derived z_i from four different PBL schemes. All z_i shown are computed using the R_b method. LST=UTC-5.

Date	Time (LST)	SNP HQ $\mathbf{z_i}$ (m msl)	YSU $\mathbf{z_i}$ (m msl)	MYJ $\mathbf{z_i}$ (m msl)	MYNN2 $\mathbf{z_i}$ (m msl)	TEMF $\mathbf{z_i}$ (m msl)
9 Apr 2009	06	385	439	456	448	433
	09	2386	1136	1165	1023	1472
	12	2872	2754	2370	2586	2383
	15	2971	3019	2443	2724	2341
23 Oct 2010	13	730	907	847	822	910
	16	669	1024	1012	802	983
	18	363	453	449	448	450

CHAPTER 5

THE IMPACT OF THE PLANETARY BOUNDARY LAYER HEIGHT ON THE DIURNAL VARIABILITY OF CO MIXING RATIOS AT A LOW MOUNTAINTOP[1]

[1] Lee, T. R., De Wekker, S. F. J., and Pal, S., draft. The impact of the planetary boundary layer height on the diurnal variability of CO mixing ratios at a low mountaintop. *Atmos. Sci. Lett.*

Abstract

Trace gas mixing ratios measured at mountaintops are oftentimes assumed to represent background values, but can be affected by air within the valley planetary boundary layer (PBL) at certain times. In particular, the height of the afternoon PBL relative to the ridgetop height is important for investigating valley air influence on mountaintop trace gas mixing ratios. In the present study, we investigate the impact of the quasi-stationary afternoon PBL height (z_i) over the adjacent valley on the diurnal variability of trace gas mixing ratios at a nearby mountaintop. We do this study using carbon monoxide (CO) mixing ratios measured at Pinnacles (38.61 N, 78.35 W, 1017 m above mean sea level), a monitoring site in the Appalachian Mountains in northwestern Virginia, USA, using four years of continuous trace gas measurements (1 January 2009 – 31 December 2012), trace gas measurements from nearby monitoring sites, and z_i estimates from a nearby sounding station. The diurnal CO amplitude decreases as a function of the maximum valley z_i relative to the ridgetop, with mean CO amplitudes of 40 ppb when z_i is below the ridgetop (z_i<800 m msl) and amplitudes of 25 ppb when z_i well exceeds the ridgetop (z_i>1600 m msl). Because previous studies have indicated that wind shifts affect the on-site CO variability, to isolate the role of z_i on the diurnal CO variability, we select fair weather days without wind shifts. On days when the afternoon valley z_i is below the ridgetop, the mean diurnal CO cycle has a daytime CO increase of 9.5 ppb caused by upslope transport of polluted valley PBL air. On days when the afternoon valley z_i

exceeds the ridgetop, the mean diurnal CO cycle shows a daytime decrease of 6.2 ppb due to vertical mixing and dilution that overwhelm the influence of upslope pollutant transport.

5.1. Introduction

Mixing processes within the planetary boundary layer (PBL) affect the exchange of heat, moisture, momentum, and aerosols between Earth's surface and adjacent free atmosphere (FA) (e.g. Stull, 1988). The height of the PBL, z_i, represents the height to which these turbulent mixing processes occur. Over flat terrain, daytime z_i growth leads to a decrease in near-surface pollutant concentrations which has been reported in many previous studies (e.g. Pochanart et al., 2003; Volz-Thomas et al., 2003; Elanksy et al., 2007; Kozlova et al., 2008; Popa et al., 2010; Winderlich et al., 2010; Sahu et al., 2011; Hidy et al., 2014; Pal et al., 2015) and is summarized in Figure 5.1a. For this reason, z_i is an essential parameter describing the vertical mixing of trace gases and pollutants in air quality dispersion studies (e.g. Dabberdt et al., 2004).

Over mountainous terrain, the relationship between z_i and the diurnal variability of aerosols and trace gases is more complicated because of local-to mesoscale transport processes occurring in these areas (e.g. De Wekker et al., 1998; Whiteman, 2000; Rotach and Zardi, 2007; van der Molen and Dolman, 2007; De Wekker et al., 2009). At mountaintop locations unaffected by major trace gas sources and sinks, the diurnal trace gas variability is governed by the trace gas variability over the adjacent valley via vertical mixing and horizontal transport. Therefore, a much different pattern of diurnal trace gas variability emerges. In situations when the valley PBL remains well below the mountaintop, there is oftentimes no clear diurnal trace gas variability, as shown in Figure 5.1b. In these situations, trace gas mixing ratios measured at mountaintops are often assumed to be representative of free atmospheric (FA) mixing ratios (e.g. Baltensperger et al., 1997; Lugauer et al., 1998). In other situations, summarized in Figure 5.1c, there is significant influence of PBL air from adjacent valley(s) on trace gas variability. During the daytime, PBL air from within the valley, which is more polluted than FA air, is transported to the mountaintop via the growth of the valley PBL and thermally-driven upslope winds, resulting in an increase in trace gas and aerosol concentrations at nearby mountaintops. This increase has been reported for carbon monoxide (CO) (e.g. Weiss-Penzias et al., 1996), methane (e.g. Necki et al., 2003), gaseous mercury (e.g. Obrist et al., 2008), and aerosols (e.g. Baltensperger et al., 1997). The magnitude of this increase and the timing of this increase vary seasonally. The increase is typically largest and begins earlier in the day during the summer when z_i is deepest, but may be non-existent during the winter when z_i remains well below the mountaintop and the mountaintop remains in the FA throughout the day (e.g. Baltensperger et al., 1997; Lugauer et al., 1998; Henne et al., 2008a; Henne et al., 2008b). On days in which there is a peak in trace gas mixing ratio, there is oftentimes a nighttime decrease in CO (e.g. Gao et al., 2005; Henne et al., 2008b; Balzani Lööv et al., 2008) and aerosols (e.g. Baltensperger et al., 1997) as the mountaintop becomes more influenced by FA air due to nocturnal sinking motions (e.g. Schmidt et al., 1996). For this reason, it is common practice to assimilate nighttime trace gas measurements from mountaintops into applications that require measurements representative of FA or background values, e.g. atmospheric chemistry studies (e.g. Novelli et al., 1998), air quality studies (e.g. Dabbert et al., 2004), and carbon cycle studies (e.g. Brooks et al., 2012).

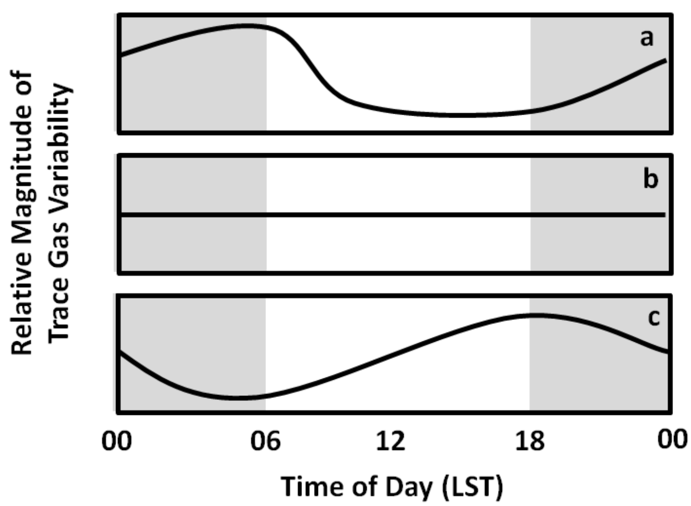

Figure 5.1: Conceptual model of the diurnal trace gas variabilty starting with a set concentration of trace gas and assuming no advection or sources or sinks for a site in flat terrain (a), a mountaintop without valley PBL influence (b), and a mountaintop with valley PBL influence (c). Shaded and non-shaded areas represent nighttime and daytime, respectively.

From the studies summarized above, one may infer that the diurnal trace gas variability at mountaintops depends on the maximum daytime z_i relative to the mountaintop height, i.e. the z_i over adjacent upwind valley. In the present study, we investigate in detail the role of z_i on mountaintop trace gas variability using measurements from a mountaintop monitoring site in the southern Appalachian Mountains that we refer to as Pinnacles. Pinnacles is an ideal location to investigate the influence of z_i relative to the mountaintop on the observed trace gas variability because z_i can either be well below or well above the mountaintop. Furthermore, trace gas (CO and CO_2) and measurements from Pinnacles are currently used to estimate regional- to continental-scale carbon fluxes in CarbonTracker, an inverse carbon transport model (Peters et al., 2007). The CO and CO_2 measurements from Pinnacles may also be used in long-term studies on trends in background trace gas mixing ratios once a better understanding of PBL effects on the measurements is achieved. In the present study, we use trace gas observations from Pinnacles and rawinsonde observations from a nearby sounding station. In Section 5.2, we describe the site characteristics and approach for determining z_i over the valley upwind of Pinnacles. We discuss the z_i variability in Section 5.3.1, and in Section 5.3.2 discuss the characteristics of the CO time series. In Section 5.3.3, we investigate the relationship between z_i and the diurnal CO variability and summarize our findings with a conceptual diagram in Section 5.3.4.

5.2. Site description and methods

5.2.1. Site description

Meteorological and trace gas measurements are obtained from an instrumented 17 m tower at Pinnacles (38.61 N, 78.35 W, 1017 m above mean sea level [msl]) along the crest of the Virginia Blue Ridge Mountains, which are along the eastern flank of the southern Appalachians in the eastern US. Further details about the site are found in Lee et al. (2012) and Lee et al. (2014).

5.2.2. CO measurements

CO and CO_2 mixing ratios have been measured at Pinnacles since 2008 at 5, 10, and 17 m agl (above ground level) through collaboration with the NOAA Earth System

Research Laboratory (ESRL). The measurement system and in situ calibrations have already been described by Lee et al. (2015), and a detailed description of the measurement uncertainties is discussed in Andrews et al. (2014). In the present study, we use half-hour means of the CO data collected 17 m agl during the site's first four full years of operation, i.e. 1 January 2009 through 31 December 2012.

5.2.3. Supplemental measurements

To help interpret the CO variability as a function of z_i, we use supplemental measurements from the mountaintop and valley. Meteorological measurements at Pinnacles began in July, 2008 and are described in previous work (Lee et al., 2012; Lee et al., 2014; Lee et al., 2015). In addition to measurements from Pinnacles, we use meteorological and trace gas measurements from nearby monitoring sites. Mountaintop ozone (O_3) measurements are obtained from Big Meadows (38.52 N, 78.44 W, 1079 m msl) and from the adjacent Page Valley (Figure 5.2) at the Luray Caverns Airport (38.66 N, 78.50 W, 275 m msl), located 13 km west of Pinnacles. At both sites, O_3 mixing ratios are measured 10 m agl using a Thermo Environmental Instruments Model 49i UV photometric O_3 analyzer that has a 1 ppb precision. The data record at Big Meadows for the period of interest is mostly complete, although there exists a data gap between late February and April 2010. At the Luray Caverns Airport, hourly O_3 mixing ratios are sampled from 1 April through 31 October annually.

5.2.4. PBL height

Reliable z_i estimates over the upwind Page Valley are required to investigate the role of valley z_i on the trace gas variability at Pinnacles. In the Page Valley, there exist no z_i observations at daily timescales for the entire period of interest. One approach is to assume that z_i obtained from nearby sounding stations, where twice-daily rawinsonde observations are made, are representative of the region (Hondula et al., 2013). However, this approach ignores z_i spatial variability. Studies in the region of interest have found that mean afternoon z_i over the Page Valley is 200-400 m larger than z_i estimated using observations from the nearest sounding station, located at Dulles Airport (IAD) (38.98 N, 77.49 W, 87 m msl) 90 km northeast of the Page Valley.

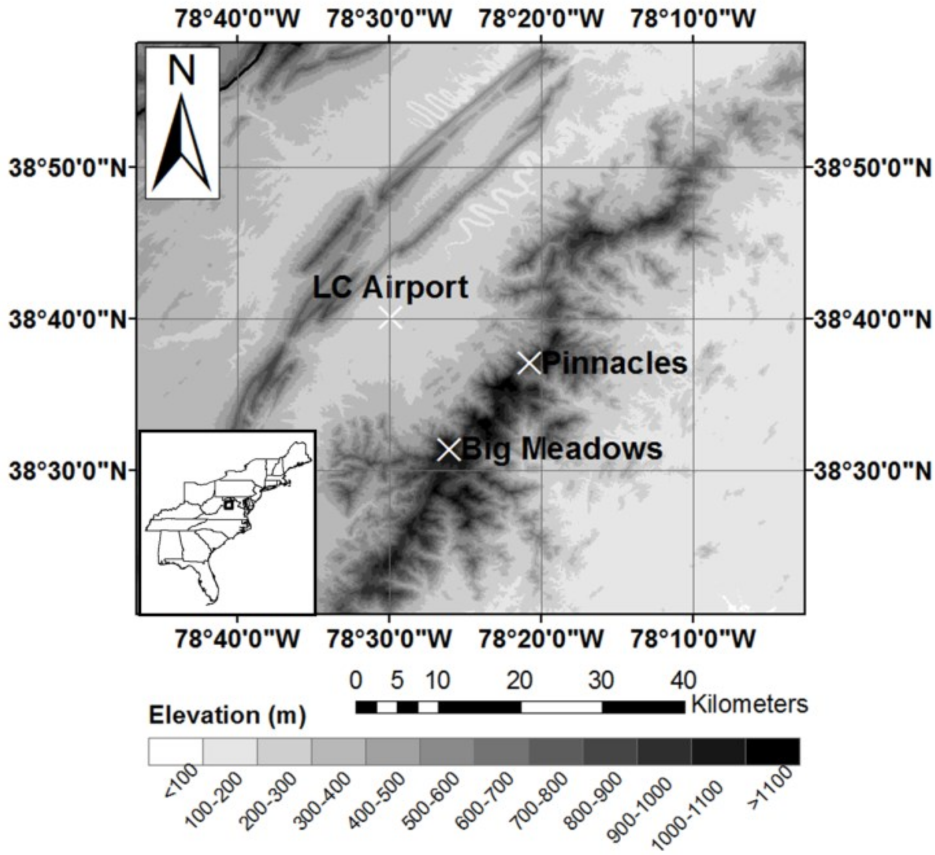

Figure 5.2: Topographic map indicating the location of Pinnacles relative to Big Meadows and the Luray Caverns (LC) Airport (white X's). Shading shows elevation msl. The inset map at the bottom left indicates the study location, denoted by a black box, in the eastern US. The topography data have a 10 m resolution and are from the US Geological Survey.

These differences arise due to drier conditions over the Page Valley, leading to more net radiation being partitioned into *SHF* and thereby larger z_i over the Page Valley than over IAD. Accounting for these z_i differences is necessary to obtain the most reliable z_i estimates over the Page Valley. Thus, to estimate z_i over the Page Valley, we determine the afternoon z_i from the 00 UTC IAD rawinsonde observations following the procedure discussed in Chapter 4. To determine the z_i over the Page Valley from the afternoon IAD z_i, we apply an offset to these z_i following the procedure discussed in Chapter 4. The offset varies as a function of season and is largest in summer and smallest in winter (Table 5.1).

Table 5.1: Offset applied to the IAD rawinsonde z_i, based on findings in Chapter 4, to better approximate z_i over the Page Valley.

Season	Offset (m)
Winter	+190
Spring	+210
Summer	+300
Fall	+250

5.3. Results

5.3.1. Seasonal z_i variability

Over the four-year period of interest, z_i in the 00 UTC sounding ranges from <500 m agl to >2500 m agl following the removal of the near-surface stable layer from the soundings discussed in Section 5.2.4 (Figure 5.3). The monthly mean and maximum z_i are largest in the late spring and early summer and lowest in the winter, consistent with other locations in the southeast US (Garrett, 1981). Much of the z_i seasonal variability is explained by the variability in *SHF*. Afternoon (1200-1600 LST) *SHF* computed at Pinnacles are around 50 W m^{-2} in the winter when z_i is smallest, but largest in the spring and summer when mean afternoon *SHF* are about 200 W m^{-2}.

5.3.2. Overview of CO measurements

The mean seasonal and diurnal cycle has already been described previously by Lee et al. (2015). Briefly, CO mixing ratios are typically highest in March and lowest in October. This seasonal cycle has been reported at other mid-latitude continental monitoring sites (e.g. Popa et al., 2010; Cristofanelli et al., 2013) and is attributed to greater anthropogenic emissions during the cool season and the seasonality of the OH radical, which acts the dominant CO sink on the global scale (e.g. Thompson, 1992; Henne et al., 2008b). The mean diurnal CO cycle at Pinnacles is characterized by a daytime CO increase, which is a common feature of other mountaintop monitoring sites

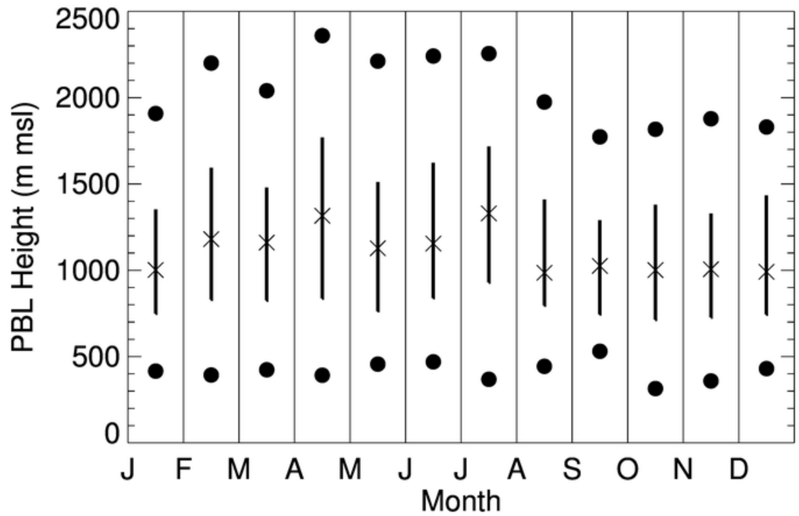

Figure 5.3: z_i at IAD as a function of time of year determined from the 00 UTC sounding with the removal of the near-surface stable layer. X's indicate medians; black bars extend out to the 25th and 75th percentiles. Dots indicate 5th and 95th percentiles.

(e.g. Atlas and Ridley, 1996; Forrer et al., 2000; Gao et al., 2005; Balzani Lööv et al., 2008; Henne et al., 2008b; MacDonald et al., 2011). The CO increase occurs in all seasons and has the largest amplitude in the winter (7.1 ppb) and smallest amplitude in the summer (4.0 ppb) (Lee et al., 2015). Standard deviations in the hourly values are 20-25 ppb and are caused by large day-to-day variability that arises due to, e.g. synoptic scale air mass changes (Lee et al. 2012) and mesoscale circulations (Lee et al., 2015). Lee et al. (2015) filtered the effects of these wind shifts and found that, under fair weather conditions, CO mixing ratios increase during the daytime on days with a wind shift, but decrease on days without wind shifts due to dilution within the daytime PBL.

In the present study, we investigate the role of z_i on the diurnal CO variability for all days, regardless of the presence or absence of a wind shift, and also for the subset of days on which a wind shift was not present to isolate the role of z_i on the diurnal CO variability. In the next section, we investigate the influence of z_i on the CO mixing ratios by determining the mean diurnal CO cycle as a function of z_i relative to the ridgetop. We then quantify the relationship between characteristic features of the diurnal CO cycle and z_i by determining the relationship between z_i and daily CO amplitude, which represents the difference between the daily maximum and daily minimum CO mixing ratio, and the relationship between z_i and the mean difference between morning and afternoon CO mixing ratios.

5.3.3. Effect of z_i on CO

5.3.3.1. Effect on the diurnal CO cycle

To determine the effect of afternoon z_i on the diurnal CO cycle as a function of z_i relative to the ridgetop height, we subtract the daily CO mean from the diurnal cycle. When all days are considered (i.e. independent of presence of fair weather conditions or the presence of a wind shift at the site), there is a CO increase on days in which the valley z_i remains below the ridgetop (Figure 5.4a), which is a pattern consistent with the mean diurnal CO cycle at Pinnacles (e.g. Lee et al. 2015).

Following Lee et al. (2015), we select only fair weather days using a clearness index (Whiteman et al., 1999a) and identify those without a wind shift present to isolate the days on which convective mixing within the PBL is expected to be the most important driver of the CO variability. We then identify days in which the PBL was either well below or well above the maximum ridgetop height in this region of 1200 m because of the uncertainties in z_i estimates for the Page Valley (c.f. Section 5.2.4). Because the uncertainties in z_i estimates can be as large as 400 m (c.f. Chapter 4), to have confidence that z_i was either below the ridgetop or above the ridgetop, we identify a day as having a z_i below (above) the ridgetop if z_i is <800 m msl (>1600 m msl). Altering these values does not significantly affect the mean diurnal CO cycles on these subsets of days.

In the 4-year period of interest, fair weather days without a wind shift occur on 16% of all days. On the subset of days when the valley z_i is below the ridgetop (18% of all fair weather days with constant winds, or 3% of all days during the 4-year period of interest), there is a daytime CO increase (Figure 5.4b). CO mixing ratios begin increasing around 0800 LST to a maximum at 1300 LST before decreasing. This afternoon decrease may be caused by dilution within the PBL over the mountaintop. In contrast, there is a CO decrease on days when the valley z_i exceeds the ridgetop (34% of all fair weather days with constant winds and 5% of all days over the 4 year period), which happens independently of whether or not a wind shift is present. This decrease is larger on fair weather days with constant winds because, on this subset of days, PBL dilution and the entrainment of FA air are the main drivers of the CO variability.

To understand the differences in the mean diurnal CO cycle between days with z_i below the ridgetop and days with z_i above the ridgetop, we use additional data sets from the mountaintop and valley. We find that the observed CO changes on days with z_i below the ridgetop and days with z_i above the ridgetop coincide with changes in water vapor mixing ratio when all days in the period of record are considered (Figure 5.4c) and on the subset of fair weather days with constant winds (Figure 5.4d). On the days with z_i below the ridgetop, the simultaneous CO and water vapor increases indicate that days with z_i below the ridgetop are characterized by vertical transport and mixing of valley PBL air to the mountaintop (e.g. Weiss-Penzias et al., 2006). The decrease in water vapor mixing ratio on days with the z_i above the mountaintop provides further evidence that PBL dilution and mixing overwhelm the transport of polluted valley PBL air to the mountaintop via convective mixing and upslope flows.

We confirm that valley PBL air influences the mountaintop CO measurements both on days with z_i below the ridgetop and on days with z_i above the ridgetop by calculating the difference in O_3 mixing ratio between the ridgetop (Big Meadows) and valley (Luray Caverns Airport). Large O_3 differences indicate less influence of valley PBL air on the mountaintop measurements, and small O_3 differences indicate more influence of valley PBL air on the mountaintop measurements. We find that O_3 mixing ratios are 20-30 ppb higher at the mountaintop than in the valley during the nighttime. The O_3 differences become smaller beginning around sunrise as air contained within the valley PBL is transported to the mountaintop by convective mixing and slope flows occurring within the growing PBL. This decrease happens when all days are considered (Figure 5.4e) and also on the subset of fair weather days with constant winds (Figure 5.4f). Mean minimum O_3 differences between the mountaintop and valley are <0.5 ppb regardless of z_i relative to the mountaintop. This finding suggests that air within the valley PBL has a significant effect on the mountaintop trace gas mixing ratios even when the daytime maximum z_i remains below the ridgetop.

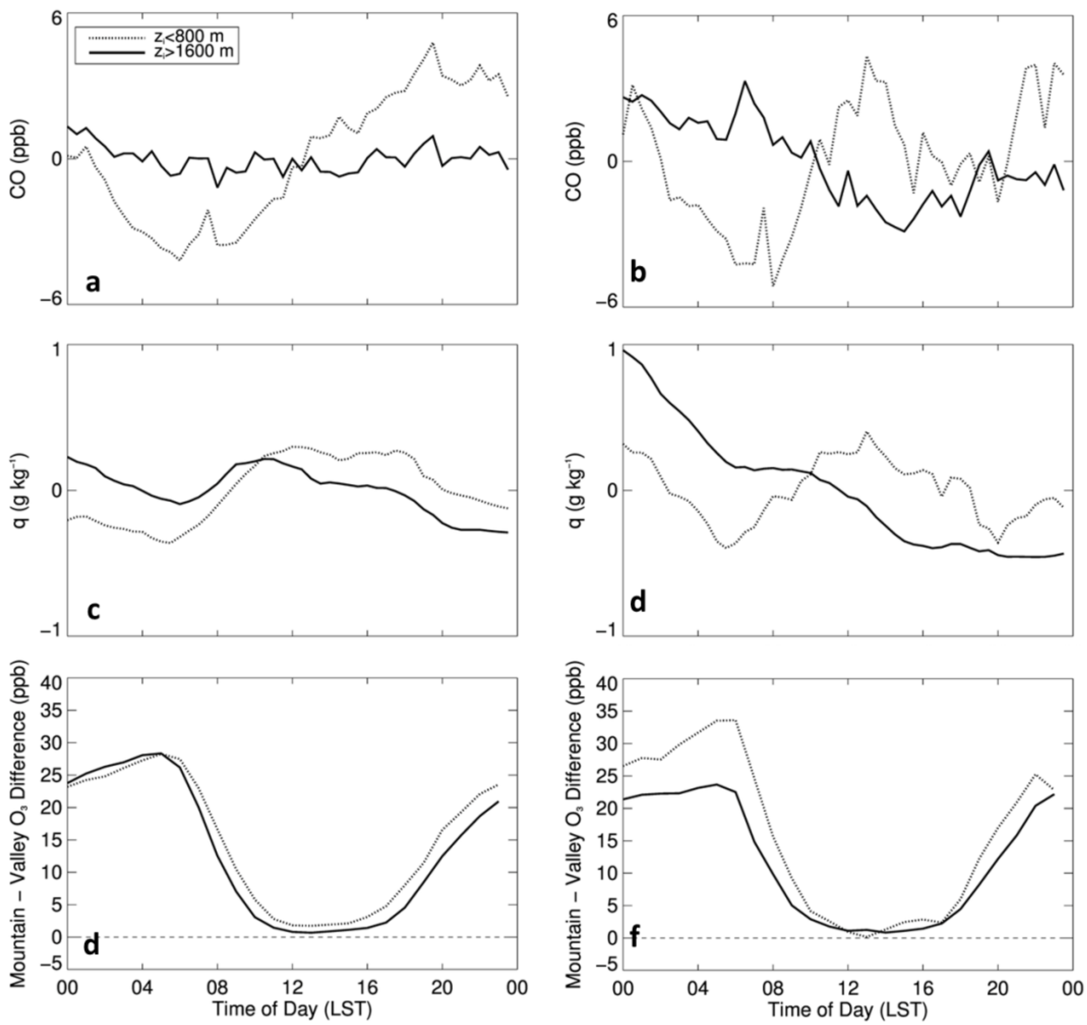

Figure 5.4: Mean diurnal variability in CO, measured 17 m agl, as a function of z_i relative to the mountaintop for all days over the period 1 Jan 2009 – 31 Dec 2012 (a) and for the subset of fair weather days with constant winds (b). Same for panels (c) and (d) but for water vapor mixing ratios measured 17 m agl at Pinnacles. Panels (e) and (f) show the diurnal variability in O_3 difference between the mountaintop and valley for all days and for the subset of fair weather days with constant winds, respectively. Note that the daily means are removed from panels (a) through (d), and there is a horizontal dashed line at 0 ppb in panels (e) and (f). Dotted and dashed lines indicate z_i <800 m msl and z_i >1600 m msl, respectively. For all days (i.e. the left column), N=465 and N=604 for z_i <800 m msl and z_i >1600 m msl, respectively; for the subset of fair weather days with constant winds (i.e. the right column), N=23 and N=87 for z_i <800 m msl and z_i >1600 m msl, respectively.

5.3.3.2. Effect on CO amplitude and daily CO change

We quantify the relationship between the CO variability and z_i by calculating the CO amplitude and sort the data into bins as a function of z_i. The largest amplitudes in CO mixing ratio occur when z_i is lowest, but these differences become smaller on days with larger z_i (r=-0.75, p<0.01) (Figure 5.5a). Above 1200 m msl, the CO amplitude is independent of z_i increases. In addition, standard deviations in the CO amplitude are highest on days with low z_i, but decrease as a function of increasing z_i and thus are smallest on days when z_i exceeds the ridgetop height. In contrast to the relationship shown in Figure 5.5a, there is no statistically significant relationship between z_i and CO amplitude (r=-0.27, p=0.33) (Figure 5.5b) on the subset of fair weather days with constant winds. The absence of a statistically significant relationship occurs because there is a mean CO increase of 9.5 ppb on days when z_i is below the ridgetop and a mean CO decrease of 6.2 ppb on days when z_i exceeds the ridgetop.

The relationship between the diurnal CO variability and z_i becomes more apparent when determining the difference between mean afternoon (1200-1600 LST) and mean morning (0600-1000 LST) CO mixing ratios. When all days are considered (i.e. independent of the presence of a wind shift), there is an inverse relationship between this difference and z_i (r=-0.78, p<0.01), but there are large standard deviations around the mean (Figure 5.6a). When z_i exceeds 2000 m msl, CO mixing ratio are typically lower in the afternoon than during the morning, indicating that, even if wind shifts are occurring, their influence on the trace gas variability is overwhelmed by the effects of PBL dilution and FA entrainment. On the subset of fair weather days with constant winds, there is also a statistically significant inverse relationship between z_i and the difference between morning and afternoon CO mixing ratios (r=-0.63, p=0.01) (Figure 5.6b). On this subset of days, standard deviations are smaller, and CO mixing ratios are typically higher in the afternoon when z_i is below the ridgetop, but lower in the afternoon when z_i exceeds the ridgetop.

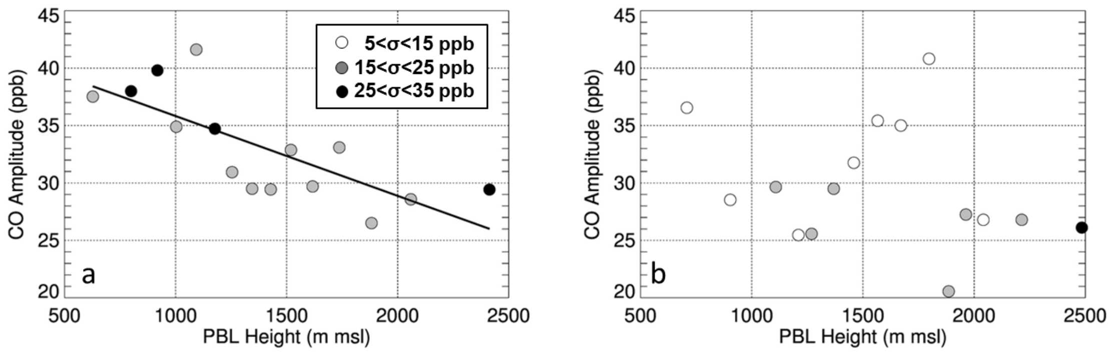

Figure 5.5: Amplitude of the diurnal CO variability as a function of z_i for 1 Jan 2009 – 31 Dec 2012 for all days (a) and for fair weather days with constant winds (b). 15 bins with 69 values per bin in panel (a); 15 bins with 11 values per bin in panel (b). White, gray, and black circles indicate standard deviations in the daily CO amplitude of 5-15 ppb, 15-25 ppb, and 25-35 ppb, respectively. Black line in (a) shows the line of best fit.

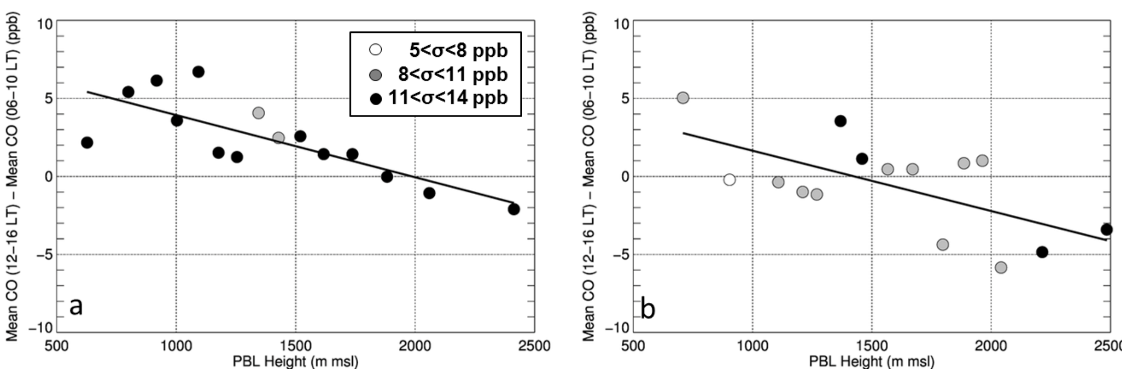

Figure 5.6: Mean difference between mean afternoon (1200-1600 LST) and mean morning (0600-1000 LST) CO mixing ratios as a function of z_i for 1 Jan 2009 – 31 Dec 2012 for all days (a) and for fair weather days with constant winds (b). 15 bins with 69 values per bin in panel (a); 15 bins with 11 values per bin in panel (b). White, gray, and black circles indicate standard deviations in the daily CO amplitude of 5-8 ppb, 8-11 ppb, and 11-14 ppb, respectively. Black line shows the line of best fit.

5.3.4. Conceptual diagram of trace gas variability as a function of z_i relative to the ridgetop

To summarize our findings, we construct a conceptual diagram to illustrate the dominant physical processes affecting the trace gas variability at mountaintops depending on whether the valley z_i is below the ridgetop or above the ridgetop. On days when the valley z_i remains below the ridgetop (Figure 5.7a), pollutants emitted within the valley PBL are confined to a smaller volume, resulting in less PBL dilution and mixing. On these days, the mountain is influenced by pollutants emitted into the PBL over the upwind valley. Pollutant transport occurs via upslope flows, resulting in a daytime trace gas increase that has been reported at other mountaintop monitoring sites (e.g. Weiss-Penzias et al., 2006; Henne et al., 2008b; Obrist et al., 2008). Therefore, trace gas measurements made in these cases cannot be considered representative of background values.

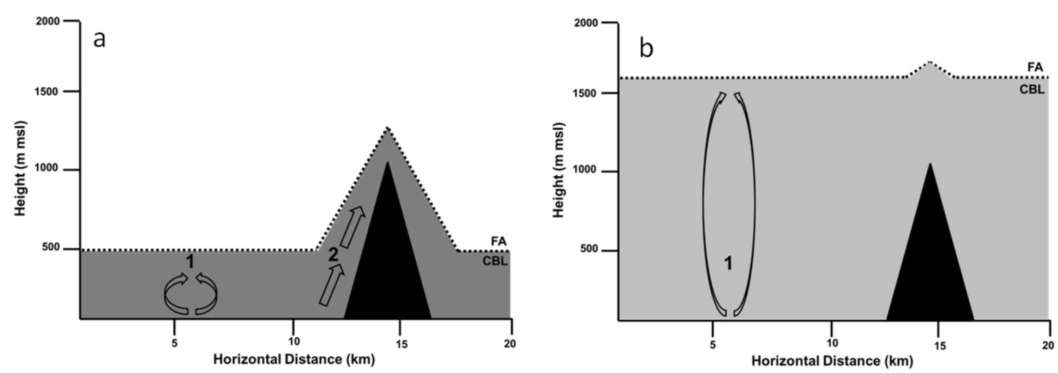

Figure 5.7: Conceptual diagram of trace gas transport as a function of z_i (dotted line) relative to the mountaintop (black triangle) on days when the valley z_i is below the mountaintop (500 m in this example) (panel a) and on days when the valley z_i is above the mountaintop (1600 m in this example) (panel b). The dominant transport mechanisms that affect the daytime CO variability as a function of z_i relative to the mountaintop are (1) convective mixing and (2) upslope flows and are indicated with arrows. Darker gray shading in panel (a) indicates higher concentrations of pollutants than in panel (b).

On days when the valley z_i exceeds the ridgetop height (Figure 5.7b), pollutants are emitted into a larger volume of air, resulting in more PBL dilution and mixing as the

PBL exceeds the ridgetop. As the valley z_i exceeds the ridgetop height, there is a decrease in pollutant concentration at the mountaintop due to PBL dilution and entrainment of FA air into the growing PBL. Because there is a decrease in the trace gas mixing ratio regardless of whether or not a wind shift is present, this finding indicates that PBL dilution and FA air entrainment overwhelm the influences of upslope pollutant transport via slope flows. The trace gas behavior on days with deep PBLs is similar to the trace gas behavior reported in studies on trace gas behavior at the tops of tall towers in flat terrain (e.g. Popa et al., 2010; Schmidt et al., 2014; Pal et al., 2015). Thus, mountaintop measurements trace gas measurements made on days with deep PBLs can be considered along with tall tower measurements in applications requiring regionally-representative values.

5.4. Conclusions and implications

We presented the first study investigating the effect of z_i on the diurnal CO variability at a low mountaintop, using a mountaintop trace gas monitoring site in the Virginia Blue Ridge Mountains as a case study. We found that the amplitude of the CO variability is largest on days when z_i remains below the ridgetop and is smallest on days when z_i exceeds the ridgetop. On days when the valley z_i is below the ridgetop, there is a daytime CO increase caused by the upslope transport of polluted valley PBL air to the mountaintop. On days when the valley PBL exceeds the ridgetop, CO decreases during the daytime due to vertical mixing and dilution that overwhelm the influence of upslope pollutant transport.

The results in this study provide additional insights into the use of trace gas measurements from low mountaintops like Pinnacles in applications requiring regionally-representative values. Measurements from these monitoring sites are affected by mesoscale meteorological processes that are unresolved in, e.g. inverse carbon transport models (e.g. Peters et al., 2007; Butler et al., 2010; Schuh et al., 2010; Pillai et al., 2011) and air chemistry models (e.g. Novelli et al., 1998) because of the models' coarse spatial resolution. The present study builds upon previous work in the region (i.e. Lee et al., 2012; Lee et al. 2015) by helping to further understand the local-scale to mesoscale meteorological processes affecting the trace gas variability at low mountaintops. The findings in the present paper underscore the impact of the valley z_i on the diurnal CO variability. The daytime CO increase on days with z_i below the ridgetop implies low mountaintops like Pinnacles sample pollution from upwind valleys, and thus measurements made on these days are not representative of regional or background trace gas mixing ratios. The daytime CO decrease on days when z_i is above the ridgetop, however, is a pattern consistent with sites in flat terrain. The daytime decrease suggests that afternoon trace gas measurements from low mountaintops made when z_i exceed the ridgetop can be used in applications requiring regionally representative measurements.

5.5. Acknowledgements

This research and maintenance of the Pinnacles research station was partly funded by an MOU between the NOAA ESRL Global Monitoring Division and the University of Virginia and by NSF-CAREER Grant ATM-1151445. We thank staff from Shenandoah National Park, especially Elizabeth Garcia, Jim Schaberl, and Alan Williams, and students from the Environmental Sciences Department at the University of Virginia for helping to maintain data collection at Pinnacles, especially Nevio Babić, Stephanie Phelps, and Mark Sghiatti. Many thanks to Željko Večenaj at the University of Zagreb for on-site support in 2008, 2009, and 2012, and to Jonathan Kofler and Jonathan Williams at NOAA ESRL.

CHAPTER 6

THE APPLICATION OF LAGRANGIAN PARTICLE DISPERSION MODEL SIMULATIONS TO INVESTIGATE THE DIURNAL TRACE GAS VARIABILITY AT A LOW MOUNTAINTOP[1]

[1] Lee, T. R., De Wekker, S. F. J., Dickerson, R. R., and Ren, X., draft. The application of Lagrangian particle dispersion model simulations to investigate the diurnal variability in atmospheric trace gas mixing ratios at a low mountaintop. *J. Geophys. Res. Atmos*.

Abstract

Atmospheric trace gas mixing ratios such as carbon monoxide (CO) are affected by multi-scale meteorological processes that are particularly complicated over mountainous terrain. An understanding of these processes is vital to help determine how the trace gas measurements can best be used in applications requiring either regionally-representative measurements or free atmospheric background measurements. Recent work from Pinnacles (38.61 N, 78.35 W, 1017 m above mean sea level [msl]), a mountaintop monitoring site in the Appalachian Mountains of the eastern US, has found that the diurnal CO variability depends on the planetary boundary layer (PBL) height, z_i, relative to the ridgetop height. These findings lead to the hypothesis that the daytime trace gas variability and concentration footprint of afternoon trace gas measurements from low mountaintops like Pinnacles on days when z_i exceeds the ridgetop height of 1100 m msl compare well with tall tower monitoring sites over flat terrain. To test this hypothesis, we investigate three days with similar meteorological conditions but with different afternoon z_i: 23 October 2010, 18 July 2011, and 9 April 2009, which had maximum z_i of 1000 m msl, 1800 m msl, and 3000 m msl, respectively. The mountaintop trace gas measurements on these days are complemented by in situ meteorological measurements, meteorological and trace gas observations from nearby sites, and numerical simulations

with the Weather Research and Forecasting (WRF) model and the FLEXPART Lagrangian particle dispersion model (LPDM). Regional observations and LPDM simulations indicate that trace gas measurements from low mountaintops like Pinnacles are affected by air within the upwind valley PBL due to upslope transport and vertical mixing during the mid-late morning that occur independent of z_i relative to the ridgetop height. During the afternoon on days with z_i well exceeding the ridgetop height, convective mixing overwhelms local-scale transport processes. On these days, afternoon trace gas measurements from low mountaintops are most similar to measurements from tall towers, based on comparisons between LPDM simulations with topography included and LPDM simulations from which the regional topography was removed. Consequently, afternoon trace gas mixing ratios from low mountaintops on days with z_i well exceeding the ridgetop height can be used like trace gas mixing ratios measured from tall towers in applications requiring regionally-representative measurements.

6.1. Introduction

Knowledge of the degree to which trace gas measurements are representative of well-mixed planetary boundary layer (PBL) air is important for many applications, including atmospheric chemistry models (e.g. Novelli et al., 1998), air quality studies (e.g. Dabbert et al., 2004), and inverse carbon transport models (e.g. Gloor et al., 2001; Haszpra et al., 2014). At sunrise, surface heating results in the growth of the PBL. As the PBL height, z_i, increases due to mechanically and convectively generated turbulence, trace gas mixing ratios decrease. The rate of decrease in the trace gas mixing ratios slows during the afternoon as the PBL reaches a near-constant height. Thus, at locations within the afternoon PBL, vertical trace gas gradients are small and are representative of spatial scales up to 10^6 km^2 (Gloor et al., 2001). For this reason, mean afternoon (1200-1600 LST) trace gas mixing ratios measured at the tops of tall towers 100-400 m above ground level (agl) over flat terrain (e.g. Andrews et al., 2014; Haszpra et al., 2014) are assimilated into inverse carbon transport models such as CarbonTracker to help quantify regional- to continental-scale carbon budgets (e.g. Peters et al., 2007).

More recently, trace gas measurements from mountaintops have been assimilated into inverse carbon transport models (e.g. Brooks et al., 2012). Unlike tall towers, only nighttime measurements from mountaintops are typically assimilated into these models. This rationale is based on the notion that mountaintops usually sample well-mixed free atmospheric (FA) air at night due to nocturnal sinking motions (e.g. Thoning et al., 1989; Schmidt et al., 1996). Daytime measurements from mountaintops are not assimilated into these models because daytime trace gas measurements are oftentimes contaminated by pollutants emitted within the PBL over the adjacent valley and plains. These pollutants are transported to the mountaintop via convective mixing and upslope flows and result in a daytime increase in trace gas mixing ratios sampled at the mountaintop (Forrer et al., 2000; Gao et al., 2005; Balzani Lööv et al., 2008; Henne et al., 2008; Obrist et al., 2008). However, this increase does not always occur. Recent studies from Pinnacles, a mountaintop monitoring site in the Appalachian Mountains, have frequently found a daytime decrease in CO mixing ratios (Lee et al., 2015). The daytime decrease is consistent with the diurnal trace gas variability observed at the tops of tall towers (e.g. Bakwin and Tans, 1995; Bakwin et al., 1998; Schmidt et al., 2014) and suggests that daytime measurements from mountaintops can sometimes be used like measurements from tall tower in applications requiring values representative of well-mixed PBL air. As of March, 2015, only nighttime measurements from Pinnacles (i.e. mean values from 0000-0400 LST) are assimilated into CarbonTracker (A. Andrews, personal communication) based on the assumption that nighttime measurements from the site are representative of FA, or background, trace gas mixing ratios. However, recent work by Lee et al. (2015) suggests there is the potential to assimilate daytime measurements from Pinnacles into CarbonTracker as well. Although daytime trace gas measurements from Pinnacles are not representative of background values, daytime measurements have the potential to be representative of well-mixed PBL air and thus may be useful to CarbonTracker. Based on previous studies in the region (e.g. Lee et al., 2015), these situations are expected to occur when z_i exceeds the ridgetop height.

In the present study, we investigate the hypothesis that the z_i relative to the ridgetop height affects how well mountaintop trace gas measurements compare with tall tower measurements, both in terms of the diurnal trace gas variability and the concentration footprint, the latter of which represents the area over which air masses arriving at the site had contact with the surface (Henne et al., 2010). We expect that daytime mountaintop trace gas measurements compare best with tall towers when z_i exceeds the ridgetop height but show the poorest agreement when z_i is at or below the ridgetop. To test this hypothesis, we use trace gas measurements from Pinnacles, regional trace gas and meteorological observations, and numerical simulations with the Weather Research and Forecasting (WRF) model and FLEXPART, a Lagrangian particle dispersion model (LPDM). We focus on three days which had similar meteorological conditions but different afternoon maximum z_i: 23 October 2010, 9 April 2009, and 18 July 2011. After summarizing the meteorological conditions on these days and using regional meteorological observations to evaluate our WRF simulations, we use WRF output as inputs for the LPDM simulations. We use the LPDM simulations to investigate the extent to which mountaintops like Pinnacles behave like tall towers. In one set of simulations, we make no modifications to the topography and remove the regional topography in an additional set of simulations.

6.2. Methods

6.2.1. Site Description

Pinnacles (38.61 N, 78.35 W, 1017 m above mean sea level [msl]) is located in the Virginia Blue Ridge Mountains along a ridgetop that varies in elevation from 1000-1200 m msl. To the immediate west of Pinnacles is the Page Valley, with a mean elevation of 200 m on the north end to 400 m on the south end. The Page Valley is part of the larger Shenandoah Valley which is bifurcated by the Massanutten Mountains. Skyline Drive, 120 m southeast of Pinnacles, is the nearest potential CO source to Pinnacles. Studies have found that vehicular traffic emissions from Skyline Drive have no significant influence on trace gas measurements measured at Pinnacles (Lee et al., 2012; Lee et al., 2015). Other nearby CO emissions sources include the town of Luray, with a population of about 5000, located 15 km west of Pinnacles in the Page Valley (Figure 6.1).

6.2.2. Surface measurements

At Pinnacles, CO and CO_2 mixing ratios have been monitored since August 2008 along a 17 m walkup tower at 5, 10, and 17 m above ground level (agl) via collaboration

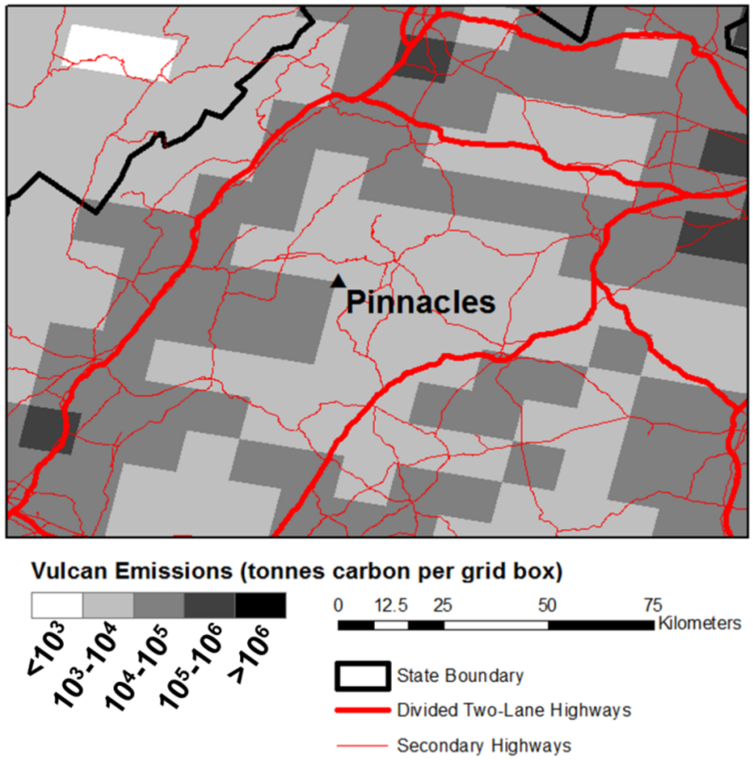

Figure 6.1: Map showing the location of Pinnacles relative to emissions sources in the region. Primary roads (i.e. interstates and divided highways) are denoted by a thick red line; secondary highways are shown with a thin red line; shading shows the total annual fossil fuel emissions (tonnes carbon per 10 km^2 grid box per year) obtained from the Vulcan emissions data base (see Gurney et al., 2009 for more details).

with the NOAA Earth System Research Laboratory (ESRL). The measurement system and in-situ calibrations are described by Lee et al. (2015), and a description of the measurement uncertainties appears in Andrews et al. (2014). The on-site trace gas measurements are complemented by meteorological measurements described in previous studies (Lee et al., 2012; Lee et al., 2014; Lee et al., 2015).

We also use trace gas measurements from nearby monitoring sites. O_3 measurements are obtained from two sites: Big Meadows (38.52 N, 78.44 W, 1079 m msl), a monitoring site part of the Environmental Protection Agency's Clean Air Status and Trends Network (CASTNET) located 14 km south of Pinnacles along the same mountain ridge as Pinnacles, and Luray Caverns Airport (38.66 N, 78.50 W, 275 m msl), a Virginia Department of Environmental Quality (DEQ) monitoring site located 13 km west of Pinnacles in the Page Valley. At both Big Meadows and the Luray Caverns Airport, O_3 mixing ratios are sampled 10 m agl using a Thermo Environmental Instruments Model 49i photometric O_3 analyzer with a 1 ppb precision.

6.2.3. Rawinsonde observations

Rawinsonde observations were made at the Shenandoah National Park Headquarters (38.67 N, 78.37 W, 351 m msl) in the Page Valley during the Education in Complex Terrain Meteorology (EDUCT) field experiment in April 2009 and October 2010 and are used for model evaluation. Rawinsondes were launched on 9 April 2009 at 0600, 0900, 1200, and 1500 LST (LST=UTC-5) and on 23 October 2010 at 1300, 1600, and 1800 LST.

6.2.4. RAMMPP

Aircraft profiles of temperature, wind, moisture, CO, and O_3 were measured during the Regional Atmospheric Measurement Modeling and Prediction Program (RAMMPP) which was a multi-year study that investigated research questions related to air quality over the Mid-Atlantic (e.g. He et al., 2014; Flynn et al., 2014). In the present study, we use morning aircraft measurements from 18 July 2011 for model evaluation. These measurements were made between the ground surface and 3000 m agl at three airports near Pinnacles: Frederick, MD (39.42 N, -77.37 W, 92 m msl); Cumberland, MD (39.62 N, -78.76 W, 236 m msl), and Luray Caverns, VA between 0717 and 1028 LST on 18 July 2011 (Figure 6.2).

6.2.5. WRF

We perform simulations with WRF, a compressible non-hydrostatic model (Skamarock, 2008), to provide the wind fields that are input into the LPDM simulations discussed in the next section. We use four model domains in our WRF simulations. These domains have two-way nesting and have a horizontal grid spacing of 64 km (domain 1), 16 km (domain 2), 4 km (domain 3), and 1 km (domain 4), respectively (Figure 6.3). The outermost domain encompasses the contiguous US, whereas the innermost domain is centered on Pinnacles and includes the ridgetop and upwind Page Valley. Terrain and

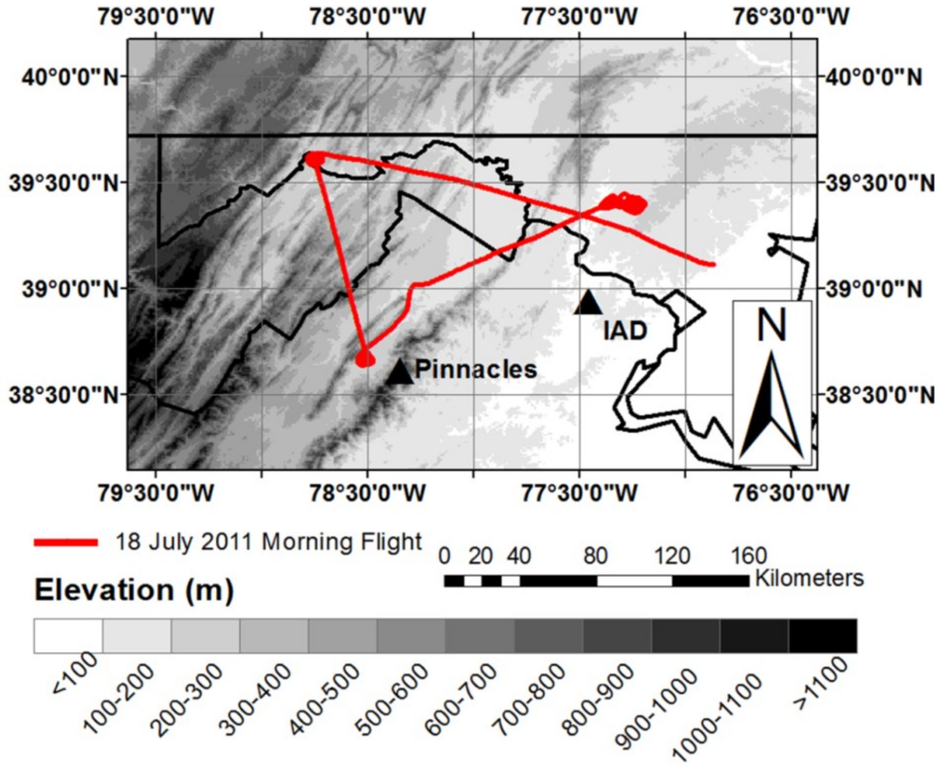

Figure 6.2: RAMMPP flight from 0717-1028 LST on 18 July 2011 (red line) relative to Pinnacles and the Page and Shenandoah Valleys. The nearest sounding station, Dulles Airport (IAD), is indicated with a black triangle. Shading shows the elevation msl. Topography data are from the US Geological Survey and have a 10 m resolution.

vegetation information are obtained from a US Geological Survey data set with a 30 arc-second (approximately 1 km) spatial resolution. Boundary conditions for the WRF simulations are obtained from the North American Regional Reanalysis (NARR), which has 29 vertical levels and a 32 km spatial resolution over North America (Mesinger et al., 2006).

The WRF simulations have 56 vertical levels; the lowest 5 sigma levels are 0.997, 0.994, 0.991, 0.988, and 0.985 and correspond to heights of approximately 23.7, 47.3, 71.0, 94.8, and 118.7 m agl, respectively. We apply the Dudhia shortwave radiation scheme (Dudhia, 1989), the rapid radiative transport model longwave scheme (Mlawer et al., 1997), the WRF 3-class simple ice microphysics scheme (Hong et al., 2004), and Pleim-Xiu land surface model (Xiu and Pleim, 2001), to all four WRF domains, and apply the Kain-Fritsch cumulus scheme (Kain and Fritsch, 1990) to the three outermost domains. We use the Yonsei University (YSU) PBL scheme (Hong et al., 2006) in all four domains. In the YSU scheme, z_i is calculated by computing the bulk Richardson number and determining the height at which a critical value, R_c, is exceeded (Hong et al., 2006; Xie et al., 2013). We set R_c to 0.25 following previous studies (Vogelezang and Holtslag, 1996; Seidel et al., 2012).

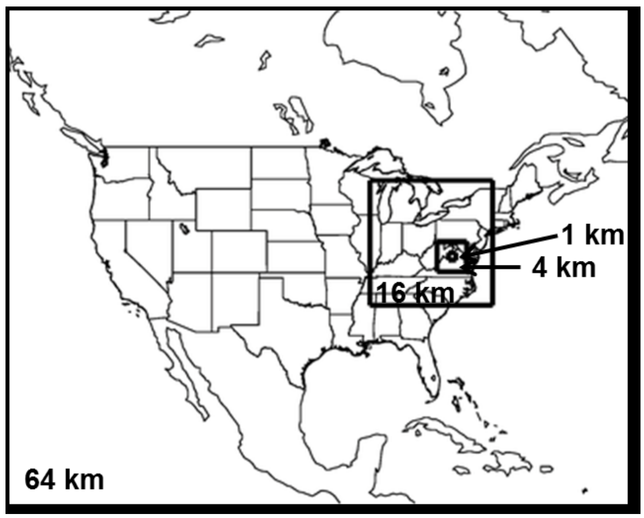

Figure 6.3: WRF 64 km (domain 1), 16 km (domain 2), 4 km (domain 3), and 1 km (domain 4) domains.

We perform additional sets of simulations in which we remove the regional topography. The meteorological conditions from these simulations are used as inputs into the LPDM, which we use to determine how the particle number concentration (PNC) and the concentration footprint from Pinnacles compares with tall towers. To make this comparison, we replace all the terrain within domains 3 and 4 with a flat surface. This surface has an elevation of 200 m, which is the mean elevation of the Page Valley west of Pinnacles and the Virginia Piedmont east of Pinnacles. Although we modify the terrain, we make no modifications to the vegetation type, soil type, or land use category in the areas where we modify terrain elevation (Alcott and Steenburgh, 2013). Once we have modified the terrain but before initializing the WRF model, we run the WRF preprocessing system to interpolate the input NARR meteorological fields to the modified terrain.

6.2.6. FLEXPART

The WRF wind fields described in Section 6.2.5 are used as inputs into FLEXPART, an LPDM that determines trajectories of individual air parcels (e.g. Stohl et al., 2005; Brioude et al., 2013). FLEXPART is one example of an LPDM that has been used in many applications describing pollutant transport and dispersion on different spatiotemporal scales (e.g. Cooper et al., 2004; Tuzson et al., 2011; Brioude et al., 2013). In the present study, we use FLEXPART to determine how mountaintops like Pinnacles compare with tall tower measurements. To investigate how the diurnal trace variability compares, we release particles upwind of the site during the three days of interest, both in the simulations with topography and the simulations from which the topography was removed. Particles are emitted continuously at a rate of 10000 particles per hour beginning at sunrise (0700 LST) and continuing through sunset (1900 LST) from a diagonal box in the center of the Page Valley (Figure 6.4). Particles are released from a height 2 m agl to simulate near-surface emissions sources. Sensitivity tests in which the particle release height is changed to 20 m agl to simulate emissions from taller point sources, as well as sensitivity tests in which the number of particles released is changed, indicate that our findings are not significantly affected by our choice of release height or by the number of particles released in the simulations.

To determine how concentration footprints from mountaintops like Pinnacles compare with tall towers, we perform backward simulations with FLEXPART. Following previous studies (e.g. Henne et al., 2010; Gheusi et al., 2011), we release particles from a 1 km x 1 km box at Pinnacles. In the simulations in which topography is included, particles are released between the surface and 100 m agl. In the simulations from which the topography is removed, particles are released between 300 and 400 m agl to correspond with the typical height from which trace gases measured at the tops of tall towers in flat terrain are assimilated in inverse carbon transport models (e.g. Bakwin and Tans, 1995; Bakwin et al., 1998). Particles are followed backward 24 h to determine when the air came into contact with near-surface emissions in both sets of simulations (i.e. those with topography included and those from which the topography was removed). Following previous studies (e.g. Tuzson et al., 2011), we define near-surface contact by determining the number of particles between 0 and 100 m agl.

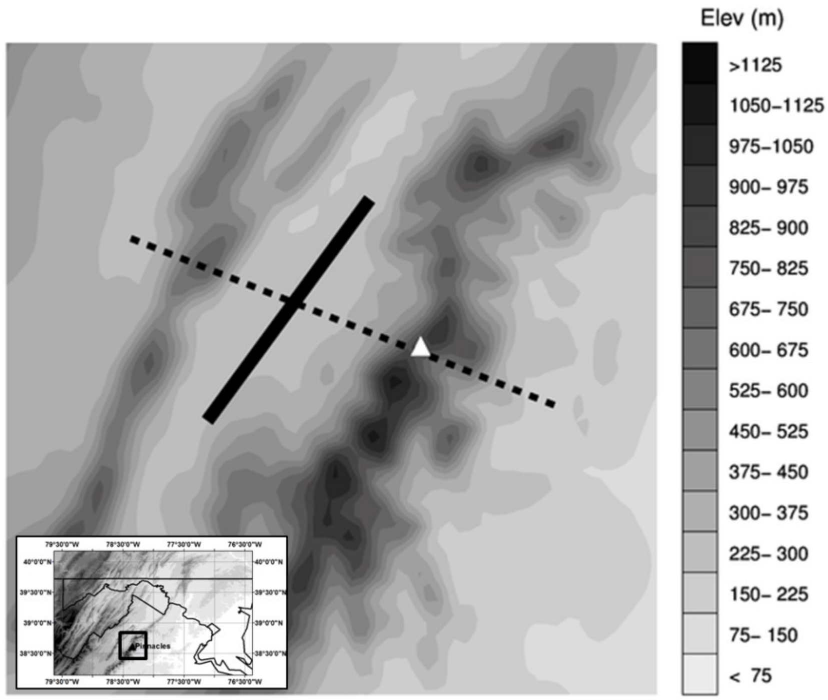

Figure 6.4: Map of the innermost WRF domain (domain 4) with the release location of the particles (black rectangle) and the location of the cross-section (dotted black line) shown in Figures 6.12-6.14 overlaid on the 1 km model topography (shading). The white triangle indicates the location of Pinnacles. The inset image in the bottom left shows the location of the innermost WRF domain in northwestern Virginia and is denoted by a black square.

6.3. Results and discussion

6.3.1. Overview of meteorological conditions and trace gas variability

6.3.1.1. 18 July 2011

Synoptic analyses indicate that the period around 18 July 2011 was characterized by weak near-surface anti-cyclonic flow over the Mid-Atlantic region. Winds at Pinnacles were light (<4 m s^{-1}) and from the northwest (Figure 6.5). Consistent with the mean diurnal CO cycle shown in previous work (Lee et al., 2015), CO mixing ratios are lowest around 0600 LST but show an increase during the morning. Following a CO and CO_2 maximum around 1000 LST due to the upslope transport of valley PBL air, both CO and CO_2 mixing ratios decrease during the late morning and early afternoon. The presence of valley PBL air at the site is also apparent from the RAMMPP aircraft observations, as linear interpolation of the CO mixing ratios from the aircraft profiles over the Page Valley to 17 m agl at Pinnacles indicate that the Pinnacles CO mixing ratios and RAMMPP CO mixing ratios agree to ±2% (Figure 6.6). Similarly good agreement is found when comparing the Pinnacles CO mixing ratios with CO measured in the RAMMPP profiles over Frederick, MD.

6.3.1.2. 9 April 2009

Consistent with 18 July 2011, there were few clouds at Pinnacles on 9 April 2009, and winds at the mountaintop were from the northwest throughout much of the day (Figure 6.7). Also consistent with 18 July is that CO mixing ratios increase during the late morning, which coincides with an increase in CO_2. Following the short-lived CO and CO_2 maximum, both CO and CO_2 mixing ratios decrease during the afternoon. O_3 mixing ratios at Big Meadows are about 35 ppb larger than O_3 mixing ratios at Luray during the nighttime. During the daytime, the O_3 differences are <2 ppb and are smallest between 1100 and 1800 LST.

6.3.1.3. 23 October 2010

Synoptic analyses and as well as the mountaintop observations indicate that 23 October had similar characteristics to 18 July and 9 April. On 23 October, there was near-surface anti-cyclonic flow over the region, clear skies, and wind speeds of 1-2 m s^{-1} during the daytime. Winds were from the northwest throughout much of the day, but became west-southwesterly around 1700 LST as the near-surface anti-cyclone moved eastward. O_3 mixing ratios at Big Meadows were 20-30 ppb higher during the nighttime; differences were <5 ppb between 1100 and 1600 LST. Unlike 9 April, CO mixing ratios increased during the daytime from a minimum of 109.9 ppb at 0800 LST to 138.7 ppb at 2130 LST (Figure 6.8).

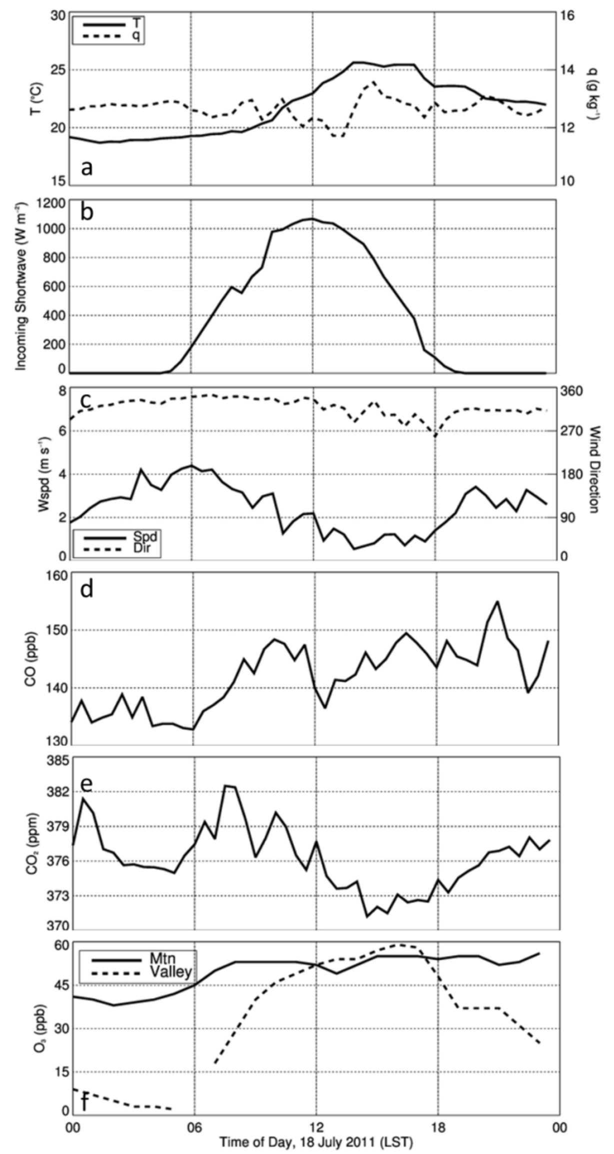

Figure 6.5: Temperature (black line) and specific humidity (dashed line) (a); incoming shortwave radiation (b); wind speed (black line) and wind direction (dashed line) (c); CO mixing ratio (d); CO_2 mixing ratio (e); and O_3 at the mountaintop (Big Meadows) (black line) and valley (Luray Caverns Airport) (dashed line) (f) on 18 July 2011. All variables in panels (a) through (e) are measured 17 m agl at Pinnacles.

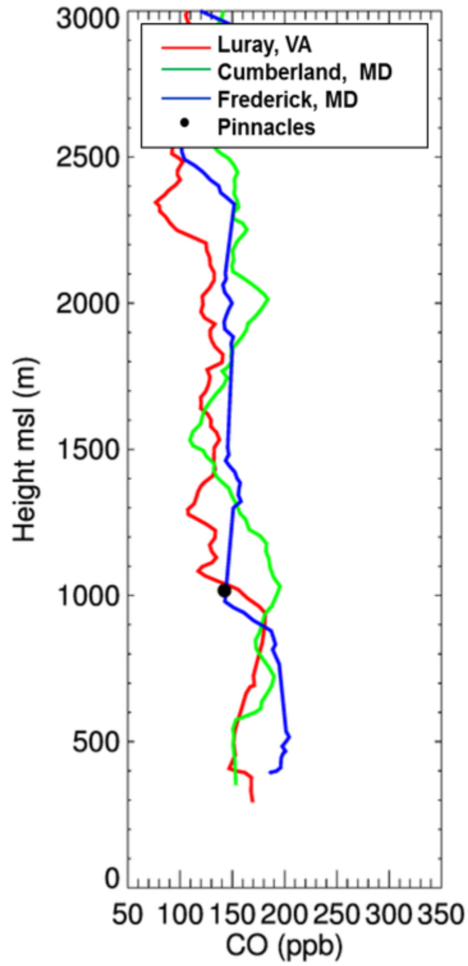

Figure 6.6: Vertical profile of CO mixing ratio (c) at Luray Caverns Airport (red), Cumberland, MD (green), and Frederick, MD (blue) between 0700 and 1000 LST on 18 July 2011. Black dots represent the corresponding Pinnacles measurements 17 m agl.

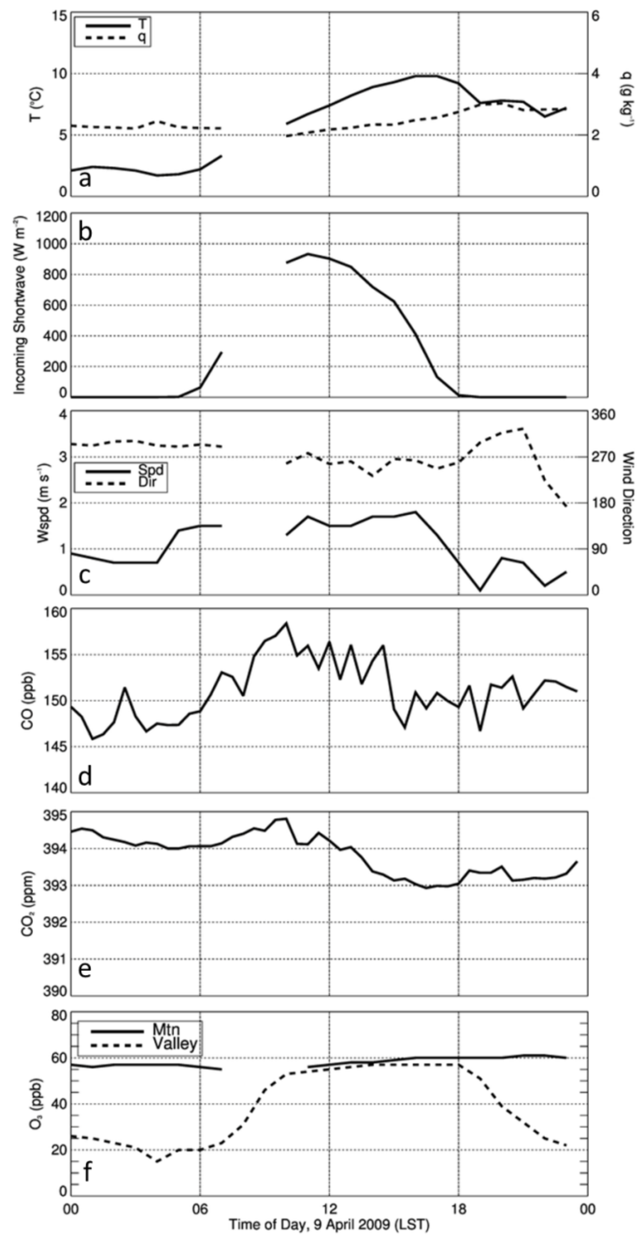

Figure 6.7: Temperature (black line) and specific humidity (dashed line) (a); incoming shortwave radiation (b); wind speed (black line) and wind direction (dashed line) (c); CO mixing ratio (d); CO_2 mixing ratio (e); and O_3 at the mountaintop (Big Meadows) (black line) and valley (Luray Caverns Airport) (dashed line) (f) on 9 April 2009. All variables in panels (a) through (c) are measured 10 m agl at Big Meadows because of missing meteorological data at Pinnacles. The CO and CO_2 mixing ratios are measured 17 m agl at Pinnacles. Note the presence of a data gap between 0800 and 1000 LST in the Big Meadows meteorological and O_3 data.

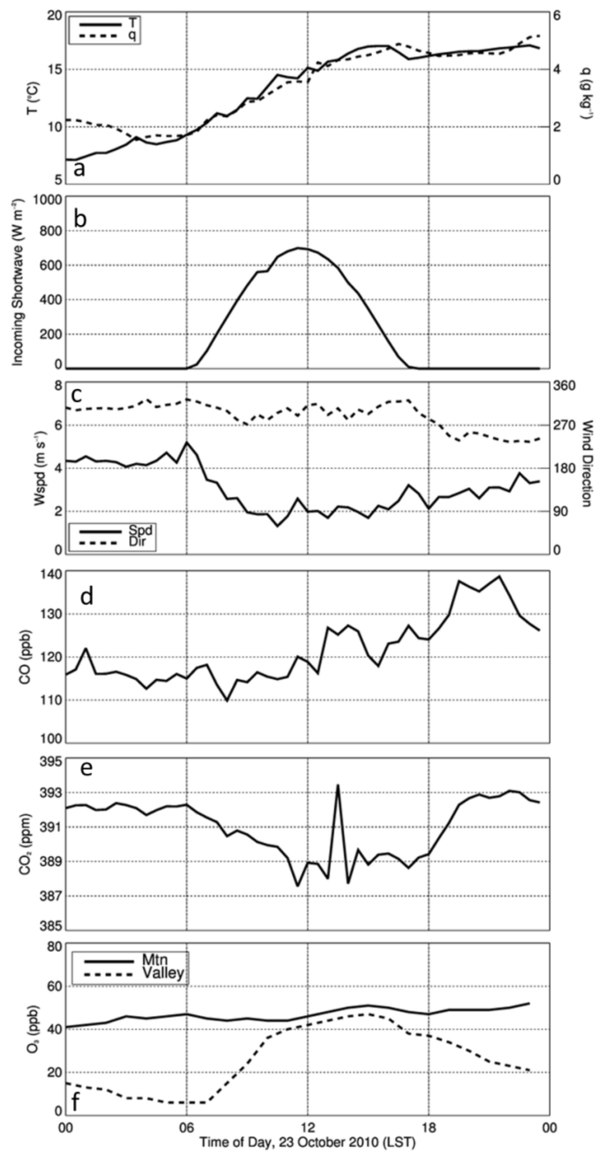

Figure 6.8: Same as Figure 6.5 but for 23 October 2010.

6.3.2. Model evaluation

6.3.2.1. WRF evaluation

We use observations from Pinnacles and surrounding locations to evaluate the model performance on the three days of interest. Comparisons between the model results and the surface observations indicate that afternoon temperatures at both Pinnacles and Big Meadows agree with model-derived temperatures to within ±1°C and indicate that the model simulates westerly flows on 18 July (Figure 6.9). Comparison between the potential temperatures obtained from the aircraft profiles over the Page Valley on 18 July and WRF simulations further show good agreement (Figure 6.10). We find similar agreement when evaluating the model performance using surface observations from the ridgetop and valley on 9 April and 23 October, as well as using the rawinsonde observations that were available from the Page Valley on these days. Details of the model evaluation on 9 April and 23 October appear in Chapter 4.

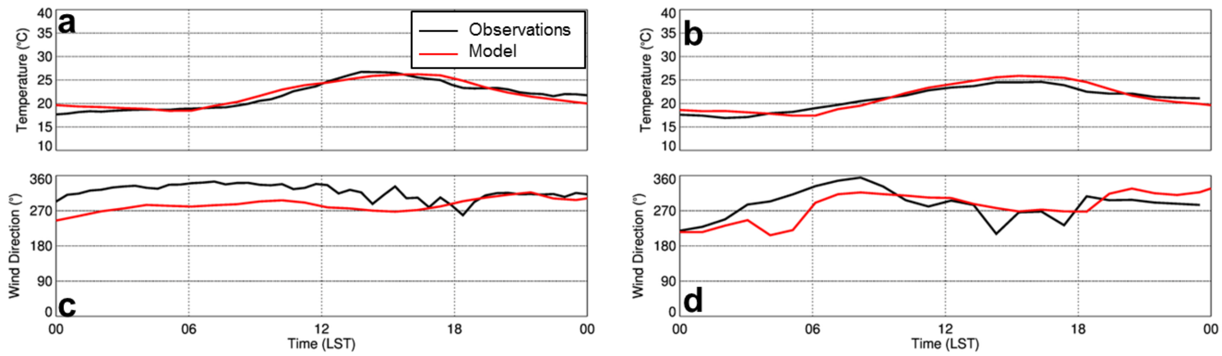

Figure 6.9: WRF simulation evaluation of temperature for the 1 km domain for 18 July 2011 at Pinnacles (a) and Big Meadows (b). Same for (c) and (d) but for wind direction. Black line shows the observations; red line shows the output from WRF.

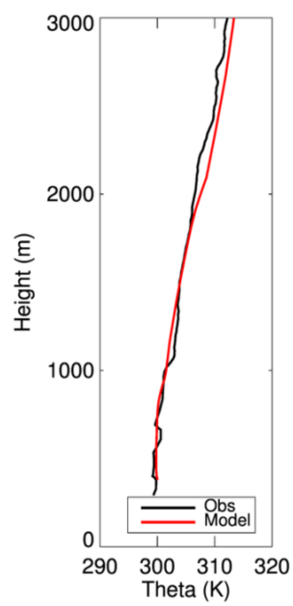

Figure 6.10: Potential temperature over the Page Valley at 0900 LST 18 July 2011 from the 1 km WRF domain (red line) and observed from RAMMPP (black line).

6.3.2.2. LPDM evaluation

To evaluate the LPDM simulations, we use CO mixing ratios measured at Pinnacles. Because of its tropospheric lifetime of weeks to months, CO is assumed to behave as a passive tracer (e.g. Dickerson et al., 1987; Staudt et al., 2001). Thus, we compare the diurnal CO variability with the diurnal variability of PNC at the mountaintop for particles released from the valley in the simulations (c.f. Figure 6.4). Sensitivity tests indicate that our results are not significantly affected by our choice of release location within the valley. Furthermore, in an additional set of simulations (not shown), particles released from dominant emissions sources east of the Blue Ridge Mountains (i.e. the Washington, DC and Baltimore, MD megalopolis) (c.f. Figure 6.1), are transported away from Pinnacles by the westerly flows. Our findings indicate that the LPDM simulations capture the daytime increase in CO mixing ratio between 0600 and 0900 LST on 18 July, the CO decrease during the late morning, and secondary afternoon increase (Figure 6.11). Evaluations using CO mixing ratios measured on 9 April and 23 October indicate that the LPDM simulations generally capture the observed daytime trends in CO mixing ratio, but the PNC peak occurs earlier than the CO peak. The reasonably good agreement between the LPDM diurnal variability and diurnal CO variability provides us with confidence that the LPDM can help investigate the extent to which mountaintop trace gas measurements compare with tall tower trace gas measurements.

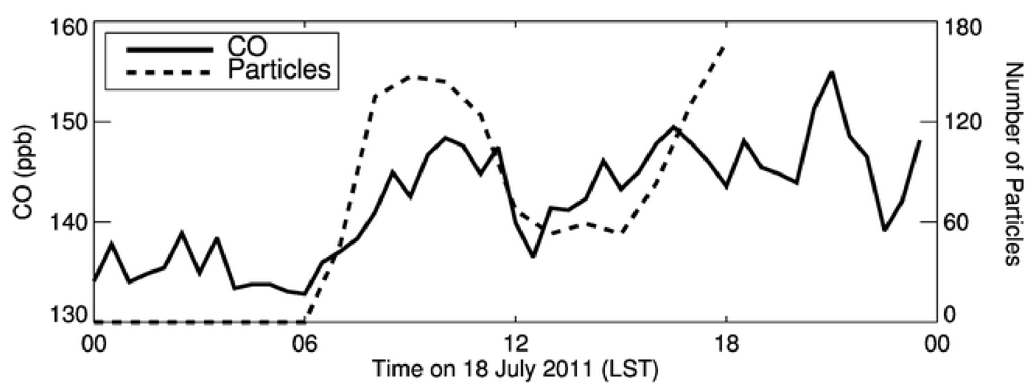

Figure 6.11: CO mixing ratio at Pinnacles as a function of time of day on 18 July 2011 (solid line) and number of particles arriving at Pinnacles in the LPDM simulation (dashed line).

6.3.3. LPDM forward simulations

6.3.3.1 . 18 July 2011

LPDM forward simulations indicate upslope transport and subsequent PBL dilution on 18 July. Particles emitted from the valley at 0700 LST are confined to within the valley PBL 1 h after their release and are transported northeastward along the valley axis due to down-valley, southwesterly flows occurring over the center of the valley (Figure 6.12). During the morning, surface heating results in the winds shifting over the valley from down-valley flows to up-valley flows. With this wind shift over the valley, pollutants emitted over the valley are transported upslope to Pinnacles, with the majority of particles reaching the site around 0900 LST. Whereas many of the particles emitted remain within the PBL, some particles are transported a few hundred meters above the PBL due to mountain venting and advective venting, which have been cited in previous studies as causes for pollutants being transported out of the PBL (e.g. De Wekker et al., 2004; Henne et al., 2004). As the PBL continues growing during the daytime, the concentration of particles sampled at the mountaintop decreases due to dilution and entrainment of less polluted FA air. Simulations indicate that z_i reaches a maximum height of 1800 m msl over the region. The z_i is about 200 m higher over the Page Valley than in locations east of the Blue Ridge Mountains in the Virginia Piedmont, the latter of which is corroborated by rawinsonde observations from Dulles Airport (not shown). During the afternoon, z_i decreases over the ridgetop by a couple hundred meters, favoring the accumulation of pollutants and resulting in the afternoon CO increase.

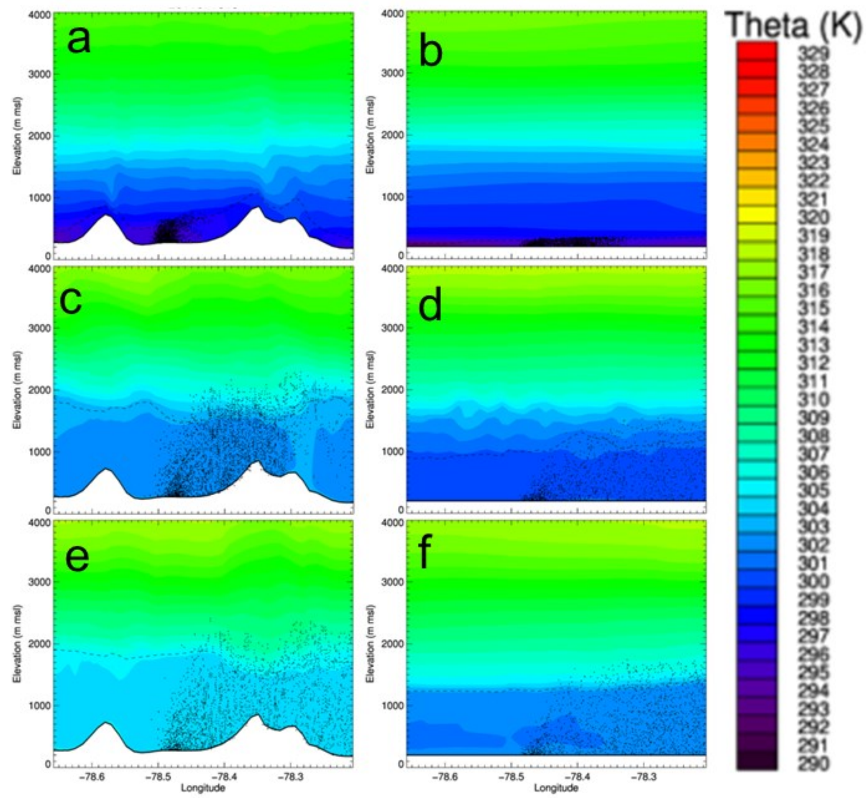

Figure 6.12: Cross-section through the Shenandoah and Page Valleys and Pinnacles (c.f. Figure 6.4) for the LPDM forward simulation initialized at 0700 LST 18 July 2011 at 1 h into the simulation (0800 LST) for the simulation with topography (a) and the simulation with the topography removed (b). Same for panels (c) and (d) and (e) and (f), but for 4 h into the simulation (1100 LST) and for 7 h into the simulation (1400 LST), respectively. The topography cross-section is shown by a black line; the dashed line shows the model-derived z_i, computed using the Bulk Richardson number approach and defined as the height at which R_c exceeds 0.25. Potential temperature is obtained from the 1 km WRF simulation and is shaded every 1 K.

To determine the extent to which the diurnal variability in PNC, and thus other passive tracers such as CO, at mountaintops like Pinnacles compares with tall towers, we perform the same simulations as above but with the removal of the model topography as discussed in Section 6.2.5. In these simulations, we release particles 2 m agl along a diagonal axis to simulate near-surface emissions sources so that we are consistent with the simulations in which the topography was not removed. The simulations without topography indicate westerly flows over the region at 0700 LST when the particles are released. Particles released from the same location as the valley are transported easterly. Unlike what was found for the simulations with topography, the majority of the particles remain within the PBL in the simulations in which the topography was removed. The times this does not occur (e.g. Figure 6.12d) occur when there is poorly-defined elevated inversion.

6.3.3.2. 9 April 2009

Much of the same conclusions regarding transport and dispersion are obtained using 9 April as a case study (Figure 6.13). Early in the morning, particles released from the valley in the LPDM simulations in which topography is included remain within the valley PBL during the first 1-2 h of the simulation (0700-0900 LST) but are transported to the mountaintop during the late morning due to convective mixing and slope flows. Unlike 18 July, however, on 9 April the valley PBL reaches a maximum height of about 3000 m msl due to afternoon sensible heat fluxes of 300-400 W m^{-2} over the region on this day (c.f. Chapter 4). The LPDM simulations without topography included further illustrate the impacts of PBL dilution on the particle number distribution. The main difference between this LPDM simulation and the 18 July LPDM simulation from which the topography removed is that z_i on 9 April is about 1000 m higher than z_i on 18 July.

6.3.3.3. 23 October 2010

Of the three days, 23 October had the smallest PBL. Simulations indicate that z_i reached a maximum height of about 1000 m over the Page Valley, which agrees with the observed z_i on this day (c.f. Chapter 4). Although the PBL stays near the ridgetop height, particles are transported a few hundred meters above the PBL to heights of 1500 msl during the afternoon (Figure 6.14). In contrast, the simulations without the topography included indicate that particles released from the surface are transported to about 1000 m msl.

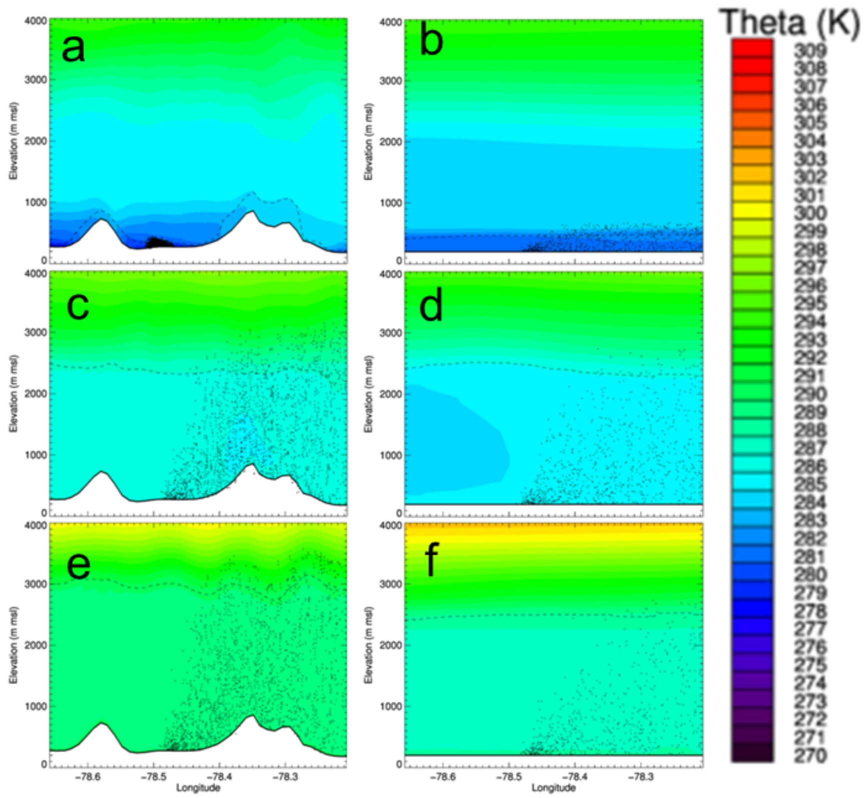

Figure 6.13: Same as Figure 6.12 but for 9 April 2009.

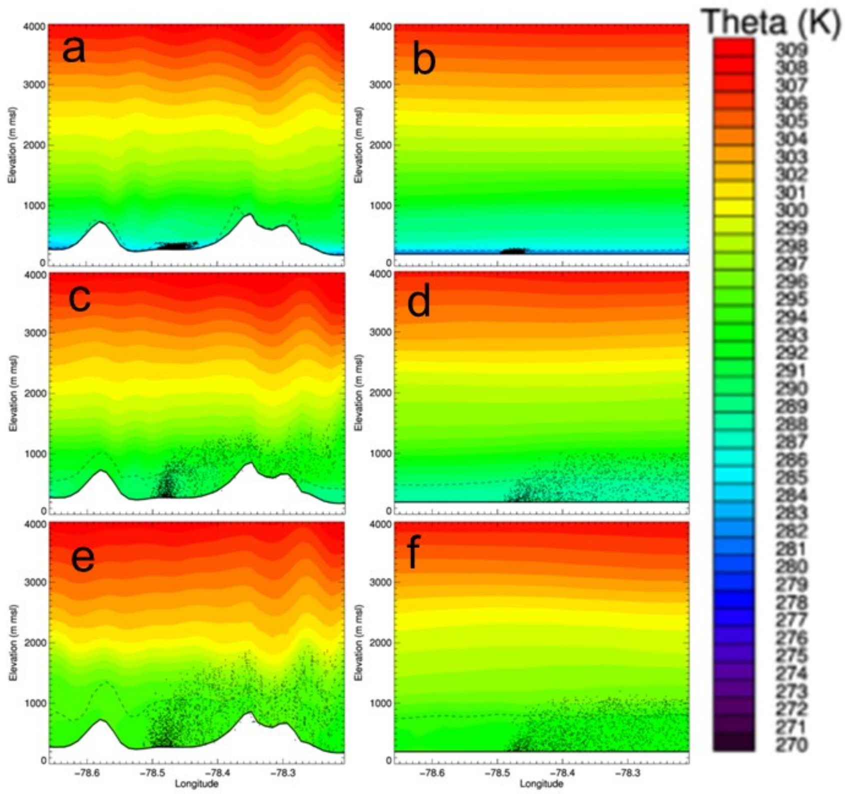

Figure 6.14: Same as Figure 6.12 but for 23 October 2010.

6.3.4. Diurnal variability in particle number concentration

From the previous sections, we infer that the main differences among the three days is the maximum afternoon z_i. The effects of these differences on the PNC and the CO mixing ratios measured at the mountaintop are determined by computing the number of particles arriving at Pinnacles as a function of time of day. In the simulations in which topography is included, we determine the number of particles arriving in a 1 km x 1 km box at Pinnacles between 0 and 100 m agl. To compare Pinnacles with tall towers, in the simulations in which the regional topography is removed, we determine the number of particles arriving in a 1 km x 1 km box in the same location as Pinnacles, but between 300 and 400 m agl (i.e. the maximum height of tall towers installed over flat terrain).

All three simulations indicate a mid-morning PNC maximum that varies as a function of the afternoon maximum z_i (Figure 6.15a). The mid-morning PNC increase has the smallest magnitude and persists for the shortest amount of time on 9 April, but persists longer and is about 3 times larger on 23 October than on 18 July and 9 April. Following the mid-morning maximum, the PNC decreases and is mostly constant between 1100 and 1700 LST on 9 April due to PBL dilution overwhelming upslope transport from the valley. There is more variability in PNC between 1100 and 1700 LST on 18 July and 23 October than on 9 April because the valley PBL has a larger influence on the mountaintop PNC due to the lower z_i on these two days. Valley PBL influence at the mountaintop is quantified by computing the total number of particles emitted from the valley that arrive at the mountaintop during the daytime (i.e. between 0700 and 1700 LST). As expected, the total number of particles sampled at the mountaintop in the LPDM simulation decreases with increasing z_i and is 1896, 1210, and 711 on 23 October, 18 July, and 9 April, respectively.

In the simulations from which the regional topography is removed, the magnitude of the diurnal changes is smaller than in the simulations in which topography is included. There is a PNC maximum at 0700 LST on 9 April, 0900 LST on 18 July, and 1000 LST on 23 October. This short-lived PNC maximum is consistent with observations in previous studies that show a mid-morning trace gas maximum at the tops of tall towers over flat terrain (e.g. Yi et al., 2001; Pal et al., 2015). Following the mid-morning PNC maxima in the LPDM simulations without topography, PNC generally decreases. As a result, the difference in PNC between the simulations with topography and the simulations without topography becomes smallest between 1100 and 1500 LST (Figure 6.15b). The smallest differences between the simulations occur on 9 April when z_i is deepest, suggesting that in these situations measurements from low mountaintops are most similar to measurements from tall towers. The similarities between low mountaintops and tall towers are further investigated by comparing the afternoon concentration footprints in the next section.

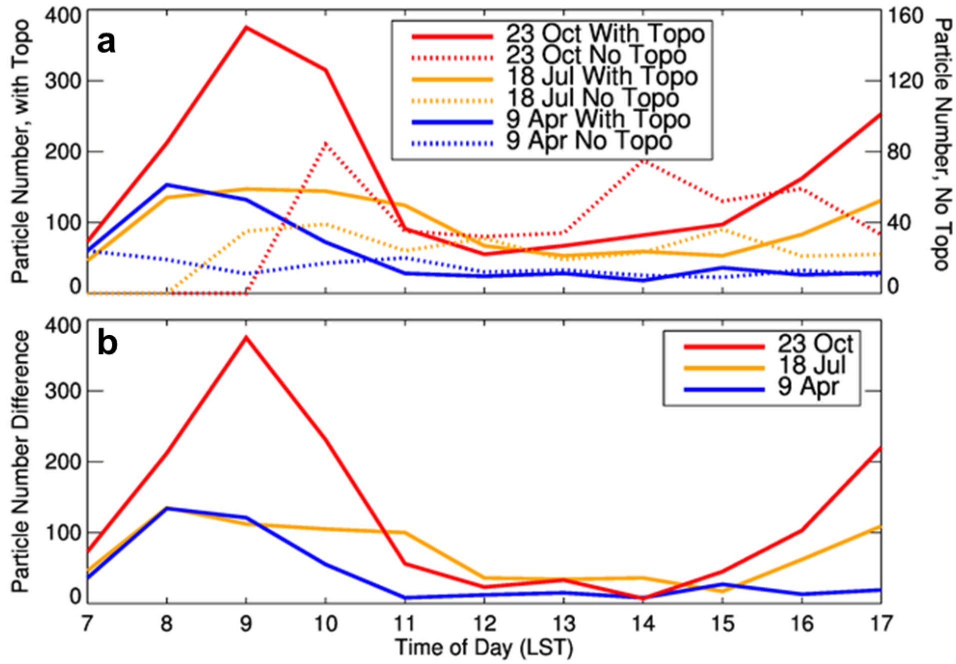

Figure 6.15: Diurnal variability in the number of particles arriving at Pinnacles. In panel (a), the solid (dotted) red line shows the LPDM simulation for 23 October 2010 with (without) topography included; solid (dotted) orange line shows the LPDM simulation for 18 July 2011 with (without) topography included; solid (dotted) blue line shows the LPDM simulation for 9 April 2009 with (without) topography included. Panel (b) shows the difference in particle number between the LPDM simulation with topography and the LPDM simulation without topography for 23 October 2010 (red line), 18 July 2011 (orange line), and 9 April 2009 (blue line).

6.3.5. Concentration footprints

We determine the concentration footprint by continuously releasing particles from Pinnacles between 1200 and 1600 LST, which correspond with the times during which trace gas measurements from tall towers are assimilated into inverse carbon transport models (e.g. Peters et al., 2007), on each of the three days. Concentration footprints indicate that near-surface emissions near Pinnacles have the largest influence on Pinnacles' trace gas measurements on the afternoons of 23 October and 18 July (Figure 6.16). For example, over parts of western Virginia and West Virginia, >50% of the particles in these locations passed below 100 m agl prior to arriving at Pinnacles. On 9

April, nearby emissions sources have a smaller influence on Pinnacles' trace gas measurements. On this afternoon, the concentration footprint is larger than on 23 October or 18 July, and the largest near-surface influences extend from Virginia into northern Illinois and southern Wisconsin. The LPDM simulations on 23 October and 18 July without topography also indicate greater contributions of near-surface emissions from locations near Pinnacles than the 9 April simulations without topography. The main differences, though, are in the source regions identified. On the afternoon of 18 July, the main source regions identified are shifted further north in the simulations without topography; on 9 April the source regions identified are shifted further south.

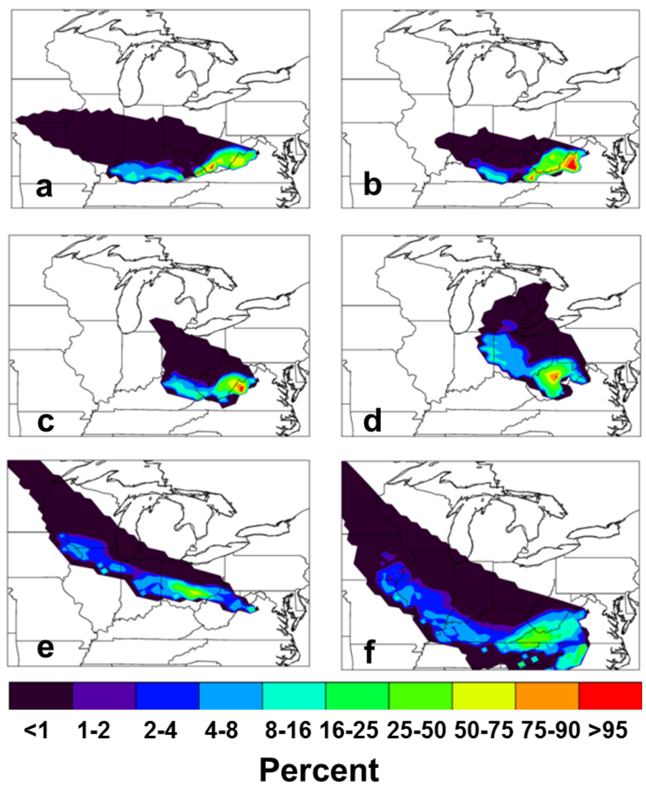

Figure 6.16: Concentration footprint, shown as a percent of the total number of particles at a given location, of particles 0-100 m agl prior to arriving at Pinnacles between 1200 and 1600 on 23 October 2010 in the simulation with topography (a) and the simulation without topography (b). Panels (c) and (e) show the same as panel (a) but for 18 July 2010 and 9 April 2009, respectively. Panels (d) and (f) show the same as panel (b) but for 18 July 2010 and 9 April 2009, respectively.

6.4. Conclusions and outlook

The goal of the present study was to investigate the hypothesis that low mountaintops behave like tall towers on days when the valley z_i exceeds the ridgetop height. To test this hypothesis, we focused on three case studies with different z_i relative to the ridgetop. We used data from Pinnacles, a mountaintop observation site in the Virginia Blue Ridge Mountains, trace gas and meteorological observations from the surrounding region, and numerical simulations with WRF and an LPDM. We found that pollutants emitted over valleys upwind of Pinnacles are transported to the mountaintop via convective mixing and slope flows during the mid-late morning. The presence of valley PBL air at the mountaintop during the daytime occurs independent of z_i relative to the ridgetop height and is evident by a morning CO increase (c.f. Figure 6.5d, Figure 6.7d, Figure 6.8d), negligible differences in O_3 mixing ratio between the mountaintop and valley during the afternoon (c.f. Figure 6.5f, Figure 6.7f, Figure 6.8f), and an increase in PNC at the mountaintop in the LPDM simulations (c.f. Figure 6.15). Due to PBL dilution, the effects of valley PBL air on the mountaintop trace gas mixing ratios are reduced on days with the largest z_i. As a result, comparisons between the LPDM simulations with topography and the LPDM simulations without topography indicate that the diurnal variability in PNC was most similar on 9 April when z_i well exceeded the ridgetop height. Additionally, the concentration footprints of the afternoon measurements are larger on the days with the largest z_i.

The present study, in addition to previous studies in the region (e.g. Lee et al., 2015), provides further evidence that afternoon trace gas measurements from low mountaintops like Pinnacles made when the valley PBL exceeds the ridgetop height are most equivalent to tall tower measurements in the mixed layer. Given the high costs of installing and maintaining monitoring equipment at tall tower monitoring sites (Andrews et al., 2014), low mountaintops may provide a cheaper alternative to monitoring at tall tower sites if insufficient resources exist. To build upon this work, additional analyses can be conducted to further investigate how mountaintops compare with tall towers. As this work focused on three case studies with similar meteorological conditions but different z_i, analyses of additional case studies in conjunction with LPDM simulations can be used to investigate how different synoptic conditions affect the comparison between mountaintop measurements and tall tower measurements. Finally, this work illustrated the potential use of LPDM simulations for investigating the diurnal trace gas variability over this region and the degree to which daytime measurements are regionally-representative. Therefore, additional LPDM simulations could be performed to help quantify the extent to which nighttime measurements from the site are representative of background, FA mixing ratios.

6.5. Acknowledgments

This research and maintenance of the Pinnacles research station was partly funded by an MOU between the NOAA ESRL Global Monitoring Division and the University of Virginia and by NSF-CAREER Grant ATM-1151445. We thank staff from Shenandoah National Park, especially Elizabeth Garcia, Jim Schaberl, and Alan Williams, and students from the Environmental Sciences Department at the University of Virginia for helping to maintain data collection at Pinnacles.

CHAPTER 7

CONCLUSIONS AND FUTURE WORK

7.1. Summary of major findings

The goal of this dissertation was to improve scientific understanding of the dominant meteorological drivers affecting the trace gas variability at low mountaintops. To fulfill this goal, this dissertation presented the first use of long-term trace gas and meteorological measurements from Pinnacles, a mountaintop monitoring site in the Appalachian Mountains. The major findings and implications from each chapter are summarized below. Following this summary, the implications of the dissertation as a whole to the broader scientific community are discussed, as are future research directions that build upon this dissertation's findings.

- In Chapter 2, it was found that diurnal changes in CO_2 mixing ratios are largest on fair weather days in the growing season due to photosynthetic uptake and during cold fronts passages outside the growing season. The magnitude and longevity of the frontal CO_2 increase depends on whether the front approaches the region from the west or from the north. There is a short-lived increase in CO_2, as well as CO, mixing ratios during eastward-moving cold fronts that occurs on timescales <3 h. There is also an increase in CO and CO_2 during southward-moving cold fronts. In contrast with eastward-moving cold fronts, southward-moving cold fronts are followed by a period of elevated CO and CO_2 mixing ratios that persists 24-48 h postfrontal due to the advection of polluted air masses from the northeastern US. Based on the findings in this chapter, postfrontal trace gas mixing ratios can be used to reduce flux estimate uncertainties in the source regions of postfrontal $CO_{2,}$ i.e. the Upper Midwest and Northeast US in the cases of eastward-moving and southward-moving fronts, respectively.
- In Chapter 3, the dominant drivers of the CO variability were investigated. The largest diurnal changes in CO mixing ratio occur in the presence of synoptic

disturbances. Under fair weather conditions, local- to regional-scale transport processes are the most important drivers of the diurnal CO variability. Fair weather days with a wind shift from the northwest to the south, which arises due to thermally-driven flows, are characterized by an afternoon CO increase, and the diurnal CO variability resembles the variability observed at mountaintops influenced by the vertical transport of polluted air from adjacent valleys. On fair weather days with steady northwesterly winds, PBL dilution causes a daytime CO decrease, resembling the variability observed atop tall towers in flat terrain.

- To quantify the impacts of PBL dilution on the trace gas measurements, knowledge of afternoon z_i over the Page Valley near Pinnacles were needed. Thus, in Chapter 4, a technique was developed to obtain estimates of the quasi-stationary afternoon z_i from the rawinsonde observations made at the nearest sounding station. Once afternoon z_i were obtained from these soundings, these afternoon z_i were used, along with reanalysis products and numerical modeling, to determine z_i over the Page Valley. Afternoon z_i obtained from the nearest sounding station were 200-400 m lower than z_i estimates over the Page Valley. Thus, an offset was applied to better approximate Page Valley z_i using the nearest sounding station as a proxy.
- The z_i estimates from Chapter 4 were used to investigate the relationship between valley z_i and mountaintop trace gas variability in Chapter 5. It was found that mountaintop CO mixing ratios increase during the daytime on days when the valley z_i is below the ridgetop height because of upslope transport of polluted valley PBL air. Upslope transport of polluted air in these cases prevents daytime trace gas measurements from being used in applications requiring regionally-representative values. However, on days when the valley z_i exceeds the ridgetop height, mountaintop CO mixing ratios decrease due to vertical mixing and dilution. Thus, the measurements in these situations can be used in applications requiring regionally-representative values.
- In Chapter 6, numerical simulations were conducted with an LPDM to investigate how mountaintop trace gas measurements from low mountaintops can best be used in applications requiring regionally-representative measurements. On days

when z_i exceeds the ridgetop height, afternoon trace gas measurements from low mountaintops are most similar to trace gas measurements from tall towers based on comparisons between LPDM simulations with topography and LPDM simulations from which the regional topography was removed. These simulations provide additional supporting evidence that, on days with constant winds and on which z_i exceeds the ridgetop height, afternoon trace gas mixing ratios from low mountaintops can be used like trace gas mixing ratios from tall towers in applications requiring regionally-representative measurements.

7.2. Implications

This dissertation generates new knowledge that benefits different scientific communities. Most notably, this dissertation provides the groundwork for better using trace gas measurements from monitoring stations installed at low mountaintops in applications requiring background and regionally-representative measurements, e.g. inverse carbon transport models and air chemistry models. The knowledge gained from this dissertation is used to provide recommendations on the factors that need to be considered when installing trace gas measurements at other mountaintop sites. These factors are addressed in Section 7.3. In addition, this dissertation provides techniques to improve estimates of daytime z_i and for using CO and CO_2 as tracers for frontal passages. All of these implications are discussed in more detail in the following sections.

7.2.1. Utility of trace gas measurements from low mountaintops

Findings from this dissertation indicate that, consistent with work from other mountaintop monitoring sites (e.g. Forrer et al., 2000; Gao et al., 2005; Balzani Lööv et al., 2008; Henne et al., 2008b), trace gas measurements from low mountaintops like Pinnacles made during the late night and predawn hours are most representative of background values. Thus, nighttime trace gas mixing ratios should continue to be assimilated into CarbonTracker. Based on the timing of the nighttime CO minimum (c.f. Chapter 3) and timing of the largest O_3 differences between the mountaintop and valley (c.f. Chapter 5; Chapter 6), though, it is suggested that measurements made later at night, e.g. between 0200 and 0600 LST, should be assimilated into CarbonTracker, rather than measurements between 0000 and 0400 LST.

However, many of the implications of this dissertation involve the use of daytime trace gas measurements. Most notably, this dissertation is the first study to identify situations when mountaintops like Pinnacles sample well-mixed daytime PBL air during the daytime, enabling trace gas measurements made during select situations to be used like measurements from the tops of tall towers in flat terrain in applications requiring regionally-representative measurements. The degree to which the measurements are representative of regional trace gas mixing ratios, though, depends on the presence or absence of wind shifts (c.f. Chapter 2, Chapter 3) and on z_i relative to the mountaintop (c.f. Chapter 5). Unlike what has been reported at tall mountaintops (e.g. Baltsensperger et al., 1997; Lugauer et al., 1998), measurements made when z_i is below the mountaintop are contaminated by nearby trace gas sources in the upwind adjacent valleys and thus the measurements are not regionally-representative. However, on days when there are no wind shifts and on which z_i exceeds the mountaintop, the mountaintop trace gas variability is most similar to measurements from tall towers. Consequently, afternoon measurements made under these conditions can be used in applications requiring regionally-representative trace gas measurements. As a result, measurements from Pinnacles made under these conditions can be used in inverse carbon transport models like CarbonTracker and can help reduce uncertainties present in regional- to continental-scale carbon budgets (e.g. Peters et al., 2007).

7.2.2. Estimates of afternoon z_i from rawinsonde observations

Besides having implications for using mountaintop trace gas measurements in applications requiring regionally-representative measurements, this dissertation presented a new technique to estimate afternoon z_i from rawinsonde observations. In locations where the 00 UTC rawinsonde observation occurs during the early evening (e.g. the eastern US) a near-surface stable layer can form, which obfuscates afternoon z_i determination from the early evening sounding. To obtain reliable afternoon z_i estimates from these soundings, a technique was presented to remove this layer (c.f. Chapter 4). The removal of this layer has not been done in previous studies that have developed continental-scale z_i climatologies (e.g. Seidel et al., 2010; Seidel et al., 2012), and thus these studies underestimate afternoon z_i. The application of the technique presented in this dissertation will improve daytime z_i estimates, which are vital as inputs into air quality models (e.g. Dabberdt et al., 2004) and inverse carbon transport models (e.g. Kretschmer et al., 2014).

7.2.3. CO and CO_2 as tracers for frontal passages

The work in this dissertation also demonstrated the use of trace gas measurements for frontal identification (c.f. Chapter 2). This dissertation found that large changes in CO and CO_2 mixing ratios, which arise due to shear and deformational flow that orient trace gases along fronts, can be used to help pinpoint the time of frontal passages. Making this determination is especially helpful in mountainous terrain where frontal identification is difficult (e.g. O'Handley and Bosart, 1996), but is vital to weather forecasting applications, e.g. diagnosing deep convection (e.g. Sanders and Doswell, 1995) and for investigating frontal interactions with orography (e.g. Whiteman, 2000).

7.3 Recommendations on installing trace gas measurements at additional mountaintops

Based on this dissertation's findings, additional trace gas monitoring sites can be installed at other low mountaintop sites when insufficient resources exist to install and instrument a tall tower monitoring site or for regions where no tall towers are available. Low mountaintops like Pinnacles behave like tall tower when z_i exceeds the mountaintop height and there is no wind shift, which occurs on 16% of all days. The percentage of days will be smaller at mountaintops taller than Pinnacles because z_i will exceed the mountaintop less frequently. Installing short towers at low mountaintops like Pinnacles may be more economical than installing monitoring stations at tall towers in flat terrain. Although preexisting radio and television transmitter towers are used for trace gas monitoring over flat terrain, the leasing costs for these towers typically depends on the height above ground level. Leasing costs, combined with the tower-climbing costs for installing and maintaining the monitoring equipment, can exceed $25000 per year for the tallest sites in the NOAA network (A. Andrews, personal communication). Startup costs for trace gas measurements at low mountaintops are comparably high because of equipment costs and the costs of fabricating a building to house the instruments, but the long-term cost maintenance of monitoring sites at mountaintops does not typically require professional tower climbers. On the other hand, data from tall towers in flat terrain may be more regionally-representative and easier for models to simulate so that a greater fraction of data is useful for constraining upwind flux estimates (thereby justifying additional costs).

The following issues need to be addressed if one considers additional mountaintop site(s) for trace gas monitoring:

- The prospective mountaintop monitoring site should be located upwind of roads used to access the site. Obtaining this information requires knowledge of wind patterns in the region. Although wind measurements from long-term monitoring sites in the region can provide this information, ideally wind measurements should be made at the prospective site for at least one year because of the potential for local, site-specific wind patterns occurring at mountaintops.
- The prospective mountaintop monitoring site should not be located upwind of from regional emissions sources, including point sources such as factories as well as cities, as emissions from these sources reduce the degree to which the trace gas measurements are regionally-representative. Information on these emissions sources can be obtained from emissions data bases, e.g. VULCAN (Gurney et al., 2009). In addition, forward LPDM simulations can be performed (c.f. Chapter 6). In these simulations, particles can be released from dominant regional emissions sources to establish the influence of these emissions at the mountaintop site. CO data can provide a useful tracer for local influences, especially when combined with wind speed measurements.
- The prospective mountaintop monitoring site should be located in a region where rawinsonde observations are routinely available because z_i was found to be an important driver of the diurnal trace gas variability (c.f. Chapter 5). Once z_i is obtained from the nearest sounding station, the approach discussed in Chapter 4 can be used to approximate z_i in the region surrounding the mountaintop.

- When selecting a potential mountaintop monitoring site, one may consider whether the site is located along a mountain ridge (like Pinnacles) or is located at an isolated mountaintop. Since mountain shape affects the site's exposure to the FA and thus affects the trace gas variability (e.g. Igarashi et al., 2006), isolated mountaintops may be more ideal candidates for long-term trace gas monitoring than sites located along mountain ridges. However, this topic has not been fully explored in the present dissertation.
- One may consider the advantages of installing a second site in close proximity to one another in regions with complex terrain. For example, the installation of identical trace gas measurements at a monitoring site a short distance from Pinnacles, e.g. 10-20 km away, would facilitate a comparison between the two sites. Small differences in the trace gas mixing ratios between the sites could be used to help determine times when the mountaintops are sampling well-mixed regionally-representative air masses.
- When considering potential sites, existing transmitter towers should be evaluated for suitability, but if none can be found then it may be necessary to install a tower on a mountaintop and a shed or structure comparable in size to the shed currently at Pinnacles (10 m x 13 m) to house the trace gas monitoring equipment.
- The height of the tower also needs to be considered, both in terms of its overall height and its height above the canopy. Although CO gradients at Pinnacles are small and typically <0.1 ppb m^{-1}, there can still exist significant CO_2 gradients due to nearby vegetation sources and sinks that occur even when there are small CO gradients. Thus, assuming that there are sufficient financial resources and permissions can be obtained, a 50 m or 80 m tower would likely be better than the 17 m tower currently at Pinnacles (A. Andrews, personal communication).
- In addition to trace gas measurements, standard meteorological measurements are needed on-site. For example, because of the importance of wind shifts to the trace gas variability, wind measurements need to be made, and on-site radiation measurements are needed to help determine clear, fair weather days.

Finally, the trace gas data from complex-terrain sites need to be filtered to determine measurements representative of well-mixed PBL air and measurements representative of FA values. Selecting daytime measurements representative of well-mixed PBL air would entail using the on-site meteorological measurements to identify fair weather days with constant wind direction. The subset of these days on which the valley z_i exceeds the mountaintop height would then be determined by calculating the afternoon z_i using measurements from the nearest sounding station and then applying an offset to these measurements following the approach discussed in Chapter 4. Whereas this approach would help to determine times when well-mixed PBL air is sampled, the approach would not select periods when FA air is sampled. Although the latter has not been thoroughly explored in this dissertation, determining the nighttime periods when the daily minimum in CO mixing ratio occurs would help to provide an estimate of the times when FA air is sampled.

7.4. Recommendations for future work

The measurements that were collected and maintained by the author of this dissertation from July 2008 through March 2015 and played an indispensable role in the findings presented can be used to address additional research topics in the areas of boundary layer meteorology and mountain meteorology which build upon this dissertation's findings. A selection of these topics is explored below:

- Given the present length of the Pinnacles data set (6 years, 9 months as of March 2015), long-term trends in the trace gas and meteorological measurements from Pinnacles can be compared with trends observed at other mountaintop monitoring sites to place measurements from Pinnacles into a global context.
- Much of the work in this dissertation focused on using the measurements made 17 m agl at Pinnacles. Although measurements at this height compared well with measurements 5 m agl and 10 m agl, there are sporadic instances when CO mixing ratios are >10 ppb higher at 5 m agl than at 17 m agl. These differences may be due to local-scale meteorological or chemical processes that have not been explored. Supporting meteorological measurements along the tower can be used to investigate these events in more detail.
- When the diurnal CO variability at Pinnacles was compared with other mountaintops, the relationship between the CO amplitude and the mountaintop's

elevation was discussed (c.f. Chapter 3). A follow up study could investigate the relationship between CO amplitude and other topographic parameters, e.g. prominence, mountain shape, etc., and quantify the extent to which these parameters are correlated with CO variability.

- In Chapter 3, it was unclear if the wind shift that occurs on Type II days is caused by the diabatic heating of the mountain slopes or is caused by larger-scale processes such as atmospheric tides. Case studies and numerical modeling studies of individual days on which this wind shift occurs can be used to better isolate the drivers of this wind shift.
- Estimates of z_i over the region were obtained from the nearest sounding station and were used in conjunction with gridded reanalysis output and numerical simulations (c.f. Chapter 4). The z_i estimates can be compared with z_i from other platforms, e.g. ceilometers, spaceborne LIDARs, or surface-based aerosol LIDARs, to further quantify errors in estimating z_i over the spatial scales considered in this dissertation.
- This dissertation demonstrated the use of aircraft observations from ACARS to assist with z_i determination (c.f. Chapter 4). Since rawinsonde observations are available twice-daily at most sites while ACARS is available throughout the daytime, ACARS can be further evaluated using sounding observations and then used to develop regional- to continental-scale climatologies of daytime z_i evolution.
- The role of the PBL evolution over the mountaintop on the trace gas variability has not been investigated. Differences in the growth rate of the PBL over the mountaintop may help explain some of the CO variability among days with constant winds and on which the valley z_i exceeds the mountaintop height. Gaining knowledge on the role of PBL evolution over the mountaintop requires continuous z_i observations obtained from, e.g. surface-based aerosol LIDARs, is the subject of a forthcoming study (Pal et al., draft).
- This dissertation used data from one day in the RAMMPP data set for a case study (c.f. Chapter 6). Preliminary analyses (not shown) of other days within the RAMMPP data set indicate that the Pinnacles trace gas measurements compare

well with trace gas measurements 800 m agl over the Page Valley in the aircraft profiles. However, there are occasionally large differences between the CO measurements at Pinnacles and the trace gas measurements in the aircraft profiles over the Page Valley. These differences and their underlying causes can be investigated in more detail using regional observations and numerical simulations. Additionally, flights were made over Pinnacles in February 2015 as part of the ongoing RAMMPP campaign (X. Ren, personal communication). Comparisons between the trace gas observations at Pinnacles and the RAMMPP aircraft observations over Pinnacles can further help distinguish trace gas measurements affected by local sources from regionally-representative trace gas measurements.

In addition to the measurements used in this dissertation, there were other data sets collected in the region by the author of this dissertation that were unexplored in the present dissertation but provide additional opportunities for research in mountain meteorology and boundary layer meteorology. These opportunities are summarized below:

- In April 2011, a network of 60 temperature/humidity sensors was deployed 10 km south of Pinnacles along transects extending from crest of the Blue Ridge Mountains into the surrounding valleys to evaluate climate downscaling approaches (Lee et al., 2014). As of March 2015, the network is still being maintained. Thus, the potential exists for studies on the controls on near-surface temperature variability and on the physical drivers responsible for lapse rate variability at hourly, daily, monthly, and inter-annual timescales.
- Micrometeorological towers and aerosol monitoring equipment were deployed at a valley site in the Blue Ridge Mountains near Crozet, Virginia during field experiments in 2013 and 2014. Data sets collected from these measurement platforms have already been used in recent work (Pal et al., 2014). The potential exists for additional analyses with these data sets to better understand controls on aerosol variability over valley atmospheres.
- Three ceilometers were installed in summer, 2013 along a 13 km west to east transect across the Blue Ridge Mountains near Pinnacles, and a fourth ceilometer was installed at Pinnacles. The ceilometer data sets, in conjunction with in situ

meteorological measurements, provide opportunities to investigate the spatiotemporal variability in cloud base heights along and across mountain ridges, as well as the opportunity to investigate the underlying physical processes responsible for this variability.

The measurements from the instrument platforms summarized above, in addition to the meteorological and trace gas monitoring equipment at Pinnacles discussed in this dissertation, all provide invaluable data sets which can continue to be used for furthering scientific understanding of the meteorological processes occurring over mountainous terrain.

REFERENCES

Adams, F., Dams, R., Guzman, L., and Winchester, J. W., 1977. Background aerosol composition on Chacaltaya Mountain, Bolivia. *Atmos. Environ*. **11**, 629-634.

Alcott, T. I. and Steenburgh, W. J., 2013. Orographic influences on a Great Salk Lake-effect snowstorm. *Mon. Weather Rev*. **141**, 2432-2450.

Andrews, A., et al., 2009. Results from the NOAA collaborative tall tower network for monitoring carbon dioxide and related gases. International CO_2 Conference, Jena, Germany, 13-18 September 2009.

Andrews, A. E., et al., 2014. CO_2, CO, and CH_4 measurements from tall towers in the NOAA Earth System Research Laboratory's Global Greenhouse Gas Reference Network: instrumentation, uncertainty analysis, and recommendations for future high-accuracy greenhouse gas monitoring efforts. *Atmos. Meas. Tech*. **7**, 647-687.

Andrews, A. E., 2015. Personal communication. 22 April 2015.

Aneja, V. P., Pal Arya, S., Li, Y., Murray, C. G., and Manuszak, T. L., 2000. Climatology of diurnal trends and vertical distribution of ozone in the atmospheric boundary layer in urban North Carolina. *J. Air Waste Manage*. **50**(1), 54-64.

Angelov, C., et al., 2011. BEO Moussala— a new facility for complex environment studies. In *Sustainable Development in Mountain Regions Southeastern Europe, Part 2*. Springer, pp. 123-139.

Angevine, W. M., Jiang, H., and Mauritsen, R., 2010. Performance of an Eddy Diffusivity-Mass Flux Scheme for Shallow Cumulus Boundary Layers. *Mon. Weather Rev*. **138**, 2895-2912.

Angevine, W. M., Eddington, L., Durkee, K., Fairall, C., Bianco, L., and Brioude, J., 2012. Meteorological Model Evaluation for CalNex 2010. *Mon. Weather Rev*. **140**, 3885-3906.

Apadula, F., Gotti, A., Pigini, A., Longhetto, A., Rocchetti, F., Cassardo, C., Ferrarese, S., and Froza, R., 2003. Localization of source and sink regions of carbon dioxide through the method of the synoptic air trajectory statistics. *Atmos. Environ.* **37**, 3757-3770.

Atlas, E. L. and Ridley, B. A., 1996. The Mauna Loa Observatory photochemistry experiment: introduction. *J. Geophys. Res*. **101**(D9), 14531-14541.

Avissar, R. and Schmidt, T., 1998. An evaluation of the scale at which ground-surface heat flux patchiness affects the convective boundary layer using large-eddy simulations. *J. Atmos. Sci.* **55**, 2666-2689.

Bakwin, P. S. and Tans, P. P., 1995. Measurements of carbon dioxide on a very tall tower. *Tellus* **47B**, 535-549.

Bakwin, P. S., Tans, P. P., Hurst, D. F., and Zhao, C., 1998. Measurements of carbon dioxide on very tall towers: Results of the NOAA/CMDL program. *Tellus* **50B**, 401-415.

Bakwin, P. S., Davis, K. J., Yi, C., Wofsy, S. C., Munger, J. W., and Haszpra, L., 2004. Regional carbon dioxide fluxes from mixing ratio data. *Tellus* **56B**, 301-311.

Ball, F. K., 1960. Control on the inversion height by surface heating. *Q. J. Roy. Meteor. Soc*. **86**(370), 483-494.

Baltensperger, U., et al., 1997. Aerosol climatology at the high-alpine site Jungfraujoch, Switzerland. *J. Geophys. Res*. **102**(D16), 19707-19715.

Balzani Lööv, et al., 2008. Estimation of background concentrations of trace gases at the Swiss alpine site Jungfraujoch (3580 m asl). *J. Geophys. Res*. **113**, D22305.

Banic, C. M., Isaac, G. A., Cho, H. R., and Iribarne, J. V., 1986. The distribution of pollutants near a frontal surface: A comparison between field experiment and modeling. *Water Air Soil Poll.* **30**, 171-177.

Banta R. M., et al., 1997. Nocturnal cleansing flows in a tributary valley. *Atmos. Environ.* **31**, 2147-2162.

Bhugwant, C., Rivière, E., Keckhut, P., and Leveau, J., 2001. Variability of carbonaceous aerosols, ozone and radon at Piton Textor, a mountain site on Réunion island (south-western Indian Ocean). *Tellus* **53B**, 546-535.

Bianco, L., Djalaova, I. V., King, C. W., and Wilczak, J. M., 2011. Diurnal evolution and annual variability of boundary-layer height and its correlation to other meteorological variables in California's Central Valley. *Bound-Lay. Meteorol*. **140**, 491-511.

Bjerknes, J., 1919. On the structure of moving cyclones. *Mon. Weather Rev*. **47**(2), 95-99.

Blay-Carreras, E. D., et al., 2014. Role of the residual layer and large-scale subsidence on the development and evolution of the convective boundary layer. *Atmos. Chem. Phys*. **14**, 4515-4530

Bluestein, H. B., 1993. *Synoptic-Dynamic Meteorology in Midlatitudes, Volume II Observations and Theory of Weather Systems*. Oxford University Press, 594 pp.

Bohnenstengel, S. I., Evans, S., Clark, P. A., and Belcher, S. E., 2011. Simulations of the London urban heat island. *Q. J. R. Meteorol. Soc*. **137**, 1625-1640.

Bonasoni, P., et al., 2008. The ABC-Pyramid Atmospheric Research Observatory in Himalaya for aerosol, ozone and halocarbon measurements. *Sci. Total Environ*. **391**, 252-261.

Bonin, T., Chilson, P., Zielke, B., and Fedorovich, D., 2013. Observations of the early evening boundary-layer transition using a small unmanned aerial system. *Bound-Lay. Meteorol.* **146**, 119-132.

Borge, R., Alexandrov V., del Vas J. J., Lumbreras, J., and Rodriguez, E., 2008. A comprehensive sensitivity analysis of the WRF model for air quality applications over the Iberian Peninsula. *Atmos. Environ*. **42**(37), 8560-8574.

Brioude, J., et al., 2013. The lagrangian particle dispersion model FLEXPART-WRF version 3.0. *Geosci. Model Dev.* **6**, 3615-3654.

Brooks, B. J., Desai, A. R., and Stephens, B. B., 2010. Reducing sampling error in Rocky Mountain atmospheric carbon dioxide time series to improve flux retrievals. 29th Conference on Agricultural and Forest Meteorology/19th Symposium on Boundary Layers and Turbulence/9th Symposium on the Urban Environment, Keystone, Colorado, 1-6 Aug. 2010.

Brooks, B. G. J., et al., 2012. Assessing filtering of mountaintop CO_2 mole fractions for application to inverse models of biosphere-atmosphere carbon exchange. *Atmos. Chem. Phys.* **12**, 2099-2115.

Butler, M . P., Davis, K. J., Denning, A. S., and Kawa, S. R., 2010. Using continental observations in global atmospheric inversions of CO_2: North American carbon sources and sinks. *Tellus B* **2010**, 1-23.

Castellanos, P., Marufu, L. T., Doddridge, B. G., Taubman, B. F., Schwab, J. J., Hains, J. C., Ehrman, S. H., and Dickerson, R. R., 2011. Ozone, oxides of nitrogen, and carbon monoxide during pollution events over the eastern United States: An evaluation of emissions and vertical mixing. *J. Geophys. Res*. **116**, D16307.

Chow F. K., De Wekker, S. F. J., and Snyder, B., editors, 2013. *Mountain Weather Research and Forecasting. Recent Progress and Current Challenges*. Springer, 760 pp.

Ciattaglia, L., Cundari, V., and Colombo, T., 1987. Further measurements of atmospheric carbon dioxide at Mt. Cimone, Italy: 1979-1985. *Tellus* **39B**, 13-20.

Clifford, S. F., Kaimal, J. C., Lataitis, R. J., and Strauch, R. G., 1994. Ground-based remote profiling in atmospheric studies: an overview. *Proc. IEEE* **82**(3), 313-355.

Coen, M. C., Weingartner, E., Furger, M., Nyeki, S., Prévôt, A. S. H., Steinbacher, M., and Baltensperger, U., 2011. Aerosol climatology and planetary boundary influence at the Jungfraujoch analyzed by synoptic weather types. *Atmos. Chem. Phys*. **11**, 5931-5944.

Cooper, O. R., 1997. An ozone climatology study for Big Meadows, Shenandoah National Park, Virginia: 1989-1994. Master's thesis, University of Virginia, Charlottesville, VA.

Cooper, O. R. and Moody, J. L., 2000. Meteorological controls on ozone at an elevated eastern United States regional background monitoring site. *J. Geophys. Res*. **105**(D5), 6855-6869.

Cooper, O. R., et al., 2004. A case study of transpacific warm conveyor belt transport: Influence of merging airstreams on trace gas import to North America. *J. Geophys. Res.* **109**, D23S08.

Cotton, W. R., Alexander, G. D., Hertenstein, R., Walko, R. L., McAnelly, R. L., and Nicholls, M., 1995. Cloud venting - a review and some new global annual estimates. *Earth-Sci. Rev.* **39**, 169-206.

Cressie, N. A. C., 1993. *Statistics for Spatial Data*. J. Wiley, New York, 900 pp.

Cristofanelli, P., Fierli, F. F, Marinoni, A., Duchi, R., Burkhart, J., Stohl, A., Maione, M., Arduini, J., and Bonasoni, P., 2013. Influence of biomass burning and anthropogenic emissions on ozone, carbon monoxide and black carbon at the Mt. Cimone GAW-WMO global station (Italy, 2165 m a.s.l.). *Atmos. Chem. Phys*. **13**, 15-30.

Crutzen, P. J., and Andreae, M. O., 1990. Biomass burning in the tropics: Impact on atmospheric chemistry and biogeochemical cycles. *Science* **250** (4988), 1669-1678.

Dabberdt, W. F., et al., 2004. Meteorological research needs for improved air quality forecasting: Report of the 11th prospectus development team of the U.S. Weather Research Program. *B. Amer. Meteorol. Soc*. **85**, 563-586.

Davis, K. J., Bakwin, P. S., Yi, C., Berger, B. W., Zhao, C., Teclaw, R. M., and Isebrands, J. G., 2003. The annual cycles of CO_2 and H_2O exchange over a northern mixed forest as observed from a very tall tower. *Glob. Change Biol*. **9**, 1278-1293.

Davis, R. E., Normile, C. P., Sitka, L., Hondula, D. M., Knight, D. B., Gawtry, S. P., and Stenger, P. J. 2010. A comparison of trajectory and air mass approaches to examine ozone variability. *Atmos. Environ*. **44**, 64-74.

Dayan, U., Shenhav, R., and Graber, M., 1988. The spatial and temporal behavior of the mixed layer in Israel. *J. Appl. Meteor*. **27**, 1382-1394.

De Wekker, S. F. J., Zhong, S., Fast, J. D., and Whiteman, C. D., 1998. A numerical study of the thermally driven plain-to-basin wind over idealized basin topographies. *J. Appl. Meteorol.* **37**, 606-622.

De Wekker, S. F. J., 2002. Structure and morphology of the convective boundary layer in mountainous terrain. Ph.D. dissertation, University of British Columbia, 191 pp.

De Wekker, S. F. J., Steyn, D. G., and Nyeki, S., 2004. A comparison of aerosol-layer and convective boundary-layer structure over a mountain range during STAARTE '97. *Bound-Lay. Meteorol*. **113**(2), 249-271.

De Wekker, S. F. J., Steyn, D. G., Fast, J. D., Rotach, M. W., and Zhong, S., 2005. The performance of RAMS in representing the convective boundary layer structure in a very steep valley. *Environ. Fluid Mech*. **5**, 35-62.

De Wekker, S. F. J., 2008. Observational and numerical evidence of depressed convective boundary layer heights near a mountain base. *J. Appl. Meteorol. Clim*. **47**, 1017-1026.

De Wekker, S. F. J., Ameen, A., Song, G., Stephens, B. B., Hallar, A. G., and McCubbin, I. B., 2009. A preliminary investigation of boundary layer effects on daytime atmospheric CO_2 concentrations at a mountaintop location in the Rocky Mountains. *Acta Geophys*. **57**(4), 904-922.

De Wekker, S. F. J. and Mayor, S. D., 2009. Observations of atmospheric structure and dynamics in the Owens Valley of California with a ground-based, eye-safe, scanning aerosol lidar. *J. Appl. Meteorol. Clim*. **48**, 1483-1499.

Desai, A. R., et al., 2006. A case study on the effects of heterogeneous soil moisture on mesoscale boundary-layer structure in the southern Great Plains, U.S.A. Part I: simple prognostic model. *Bound-Lay. Meteorol.* **119**, 195-238.

Dickerson, R. R., et al., 1987. Thunderstorms: an important mechanism in the transport of air pollutants. *Science* **235**(4787), 460-465.

Dils, B., Cui, J., Henne, S., Mahieu, E., Steinbacher, M., and De Mazière, M., 2011. 1997-2007 CO trend at the high Alpine site Jungfraujoch: a comparison between NDIR surface in situ and FTIR remote sensing observations. *Atmos. Chem. Phys*. **11**, 6735-6748.

Draxler, R. R. and Hess, G. D., 2004. Description of the HYSPLIT 4 Modeling System (NOAA Technical Memorandum ERL ARL-224). NOAA Air Resources Laboratory, Silver Spring, MD. http://www.arl.noaa.gov/data/web/models/hysplit4/win95/arl-224.pdf Dec., 1997, revised Jan., 2004.

Drüe, C., Hauf, T., and Hoff, A., 2010. Comparison of boundary-layer profiles and layer detection by AMDAR and WTR/RASS at Frankfurt Airport. *Bound-Lay. Meteorol.* **135**, 407-432.

Dudhia, J., 1989. Numerical study of convection observed during the winter monsoon experiment using a mesoscale two-dimensional model. *J. Atmos. Sci*. **46**(20), 3077-3107.

Elanksy, N. F., Lokoshchenko, M. A., Belikov, I. B., Skorokhod, A. I., and Shumskii, R. A., 2007. Variability of trace gases in the atmospheric boundary layer from observations in the city of Moscow. *Atmos. Ocean. Phys*. **43**(2) 219-231.

Fahey, D. W., et al., 1986. Reactive nitrogen species in the troposphere: measurements of NO, NO_2, HNO_3, particulate nitrate, peroxyacetyl nitrate (PAN), O_3, and total reactive odd nitrogen (NO_y) at Niwot Ridge, Colorado. *J. Geophys. Res.* **91**(D9), 9781-9783.

Fang, S. X., Zhou, L. X., Tans, P. P., Ciais, P., Steinbacher, M., Xu, L., and Luan, T., 2013. In-situ measurement of atmospheric CO_2 at the four WMO/GAW stations in China. *Atmos. Chem. Phys. Disc*. **13**, 27287-27326.

Fast J. D., Allwine, K. J., Dietz, R. N., Clawson, K. L., and Torcolini, J. C., 2006. Dispersion of perfluorocarbon tracers within the Salt Lake Valley during VTMX 2000. *J. Appl. Meteorol. Climatol*. **45**, 793-812.

Fischer, E. V., Talbot, R. W., Dibb, J. E., Moody, J. L., and Murray, G. L., 2004. Summertime ozone at Mount Washington: Meteorological controls at the highest peak in the northeast. *J. Geophys. Res*. **109**, D24303.

Fischer, E. V., Jaffe, D. A., Reidmiller, D. R., and Jaeglé L., 2010. Meteorological controls on observed peroxyacetyl nitrate at Mount Bachelor during the spring of 2008. *J. Geophys. Res.* **115**, D03302.

Flynn, C. M., et al., 2014. Relationship between column-density and surface mixing ratio: Statistical analysis of O_3 and NO_2 data from the July 2011 Maryland DISCOVER-AQ mission. *Atmos. Environ*. **92**, 429-441.

Forrer, J., et al., 2000. Variability of trace gases at the high-Alpine site Jungfraujoch caused by meteorological transport processes. *J. Geophys. Res.* **105**(D10), 12241-12251.

Francis, T., 2012. Temporal trends in ambient SO_2 at a high altitude site in semi-arid Western India: observations versus chemical transport modeling. *J. Environ. Prot*. **3**, 657-680.

Gallagher, J. P., McKendry, I. G., Macdonald, A. M., and Leaitch, W. R., 2011. Seasonal and diurnal variations in aerosol concentration on Whistler Mountain: Boundary layer influence and synoptic-scale controls. *J Appl. Meteorol. Climatol*. **50**, 2210-2222.

Gangoiti, G., Millán., M. M., Salvador., R., and Mantilla., E., 2001. Long-range transport and re-circulation of pollutants in the western Mediterranean during the project Regional Cycles of Air Pollution in the west-central Mediterranean area. *Atmos. Environ*. **35**(36), 6267-6276.

Gao, J., Wang, T., Ding, A. and Liu, C., 2005. Observational study of ozone and carbon monoxide at the summit of mount Tai (1534 m a.s.l.) in central-eastern China. *Atmos. Environ*. **39**, 4779-4991.

Garrett, A. J., 1981. Comparison of observed mixed-layer depths to model estimates using observed temperatures and winds, and MOS forecasts. *J. Appl. Meteorol*. **20**, 1277-1283.

Geels, C., Doney, S. C., Dargaville, R., Brandt, J., and Christensen, J. H., 2004. Investigating the sources of synoptic variability in atmospheric CO_2 measurements over the Northern Hemisphere continents: a regional model study. *Tellus* **56B**, 35-50.

Gerbig, C., Dolman, A. J., and Heimann, M., 2009. On observational and modelling strategies targeted at regional carbon exchange over continents. *Biogeosciences* **6**, 1949-1959.

Gibert, F., Schmidt, M., Cuesta, J., Ciais, P., Ramonet, M., Xueref, I., Larmanou, E., and Flamant, P. H., 2007. Retrieval of average CO_2 fluxes by combining in situ CO_2 measurements and backscatter lidar information. *J. Geophys. Res.* **112**, D10301.

Giglio, L., Descloitres, J., Justice, C. O., and Kaufman, Y. J., 2003. An enhanced contextual fire detection algorithm for MODIS. *Remote Sens. Environ.* **87**, 273-282.

Gilge, S., Plass-Duelmer, C., Fricke, W., Kaiser, A., Ries, L., Buchmann, B., and Steinbacher, M., 2010. Ozone, carbon monoxide and nitrogen oxides time series at four alpine GAW mountain stations in central Europe. *Atmos. Chem. Phys*. **10**, 12295-12316.

Gilliam, R. C. and Pleim, J. E, 2010. Performance assessment of new land surface and planetary boundary layer physics in the WRF-ARW. *J. Appl. Meteorol. Clim*. **49**(4), 760-774.

Gloor, M., Bakwin, P., Hurst, D., Lock, L., Draxler, R., and Tans, P., 2001. What is the concentration footprint of a tall tower? *J. Geophys. Res*. **106**(D16), 17831-17840.

Gohm, A., Harnisch, F., Vergeiner, J., Obleitner, F., Schnitzhofer, R., Hansel, A., Fix, A., Neininger, B., Emeis, S., and Schäfer, K., 2009. Air pollution transport in an

Alpine valley: Results from airborne and ground-based observations. *Bound-Lay. Meteorol.* **131**(3), 441-463.

Gong, Q. and Demerjian, K. L., 1997. Measurement and analysis of C_2-C_{10} hydrocarbons at Whiteface Mountain, New York. *J. Geophys. Res*. **102**(D23), 28059-28069.

Greco, S. and Baldocchi, D. D., 1996. Seasonal variations of CO_2 and water vapour exchange rates over a temperate deciduous forest. *Glob. Change Biol*. **2**, 183-197.

Grimsdell, A. W. and Angevine, W. M., 1998. Convective boundary layer height measurement with wind profilers and comparison to cloud base. *J. Atmos. Ocean Tech*. **15**, 1331-1338.

Gupta, P., Christopher, S. A., Wang, J., Gehrig, J., Lee, Y. C., and Kumar, N. 2006. Satellite remote sensing of particulate matter and air quality over global cities. *Atmos. Environ*. **40**, 5880-5892.

Gurney, K. R., Mendoza, D. L., Zhou, Y., Fischer, M. L., Miller, C. C., Geethakumar, S., and De La Rue Du Can, S., 2009. High resolution fossil fuel combustion CO_2 emissions fluxes for the United States. *Environ. Sci. Technol*. **43**(14), 5535-5541.

Haszpra, L., Barcza, Z., Haszpra, T., Pátkai, Z., and Davis, K. J., 2014. How well do tall tower measurements characterize the CO_2 mole fraction distribution in the planetary boundary layer? *Atmos. Meas. Tech. Discuss*. **7**, 12249-12282.

He, H., et al., 2014. An elevated reservoir of air pollutants over the Mid-Atlantic States during the 2011 DISCOVER-AQ campaign: Airborne measurements and numerical simulations. *Atmos. Environ*. **85**, 18-30.

Henne, S., et al., 2004. Quantification of topographic venting of boundary layer air to the free troposphere. *Atmos. Chem. Phys.* **4**, 497-509.

Henne, S., et al., 2005. Influence of mountain venting in the Alps on the ozone chemistry of the lower free troposphere and the European pollution export. *J. Geophys. Res*. **110**, D22307.

Henne, S., Junkermann, W., Kariuki, J. M., Aseyo, J., and Klausen, J., 2008a. Mount Kenya Global Atmospheric Watch Station (MKN): Installation and meteorological characterization. *J. Appl. Meteorol. Clim.* **47**, 2946-2962.

Henne, S., et al., 2008b. Representativeness and climatology of carbon monoxide and ozone at the global GAW station Mt. Kenya in equatorial Africa. *Atmos. Chem. Phys*. **8**, 3119-3139.

Henne, S., Brunner, D., Folini, D., Solberg, S., Klausen, J., and Buchmann, B., 2010. Assessment of parameters describing representativeness of air quality in-situ measurement sites. *Atmos. Chem. Phys*. **10**, 3561-3581.

Hess, S. L., 1959. *Introduction to Theoretical Meteorology*. Florida State University, Holt, Rinehart and Winston, 361 pp.

Hidy, G. M., et al., 2014. Chemical climatology of the southeastern United States, 1999-2013. *Atmos. Chem. Phys*. **14**, 11893-11914.

Holzworth, G. C., 1964. Estimates of mean maximum mixing depths in the contiguous United States. *Mon. Weather Rev*. **92**, 235-242.

Hondula, D. M., Davis, R. E., Knight, D. B., Sitka, Sitka, L. J., Enfield, K., Gawtry, S. B., Stenger, P. J., Deaton, M. E., Normile, C. P., and Lee, T. R., 2013. A respiratory alert model for the Shenandoah Valley, Virginia, USA. *Int. J. Biometeorol*. **57**, 91-105.

Hong, S. Y., Dudhia, J., and Chen, S. H., 2004. A revised approach to ice microphysical processes for the bulk parameterization of clouds and precipitation. *Mon. Weather Rev*. **132**(1), 103-120.

Horel, J., et al., 2002. Mesowest: Cooperative mesonets in the western United States. *B. Amer. Meteorol. Soc.* **82**, 211-225.

Hu, X. M., Doughty, D. C., Sanchez, K. J., Joseph, E., and Fuentes, J. D., 2012. Ozone variability in the atmospheric boundary layer in Maryland and its implications for vertical transport model. *Atmos. Environ*. **46**, 354-364.

Hurwitz, M. D., Ricciuto, D. M., Bakwin, P. S., Davis, K. J., Wang, W., Yi, C., and Butler, M. P., 2004. Transport of carbon dioxide in the presence of storm systems over a northern Wisconsin forest. *J. Atmos. Sci.* **61**, 607-618.

Igarashi, Y., et al., 2006. Seasonal variations in SO_2 plume transport over Japan: Observations at the summit of Mt. Fuji from winter to summer. *Atmos. Environ*. **40**, 7018-7033.

Jaffe, D., et al., 2005. Export of atmospheric mercury from Asia. *Atmos. Environ*. **39**, 3029-3038.

Janjić, Z. I., 1990. The step-mountain coordinate: Physical package. *Mon. Weather Rev*. **118**, 1429-1443.

Janjić, Z., Gall, R., and Pyle, M. E., 2010. Scientific documentation for the NMM solver. NCAR Technical Note NCR/TN 477+STR.

Janjić, Z., et al., 2011. User's guide for the NMM core of the Weather Research and Forecast (WRF) modeling system version 3. 195 pp.

Jordan, N. S., Hoff, R. M., and Bacmeister, J., 2010. Validation of Goddard Earth Observing System-version 5 MERRA planetary boundary layer heights using CALIPSO. *J. Geophys. Res*. **115**, D24218.

Justice, C. O., et al., 2002. The MODIS fire products. *Rem. Sens. Environ*. **83**, 244-262.

Kain, J. S. and Fritsch, J. M., 1990. A one-dimensional entraining/detraining plume model and its application in convective parameterization. *J. Atmos. Sci*. **47**(23), 2784-2802.

Kalthoff, N., Binder, H.-J., Kossmann, M., Vögtlin, R., Corsmeier, U., Fiedler, F., and Schlager, H., 1998. Temporal evolution and spatial variation of the boundary layer over complex terrain. *Atmos. Environ*. **32**(7), 1179-1194.

Kasper, A. and Puxbaum, H., 1998. Seasonal variation of SO_2, HNO_3, NH_3, and selected aerosol components at Sonnblick (3106 m a.s.l.). *Atmos. Environ.* **32**(23), 3925-3939.

Keeling, C. D., Bacastow, R. B., Bainbridge, A. E., Ekdahl, C. A. Jr., Guenther, P. R., and Waterman, L. S., 1976. Atmospheric carbon-dioxide variations at Mauna-Loa Observatory, Hawaii. *Tellus* **28** (6), 538-551.

Keeling, C. D., 1978. The influence of Mauna Loa Observatory on the development of atmospheric CO_2: research, Mauna Loa Observatory 20th Anniversary Report, edited by J. Miller, special report, pp. 36-54, Nat. Oceanogr. Atmos. Admin., Wash., D.C.

Kentarchos, A. S., Roelofs, G. J., Lelieveld, J., and Cuevas, E., 2000. On the origin of elevated surface ozone concentrations at Izana Observatory, Tenerife during late March 2006. *Geophys. Res. Lett*. **27** (22), 3699-3702.

Ketterer, C., Zieger, P., Bukowiecki, N., Collaud Coen, M., Maier, O., Ruffieux, D., and Weingartner, E., 2014. Investigation of the planetary boundary layer in the Swiss Alps using remote sensing and in situ measurements. *Bound-Lay. Meteorol.* **151**, 317-334.

Kleissl, J., et al., 2007. Occurrence of upslope flows at the Pico mountaintop observatory: a case study of orographic flows on a small, volcanic island. *J. Geophys. Res*. **112**, D10S35.

Korhonen, K., et al., 2014. Atmospheric boundary layer top height in South Africa: measurements with lidar and radiosonde compared to three atmospheric models. *Atmos. Chem. Phys.* **14**, 4263-4278.

Kossmann, M., et al., 1998. Aspects of the convective boundary layer structure over complex terrain. *Atmos. Environ*. **32**(7), 1323-1348.

Kozlova, E. A., Manning, A. C., Kisilyakhov, Y., Seifert, T., and Heimann, M., 2008. Seasonal, synoptic, and diurnal-scale variability of biogeochemical trace gases and O_2 from a 300-m tall tower in central Siberia. *Global Biogeochem. Cycles* **22**, GB4020.

Kretschmer, R., Koch, F., Feist, D., Biavati, G., Karstens, U., and Gerbig, C., 2013. Toward assimilation of observation-derived mixing heights to improve atmospheric tracer transport models. In Lagrangian Modeling of the Atmosphere, edited by: Lin, J., Brunner, D., Gerbig, C., Stohl, A., Luhar, A., and Webley, P., American Geophysical Union, Washington, DC.

Kretschmer, R., Gerbig, C., Karstens, U., Biavati, G., Vermeulen, A., Vogel, F., Hammer, S., and Totsche, K. U., 2014. Impact of optimized mixing heights on simulated regional atmospheric transport of CO_2. *Atmos. Chem. Phys*. **14**, 7149-7172.

Kunz, H. and Speth, P., 1997. Variability of near-ground ozone concentrations during cold front passages - a possible effect of tropopause folding events. *J. Atmos. Chem*. **28**, 77-95.

Lac, C., et al., 2013. CO_2 dispersion modelling over Paris region within the CO_2-MEGAPARIS project. *Atmos. Chem. Phys*. **13**, 4941-4961.

Lee, T. R., 2011. Frontal impacts on carbon dioxide concentrations at a forested site in the Virginia Blue Ridge Mountains. Master's thesis, University of Virginia, Charlottesville, VA.

Lee, T. R., De Wekker, S. F. J., Andrews, A. E., Kofler, J. and Williams, J., 2012. Carbon dioxide variability during cold front passages and fair weather days at a forested mountaintop site. *Atmos. Environ*. **46**, 405-416.

Lee, T. R., De Wekker, S. F. J. and Wofford, J. E. B. 2014. Downscaling maximum temperature projections to subkilometer resolutions in the Shenandoah National Park of Virginia, USA. *Adv. Meteorol*. **2014**(594965).

Lee, T. R., De Wekker, S. F. J., Pal, S., Andrews, A., and Kofler, J., 2015. Meteorological controls on the diurnal variability of carbon monoxide mixing ratio at a mountaintop monitoring site in the Appalachian Mountains. *In review*.

Lee, T. R. and De Wekker, S. F. J., draft. Estimating planetary boundary layer heights over a valley from rawinsonde observations at a nearby airport: A case study for the Page Valley in Virginia, USA. *J. Appl. Meteorol. Climatol*.

Levin, I., Graul, R., and Trivett, N. B. A., 1995. Long-term observations of atmospheric CO_2 and carbon isotopes at continental sites in Germany. *Tellus* **47B**, 23-34.

Li, J., Wang, Z., Akimoto, H., Gao, C., Pochanart, P., and Wang X., 2007. Modeling study of ozone seasonal cycle in lower troposphere over east Asia. *J. Geophys. Res*. **112**, D22S25.

Lin, Y. C., et al., 2011. Observations of ozone and carbon monoxide at Mei-Feng mountain site (2269 m a.s.l.) in Central Taiwan: Seasonal variations and influence of Asian continental outflow. *Sci. Total Environ*. **409**, 3033-3042.

Liu, S. and Liang, X.-Z., 2010. Observed diurnal cycle climatology of planetary boundary layer height. *J. Climate* **23**, 5790-5809.

Lugauer, M., Baltensperger, U., Furger, M., Gäggeler, H. W., Jost, D. T., Schwikowski, M., and Wanner, H., 1998. Aerosol transport to the high Alpine sites Jungfraujoch (3454 m asl) and Colle Gnifetti (4452 m asl). *Tellus B* **50**, 76-92.

Lugauer, M. and Winkler, P., 2005. Thermal circulation in South Bavaria - climatology and synoptic aspects. *Meteorol. Z*. **14**, 15-30.

Ma, M., Pu, Z., Wang, S., and Zhang, Q., 2011. Characteristics and numerical simulations of extremely large atmospheric boundary-layer heights over an arid region in North-west China. *Bound-Lay. Meteorol*. **140**, 163-176.

MacDonald, A. M., Anlauf, K. G., Leaitch, W. R., Chan, E., and Tarasick, D. W., 2011. Interannual variability of ozone and carbon monoxide at the Whistler high elevation site: 2002-2006. *Atmos. Chem. Phys*. **11**, 11431-11446.

Marenco, A., Gouget, H., Nédélec, P., Pagés, J.-P., and Karcher, F., 1994. Evidence of a long term increase in tropospheric ozone from Pic du Midi data series: Consequences: positive radiative forcing. *J. Geophys. Res*. **99** (16), 617-632.

McGrath, R., Semmler, T., Sweeney, S., and Wang, S., 2006. Impact of balloon drift errors in radiosonde data on climate statistics. *J. Climate* **19**, 3430-3442.

McGrath-Spangler, E. L. and Denning, A. S., 2013. Global seasonal variations of midday planetary boundary layer depth from CALIPSO space-borne LIDAR. *J. Geophys. Res. Atmos*. **118**, 1-8.

McKendry, I. G., Steyn, D. G., Banta, R. M., Strapp, W., Anlauf, K., and Pottier, J., 1998. Daytime photochemical pollutant transport over a tributary valley lake in southwestern British Columbia. *J. Appl. Meteorol.* **37**, 393-404.

Mesinger, F., et al., 2006. North American Regional Reanalysis. *Bull. Am. Meteorol. Soc*. **87**, 343-360.

Mlawer, E. J., Taubman, S. J., Brown, P. D., Iacono, M. J., and Clough, S. A., 1997. Radiative transfer for inhomogeneous atmospheres: RRTMa validated correlated-k model for the longwave. *J. Geophys. Res*. **102**(D14), 16663-16682.

Nakanishi, M., and Niino, H., 2009. Development of an improved turbulence closure model for the atmospheric boundary layer. *J. Meteorol. Soc. Jpn*. **87**(5), 895-912.

National Cartography and Geospatial Center, 1999. Virginia precipitation data/maps, Natl. Resour. Conserv. Serv., U.S. Dep. of Agric., Fort Worth, Tex.

Necki, J., Schmidt, M., Rozanski, K., Zimnoch, M., Korus, A., Lasa, J., Graul, R., and Levin, I., 2003. Six-year record of atmospheric carbon dioxide and methane at a high-altitude mountain site in Poland. *Tellus* **55B**, 94-104.

Novelli, P. C., Masarie, K. A. and Lang, P. M., 1998. Distributions and recent changes of carbon monoxide in the lower troposphere. *J. Geophys. Res*. **103**(D15), 19015-19033.

Nyeki, S., et al., 2000. Convective boundary layer evolution to 4 km asl over high-alpine terrain: airborne lidar observations in the Alps. *Geophys. Res. Lett*. **27**(5), 689-692.

O'Handley, C. and Bosart, L. F., 1996. The impact of the Appalachian Mountains on cyclonic weather systems. Part I: A climatology. *Mon. Weather Rev*. **124**, 1353-1373.

Obrist D., Hallar, A. G., McCubbin, I., Stephens, B. B., and Rahn, T., 2008. Measurements of atmospheric mercury at Storm Peak Laboratory in the Rocky Mountains: Evidence for long-range transport from Asia, boundary layer contributions, and plant mercury uptake. *Atmos. Environ*. **42**, 7579-7589.

Olson, J., and Grell, G., 2014. Improving the rapid refresh and high resolution rapid refresh physics to better perform across a wide range of spatial scales. EGU General Assembly, Vienna, Austria, 27 April – 2 May, 2014.

Ou Yang, et al., 2014. Characteristics of atmospheric carbon monoxide at a high-mountain background station in East Asia. *Atmos. Environ*. **89**, 613-622.

Pal, S., Lee, T. R., Phelps, S., and De Wekker, S. F. J., 2014. Impact of atmospheric boundary layer depth variability and wind reversal on the diurnal variability of aerosol concentration at a valley site. *Sci. Total Environ*. **496**, 424-434.

Pal, S., Lopez, M., Schmidt, M., Ramonet, M., Gibert, F., Xueref-Remy, I., and Ciais, P., 2015. Investigation of the atmospheric boundary layer depth variability and its impact on the ^{222}Rn concentration at a rural site in France. *J. Geophys. Res. Atmos*. **120**.

Pal, S., Lee, T. R., and De Wekker, S. F. J., draft. On the contribution of CO concentration in the nocturnal boundary layer in determining the CO diurnal cycle over a low mountaintop. *J. Geophys. Res. Atmos.*

Pandey Deolal, S., et al., 2014. Analysis of elevated springtime levels of peroxyacetyl nitrate (PAN) at the high alpine research sites Jungfraujoch and Zugspitze. *Atmos. Chem. Phys*. **14**, 12553-12571.

Parazoo, N. C., Denning, A. S., Kawa, S. R., Corbin, K. D., Lokupitiya, R. S., and Baker, I. T., 2008. Mechanisms for synoptic variations of atmospheric CO_2 in North America, South America and Europe. *Atmos. Chem. Phys*. **8**, 7239-7254.

Parazoo, N. C., Denning, A. S., Berry, J. A., Wolf, A., Randall, D. A., Kawa, S. R., Pauluis, O., and Doney, S. C., 2011. Moist synoptic transport of CO_2 along the mid-latitude storm track. *Geophys. Res. Lett*. **38**, L09804.

Patra, P. K., et al., 2008. TransCom model simulations of hourly atmospheric CO_2: analysis of synoptic-scale variations for the period 2002-2003. *Glob. Biogeochem. Cycles* **22**, GB4013.

Pérez-Landa, G., et al., 2007. Mesoscale circulations over complex terrain in the Valencia coastal region, Spain - Part 2: Modeling CO_2 transport using idealized surface fluxes. *Atmos. Chem. Phys*. **7**, 1851-1868.

Peters, W. et al., 2007. An atmospheric perspective on North American carbon dioxide exchange: CarbonTracker. *P. Natl. Acad. Sci*. **104**(48), 18925-18930.

Pillai, D., et al., 2011. High-resolution simulations of atmospheric CO_2 over complex terrain - representing the Ochsenkopf mountain tall tower. *Atmos. Chem. Phys*. **11**, 7445-7464.

Pleim, J. E. and Xiu, A., 1995. Development and testing of a surface flux and planetary boundary layer model for application in mesoscale models. *J. Appl. Meteorol*. **34**, 16-32.

Pochanart, P., Akimoto, H., Kajii, Y., and Sukasem, P., 2003. Carbon monoxide, regional-scale transport, and biomass burning in tropical continental Southeast Asia: Observations in rural Thailand. *J. Geophys. Res*. **108**(D17), 4552.

Popa, M. E., Gloor, M., Manning, A. C., Jordan, A., Schultz, U., Haensel, F., Seifert, T., and Heimann, M., 2010. Measurements of greenhouse gases and related tracers at Bialystok tall tower station in Poland. *Atmos. Meas. Tech*. **3**, 407-427.

Poulida, O., Dickerson, R. R., Doddridge, B. G., Holland, J. Z., Wardell, R. G., and Watkins, J. G., 1991. Trace gas concentrations and meteorology in rural Virginia, 1, ozone and carbon monoxide. *J. Geophys. Res*. **96**, 22461-22475.

Qi, H., Lin, W., Xu, X., Yu, X., and Ma, Q., 2012. Significant downward trend of SO_2 observed from 2005 to 2010 at a background station in the Yangtze Delta region, China. *Sci. China Chem.* **55**(7), 1451-1458.

Ramonet, M., et al., 2010. A recent build-up of atmospheric CO_2 over Europe. Part 1: observed signals and possible explanations. *Tellus* **62B**, 1-13.

Ren, X., 2015. Personal communication. 10 February 2015.

Roberts, J. M., et al., 1995. Relationships between PAN and ozone at sites in eastern North America. *J. Geophys. Res*. **100**(22), 22821-22830.

Rotach, M. W. and Zardi, D., 2007. On the boundary-layer structure over highly complex terrain: Key findings from MAP. *Q. J. Roy. Meteor. Soc*. **133**, 937-948.

Roth, D. M., 2006. Unified Surface Analysis Manual, NOAA Hydrometerological Prediction Center. Last access: 24 May 2010.

Saha, S., and co-authors, 2010. The NCEP climate forecast system reanalysis. *B. Amer. Meteorol. Soc*. **91**, 1015-1057.

Sahu, L. K., Kondo, Y., Miyazaki, Y., Pongkiatkul, P., and Oanh, N. T. K., 2011. Seasonal and diurnal variations of black carbon and organic carbon aerosols in Bangkok. *J. Geophys. Res*. **116**, D15302.

Saito, R., Tanaka, T., Hara, H., Oguma, H., Takamura, T., Kuze, H., and Yokota, T., 2009. Aircraft and ground-based observations of bounday layer CO_2 concentration in anticyclonic synoptic condition. *Geophys. Res. Lett*. **36**, L07807.

Sanders, F. and Doswell, C. A., 1995. A case study for detailed surface analysis. *B. Amer. Meteorol. Soc*. **6**(4), 505-521.

Sanders, F., 1999. A proposed method of surface map analysis. *Mon. Weather Rev*. **127**, 945-955.

Sarangi, T., Naja, M., Ojha, N., Kumar, R., Lal, S., Venkatarmani, S., Kumar, A., Sagar, R., and Chandola, H. C., 2014. First simultaneous measurements of ozone, CO, and NO_y at a high-altitude regional representative site in the central Himalayas. *J. Geophys. Res. Atmos*. **119**, 1592-1611.

Schmid, P. and Niyogi, D., 2011. A method for estimating planetary boundary layer heights and its application over the ARM Southern Great Plains Site. *J. Atmos. Ocean Tech*. **29**, 316-322.

Schmidli, J., Poulos, G. S., Daniels, M. H., and Chow, F. K., 2009. External influences on nocturnal thermally driven flows in a deep valley. *J. Appl. Meteorol. Climatol*. **48**, 3-23.

Schmidt, M., Graul, R., Sartorius, H. and Levin, I., 1996. Carbon dioxide and methane in continental Europe: a climatology, and ^{222}Radon-based emission estimates. *Tellus* **48B**, 457-473.

Schmidt, M., Graul, R., Satorius, H. and Levin, I., 2003. The Schauinsland CO_2 record: 30 years of continental observations and their implications for the variability of the European CO_2 budget. *J. Geophys. Res*. **108**(D19), 4619.

Schmidt, M., et al., 2014. High-precision quasi-continuous atmospheric greenhouse gas measurements at Trainou tower (Orléans forest, France). *Atmos. Meas. Tech.* **7**, 2283-2296

Schuh, A. E., Denning, A. S., Corbin, K. D., Baker, I. T., Uliasz, M., Parazoo, N., Andrews, A. E., and Worthy, D. E. J., 2010. A regional high-resolution carbon flux inversion of North America for 2004. *Biogeosciences* **7**, 1625-1644.

Segall, M., Avissar, R., McCumber, M. C., and Pielke, R. A., 1988. Evaluation of vegetation effects on the generation and modification of mesoscale circulations. *J. Atmos. Sci*. **45**(16), 2268-2292.

Seibert, P., Kromp-Kolb, H., Kapser, A., Kalina, M., Puxbaum, H., Jost, D. T., Schwikowski, M., and Baltensperger, U., 1998. Transport of polluted boundary layer air from the Po Valley to high-alpine sites. *Atmos. Environ.* **32**(23), 3953-3965.

Seibert, P., Beyrich, F., Gryning, S.-E., Joffre, S., Rasmussen, A., and Tercier, P., 2000. Review and intercomparison of operational methods for the determination of the mixing height. *Atmos. Environ*. **34**, 1001-1027.

Seidel, D. J., Ao, C. O., and Li, K., 2010. Estimating climatological planetary boundary layer heights from radiosonde observations: Comparison of methods and uncertainty analysis. *J. Geophys. Res.* **115**, D16113.

Seidel, D. J., Sun, B., Pettey, M., and Reale, A., 2011. Global radiosonde balloon drift statistics. *J. Geophys. Res*. **116**, D07102.

Seidel, D. J., Zhang, Y., Beljaars, A., Golaz, J.-C., Jacobson, A. R., and Medeiros, B., 2012. Climatology of the planetary boundary layer over the continental United States and Europe. *J. Geophys. Res*. **117**, D17106.

Seinfeld, J. H and Pandis, S. N., 2006. Atmospheric chemistry and physics: from air pollution to climate change. John Wiley and Sons, New York, NY.

Shafer, J. C. and Steenburgh, W. J., 2007. Climatology of strong intermountain cold fronts. *Mon. Weather Rev*. **136**, 784-807.

Shaw, G. E., 2007. Aerosols at a mountaintop observatory in Arizona. *J. Geophys. Res*. **112**, D07206.

Skamarock, W. C., Klemp, J. B., Dudhia, J., Gill, D. O., Barker, D. M., Duda, M. G., Huang, X. Y., Wang, W., and Powers, J. G., 2008: A description of the Advanced Research WRF version 3. NCAR Technical Note 475, Boulder: National Center for Atmospheric Research, 133.

Staudt, A. C., Jacob, D. J., Logan, J. A., Bachiochi, D., Krishnamurti, T. N., and Sachse, G. W., 2001. Continental sources, transoceanic transport, and interhemispheric exchange of carbon monoxide over the Pacific. *J. Geophys. Res*. **106**(D23), 32571-32589.

Steenburgh, W. J. and Blazek, T. R., 2001. Topographic distortion of a cold front over the Snake River Plain and Central Idaho Mountains. *Weather Forecast*. **16**, 301-314.

Stensrud, D. J., 2007. *Parameterization Schemes: Keys to Understanding Numerical Weather Prediction*. Cambridge University Press, 459 pp.

Stephens, B. B., De Wekker, S. F. J., Schimel, D., and Watt, A., 2005. A Regional Atmospheric Continuous CO_2 Network in the Rocky Mountains (Rocky RACCOON). 13th WMO/IAEA Meeting of Experts on Carbon Dioxide Concentration and Related Tracer Measurement Techniques, Boulder, CO. 2005.

Stohl, A., Hittenberger, M., and Wotawa, G., 1998. Validation of the Lagrangian particle dispersion model FLEXPART against large scale tracer experiment data. *Atmos. Environ*. **32**, 4245-4264.

Stohl, A., Eckhardt, S., Forster, C., James, P., Spichtinger, N., and Seibert, P., 2002. A replacement for simple back trajectory calculations in the interpretation of atmospheric trace substance measurements. *Atmos. Environ*. **36**, 4635-4648.

Stohl, A., Forster, C., Frank, A., Seibert, P., and Wotawa, G., 2005. Technical note: The Lagrangian particle dispersion model FLEXPART version 6.2. *Atmos. Chem. Phys*. **5**, 2461-2474.

Steyn, D. G., De Wekker, S. F. J., Kossmann, M., and Martilli, A., 2012. Boundary layers and air quality in mountainous terrain. In: Chow, F. K., De Wekker, S. F. J., and Snyder, B. J. (eds) *Mountain Weather Research and Forecasting: Recent Progress and Current Challenges*. Springer, Dordrecht, pp 261-289.

Stull, R. B., 1988. *An Introduction to Boundary Layer Meteorology*. Kluwer Academic Publishers, 666 pp.

Sun, J., Burns, S. P., Delany, A. C., Oncley, S. P., Turnipseed, A. A., Stephens, B. B., Lenschow, D. H., LeMone, M. A., Monson, R. K., and Anderson, D. E., 2007. CO_2 transport over complex terrain. *Agr. Forest Meteorol*. **145**, 1-21.

Sun, J., et al., 2009. A multi-scale and multi-disciplinary investigation of ecosystem-atmosphere CO_2 exchange over the Rocky Mountains of Colorado. *B. Amer. Meteorol. Soc*. **91**, 209-230.

Sun, J., and De Wekker, S. F. J., 2011. Atmospheric carbon dioxide transport over mountainous terrain, in: Mountain Ecosystem Dynamics, Nova Publishers. *In Press*.

Sun, W.-Y., and Ogura, Y., 1980. Modeling the evolution of the convective planetary boundary Layer. *J. Atmos. Sci*. **37**, 1558-1572.

Taubman, B. F., Marufu, L. T., Piety, C. A., Doddridge, B. G., Stehr, J. W., and Dickerson, R. R., 2004. Airborne characterization of the chemical, optical, and meteorological properties, and origins of a combined ozone-haze episode over the eastern United States. *J. Atmos. Sci*. **61**, 1781-1793.

Thompson, A. M., 1992. The oxidizing capacity of the earth's atmosphere: probable past and future changes. *Science* **256**(5060), 1157-1165.

Thompson, R. L., et al., 2009. In-situ measurements of oxygen, carbon monoxide and greenhouse gases from Ochsenkopf tall tower in Germany. *Atmos. Meas. Tech*. **2**, 573-591.

Thoning, K. W., Tans., P. P., and Komhyr, W. D., 1989. Atmospheric carbon dioxide at Mauna Loa Observatory. 2: Analysis of the NOAA/GMCC data, 1974-1985. *J. Geophys. Res*. **94**, 8549-8565.

Tohjima, Y., Mukai, H., and Patra, P. K., 2010. Increasing synoptic variability in atmospheric CO_2 at Hateruma Island associated with increasing East-Asian emissions. *Atmos. Chem. Phys.* **10**, 453-462.

Tsamalis, C., Favetta, R., Gheusi, F., Belbarre, H., and Augustin, P., 2014. Mixing of free-tropospheric air with the lowland boundary layer during anabatic transport to a high altitude station. *Atmos. Res*. **143**, 425-437.

Tuzson, B., et al. 2011. Continuous isotopic composition measurements of tropospheric CO_2 at Jungfraujoch (3580 ma.s.l.), Switzerland: real-time observation of regional pollution events. *Atmos. Chem. Phys*. **11**, 1685-1696.

Uccellini, L. W., Corfidi, S. F., Junker, N. W., Kocin, P. J., and Olson, D. A., 1992. Report on the surface analysis workshop at the National Meteorological Center 25-28 Mar. 1991. *B. Amer. Meteorol. Soc*. **73**, 459-471.

van der Molen, M. K. and Dolman, A. J., 2007. Regional carbon fluxes and the effect of topography on the variability of atmospheric CO_2. *J. Geophys. Res. Atmos*. **112**, D01104.

Venzac, H., Sellegri, K., Villani, P., Picard, D., and Laj, P., 2009. Seasonal variation of aerosol size distributions in the free troposphere and residual layer at the puy de Dôme station, France. *Atmos. Chem. Phys*. **9**, 1465-1478.

Vogelezang, D. H. P. and Holtslag, A. A. M., 1996. Evaluation and model impacts of alternative boundary-layer height formulations. *Bound-Lay. Meteorol*. **81**, 245-269.

Volz-Thomas, A., Patz, H.-W., Houben, N., Konrad, S., Mihelcic, D., Klüpfel. T., and Perner, D., 2003. Inorganic trace gases and peroxy radicals during BERLIOZ at Pabstthum: An investigation of the photostationary state of NO_x and O_3. *J. Geophys. Res*. **108**(D4), 8248.

von Engeln, A. and Teixeira, J., 2013. A planetary boundary layer height climatology derived from ECMWF re-analysis data. *J. Climate* **26**, 6575-6590.

Vögtlin, R., et al., 1996. Transport of trace gases from the Upper Rhine Valley to a mountain site in the Northern Black Forest. *Phys. Chem. Earth* **21**(5-6), 425-428.

Wang, J. W., Denning, A. S., Lu, L., Baker, I. T., Corbin, K. D., and Davis, K. J., 2007. Observations and simulations of synoptic, regional, and local variations in atmospheric CO_2. *J. Geophys. Res*. **112**, D04108.

Wang, Y., Zhang, Y., Hao, J., and Luo, M., 2011. Seasonal and spatial variability of surface ozone over China: contributions from background and domestic pollution. *Atmos. Chem. Phys.* **11**, 3511-3525.

Wang, X. Y. and Wang, K. C., 2014. Estimation of atmospheric mixing layer height from radiosonde data. *Atmos. Meas. Tech*. **7**, 1701-1709.

Weiss-Penzias, P., Jaffe, D. A., Swartzendruber, P., Dennison, J. B., Chand, D., Hafner, W., and Prestbo, E., 2006. Observations of Asian air pollution in the free troposphere at Mount Bachelor Observatory during the spring of 2004. *J. Geophys. Res*. **111**, D10304.

Whiteman, C. D. and Allwine, K. J., 1986. Extraterrestrial solar radiation on inclined surfaces. *Environ. Softw.* **1**(3), 164-169.

Whiteman, C. D., Zhong, S., and Bian, X., 1997. Wintertime boundary layer structure in the Grand Canyon. *J. App. Meteorol*. **38**, 1084-1102.

Whiteman, C. D., Bian, X., and Zhong, S. 1999a. Wintertime evolution of the temperature inversion in the Colorado Plateau Basin. *J. Appl. Meteor*. **38**, 1103–1117.

Whiteman, C. D., Bian, X., and Sutherland, J. L., 1999b. Wintertime surface wind patterns in the Colorado River Valley. *J. Appl. Meteor*. **38**, 1118–1130.

Whiteman, C. D., 2000. *Mountain Meteorology: Fundamentals and Applications*. Oxford University Press, 355 pp.

Winderlich, J., Chen, H., Gerbig, C., Seifert, T., Kolle, O., Lavrič, J. V., Kaiser, C., Höfer, A., and Heimann, M., 2010. Continuous low-maintenance $CO_2/CH_4/H_2O$ measurements at the Zotino Tall Tower Observatory (ZOTTO) in Central Siberia. *Atmos. Meas. Tech*. **3**, 1113-1128.

Winker, D. M., Hunt, W. H., and McGill, M. J., 2007. Initial performance assessment of CALIOP. *Geophys. Res. Lett*. **34**, L19803.

Xie, B., Fung, J. C. H., Chan, A., and Lau, A., 2012. Evaluation of nonlocal and local planetary boundary layer schemes in the WRF model. *J. Geophys. Res*. **117**, D12103.

Xie, B., Hunt, J. C. R., Carruthers, D. J., Fung, J. C. H., and Barlow, J. F., 2013. Structure of the planetary boundary layer over Southeast England: modeling and measurements. *J. Geophys. Res. Atmos*. **118**, 7799-7818.

Xiu, A. and Pleim, J. E., 2001. Development of a land surface model. part I: application in a mesoscale meteorological model. *J. Appl. Meteorol*. **40**, 192-209.

Xu, J., et al., 2013. Seasonal and diurnal variations in aerosol concentrations at a high-altitude site on the northern boundary of Qinghai-Xizang Plateau. *Atmos. Res.* **120-121**, 240-248.

Yi, C., Davis, K. J., Berger, B. W. and Bakwin, P. S., 2001. Long-term observations of the dynamics of the continental planetary boundary layer. *J. Atmos. Sci*. **58**, 1288-1299.

Yver, C. E., Graven, H. D., Lucas, D. D., Cameron-Smith, P. J., Keeling, R. F., and Weiss, R. F., 2013. Evaluating transport in the WRF model along the California coast. *Atmos. Chem. Phys*. **13**, 1837-1852.

Zellwegger, C., et al., 2003. Partitioning of reactive nitrogen (NO_y) and dependence on meteorological conditions in the lower free troposphere. *Atmos. Chem. Phys*. **3**, 779-796.

Zhang, D.-L. and Zheng, W.-Z., 2004. Diurnal cycles of surface winds and temperatures as simulated by five boundary layer parameterizations. *J. Appl. Meteorol*. **43**, 157-169.

Zhang, F. and Zhou, L. X., 2013. Implications for CO_2 emissions and sinks changes in western China during 1995-2008 from atmospheric CO_2 at Waliguan. *Tellus B* **65**(1), 1-14.

Zhang, Y., Gao, Z., Li, D., Li, Y., Zhang, N., Zhao, X., and Chen, J., 2014. On the computation of planetary boundary layer height using the bulk Richardson number method. *Geosci. Model Dev. Discuss.* **7**, 4045-4079.

Zhao, C. L. and Tans, P. P., 2006. Estimating uncertainty of the WMO mole fraction scale for carbon dioxide in air. *J. Geophys. Res*. **111**, D08S09.

Zhou, L., Tang, J., Wen, Y., Li, J., Yan, P., and Zhang, X., 2003. The impact of local winds and long-range transport on the continuous carbon dioxide record at Mount Waliguan, China. *Tellus* **55B**, 145-158.

Zimmerman, P. R., Chatfield, R. B., Fishman, J., Crutzen, P. J. and Hanst, P. L., 1978. Estimates on the production of CO and H_2 from the oxidation of hydrocarbon emissions from vegetation. *Geophys. Res. Lett*. **5**(8), 679-682.

Zong, S. and Chow, F. K., 2012. Meso- and fine-scale modeling over complex terrain: parameterizations and applications. In: Chow, F. K., De Wekker, S. F. J., and Snyder, B. J. (eds) *Mountain weather research and forecasting: recent progress and current challenges*. Springer, Dordrecht, pp 591-654.

Appendix

A.1. Data quality control

This section summarizes the maintenance and quality control procedures that were followed at Pinnacles, both for the site and for the instruments installed at Pinnacles as of March 2015 (Figure A.1.1, Table A.1.1), from July 2008 through March 2015 to ensure the highest quality data set possible. Following the procedures summarized in this section is vital to ensure that long-term, high-quality measurements continue.

A.1.1. Site maintenance

Visits to the site should be performed at a frequency of every 2-3 weeks. For the purposes of safety, it is strongly advised that at least two people visit the site. During each visit, the following tasks need to be performed. These tasks are necessary to ensure the integrity of the tower, as well as the instruments installed on-site.

- Download data from the CR-1000 logger 2 m agl
- Download data from the CR-3000 logger 14 m agl
- Download data from the temperature/relative humidity sensors deployed 1.5 m agl adjacent to tower
- Check the tension in the guy wires
- Clean the pyranometer and net radiometer with moist paper towels
- Remove debris from the two rain gauges, located on opposite corners of the on-site shed
- Verify that the cup anemometers installed 10 m agl and 17 m agl are spinning freely
- Verify that the temperature aspirator blower motor 2 m agl is functioning properly
- Confirm there are no loose wires or cables, and secure if necessary using zip ties
- Perform any necessary maintenance activities on the CO/CO_2 monitoring system as per the request of Arlyn Andrews or Jonathan Kofler at NOAA ESRL. The most common maintenance activity is to replace one of the ten on-site calibration cylinders, typically at a frequency of 1-2 months. However, other maintenance

activities, e.g. replacing the pump box, replacing the peristaltic pump, verifying on-site internet connectivity, etc., may be performed depending on the specific needs.

- Sweep the floors in the shed, and ensure that the interior of the shed is tidy
- Document the site visit to include the time spent at the site, maintenance activities performed, visitors, etc., into the site maintenance log book on EverNote

At times, other students may visit the site as part of, e.g. undergraduate or graduate courses at UVA or neighboring universities. If there are visitors to the site and the visitors wish to climb the on-site tower, it is advised that no more than three people are allowed to climb the tower at one time.

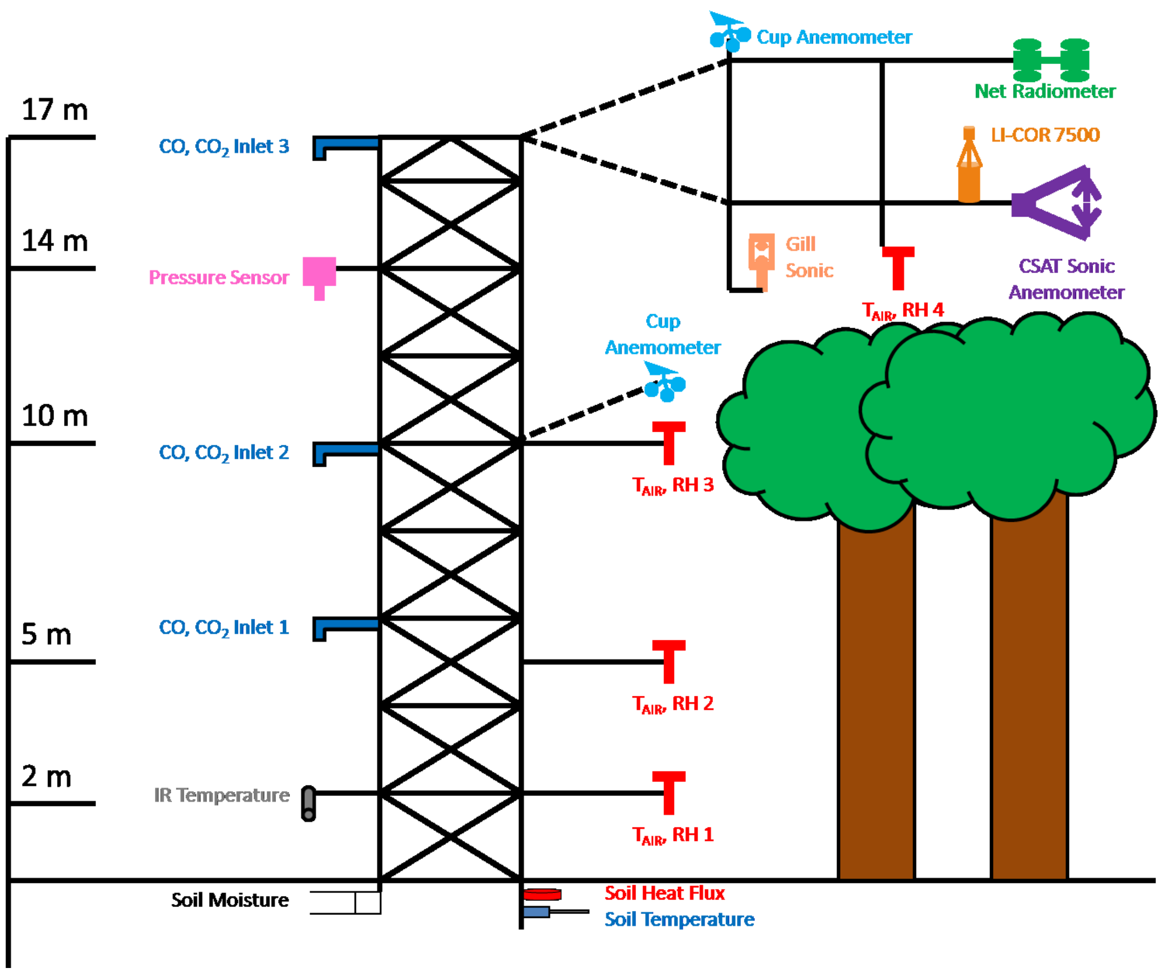

Figure A.1.1: Diagram of instruments at Pinnacles as of March 2015. Instruments are not to scale. Figure modified from Lee (2011).

Table A.1.1: Meteorological instruments at Pinnacles, manufacturer, installation date, data logger to which the instrument is wired, sampling technique, and manufacturer-stated accuracy.

Name	Height (m agl)	Company	Model Number	Date Installed	Data Logger	Sampling Technique	Instrument Accuracy
Soil heat flux plate	-0.1	Hukseflux	HFP01SC	Feb, 2011	CR-1000	1 min mean of 1 Hz sample	±3% of reading
Soil moisture sensor	-0.1	Campbell Scientific	CS616	Feb, 2011	CR-1000	1 min mean of 1 Hz sample	±2.5% of reading
Soil temperature sensor (ST1)	-0.1	Campbell Scientific	109SS	Feb, 2011	CR-1000	1 min mean of 1 Hz sample	±0.6°C over the range -20°C to 70°C
Soil temperature sensor (ST2)	-0.1	Campbell Scientific	109SS	Feb, 2011	CR-1000	1 min mean of 1 Hz sample	±0.6°C over the range -20°C to 70°C
Aspirated temperature sensor	2	RM Young	43347	Feb, 2011	CR-1000	1 min mean of 1 Hz sample	±0.3°C at 0°C
IR temperature sensor	2	Apogee	SI-111	Feb, 2011	CR-1000	1 min mean of 1 Hz sample	±0.2°C over the range -20°C to 65°C
Temperature probe with radiation shield (T-RH1)	2	Vaisala	HMP45C	May, 2008	CR-3000	30 min mean of 1 Hz sample	±0.2°C at 20°C (T); ±2% (RH)
Tipping bucket rain gage	2.5	Texas Instruments	TR-525I	May, 2008	CR-3000	30 min total	±1% at 1 in hr^{-1}
Temperature-relative humidity probe with radiation shield (T-RH2)	5	Vaisala	HMP45C	May, 2008	CR-3000	30 min mean of 1 Hz sample	±0.2°C at 20°C (T); ±2% (RH)
Temperature-relative humidity probe with radiation shield (T-RH3)	10	Vaisala	HMP45C	May, 2008	CR-3000	30 min mean of 1 Hz sample	±0.2°C at 20°C (T); ±2% (RH)
Wind sensor (WS-1)	10	MetOne	034B	May, 2008	CR-3000	30 min mean of 1 Hz sample (w. spd.); 30 min sample (w. dir.)	±0.12 ms^{-1} for speed <10.1 ms^{-1} (speed); ±4° (direction)
Barometer	14	Vaisala	PTB110	May, 2008	CR-3000	30 min mean of 1 Hz sample	±2 mb over T range -20°C to 45°C
4 component net-radiation Sensor	17	Hukseflux	NR-01	May, 2008	CR-3000	30 min mean of 1 Hz sample	±5% of reading
CSAT	17	Campbell Scientific	CSAT3	May, 2008	CR-3000	10 Hz sample	±8 cm s^{-1} (u_x, u_y); ±3 cm s^{-1} (u_z)
Licor gas analyzer	17	LI-COR	Li-7500	May, 2008	CR-3000	10 Hz sample	Frequency of calibration
Pyranometer	17	Kip and Zonen	CMP3	May, 2008	CR-3000	30 min mean of 1 Hz sample	±5% of reading
Temperature-relative humidity probe with radiation shield (T-RH4)	17	Vaisala	HMP45C	May, 2008	CR-3000	30 min mean of 1 Hz sample	±0.2°C at 20°C (T); ±2% (RH)
Wind sensor (WS-2)	17	MetOne	034B	May, 2008	CR-3000	30 min mean of 1 Hz sample (w. spd.); 30 min sample (w. dir.)	±0.12 ms^{-1} for speed <10.1 ms^{-1} (speed); ±4° (direction)

A.1.2. Instrument maintenance

Below are the recommended maintenance procedures for the on-site meteorological instruments, based on the recommendations in the each instrument's instruction manual referenced in parentheses. Following these procedures is vital to ensure a high-quality data set from each instrument.

- Temperature/humidity probe (Campbell Scientific, 2009a):
  - Once per month: verify radiation shield is free from debris
  - Once per year: return the instrument to the factory for recalibration
- Aspirated temperature instrument (Campbell Scientific, 2010a):
  - Once per month: inspect and clean the shield and probe; wash the shield with warm water when the instrument apparatus is dirty
  - Once per year: return the instrument to the factory for recalibration
- CMP3 shortwave radiation (Campbell Scientific, 2009b):
  - Once per month:
    - Clean the instrument's dome using water or alcohol
    - Inspect the instrument's dome to ensure that no condensation is present
  - Once every 2 years
    - Return the instrument to the factory for recalibration
- Net radiometer (Campbell Scientific, 2010b):
  - Once per month:
    - Clean the instrument's dome using water or alcohol
    - Inspect the instrument's dome to ensure that no condensation is present
  - Once every 2 years: return the instrument to the factory for recalibration
- Cup anemometer (Campbell Scientific, 2011):
  - Once per month:
    - Visually inspect the anemometer for any physical damage
    - Verify that the cups and wind vane are rotating
  - Once per year: replace the anemometer bearings
  - Once every 2 years: replace the wind vane potentiometer and bearings

- CSAT sonic anemometer (Campbell Scientific, 2012):
    - Once per month: confirm the orientation of the anemometer by following the instructions in the instrument manual
    - Once every 1-2 years: return the instrument to the factory for recalibration
- LI-COR (LI-COR Environmental Division, 2001):
    - Once per month: clean the instrument's windows with a glass cleaner
    - Weekly-monthly: recalibrate the instrument following the instructions from the manual
- Pressure sensor (Vaisala):
    - No routine maintenance is required
- Tipping bucket rain gauge (Campbell Scientific, 2010c):
    - Once per month: check for and remove any debris
    - Once per year: recalibrate on-site following the instructions in the instrument's manual
- Soil temperature sensor (Campbell Scientific, 2010d):
    - Once per month: check the cables for damage
- Soil moisture sensor (Campbell Scientific, 2014a):
    - Once per month: check the cables for damage
- Soil heat flux plate (Campbell Scientific, 2014b):
    - Once per month: check the cables for damage

A.1.3. Data processing and quality control

The data sets from the instruments installed at Pinnacles are saved into three separate files. Measurements from the instruments connected to the CR-1000 data logger (c.f. Table A.1.1) store one-minute means of the data; half-hour means from the instruments connected to the CR-3000 data logger are stored (Figure A.1.2). In addition, 10 Hz wind, water vapor, and CO_2 mixing ratios from the CSAT and LI-COR are saved to separate file on the CR-3000 data logger. The files are stored onto a compact flash (CF) card connected to the respective data loggers, and the files are downloaded from the CF card onto a laptop during each site visit. These data files are then stored onto an external hard drive. These data files undergo the following quality control procedures that are specific to each measurement to produce one file that contains the quality-controlled half-hour data for the site. In this section, the focus is on processing the subset of meteorological measurements from Pinnacles that were used in this dissertation.

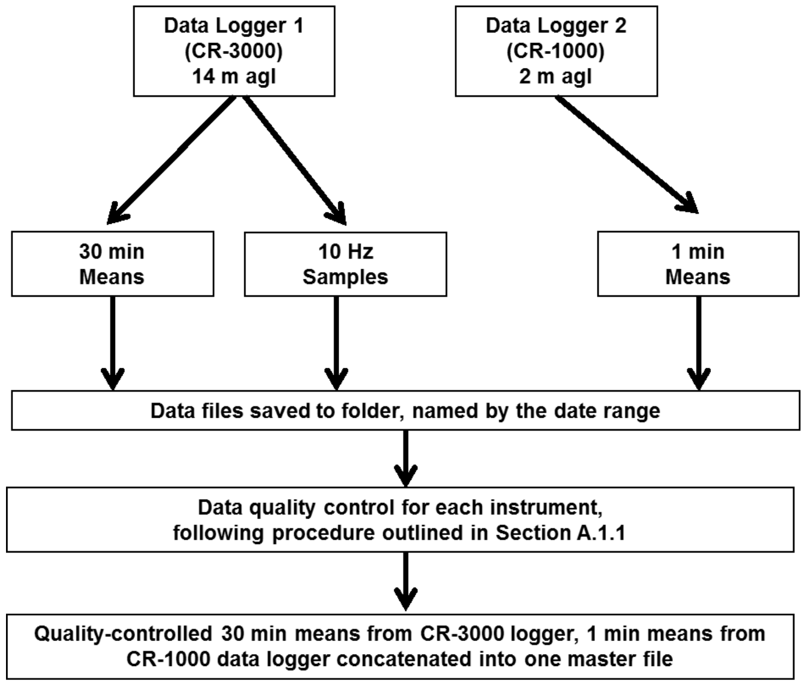

Figure A.1.2: Data acquisition and quality control procedure used to generate one file containing quality-controlled half-hour means of all meteorological measurements from Pinnacles (excluding the 10 Hz data).

A.1.3.1. Temperature and humidity measurements

Temperature and relative humidity measurements outside the thresholds listed in Table A.1.2 are replaced with NaN values. Because temperature and humidity are measured at four heights, measurements that are unrealistically different from the others are removed and replaced with NaN values (i.e. differences >±15°C for temperature and >±20% for relative humidity).

A.1.3.2. Wind measurements

Wind measurements made when the wind speed is 0 m s^{-1} for >30 min are removed and replaced with NaN values. Extended periods (sometimes >12 h) of 0 m s^{-1}

wind speeds are caused by rime ice on the instruments that occasionally occurs between late October and early April. Wind speeds of 0 m s^{-1} for >12 h also occurred when the cup anemometer's potentiometer malfunctioned for several periods in summer, 2009 and summer, 2011. Values outside the thresholds listed in Table A.1.2 are also replaced with NaN values.

A.1.3.3. Precipitation measurements

Because the rain gauges at Pinnacles are not heated, they cannot measure frozen precipitation, which is a routine occurrence between late October and early April. For this reason, precipitation data from Big Meadows, a quality-controlled precipitation monitoring site with a heated rain gauge, are used as a surrogate for precipitation at Pinnacles.

Table A.1.2: Thresholds of half-hour data for the meteorological variables sampled at Pinnacles that were used in this dissertation. If a value does not fall within the above range, it is replaced with NaN in the processed data file. *Note that pressure recorded at Pinnacles is not adjusted to msl.

Variable	Minimum Threshold	Maximum Threshold
Wind speed	0 m s^{-1}	30 m s^{-1}
Wind direction	0°	360°
Temperature	-40°C	40°C
Relative humidity	0%	100%
Radiation	-100 W m^{-2}	1200 W m^{-2}
Sensible heat flux	-100 W m^{-2}	1200 W m^{-2}
Latent heat flux	-100 W m^{-2}	1200 W m^{-2}
Precipitation	0 mm	100 mm
Pressure*	800 mb	1000 mb

A.1.3.4. Flux measurements

The CSAT sonic anemometer is unable operate during periods when water droplets adhere to the instrument's transducers and obscure the signal transfer (e.g. Campbell Scientific, 2012). For this reason, CSAT measurements made during periods of precipitation are removed and replaced with NaN values. These data are then used to compute the half-hour fluxes, which are stored onto the CR-3000 data logger. The computation of these fluxes is summarized below following Lee (2011). First, the half-hour means of air and vapor densities are determined:

$$\rho_v = \frac{e}{R_v T_{vaisala}} \tag{A.1.3.1}$$

$$\rho_D = \frac{\bar{P} - e}{R_D T_{vaisala}} \tag{A.1.3.2}$$

$$\rho_a = \frac{\rho_d + \rho_v}{R_D T_{vaisala}} \tag{A.1.3.3}$$

$$\sigma = \frac{\rho_v}{\rho_D} \tag{A.1.3.4}$$

where $\bar{P}$ is the mean half-hour pressure, e is the vapor pressure, R_v is the water vapor gas constant, ρ_v is the vapor density, $T_{vaisala}$ is the half-hour mean temperature from the 17 m Vaisala temperature sensor, R_D is the dry air gas constant, ρ_D is the density of dry air, and ρ_a is the mean air density. These quantities are used to compute the latent heat flux. Following Webb et al. (1980), a correction is included to correct the fluxes for density effects that arise because of water vapor and heat transfer:

$$LE_{irga} = L_v * cov(H_2O * U_z) \tag{A.1.3.5}$$

$$LE_{WPL} = \mu\sigma LE_{irga} \tag{A.1.3.6}$$

$$LE_H = (1 + \mu\sigma)\frac{\rho_v}{\bar{T}} * L_v * cov(T_s * U_z) \tag{A.1.3.7}$$

$$H_s = \rho_a C_p * cov(T_s * U_z) \tag{A.1.3.8}$$

$$H_c = H_s - \frac{0.51 * LE * \overline{\rho_a} c_p R_d \overline{(T_s)(T_{vaisala})}}{\bar{P} L_v \frac{\overline{T_{vaisala}}}{\overline{T_s}}} \tag{A.1.3.9}$$

where c_p is the specific heat capacity of air, L_v is the latent heat of vaporization, H_2O is the water vapor mixing ratio obtained from the LI-COR, U_z is the CSAT-derived vertical wind velocity, μ is the ratio of the molecular weight of dry air to moist air, σ is the density of water vapor to the density of dry air, $\overline{T_s}$ is the temperature from the CSAT sonic anemometer, H_s is the sensible heat flux computed using the sonic temperature, H_c is the sensible heat flux computed using H_s and LE_{WPL}, LE_{irga} is the latent heat flux without the Webb et al. term, LE_{WPL} is the latent heat flux with the Webb et al. (1980) term, and LE_H is the latent heat flux with the Webb et al. (1980) term due to sensible heat flux. These terms are used to calculate the CO_2 flux, F_{CO_2}:

$$F_H = 1 + \mu\sigma \frac{\overline{CO_2}}{\overline{T}} * C_p \frac{H_c}{\overline{\rho_a}} \tag{A.1.3.10}$$

$$F_{WPL} = \mu \frac{\overline{CO_2}}{\overline{\rho_D}} cov(H_2O * U_z) \tag{A.1.3.11}$$

$$F_{C_{irga}} = cov(CO_2 * U_z) \tag{A.1.3.12}$$

$$F_{CO_2} = F_H + F_{WPL} + F_{C_{irga}} \tag{A.1.3.13}$$

where F_H is the CO_2 flux with the Webb et al. (1980) term due to sensible heat flux, F_{WPL} is the CO_2 flux with the Webb et al. (1980) term, and $F_{C_{irga}}$ is the CO_2 flux without the Webb et al. (1980) term.

A.1.4. References

Campbell Scientific, 2009a. Model HMP45C temperature and relative humidity probe. Instruction manual, Campbell Scientific, Logan, UT.

Campbell Scientific, 2009b. CMP3-L pyranometer. Instruction manual, Campbell Scientific, Logan, UT.

Campbell Scientific, 2010a. 43347 RTD temperature probe and 43502 aspirated radiation shield. Instruction manual, Campbell Scientific, Logan, UT.

Campbell Scientific, 2010b. NR01 four-component net radiation sensor. Instruction manual, Campbell Scientific, Logan, UT.

Campbell Scientific, 2010c. TE525 tipping bucket rain gage. Instruction manual, Campbell Scientific, Logan, UT.

Campbell Scientific, 2010d. Model 109SS temperature probe. Instruction manual, Campbell Scientific, Logan, UT.

Campbell Scientific, 2011. Met One 034B windset. Instruction manual, Campbell Scientific, Logan, UT.

Campbell Scientific, 2012. CSAT3 three dimensional sonic anemometer. Instruction manual, Campbell Scientific, Logan, UT.

Campbell Scientific, 2014a. CS616 and CS625 water content reflectometers. Instruction manual, Campbell Scientific, Logan, UT.

Campbell Scientific, 2014b. Model HFP01SC self-calibrating soil heat flux plat. Instruction manual, Campbell Scientific, Logan, UT.

Lee, T. R., 2011. Frontal impacts on carbon dioxide concentrations at a forested site in the Virginia Blue Ridge Mountains. Master's thesis, University of Virginia, Charlottesville, VA.

LI-COR Environmental Division, 2001. LI-7500 CO_2/H_2O analyzer. Instruction manual, LI-COR, Lincoln, NE.

Vaisala. Vaisala BAROCAP Barometer PTB110 Series. User's Guide.

Webb, E. K., Pearman, G. I., and Leuning, R., 1980. Correction of flux measurements for density effects due to heat and water vapour transfer. *Q. J. Roy. Meteor. Soc*. **106**(447), 85-100.